OPTIMAL SPEED TRAJECTORY AND ENERGY MANAGEMENT CONTROL FOR CONNECTED AND AUTOMATED VEHICLES

Xiao Pan

Supervisor: Dr. Simos A. Evangelou

Department of Electrical and Electronic Engineering
Imperial College London

This dissertation is submitted for the degree of
Doctor of Philosophy

May 2023

I would like to dedicate this thesis to my loving parents.

Declaration of Originality

This is to certify that to the best of my knowledge, the content of this thesis is my own work. This thesis has not been submitted for any degree or other purposes.

I certify that the intellectual content of this thesis is the product of my own work and that all the assistance received in preparing this thesis and sources have been properly acknowledged.

Xiao Pan
May 2023

Declaration of Copyright

Xiao Pan
May 2023

Acknowledgements

This thesis is the result of research work carried out at the Department of Electrical and Electronic Engineering, Imperial College London. First and foremost, I would like to express my deepest gratitude to my supervisor, Dr. Simos A. Evangelou, for providing me with an opportunity, an excellent atmosphere, and particularly a remote working condition during the pandemic period to improve technically as well as to better understand the academic world and its intricacies. Without your persistent guidance, and caring, this thesis would not have been completed.

I wish to thank Boli Chen from University College London for his invaluable advice and help during the highs and lows of the PhD. I am very fortunate to have had him as a collaborator since the beginning of my PhD. I am indebted to Dr. Stelios Timotheou from the University of Cyprus for his precious feedback that improved the works in this thesis from many directions. A very special thank you to Dr. Li Dai from the Beijing Institute of Technology for her priceless advice since I was an undergraduate student. In particular, the opportunity you offered me allowed me to continue my research remotely in China during the pandemic period. I would also like to thank Sheng Yu, Anastasis Georgiou and Dr. Imad M. Jaimoukha of the Control and Power Research Group at Imperial College London for sharing their inspiration during our collaboration. Without your thoughtful and candid advice, I would not have been able to complete my research and get through to the end of my PhD.

I would also like to thank my friends in no particular order. During these years in London, my friends at Imperial have been the spice of my life. Thanks to Youwen Li, Jieming Ye, Zilin Feng and Jiayi Sun for the joyful moments as well as the hard times we shared when I was in London. The bonds between us are like family, and I am extremely grateful to meet you and have you as my friend. Conghui Li was my GTA of probability and stochastic process and is also a friend of mine, and I still remember it was you inviting me to have dinner with your friends after I just arrived in London. Thanks to Runyu Xu for being my guide in pursuing my academic in the U.K., and providing me with internship opportunities.

My best friends in China also contributed to making this journey sweeter and I am glad our paths crossed. Tianqi Yang, my best friend with whom I have talked literately everything, persuaded me to pursue the degree of PhD when I was hesitating after I completed my MSc at Imperial, and I am particularly thankful for that. Yi Xiong is my perfect PhD mate and I will always remember the days we had fun and joy in Oxford. Hang Du, who is one of the few people I found so easy to talk to, has always been ready for games and sports in the evenings and weekends, and these leisure moments help me get rid of the tiredness after a long day of work. Ding Wu is also a key member of our sport and game group, and your sweet love life encourages me to find my true love, which I am always grateful for, and I wish your love can last forever. Zihao Wang, who I get along with since we are high school roommate, and I am grateful we become a friends for life to share happiness. Shengqi Li, Yuanjing Wang, Yuying Zhao, and Beidi Li, who always came to my rental residence 2708 in Beijing during weekends, and those happy memories will always be kept in my heart. Haochen Hou, who I sincerely thank for helping me establish confidence in my industrial career and providing residence for my internship in Shanghai. Yijia Zhang, whose talks are always enlightening, and the memories in Shanghai I will always cherish. Hao Wu, who I got along with since I moved to Beijing, provides me with lots of advises in life and is always supportive, and I am thankful to have you as my friend. Runze Gao, who was my roommate since my undergraduate, and I am delighted to have you to experience brainstorming on academics. Also, I would like to thank my cousins, Sihang Liu who provided me with guidance and helps when I was facing difficulties in academics, and Shengning Zhang who is a great jungle player when we played games together and those happy game memories I will always treasure.

A very special thank you to Xueyan Niu for having you as my partner. I strongly believe that this work would have not been possible without your love, encouragement, and belief in me.

Finally, I owe my deepest gratitude towards my family, for their unceasing understanding and support. Without them, I could have never achieved any of these results. Thank you for supporting me when it mattered the most.

Abstract

Connected and automated vehicles (CAVs) emerge as a promising solution to improve urban mobility, safety, energy efficiency, and passenger comfort with the development of communication technologies, such as vehicle-to-vehicle (V2V) and vehicle-to-infrastructure (V2I). This thesis proposes several control approaches for CAVs with electric powertrains, including hybrid electric vehicles (HEVs) and battery electric vehicles (BEVs), with the main objective to improve energy efficiency by optimising vehicle speed trajectory and energy management system. By types of vehicle control, these methods can be categorised into three main scenarios, optimal energy management for a single CAV (single-vehicle), energy-optimal strategy for the vehicle following scenario (two-vehicle), and optimal autonomous intersection management for CAVs (multiple-vehicle).

The first part of this thesis is devoted to the optimal energy management for a single automated series HEV with consideration of engine start-stop system (SSS) under battery charge sustaining operation. A heuristic hysteresis power threshold strategy (HPTS) is proposed to optimise the fuel economy of an HEV with SSS and extra penalty fuel for engine restarts. By a systematic tuning process, the overall control performance of HPTS can be fully optimised for different vehicle parameters and driving cycles.

In the second part, two energy-optimal control strategies via a model predictive control (MPC) framework are proposed for the vehicle following problem. To forecast the behaviour of the preceding vehicle, a neural network predictor is utilised and incorporated into a nonlinear MPC method, of which the fuel and computational efficiencies are verified to be effective through comparisons of numerical examples between a practical adaptive cruise control strategy and an impractical optimal control method. A robust MPC (RMPC) via linear matrix inequality (LMI) is also utilised to deal with the uncertainties existing in V2V communication and modelling errors. By conservative relaxation and approximation, the RMPC problem is formulated as a convex semi-definite program, and the simulation results prove the robustness of the RMPC and the rapid computational efficiency resorting to the convex optimisation.

The final part focuses on the centralised and decentralised control frameworks at signal-free intersections, where the energy consumption and the crossing time of a group of CAVs are minimised. Their crossing order and velocity trajectories are optimised by convex second-order cone programs in a hierarchical scheme subject to safety constraints. It is shown that the centralised strategy with consideration of turning manoeuvres is effective and outperforms a benchmark solution invoking the widely used first-in-first-out policy. On the other hand, the decentralised method is proposed to further improve computational efficiency and enhance the system robustness via a tube-based RMPC. The numerical examples of both frameworks highlight the importance of examining the trade-off between energy consumption and travel time, as small compromises in travel time could produce significant energy savings.

Table of contents

Notation

$\mathrm{sign}(\cdot)$	Signum function
$\emptyset$	Empty set
$\mathbb{N}$	Natural number
$\mathbb{R}$	Real number
$\mathbb{Z}$	Integer number

Symbols used in this thesis

$a_{\min}$	Peak deceleration during an emergency brake
$\mathcal{C}_h$	the set collects vehicles travelling in the same direction as the ith vehicle
E	Kinetic Energy of a vehicle
E_{ref}	Kinetic Energy of a reference vehicle
F_d	Resistance forces of aerodynamics drag
F_h	Mechanical braking force acting on the wheels
F_{PS}	Powertrain driving force acting on the wheels from the primary source
F_{SS}	Powertrain driving force acting on the wheels from the secondary source
F_t	Powertrain driving force acting on the wheels
F_w	Powertrain driving or braking force acting on the wheels
f_d	Coefficient of resistance forces of aerodynamics drag
f_r	Coefficient of resistance forces of rolling
g	Gravity
g_r	Gear ratio
J_b	Battery energy usage
$\mathcal{L}_h$	the set collects vehicles travelling in the vertical directions to the ith vehicle
m	Mass of a vehicle
m_f	Fuel consumption
m_{ref}	Mass of a reference vehicle
$N(t)$	the total number of CAVs

$\mathcal{N}$	Intersection crossing order of a group of CAVs
N_p	Prediction horizon
$\mathcal{O}_h$	the set collects vehicles travelling in the opposite direction to the *i*th vehicle
P_b	Battery output power
P_{drive}	Power at the driving wheels
P_h	Power of mechanical braking
P_{PL}	Output power of propulsion load branch
P_{PS}	Output power of primary source branch
P_{SS}	Output power of secondary source branch
$Q_{\max}$	Battery capacity
q_f	Fuel mass rate
R_b	Internal resistance
r_w	Wheel radius
SOC	Battery state-of-charge
s	Travelled distance
s_{ref}	Travelled distance of a reference vehicle
T_m	Motor torque
T_s	Sampling time
t	Time
t_{ref}	Time of a reference vehicle
u	System control input
$\mathbf{u}$	System control input set
V_b	Battery voltage
V_{oc}	Open circuit voltage of the battery,
v	Linear forward velocity of a vehicle
v_{ref}	Linear forward velocity of a reference vehicle
x	System state
$\mathbf{x}$	System state set
y	System output
η_{dc}	Converter efficiency
η_i, η_r	Inverter efficiency
η_m	Motor/generator efficiency
η_t	Transmission efficiency
θ	Road slope angle

ν	Measurement disturbance
ω	Process disturbance
ω_m	Motor angular velocity

Subscripts, superscripts and accents

$\hat{x}$	Estimate system state
$\bar{x}$	Nominal system state
x^*	Optimal system state
$\bar{u}$	Nominal system control input
u^*	Optimal system control input
x_i	System state of ith vehicle
u_i	System control input of ith vehicle

Abbreviations

ACC	Adaptive Cruise Control
BEV	Battery Electric Vehicle
CAV	Connected and Automated Vehicle
CO	Carbon Monoxide
ComZ	Communication Zone
CS	Charge Sustaining
CZ	Control Zone
DP	Dynamic Programming
EACC	Enhanced Adaptive Cruise Control
ECMS	Equivalent Consumption Minimisation Strategies
EFC	Equivalent Fuel Consumption
EM	Energy Management
FCM	Fuel Consumption model
FIFO	First-In-First-Out
HC	Hydrocarbon
HEVs	Hybrid Electric Vehicles
HPTS	Hysteresis Power Threshold Strategy
HRCS	Hierarchical Robust Control Strategy
ICE	Internal Combustion Engine
LMI	Linear Matrix Inequality
MPC	Model Predictive Control
MZ	Merging Zone
NMPC	Nonlinear Model Predictive Control
NN	Neural Network
NOx	Nitrogen Oxide
OCP	Optimal Control Problem

PL	Propulsion Load
PMP	Pontryagin’s Minimum Principle
PS	Primary Source
RMPC	Robust Model Predictive Control
SOC	State of Charge
SOCP	Second-Order Cone Programming
SDPR	Semi-Definite Programming Relaxation
SS	Secondary Source
SSS	Start-Stop System
TTC	Time-To-Collision
V2V	Vehicle-to-Vehicle
V2I	Vehicle-to-Infrastructure
V2X	Vehicle-to-Everything
WLTP	Worldwide harmonised Light vehicles Test Procedure
XOS	Exclusive Operation Strategy

List of Figures

List of Tables

Chapter 1

Introduction

1.1 Background

In recent years, urbanisation and the steady increase in vehicle numbers are pushing transportation to its limits, resulting in severe congestion, energy consumption, driver discomfort and safety issues. These issues have promoted the development of connected and autonomous vehicles (CAVs), which can potentially mitigate the underlying problems [1, 2]. CAVs encompass connected vehicles (CVs) and automated vehicles (AVs). The former relies on two-way wireless communication supported by the intelligent transportation system (ITS), which enables real-time information sharing and cooperation among agents within a transportation system, whereas the latter eliminates human driver errors that may cause crashes, traffic flow oscillations, and shock waves. As shown in Table. 1.1, Society of Automotive Engineers (SAE) International has classified the automation of vehicles according

Table 1.1 SAE automation levels.

Level 0	Level 1	Level 2	Level 3	Level 4	Level 5
User are driving even when driver support features are engaged.			User are not driving if automated driving features are engaged.		
Drivers supervise the support features.			Drivers must drive if features request them to drive.	Automated driving features do not require users to drive.	
Driver support features			Automated driving features		
Warning AND Momentary assistance	Steering OR braking and acceleration support	Steering AND braking and acceleration support	Automated driving features can drive the vehicle under limited conditions		Automated driving features can drive the vehicle in all conditions

to six different levels [3]. The two-way wireless communication, vehicular ad-hoc network (VANET), such as vehicle-to-vehicle (V2V) communication, vehicle-to-infrastructure (V2I) communication, infrastructure-to-vehicle-to (I2V) communication, and vehicle-to-everything (V2X) communication, can be achieved by the development of ITS, of which the objective is to provide an improved system by informing users about traffic situations and by making mobility coordination safer and smarter [4, 5].

The emerging CAV technologies offer intriguing opportunities to enhance urban mobility and traffic safety, and the introduction of CAVs enables innovative often more responsive and efficient options for travelling which may change the way people use mobility services. The major concepts that can be improved by the development of CAVs, namely sensing environments, data collection and analysis, planning, decision-making, and vehicle control, have the potential to solve current problems with traffic management systems. By using the VANET communication technique supported by ITS and sensing technology including onboard camera, radar, LiDAR, laser, ultrasonic sensors, and global positioning system (GPS), sophisticated control systems are expected to be designed for CAVs so as to improve the overall vehicle and transportation performance, in terms of mobility, safety, energy saving and passenger comfort (as shown in Fig. 1.1) [6].

In terms of vehicle powertrains, due to their better performance on energy efficiency, the air quality could also be improved as the number of electrified vehicles increases. The European Automobile Manufacturers' Association (ACEA) provides statistical data on the sales of various electrified vehicle types in Europe from 2021 Q1 to 2022 Q4 with increases of 31.6% of battery electric vehicles (BEVs), 22% of hybrid electric vehicles (HEVs) and 29.5% of plug-in HEVs (PHEVs), respectively [7]. Goldman Sachs provides a report in 2022 [8], which predicts the proportion of the electrified vehicles of the whole global automobile market will rise from 3% in 2020 to 15% in 2025 and then 32% and 58% in 2030 and 2040, respectively. Moreover, according to the UK government roadmap [9], BEVs are considered as one of the final goals in transport electrification and decarbonisation by 2050, where HEVs, such as series HEVs, parallel HEVs and series-parallel HEVs, and PHEVs play a role in the transition to a full capacity of BEVs [10].

1.2 Aims and Contributions

1.2.1 Research Interests and Challenges

Based on the literature review, which will be described in detail in Chapter 2, the interests and challenges in designing advanced control methodologies for CAVs for three different scenarios (energy management (EM) of a single automated vehicle, vehicle following strategy,

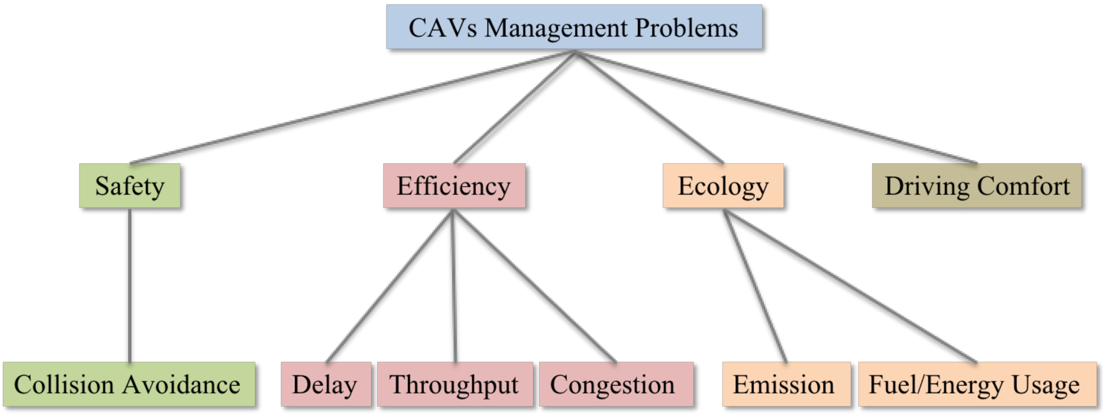

Fig. 1.1 Main research goals of CAVs management problems.

and autonomous intersection management) are now presented, which this thesis will address. The mathematical models of CAVs utilised and studied in this thesis are developed based on series HEV and BEV powertrains, which have a relatively simpler powertrain architecture for design purposes and an advantage of achieving higher energy efficiency in urban driving, particularly in stop-and-go driving conditions, as compared to vehicles with purely internal combustion engine (ICE) and other HEV types [11].

Engine start-stop system in EM of a single automated HEV: Nowadays, modern HEVs are usually equipped with an engine start-stop system (SSS). The solutions of existing control strategies for series HEVs without SSS suggest that the engine should be idle sometimes even when the vehicle is moving [12, 13], which motivate the incorporation of SSS into the EM control to achieve the best possible solution in reducing idling losses. The SSS would automatically shut off the engine at certain times and then quickly restart the engine when it is needed again. As a result, the SSS would enable the HEV to improve fuel efficiency and reduce emissions. Therefore, engine on/off control needs to be embedded into the EM control design of an HEV to account for SSS dynamics, and therefore to avoid inefficient engine idling operation. The vast majority of the literature assumes the SSS to be ideal with no extra cost for engine restarts [12–15], which may lead to EM strategies that force the engine to a very rapid succession of starts/stops. To prevent this unnecessarily inefficient behaviour, [16–18] propose an enhanced SSS modelling framework in the context of conventional heuristic or numerical optimisation of parallel HEV EM, where the fuel required to accelerate the engine from rest to idle speed is taken into account so that fast ICE start/stop transitions are penalised and avoided as a consequence. However, the optimality of these rule-based methods cannot be guaranteed for different driving cycles. In contrast, optimisation-based approaches for this problem would have issues of computational burden and causality. Hence, there still remains a gap in designing HEV EM strategies with the SSS considered that combine rule-based and optimisation-based EM strategies, such that they can be implemented in real-time with results close to the globally optimal solutions.

Uncertainties existing in vehicle following paradigm: In most cases, the optimal control strategies during the vehicle following paradigm are designed to optimise the energy economy of the ego CAV within a safe inter-vehicular distance range to a reference vehicle. However, inevitable disturbance and uncertainties are found in the vehicle modelling and V2V communication, which are not taken into consideration until recent years [19–22]. More specifically, a disturbance predictor has been integrated into the model predictive control (MPC) proposed in [20] so as to enhance system robustness with the disturbance forecast. In [21], the authors proposed a tube-based robust MPC (RMPC) method to solve vehicle following problems subject to inaccurate or delayed information of the lead vehicle and modelling errors. An alternative tube-based RMPC was proposed in [22], where two types of disturbances are addressed including both unmodelled dynamics and traffic perturbations, such as cut-in, lane change and emergency braking. In this context, there are issues of ubiquitous modelling uncertainties and external disturbances in the vehicle following paradigm that deserve further investigation from a perspective of potential practical implementation in terms of smooth control and computational complexity.

Nonlinearity in autonomous intersection management: Though significant research efforts have been made on the autonomous intersection problem, the computational burden remains a major concern for practical application. The computational burden can be spread across the vehicles within the decentralised and distributed coordination scheme [23, 24]. Moreover, the appropriate design of spatial-temporary reservation systems such as tile-based systems can lead to less computational load while maintaining its accuracy and feasibility for collision avoidance at the centre of an intersection [25]. The nonlinearity in problem formulations can also lead to a reduction in computational efficiency. In [26], a centralised MPC method for a convexified modelling framework is proposed. However, this work utilises a lossless linear longitudinal vehicle model, which neglects the powertrain dynamics as well as the friction and aerodynamics losses. As a result, further research investigation is required on relaxation or approximation of the nonlinear autonomous intersection problems with the powertrain considered into a computationally efficient convex problem. Moreover, there is a lack of rigorous proof between the relaxed convex optimisation problem and the original optimisation problem.

Disturbance in autonomous intersection management: Despite a rich literature on autonomous intersection management techniques, there are only a few works that deal with uncertainties entailed in the system. To cope with unreliable communication links (noise, packet drops, delays) in autonomous vehicle trajectory planning, Kalman estimation techniques are utilised in [27]. The issues of model mismatches and position uncertainties resulting from sensor and prediction errors are addressed by robust control strategies [28, 29]. Reference [29] considers vehicle position uncertainties resorting to sensor and prediction errors in linear Gaussian motion models for a centralised coordination scheme. To cope with the deviations in the trajectory following, a priority-aware resequencing mechanism is introduced in [30] through indirect feedback in the system. In [31], a robust coordination scheme is proposed by incorporating date-driven and Gaussian process regression methods to learn the deviation from the nominal trajectories of CAVs. However, the vehicle crossing order in [27, 28] is predetermined instead of being optimised and the vehicle dynamics in [29–31] neglects the consideration of the powertrain dynamics and various friction losses. Hence, there remains a gap in designing a robust control strategy for autonomous intersection management in a more general context with uncertainties considered.

1.2.2 Research Aims and Contributions

Concerning the research interests and challenges mentioned above, the research aims of this thesis for optimal speed trajectory and energy management control for CAVs can be mainly summarised into three aspects, which are:

1. To address the complex optimisation problem involved in EM of a single automated series HEV with consideration of engine SSS and penalty fuel for engine restarts.
2. To counter the impact of uncertainties existing in vehicle control problems for both the vehicle following paradigm and intersection management.
3. To provide computationally efficient traffic coordination strategies of large-scale cooperative CAV control at a signal-free intersection.

The contribution of this thesis contains several control methodologies to address the listed three research aims above. Detailed contributions are listed as below:

1. A novel heuristic strategy, the hysteresis power threshold strategy (HPTS), is proposed for EM control of series HEVs with a more realistic SSS for which engine restarts are associated with a fuel penalty. The design of this simple and effective control strategy is inspired by the fundamental analysis and solutions of the closed-form optimal EM

solution for a simplified vehicle/powertrain model. Moreover, rigorous proof that charge-sustaining (CS) operation is a necessary condition to reach globally optimal fuel economy in series HEVs is provided. By a systematic tuning process, the overall control performance of HPTS can be fully optimised for different vehicle parameters and driving cycles.

2. An optimal vehicle following strategy, enhanced adaptive cruise control (EACC), for joint velocity and EM control of series HEVs, is proposed. The control sequence of the ego vehicle is derived by an optimisation-based approach via the NMPC framework. The future uncertain behaviour of the preceding vehicle is predicted by the neural-network (NN) predictor. Compared to the solutions derived by a suitably designed adaptive cruise control (ACC) strategy and a full-horizon optimal control problem (OCP), EACC yields the optimal solutions with the performance of energy efficiency bridging the gap between two benchmark approaches. Moreover, a remarkable increase in computational efficiency can be found as compared to that of OCP.

3. Though EACC considers the uncertainties in an nonlinear MPC (NMPC) framework, the accuracy of the velocity predictor and the nonlinearities existing in the system dynamics could lead to a deterioration of the optimality or even infeasible solutions. As such, an RMPC based on linear matrix inequality (LMI) with consideration of external disturbances is presented. Convex modelling technique and semi-definite programming relaxation (SDPR) are employed in this method to further reduce the problem complexity and computational efficiency. The validation of the proposed convex approach is verified through proof of the equivalence between the convexified and the original problems. The robustness of the RMPC is verified against the solutions derived by a nominal MPC under the same initial condition.

4. In terms of autonomous intersection management problem, a centralised convex hierarchical optimal control approach for a group of CAVs, of which the turning manoeuvres and battery electric powertrain are integrated. The control problems are conservatively relaxed and approximated as second-order cone programs (SOCPs), which can enhance computational efficiency and guarantee a unique optimal solution. The proof of the equivalence between the convexified and the original problems is also provided to validate the optimality of the proposed strategy. By comparing the optimal solutions derived by two benchmarking methods, the effectiveness and optimality of the proposed hierarchical scheme are validated.

5. To deal with the potential disturbances in the autonomous intersection management problem, a convex hierarchical robust control strategy (HRCS) is proposed. This strategy is formulated in a decentralised coordination manner to further improve computational efficiency. The system robustness is enhanced via a tube-based RMPC. Further investigation of the computational efficiency and the trade-off between robustness and optimality shows the potential of HRCS for practical implementation.

1.3 Thesis Outline

The rest of this thesis is structured as follows. A literature review of the control approaches for CAVs is presented in Chapter 2. Then, the vehicle dynamics models of the series HEV and the BEV utilised in this thesis are introduced in Chapter 3, followed by three main parts. Part I includes Chapter 4, where the HPTS is introduced for EM control of a single HEV with consideration of the engine SSS. Part II includes two energy-optimal strategies for the vehicle following scenario, where the EACC controller with neural network predictor is proposed in Chapter 5 and the LMI-based robust model predictive controller is designed in Chapter 6, respectively. Part III includes two optimal control strategies for CAV at signal-free intersections via convex optimisation technique. The first strategy is formulated within a centralised framework in Chapter 7 with the cornering scenario considered and the other approach is formulated within a decentralised framework in Chapter 8 with external disturbances considered, respectively. The conclusions and appendixes are included in Part IV, where concluding remarks and future works of the whole thesis are given in Chapter 9 and appendixes are provided in Chapter 9.2.

1.4 Publications

The research results illustrated in the thesis have been published or are currently under review in several archival journals and international conferences. Chapter 4 in Part I includes publication [P2]. Chapters 5 and 6 in Part II include publications [P4] and [P9], respectively. Chapters 7 and 8 in Part III include publications [P1] and [P3], respectively. The publications [P1] and [P3] are developed based on publications [P5]-[P6] and [P8], respectively. Although publications [P7], [P10] and [P11] are not directly included in any of the chapters in this thesis, some of the ideas developed in this thesis are used in these publications.

Note that while the publications [P2] and [P9] included in Chapter 4 and 6 list the thesis author as the second contributing author, there are main contributions made by the thesis author in these publications. Specifically, in publication [P2], the thesis author derives the analytical solutions of the EM strategy of a series HEV with lossless engine SSS in Section 4.3.2, and proposes the novel heuristic strategy, HPTS, for a complete EM of a series HEV with engine SSS considered in Section 4.3.3. Moreover, simulation results and discussions of investigating the proposed HPTS performance in Section 4.4 are also provided by the thesis author. In publication [P9], the thesis author formulates the vehicle following problem as a convex optimisation problem along with a rigorous proof of the equivalence between the convexified and original problems as presented in Section 6.2, which provides a basis for developing the LMI-based RMPC strategy to counter the uncertainties.

The list of the author's publications during the period of pursuing the degree of Doctor of Philosophy is reported and listed by the publication date as follows:

- Papers in international journals

  [P1] **Xiao Pan**, Boli Chen, Simos A. Evangelou and Stelios Timotheou."*A Convex Optimal Control Framework for Autonomous Intersection Crossing*", IEEE Transactions on Intelligent Transportation Systems, vol. 24, no. 1, pp. 163–177, 2023.

  [P2] Boli Chen, **Xiao Pan** and Simos A. Evangelou. "*Optimal Energy Management of Series Hybrid Electric Vehicles with Engine Start-Stop System*", IEEE Transactions on Control Systems Technology, vol. 31, no. 2, pp. 660-675, 2023.

  [P3] **Xiao Pan**, Boli Chen, Li Dai, Simos A. Evangelou and Stelios Timotheou. "*A Hierarchical Robust Control Strategy for Decentralized Signal-Free Intersection Management*", IEEE Transactions on Control System Technology, 2023.

- Papers included in proceedings of international conferences

  [P4] **Xiao Pan**, Boli Chen and Simos A. Evangelou. "*Optimal Vehicle Following Strategy for Joint Velocity and Energy Management Control of Series Hybrid Electric Vehicles*", IFAC-PapersOnLine, vol. 53, no. 2, pp. 14161-14166, 2020.

  [P5] Boli Chen, **Xiao Pan**, Simos A. Evangelou and Stelios Timotheou. "*Optimal Control for Connected and Autonomous Vehicles at Signal-free Intersections*", IFAC-PapersOnLine, vol. 53, no. 2, pp. 15306-15311, 2020.

  [P6] **Xiao Pan**, Boli Chen, Simos A. Evangelou and Stelios Timotheou. "*Optimal Motion Control for Connected and Automated Electric Vehicles at Signal-Free Intersections*", in Proceeding of 2020 59th IEEE Conference on Decision and Control (CDC). IEEE, pp. 2831-2836, 2020.

  [P7] Ruikuan Hu, **Xiao Pan**, Boli Chen and Simos A. Evangelou. "*Optimal Energy Management for Fuel and Emissions minimisation of Series Hybrid Electric Vehicles with Consideration of Engine Preheating*", in Proceeding of 2021 European Control Conference (ECC), pp. 1347-1352, 2021.

  [P8] **Xiao Pan**, Boli Chen, Li Dai, Simos A. Evangelou and Stelios Timotheou. "*Decentralized Model Predictive Control for Automated and Connected Electric Vehicles at Signal-free Intersections*", in Proceeding of 2021 60th IEEE Conference on Decision and Control (CDC), pp. 2659-2664, 2021.

[P9] Sheng Yu, **Xiao Pan**, Anastasis Georgiou, Boli Chen, Imad M. Jaimoukha and Simos A. Evangelou. "*Robust Model Predictive Control Framework for Energy-Optimal Adaptive Cruise Control of Battery Electric Vehicles*", in Proceeding of 2022 European Control Conference (ECC), pp. 1728-1733, 2022.

[P10] Sheng Yu, **Xiao Pan**, Anastasis Georgiou, Boli Chen, Imad M. Jaimoukha and Simos A. Evangelou. "*A Robust Model Predictive Control Framework for Ecological Adaptive Cruise Control Strategy of Electric Vehicles*", in Proceeding of 2023 IEEE International Conference on Mechatronics (ICM), pp. 1-6, 2023.

[P11] Kai Tang, Weijie Wang, **Xiao Pan**, Boli Chen, Simos A. Evangelou. "*Economic Potential for Hybrid Electric Vehicles in Urban Signal-free Intersections with Decentralized MPC*", in Proceeding of the 22nd IFAC World Congress, 2023. (Accepted)

Chapter 2

Literature Review

Control approaches for CAVs are classified into three categories, i.e., in terms of single-vehicle, two-vehicle, and multi-vehicle, as illustrated in Fig. 2.1. The primary goal of the single-vehicle scenario is to design an EM system so as to optimise the energy efficiency for a single HEV or BEV considering traffic or road information, which generally does not take into account the constraints of the movement of preceding vehicles and other performance concerns (e.g. safety) [32–38]. The two-vehicle (vehicle-following) scenario aims to develop a control system for the subject vehicle to gain trade-offs among energy consumption, mobility, and safety during car-following paradigms, which considers the interaction of two vehicles, as well as traffic information [39–43]. The objective of a multi-vehicle scenario is to cooperatively control a group of vehicles in a coordination scheme (centralised, decentralised, or distributed) by optimising the velocity trajectories and the EM at various traffic scenarios (e.g. intersections, on-ramp merging), resulting in improvements of the overall performance (e.g. mobility and energy efficiency). The external information (e.g. traffic status and interactions among vehicles) is fully exploited in these scenarios [23, 24, 44–47].

2.1 Optimal Energy Management for a Single CAV

As shown in Fig. 2.2, the advanced communication technologies enable a single CAV to acquire external information in real-time, which provides the freedom of the CAV to adjust its driving strategy. In this thesis, the study of finding the optimal driving strategy of a single CAV focuses on the energy management of a single automated HEV, of which the optimal driving strategy can be determined by optimising the fuel consumption from a freely optimised power-split between the two energy sources of an ICE and a battery-driven electric motor. The problem of finding a fuel-efficient power-split for HEVs, known as the EM control problem, has drawn considerable attention in the past decade. A comprehensive

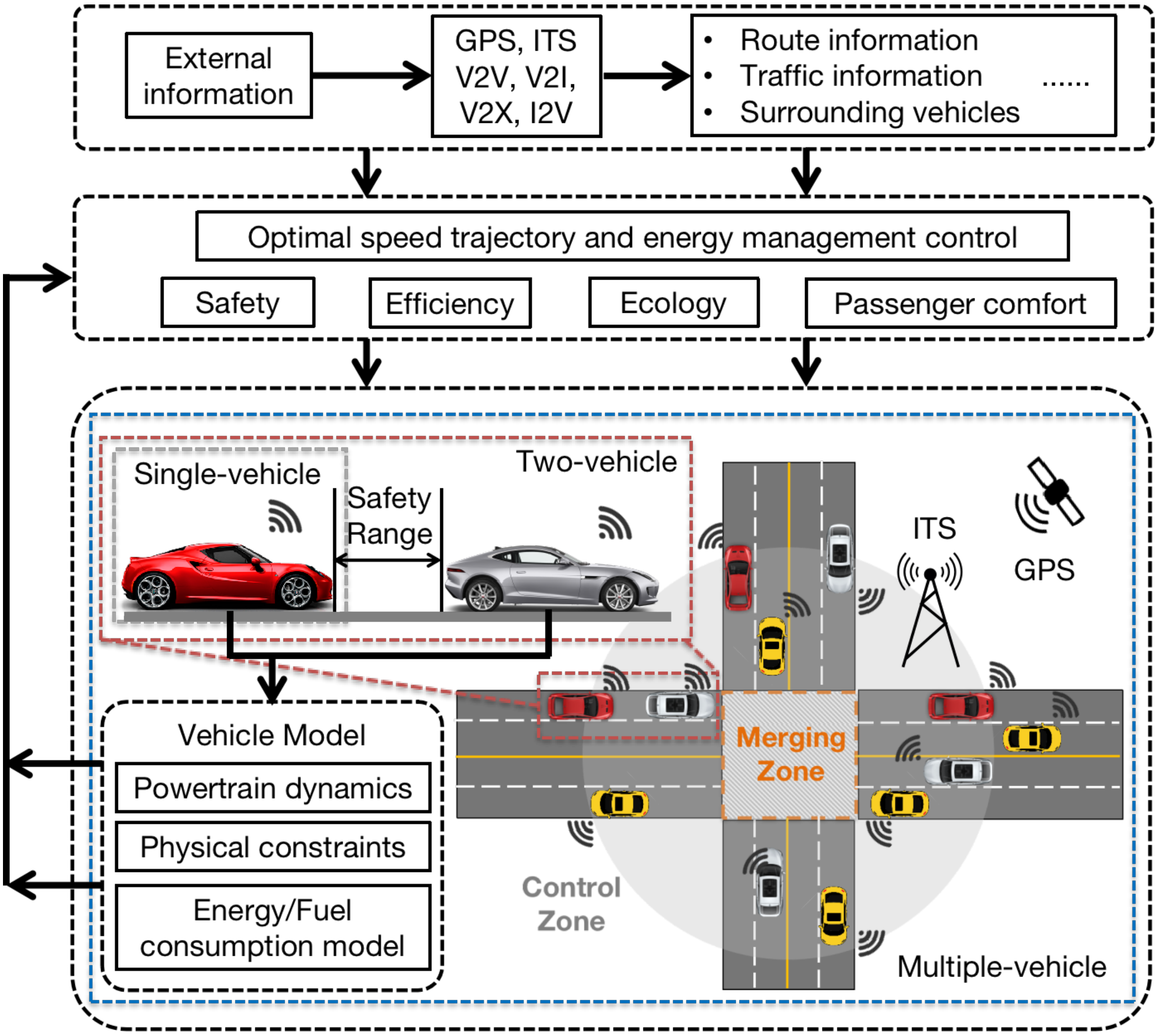

Fig. 2.1 The scenarios of cooperative CAVs management with the VANET communication technique, including single-vehicle, two-vehicle, and multiple-vehicle scenarios.

overview of existing EM techniques for a single HEV can be divided into three principle groups, rule-based, optimisation-based, and learning-based strategies [32–38].

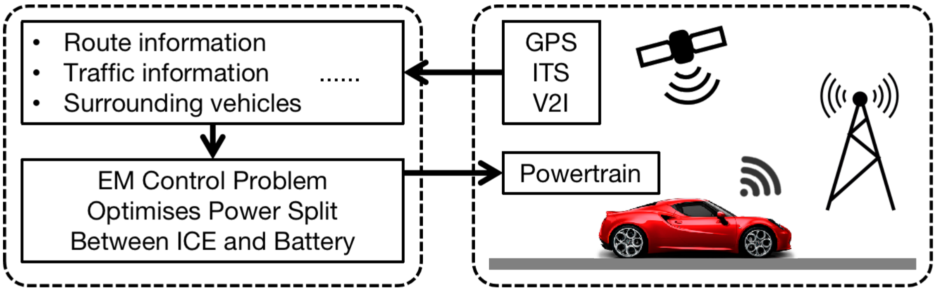

Fig. 2.2 The scheme of single HEV energy management with V2I and VANET technologies.

2.1.1 Rule-Based Strategies for a Single HEV:

The rule-based methods can be mainly classified into deterministic and fuzzy logic control strategies, whose mechanisms are based on a set of rules that compute the control signals based on pre-established thresholds over the controlled variables without the necessity of prior knowledge of the traffic conditions. These thresholds are often determined by analyses of optimal control policies, which are easy to be understood and implemented in real-time by using a look-up table or state machine logic on vehicle powertrain, and thus, they are more prevalent in industrial applications [48, 49].

2.1.1.1 Deterministic methods: In a deterministic rule-based method, the rules can be extracted from experience, in which the main energy sources (i.e. ICE) are controlled to perform mostly under optimal working conditions or in a high efficiency region to enhance the energy economy and minimise the energy transmission loss [12, 13, 50–54]. The thermostat control strategy (TCS) [50] and power follower control strategy (PFCS) [53, 55] are the two most conventional rule-based techniques, yet their fuel economies are not optimised. The operational rules behind them are respectively load following and load levelling mechanisms that have been extensively used in rule-based EM techniques of HEVs. In [54] a torque-levelling threshold-changing strategy for parallel HEVs is proposed, which can reduce hydrogen fuel consumption while achieving the charge-sustaining state of the battery with solutions close to the ideal value. While other recently proposed exclusive operation strategy (XOS) [12] and optimal primary source strategy (OPSS) [13] also dramatically improve the optimality of the existing rule-based approaches, their performance still falls behind optimisation-based benchmarks by some margin.

2.1.1.2 Fuzzy logic methods: While fuzzy logic methods are still based on predefined rules, the behaviour of the system is translated into fuzzy sets, which provide a wider margin of improvement in dealing with model uncertainty and complex decisions via a map-based format. In terms of EM of HEVs, fuzzy logic methods are used to determine the power-split between ICE and battery pack such that the ICE is controlled to perform mostly under high efficiency region or low emission region. An electric assist control strategy based on fuzzy logic is proposed in [56] so as to minimise fuel consumption and engine-out emissions. The robustness of the fuzzy logic is studied and verified in [57], where a comparison between a proportional–integral–differential (PID) controller and a fuzzy logic strategy is investigated under different road driving cycles. An evolution algorithm is designed by [58], where a genetic algorithm is used to optimise the parameters of fuzzy logic rules. Simulation results showed that the fuzzy logic method can achieve better performance with the optimised parameters as compared to the results obtained by a non-optimised fuzzy logic method. [59] proposes a neuro-fuzzy logic strategy by combining fuzzy logic and neural network in order to improve the self-adaptive ability. However, the advantage of the robustness of fuzzy logic methods also leads to an inevitable disadvantage. As the rules of fuzzy logic methods are obtained based on a qualitative rather than a numerical description of a system, the optimality in terms of complex hybrid systems and a large number of uncertainties cannot be guaranteed.

Overall, while rule-based methods can be easily applied to practical use as long as the rules are determined, a significant calibration effort is required to guarantee the performance within a satisfactory range for any driving mission. Besides, the thresholds are devised in advance for a particular set of powertrain architectures or component sizes, which leads to a lack of optimality. Numerical analysis of the optimality between rule-based and optimisation-based approaches can be found in [60, 61].

2.1.2 Optimisation-Based Strategies for a Single HEV:

Given the inherent rigidity of rule-based approaches, e.g., robustness, and sensitivity to drive cycle information and characteristics, optimisation-based strategies are popular in recent years due to usually guaranteeing the optimal and sub-optimal solutions. Most of the existing optimisation-based EM approaches are formulated as usually OCPs, where the objective of optimisation-based methods is to find the optimal control sequence that minimises a cost function while meeting the vehicle powertrain model and the operational constraints. As such, these OCPs can be applied to any type of HEV configuration rather than the powertrain architecture dependent rule-based methods. Although optimisation-based methods have the limitation that they require certain future information, the development of VANET technologies provides access for potential practical application by preview or prediction of traffic information (e.g. traffic signal phase and timing), as well as road conditions (e.g., speed limits). There exists a variety of techniques in the literature for optimisation-based approaches, in which dynamic programming (DP) [62–64], Pontryagin's Minimum Principle (PMP) [65–68], and derivative-Free algorithms (DFAs) are widely used offline for a global optimisation search [69–72], while equivalent consumption minimisation strategies (ECMS) [73–75] and MPC [76–81] are extensively used online.

2.1.2.1 DP: dynamic programming is able to guarantee global optimal solutions in general optimisation problems, where the control action is obtained by minimising a cost-to-go function in a backward way [82, 83]. The authors in [62] calculate the optimal power setpoints for the alternator connected to the engine and battery pack by solving a DP problem, where several modifications and simplifications are made to improve the computational efficiency. To obtain the optimal power-split and gear shift commands of a hybrid powertrain, DP is utilised in [63] by minimising an integrated cost function of both fuel consumption and emission. In [64], optimal energy management strategies of two different HEVs with automatic transmissions are studied and solved by DP. However, one of the disadvantages of DP methods is that the computational burden increases exponentially as the size of the problem increases [82], and therefore DP is limited to simplified models and usually used as a benchmark method.

2.1.2.2 PMP: Pontryagin's Minimum Principle is an analytical optimisation method, which converts the constrained global optimisation problem into the local Hamiltonian minimisation problem. The optimality is guaranteed through a necessary condition. The Hamiltonian problem is characterised by a costate, of which the initial value is determined and varies if full knowledge of a driving cycle is predetermined. Therefore, VANET and GPS techniques are incorporated with the PMP to deal with the underlying issue. In [65], the GPS and ITS are utilised to acquire the information of the effective battery state-of-charge (SOC) rate and mean power of driving cycles so as to approximate the optimal costate. A predictive energy management strategy is proposed in [66], where future driving profiles generated by the navigation systems are utilised for PMP to update the costate. Besides, the VANET and GPS techniques also enable co-optimisation of energy management and speed driving of a series HEV, which is achieved by PMP to further improve fuel economy [67]. An approximate PMP is proposed in [68], where the convex approximation to the local Hamiltonian is adopted to plan the optimal SOC and control policies over the entire driving cycle with a reduction in the computational burden. However, as the problem becomes complex, the size of the look-table for PMP increases exponentially with the number of dimensions, which requires a large enough storage capacity and computational power of the controller to deal with the heavy computation load of PMP. As such, PMP is limited for application in real-time and widely used for offline optimisation.

2.1.2.3 DFAs: Derivative-free algorithms are able to solve the optimisation problem on the conditions that the derivative information is unavailable. Most of the existing DFAs for the EM problem of HEVs employ metaheuristic algorithms, such as simulated annealing (SA), particle swarm optimisation (PSO), and genetic algorithm (GA), which derive solution candidates in an iterative scheme for the optimisation problem to avoid local optimum and improve optimality. In [69], the energy management problem for a series HEV is optimised by SA and a rule-based method for short-term and long-term, respectively. The optimal engine-on power threshold and battery current in [70] are optimised by GA and quadratic programming so as to minimise the fuel consumption of a power-split PHEV. Authors in [71] utilise the PSO algorithm to reduce fuel consumption and engine-out emission by optimising the strategy parameters for a series HEV. However, it is worth noting that the optimality of DFAs is not guaranteed in a limited number of iterations, which highlights the importance of examining the computational effort and solution accuracy. A DFA-based energy management strategy for a PHEV in [72] yields satisfactory solutions within an overwhelming computational time, which indicates its difficulty in online implementation.

2.1.2.4 ECMS: The equivalent consumption minimisation strategy is extensively used as an online optimisation-based method of HEVs. ECMS is derived by using the PMP, where a local optimisation problem is formulated and solved through the minimisation of equivalent fuel consumption. The costate in ECMS is introduced as a fuel equivalence factor, which is used to calculate the equivalent fuel consumption. The fuel equivalence factors represent the correlation of the electrical energy and the fuel chemical energy required (for battery discharging and charging respectively) when following a driving cycle. Therefore, the preview information of a driving cycle provided by VANET and GPS can be utilised for online implementation of the ECMS technique. In terms of different driving conditions the vehicle is operating at, [73] predetermines a set of equivalence factors to be optimally selected, which are identified by the preview information of driving cycles. An adaptive ECMS is proposed to online tune the fuel equivalence factors, which are automatically and periodically calibrated based on the driving cycle information [74]. Besides, [75] proposes a telemetric-ECMS, where the best values of equivalence factors are determined by a level of the preview information, including past, present and future speed profiles obtained from in-vehicle 3D maps, a navigation system, and a telemetry system.

2.1.2.5 MPC: Model predictive control offers a computationally efficient alternative to global optimal control in yielding near-optimal solutions. In particular, the global optimisation problem regarding the energy management of HEVs is converted to a series of local optimisation problems over the entire driving mission. Each local optimisation problem optimises the power-split over a prediction horizon. As already mentioned, the preview of trip information is essential for designing an optimal energy management strategy for HEVs. The characteristic of MPC can incorporate future driving information through a receding horizon control scheme. Hybrid modelling and MPC are developed in [76], where power distortion and gearshift control of an HEV are optimised through a hybrid logic dynamic system framework. [77] proposes a nonlinear MPC controller to optimise the power-split in real-time based on a continuation/generalised minimum residual algorithm, although the performance of MPC is sensitive to model quality, such as model mismatch and disturbances. The model mismatch accounts for the models of vehicle dynamics, weather, and road conditions, which can be compensated by VANET and GPS to improve the prediction results [78].

To further tackle the presence of uncertainties, RMPC is developed, which can be mainly categorised into min-max RMPC, tube-based RMPC, and LMI-based RMPC [84, 85]. The mix-max procedures assumed worst-case predictions for variables, bounding them with respect to the bounds of uncertainties. The tube-based RMPC algorithm does not compute the worst-case predictions, but predicts a nominal system trajectory without uncertainties and guarantees that the deviation that the real system has from this nominal trajectory lies inside a tube (which is exploited by using the bounds of the uncertainties). The LMI-based RMPC has the advantages of the explicit incorporation of uncertainty and the easier implementation effort as compared to the other two RMPC techniques. The trade-offs and advantages of the three different types of RMPC techniques are reviewed and quantified in [84]. In terms of energy management of HEVs, a min-max RMPC control strategy is proposed in [79] for HEVs to deal with the external disturbances, the time varying delays, and the model uncertainties. A tube-based RMPC control strategy is developed in [80] to minimise the fuel consumption of an HEV with consideration of uncertainties in the driver torque demand caused by the driving style or traffic conditions. A LMI-based supervisory robust control for hybrid vehicles is developed in [81], where an output feedback controller is designed to minimize fuel consumption for a group of possible torque/power input profiles.

2.1.3 Learning-Based Strategies

Due to the development of machine learning, artificial intelligence techniques, and online data-based network processing approaches, the learning-based methods are able to be employed for EM of HEVs to efficiently yield optimal control laws under large data sets from external driving conditions. These sets incorporated by learning-based methods are utilised to adaptively and optimally tune certain parameters and thresholds for different driving scenarios, such as road types, which subsequently are utilised to derive control laws. Based on learning types, two main learning-based methods can be identified, NN [86–88] and reinforcement learning (RL) [89, 90].

2.1.3.1 NN Neural network learning-based methods are designed based on neurons in the human brain, which have multiple inputs and outputs. By jointly linking neurons into layers, a network can be formed to model a behaviour of a system. The number of neurons and layers is determined based on prior training progress, of which the amount and quality directly influence the performance of the neural network. An artificial NN is embedded into a machine learning framework in [86] for optimal energy control of a power-split HEV by predicting the traffic conditions including road types and congestion level. [87] Dynamic traffic feedback data are utilised by NN-based MPC in [91], where an energy management strategy is proposed for plug-in hybrid electric vehicles. Authors in [88] propose an NN-based adaptive fuzzy logic energy management strategy, which combines NN and fuzzy logic controller to optimise SOC for a plug-in hybrid electric bus.

2.1.3.1 RL Unlike NN methods, which are learnt from training progress and applied to new data sets, reinforcement learning is a dynamic learning progress where the agent in

RL learns from its experiences and tries to adopt the best possible behaviour by receiving continuous feedback from the environment to maximise a reward function. As such, the RL-based methods can adaptively and autonomously adjust optimal control actions based on the new data inputs. A nested RL framework is presented in [89], where both the control actions and limits on the range of the battery SOC are learned and optimised in an inner-loop and an outer-loop, respectively. In [90], a deep RL-based EM strategy is proposed for HEVs, which combines RL and deep NN to directly yield control action from the driving state.

For the purpose of intuitive illustration, Table. 2.1 organises and summarises the above literature reviews of the main optimal energy management strategies of a single automated HEV with an illustration of the main features and challenges of each technique. However, there are few existing works focusing on developing optimal EM of HEVs with engine start-stop system in the context of rule-based and optimisation-based methods. There still remains gap in designing a real-time EM strategy of HEVs with the SSS considered, which is also capable of yielding solutions close to global optimum.

Table 2.1 Summary of main optimal EM strategies of a single automated HEV.

Algorithm Type	Strategy	Main Advantages	Main Challenges	Literature
Rule-based	Deterministic	• Simplicity	• lack of robustness, and optimality	[12, 13, 50–54]
	Fuzzy-Logic	• Improved robustness, adaptiveness, predictability	• Huge efforts on calibration • Lack of optimality	[56–59]
Offline Optimisation-based	DP	• Global optimality • Benchmark method	• High computational burden • Curse of dimensionality	[17, 18, 62–64]
	PMP	• Analytical solution • Guaranteed optimality	• High computational burden • Complex mathematics	[65–68]
	DFAs	• Iteratively search candidates to avoid local optimum	• Lack of optimality in limited iteration times	[69–72]
Online Optimisation-based	ECMS	• Guaranteed optimality • Equivalent fuel consumption	• Local optimum • Equivalence factors are sensitive to driving cycles	[16, 73–75]
	MPC	• Guaranteed optimality • Predictability • Robustness (RMPC)	• Local optimum • Performance is sensitive to model quality (mismatch, disturbances)	[76–81]
Learning-based	NN	• Learning and adaptiveness	• Quality and quantity of training data	[86–88]
	RL	• Dynamic learning • Feedback (reward function)	• Time consuming for preparing database	[89, 90]

2.2 Energy-Optimal Strategy for Vehicle Following Scenario

To further improve energy efficiency, external information, such as road traffic, human-driven vehicles and communication errors and delays, is considered, and the safety issue of CAVs becomes another main concern. With the advent of advanced V2V and V2I communication technologies, interconnected vehicle control is gaining momentum [39, 40]. This leads to the investigation of a novel optimisation framework of the vehicle following scenario that considers the interaction between two connected vehicles as well as the traffic information [41–43]. In this context, the development of cruise control with the VANET and GPS is critical for CAVs to improve overall their efficiency, while satisfying the safety requirement and maintaining or even improving the traffic throughput, as shown in Fig. 2.3. The methodologies of cruise control can be mainly divided into two principal groups, ecological adaptive cruise control (eco-ACC) [21, 92–103] and predictive cruise control (PCC) [104–114]. Both control strategies consider the traffic information, and the velocity of the preceding vehicle can be obtained by the communication technologies. The eco-ACC integrates ecological driving and ACC to optimise both the driving speed and EM system of the following vehicle with static traffic information. The ecological driving system can yield optimal speed trajectory for the vehicle to reduce energy usage. Moreover, in an ACC system, the following vehicle automatically adjusts its velocity to maintain a safe range to the preceding vehicle through V2V and sensing technologies, such as cameras, laser, radar and LiDAR. Existing research efforts have been made on designing ACC for both conventional and electrified vehicles. Furthermore, by utilising the relevant traffic context information (e.g. GPS and VENET), PCC is developed for energy-optimal control of the following CAV with consideration of dynamic traffic conditions. By combing ACC methods and the future driving condition, PCC

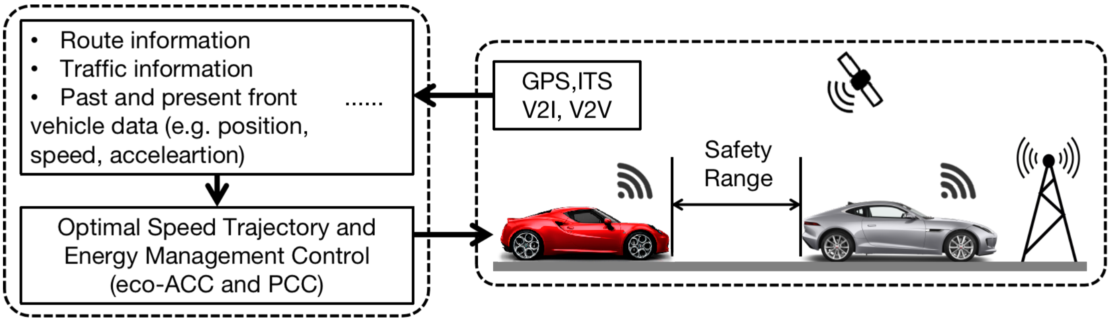

Fig. 2.3 The scheme of eco-ACC and PCC methods for optimal speed trajectory and energy management control during vehicle following paradigm.

is able to predict the velocity of the preceding vehicle and exploit available traffic information from the V2I and real-time high-definition maps.

2.2.1 Ecological Adaptive Cruise Control (eco-ACC)

Traditional research studies on ACC mainly focus on driving safety instead of considering energy efficiency and driving comfort, which leads to an investigation and development of eco-ACC. The eco-ACC is formulated by optimising the energy efficiency of the following vehicle while maintaining a safe range to the front vehicle by using static traffic information, generally derived from standardised driving cycles. Hence, a classification of eco-ACC can be established based on two different assumptions of the future velocity profile of the preceding vehicle, predefined rules [92–96] or prior knowledge (e.g. GPS and V2I) [97–99, 21, 100–103].

2.2.1.2 Predefined future velocity profile of the preceding vehicle: The predefined rules for the future velocity profile of the preceding vehicle usually set the speed or acceleration of the preceding vehicle to be constant or a function with respect to time. In [92], an MPC-based ACC is utilised to yield kinematic states of longitudinal vehicle dynamics with a preceding vehicle cruising at a fixed constant speed. The kinematic states are then utilised for optimal battery control via the ECMS technique. A Pulse-and-Gliding (PnG) strategy is proposed in a servo-loop control design, which contains a safety range regulator and switching logic for generating control actions [93]. An assumed constant acceleration of the preceding vehicle is utilised to predict its future velocity within each switch phase. The simulation results show the minimisation of fuel consumption is improved by 20% as compared to the solutions obtained by the benchmark controllers. The similar assumption can be found in [94, 95], where a constant acceleration for the prediction of the preceding vehicle is assumed. A deep fusion eco-ACC is imposed in [94] via NMPC for a smart parallel HEV to optimise fuel consumption. [95] proposes a two-stage eco-ACC control hierarchy where the first stage yields the optimal speed profiles at a global level by GA while the local speed adaption of the vehicle is applied by solving a quadratic programming optimisation in the second stage. Time dependent exponential function is used to predict the acceleration of the preceding vehicle in [96], which exploits a Newton/GMRES approach for fast computation to optimise the energy cost while guaranteeing a safety vehicle following paradigm by an NMPC eco-ACC.

2.2.1.1 Prior known future velocity profile of the preceding vehicle: With the traffic context information from VANET and GPS, the driving cycle information of the preceding vehicle can be acquired in advance. Authors in [97] propose two eco-ACC methods under the condition that the trip distance of the driving mission is prior known. The longitudinal motion characteristics are optimised under specific application conditions, which include a DP-based offline acceleration optimisation for a BEV and an ECMS-based supervisory controller for an HEV. An eco-ACC considering traffic signals is designed in [98], where the energy-optimal velocity profiles and control actions for the rear-end collision avoidance are solved successively in a two-level optimisation framework. The information of the traffic signals and the preceding vehicle are provided by V2I communication, and vehicle sensing technologies, respectively. The eco-driving and ACC are realised by continuously updating the DP and MPC optimisation problems, respectively. Standard driving cycles are utilised for the velocity profiles of the preceding vehicle in [21, 99]. The research effort in [99] combines eco-ACC with a stop-and-go system and stochastic MPC (SMPC) to minimise energy consumption. An optimal speed profile of the following PHEV is generated first, which is then utilised for optimisation of its power-split. In [21], an adaptive robust Eco-ACC is proposed for a PHEV with a tube-based RMPC and an online parameter estimator to deal with uncertainties, modelling errors, and delayed data. Simulation results show an improvement in energy efficiency and the potential for practical application.

Experimental driving cycles, obtained from real driving data or designed to emulate a real driving situation, are exploited for the velocity profile of the preceding vehicle in [100–103]. In [100], an energy-optimal ACC approach is proposed, where the energy-optimal speed trajectory is precalculated by DP while control actions of the following vehicle to track the optimal speed trajectory are obtained by an MPC controller. A multi-optimisation eco-ACC system via MPC framework is proposed in [101], where the fuel consumption and driving comfort are optimised by minimising the acceleration and the derivative of acceleration. [102] proposes an eco-ACC system based on an NMPC optimisation framework where, analytical formulations are derived and a balance among fuel economy, mobility, and safety is achieved for an intelligent HEV. To reduce the computational complexity, a lower dimensional MPC algorithm is proposed in [103], where a multi-objective function is designed to optimise the tracking capability, fuel economy and driving comfort. The problem scale is reduced by partially relaxing inequality constraints in the prediction horizon.

2.2.2 Predictive Cruise Control (PCC)

Furthermore, to deal with complicated traffic conditions, PCC is developed based on the incorporation of eco-ACC and techniques for future driving condition prediction. The core of PCC is an exploitation of the prediction information of the future velocity of the preceding vehicle with available traffic or road information from VANET and GPS. Various speed prediction methods are presented in [115, 116]. The dynamic traffic information, such as varying traffic conditions, is considered in PCC, which renders more robust and energy efficient control actions for the following CAV. Existing literature on PCC can be divided into two main groups based on the types of prediction, function-based (e.g., Gaussian Process and Markov Chain) [104–109] and learning-based (e.g. NN and RL) [110–114].

2.2.2.1 Function-based prediction of the future velocity of the preceding vehicle: In [104], a novel control scheme of PCC, which utilises HD map information to access additional road and traffic information, is formulated as an NMPC problem to minimise fuel consumption. The future speed of the preceding vehicle is predicted by a correction function to emulate the real driving behaviour. PMP is utilised in eco-driving strategy to achieve fuel minimisation via the PCC technique based on a mixed-integer MPC [105], where the prediction of the preceding vehicle is achieved by introducing a tuneable multiplier in the exponentially varying predictor with respect to varying speed. Simulation results present a better performance on the velocity profile and the reference SOC trajectory.

In [106], a Gaussian learning-based fuzzy PCC for CAVs in the VANET is proposed to optimise the overall fuel efficiency. The prediction of the preceding vehicle is estimated by a Gaussian process regression model and a fuzzy decision method is utilised to adaptively adjust the weights of different objectives in real-time. With traffic data obtained from a cloud server, [107] devised an economic PCC for BEVs in the context of an MPC framework, where a Gaussian Process model is exploited for speed prediction of the leading vehicle. The combination of cloud server and Gaussian Process prediction is proven to be capable of greatly improving the prediction accuracy. Markov Chain is utilised in [108] to stochastically predict the future speed of the preceding vehicle, which is then exploited to formulate deterministic linear MPC problem for the PCC system. Moreover, an SMPC method with a conditional linear Gaussian model for future velocity prediction of the preceding vehicle is presented in [109].

2.2.2.2 Learning-based prediction of the future velocity of the preceding vehicle: In [110], an MPC-based PCC is formulated to reduce risky cut-in scenarios (near lane-change and lane-keeping) based on an artificial NN, radial base function network (RBFN), which estimates the future behaviour of the surrounding vehicle. An enhanced PCC system is designed in [111], where the future traffic information is predicted by a cloud-based convolutional neural network (CNN) through a data-driven method. The optimisation is formulated via the MPC framework with results on energy reduction. Bayes network (BN) is utilised in [112] to predict the preceding vehicle movement, and a BN-based PCC is formulated via NMPC framework for BEVs to maintain a safe vehicle following paradigm as well as to minimise the motor energy consumption. By combining power management and adaptive velocity control of a PHEV, an MPC-based PCC is proposed in [113], which improves the performance on fuel economy and safety. The speed of the preceding vehicle over each prediction horizon is predicted by the back-propagation neural network (BPNN). [114] for a power-split PHEV energy management, where the velocity prediction is realised by a data-driven Q learning algorithm. The hardware-in-the-loop test validates the effectiveness of the RL-based method on better fuel and computational efficiency.

For the purpose of intuitive illustration, Table. 2.2 organises and summarises the above literature reviews of the vehicle following strategies with an illustration of the main features and challenges of eco-ACC and PCC methods. Although there are several cruise control strategies developed to counter the impact of uncertainties, further investigation on designing advanced ecological cruise control strategies is crucial and necessary to deal with ubiquitous modelling uncertainties and external disturbances from a perspective of potential practical implementation.

Table 2.2 Summary of main vehicle following control strategies.

Category		Features		Methodologies	Literature
Eco-ACC	• Static traffic information	• Combination of eco-driving and ACC	• **Predefined** future velocity profile of the preceding vehicle	MPC, NMPC, PnG, ECMS, GA	[22, 92–96]
			• **Prior known** future velocity profile of the preceding vehicle (derived from driving cycles)	MPC, NMPC, RMPC, SMPC, ECMS, DP	[20, 97–103]
PCC	• Dynamic traffic information	• Robustness on varying driving conditions	•**Function-based prediction** of future velocity of the preceding vehicle	MPC, NMPC, SMPC, PMP, Gaussian Progess, Markov Chain	[19, 21, 104–109]
			• **Learning-based prediction** of future velocity of the preceding vehicle	MPC, NMPC, CNN, BPNN, RBFN, BN, RL, Data-Driven	[110–114]

2.3 Optimal Autonomous Intersection Management for CAVs

With the development of CAVs and VANET technology, numerous research efforts have been made on the optimal control strategies for multi-vehicle scenarios, particularly the intersection crossing problem, which greatly impacts the overall efficiency of road traffic systems, especially in urban areas. This incentives innovative intersection control schemes, which can leverage advanced vehicular communication systems. According to the existing overviews, the intersection management problem formulation technique can be mainly categorised into model-based [117, 118] and data-driven [119] approaches. The former relies on first-principle parametric models while the latter utilises non-parametric learning approaches for control decision-making, but the majority of the data-driven methods focus on signalised intersections. The intersection management control problems can be divided into two main groups, signalised and autonomous (signal-free) intersections. Cooperative control strategies for a signalised intersection coordinate the velocity of each CAV by utilising signal phasing and timing (SPaT), which are received via V2I communication to minimise the vehicle queuing time [120–123]. In [124], a trajectory planning-based centralised intersection management strategy for CAVs at a signalised intersection allocates the optimal path considering various inputs such as the position and speed of vehicles, signal status and current traffic, which results in a reduction in delay, travel time and fuel consumption. However, the performance of traditional traffic light control systems is limited due to the lack of sensing and communication capabilities and human driving, which results in major traffic congestion in urban traffic.

On the other hand, the development of VANET technology provides access to achieve autonomous intersections, where the constraints introduced by the traffic lights are removed, have the potential of further reducing traffic delays and vehicle energy usage by sharing traffic information among vehicles [125]. An example schematic of an autonomous intersection with the VANET communication technique is presented in Fig. 2.4. As can be seen, the intersection

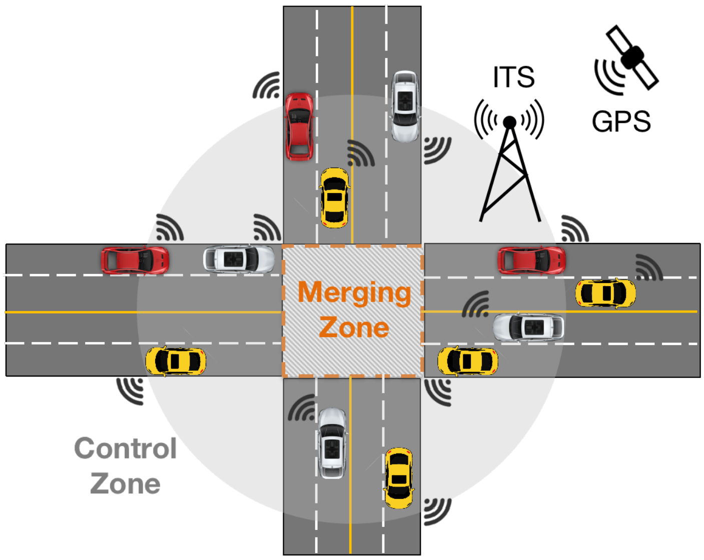

Fig. 2.4 The schemes of autonomous intersection with VANET communication technique.

is formed by two perpendicular roads with two lanes per road. Vehicles approaching the intersection will first enter a *Control Zone* (CZ). The centre of the intersection is called the *Merging Zone* (MZ), where vehicles merge from different directions, and therefore lateral collision may occur. The area of MZ is considered to be a square, where CAVs are allowed to go straight through and turn left or right at the MZ. In practice, the size of CZ is determined by the communication range capability of the CAVs and the ITS. Hence, this part mainly focuses on investigating the unsignalised intersection management strategies via model-based techniques and deals with autonomous vehicle coordination through advanced vehicular communication systems (e.g., V2I) to reduce traffic delays and energy usage. To address these issues, the potential improvements require addressing three main challenges: scheduling policy, reservation system, coordination scheme [23, 24, 45–47].

2.3.1 Scheduling Policy

The first important challenge of autonomous intersection management is the scheduling policy, which defines the crossing sequence of the CAVs through the intersection. An appropriate scheduling policy can improve traffic throughput and reduce waiting times for CAVs. The prevalent approaches for scheduling policy consider fairness and communication efficiency, which can be classified into three cases: first-in-first-out (FIFO), heuristic (rule-based), and system optimal (optimisation-based).

2.3.1.1 FIFO: The first-in-first-out scheduling mechanism is a fair queuing protocol that ensures all the CAVs enter and leave the MZ in the same order they arrive at the CZ [126–128]. As such, it is straightforward for the FIFO policy to be implemented in autonomous intersection management with low computational costs. In [127], the augmented Lagrangian-based alternating direction inexact Newton method (ALADIN) and quadratic programming (QP) are utilised to cooperatively and optimally control the autonomous intersection. An analytic control strategy for CAVs to cross the intersection is derived in [128] based on PMP. However, the optimality of the intersection management performance cannot be guaranteed by exploiting the crossing sequence yielded by the FIFO policy. Moreover, the performance could dramatically deteriorate as the traffic density increases.

2.3.1.2 System optimal (optimisation-based): The system optimal scheduling policies are based on optimisation, which provides optimal crossing sequence by minimising traffic throughput at a cost of computational time. In [129], the passing order of CAVs is determined by a CNN predictor and the mean travel time of the intersection can be reduced as compared to the FIFO policy. The optimality can be guaranteed even with expanded traffic density. The autonomous intersection problem usually involves a hierarchical optimisation framework to implement system optimal scheduling policies to predetermine the optimal crossing sequence of CAVs. For example, a three-layered coordination strategy is proposed in [130], where the cooperative vehicles are optimally managed at multiple intersections via a fast MPC technique.

2.3.1.3 Heuristic (rule-based): The mechanism of heuristic scheduling works akin to a trade-off between FIFO and system optimal policies. Compared to the FIFO policy, heuristic scheduling approaches are designed to reach higher throughput with a limited delay [131]. A heuristic mixed integer quadratic program (MIQP) is exploited in [132] to compute the crossing order of CAVs for autonomous intersection coordination. In [133], a greedy algorithm is designed to seek the best sequence among all possible schedules for vehicles to cross an autonomous intersection. Besides, heuristic scheduling approaches can yield fast solutions at a compromise of optimality with respect to throughput compared to system optimal scheduling methods.

2.3.2 Reservation System

The reservation systems, independent of scheduling policy, with the main objective to separate conflict movements, can be specified into four types: intersection-based (IB), tile-based (TB), Conflict points-based (CP-based), and lane-free.

2.3.2.1 IB: The intersection-based reservation allows one–and only one–vehicle within the MZ for intersection crossing, which is the most conservative but safety guaranteed. In [134, 135], the lateral collision constraint for vehicle merging at the CZ enforces the latter vehicle enters the CZ only after the former vehicle leaves the CZ. The decentralised control problem in [134] involves multiple intersections, whose control strategy of CAVs is derived by analytical solutions. The collision avoidance constraints are designed such that the MZ is reserved for a and only a single CAV to cross at each time. The study in [135] also proposes a hierarchical control algorithm for CAVs based on the concept of reserving the MZ for one CAV at a time. Mixed-integer programming (MIP) and a heuristic convex-concave procedure (CCP) are combined in this hierarchical scheme to derive optimal solutions.

2.3.2.2 TB: The tile-based reservation is constructed by dividing the space of MZ into a grid of tiles [136, 137]. A reservation is rejected if a tile is occupied by two CAVs at the same. In [136], a window-searching algorithm is applied based on the tile-based reservation system to yield collision-free trajectories for vehicles. The optimal solutions for CAVs to cross an autonomous intersection are derived by DP. Tile-based reservation formulation is also considered in [137], where the mixed-integer linear programming (MILP) is utilised to optimally control CAVs within an intersection to cope with the high traffic demand.

2.3.2.3 CP-based: The conflict points-based reservation is able to take full advantage of the MZ area by reserving a finite number of specific points (called conflict points) instead of the whole of the intersection. In [138], the MZ is specified into 16 conflict points, which are reserved for CAVs prior to their arrivals such that collisions can be avoided in the proposed method. A recent study in [139] considers turning manoeuvres of CAVs with a CP-based reservation system. The Monte Carlo Tree Search is utilised to find the passing order of CAVs with the best performance in fuel and throughput efficiency as compared to other existing strategies.

2.3.2.4 Lane-free : Different from the other three reservation-based collision avoidance approaches, the lane-free system has no restriction on CAVs to follow a predefined path. As such, the whole space of the intersection can be freely exploited for the trajectory planning of CAVs to avoid collisions without abiding by lane discipline [140, 141]. This reservation scheme is capable of further improving the traffic throughput and capacity at a cost of high computational load to find the best travel plan for CAVs. To address this issue, a real-time lane-free reservation system is designed in [142] by fixing the crossing time to a constant value.

2.3.3 Coordination Scheme

The coordination schemes for the autonomous intersection management problem can be categorised into three main types: centralised, decentralised, and distributed. The centralised and decentralised coordination schemes are based on V2I with the main difference being that the vehicle control policy is derived globally (intersection central controller) or locally (vehicle). Thus, it is straightforward for centralised coordination schemes to achieve global optimality by the central controller. However, there are inevitable drawbacks of the centralised scheme, including high computational burden and less resilience against the failure of the central controller, as the whole system relies on the central controller. To address these issues, the decentralised scheme is developed such that the control decision is independent of the central controller. The shared information between vehicles is realised through an intersection coordinator. This scheme cannot guarantee global optimality but improve the computational efficiency and resilience compared to the centralised scheme. On the other hand, CAVs in distributed coordination scheme share information through V2V rather than V2I. As such, the control decision is made locally by each individual CAV without the involvement and requirement of communication infrastructure, such as a central controller or a coordinator.

2.3.3.1 Centralised: The foundation of a centralised coordination scheme involves a single central controller that determines the velocity trajectories of all the CAVs to safely cross the intersection. Common centralised approaches are optimisation-based with the main objective of either increasing the throughput of an intersection (which can be achieved by minimising the travel time) or reducing the vehicle energy consumption [143, 144]. In particular, the trade-off between travel time and energy consumption minimisation is investigated in [135], where a hierarchical optimisation approach is developed subject to a

FIFO policy. [26] proposes a centralised autonomous intersection crossing strategy based on the MPC framework and convex modelling technique. The electric powertrain and various friction losses are also included in the recent centralised coordination control approaches, where [145] involves turning manoeuvres and [146] utilise convex modelling technique to alleviate the overall computational complexity. Moreover, a multi-objective optimisation problem with driving comfort included is presented in [128].

2.3.3.2 Decentralised: In the decentralised coordination framework, the velocity of each individual CAV is found based on information received from other vehicles on the road or from a coordinator [147–150]. An analytic optimisation method is proposed in [151] to address each local optimisation problem subject to a throughput maximisation requirement. [152] presents a sequential optimal control approach that is combined with a computationally efficient scheduling method to maximise throughput. In [153], the sequential movement of CAVs is modelled using multi-agent Markov decision processes, while reinforcement learning is employed to find each velocity trajectory. Turning manoeuvres are integrated into [154], which present decentralised coordinated frameworks capable of finding near-optimal solutions. The work in [154] solves the problem by resorting to analytic optimisation techniques. More computationally efficient alternatives to optimisation-based approaches are heuristic control strategies [155, 156], which however do not have optimality guarantees in most cases.

2.3.3.3 Distributed: In distributed control, the CAVs communicate with each other and make their own control action locally through V2V technique [157–159]. This allows the distributed coordination scheme to be independent of the communication with the roadside unit. In this way, distributed approaches are more reliable and robust compared to the other two coordination schemes because the whole system is still functional even if there exists one vehicle failure. In [160], distributed fault-tolerance control method is proposed for the intersection management problem with communication failure, which guarantees collision avoidance and minimises traffic delays. Distributed MPC control approach in [161] is applied to cooperatively control vehicles to cross the intersection based on predefined routes and priorities. Authors in [162] propose a distributed conflict resolution strategy for CAVs at a signal-free intersection based on V2V communication among vehicles. This strategy minimises traffic delays through distributed local optimisation on each vehicle. In [163], a V2V-based distributed motion planning scheme is designed to locally optimise the trajectory of each CAV via the nonlinear MPC framework, which is solved efficiently by the proximal averaged Newton method for optimal control.

For the purpose of intuitive illustration, Table. 2.3 organises and summarises the above literature reviews of autonomous intersection crossing control strategies in terms of three coordination schemes (centralised, decentralised, and distributed) with respect to different scheduling policies and reservation system. Nevertheless, there remains a gap in the existing literature surveys for the autonomous intersection crossing problem to develop computationally efficient cooperative CAV control strategies with solutions close to the global optimum. Moreover, there are only a few works that deal with the uncertainties entailed in the autonomous intersection management system.

Table 2.3 Summary of main autonomous intersection crossing control strategies in terms of coordination schemes with respect to different scheduling policies and reservation system.

Literature	Scheduling Policies			Reservation System			
	FIFO	System optimal	Heuristic	IB	TB	CP-based	Lane-free
• Centralised							
[26]		✓		✓			
[28]	✓				✓		
[128]	✓					✓	
[129, 138, 146]		✓				✓	
[131, 145]			✓			✓	
[133]			✓	✓			
[135, 143]	✓			✓			
[29, 137]			✓		✓		
[141]	✓						✓
[140, 142]			✓				✓
[144]		✓			✓		
• Decentralised							
[126]	✓					✓	
[30, 31, 132, 152]			✓			✓	
[134, 150]	✓			✓			
[139, 148]		✓				✓	
[147]			✓	✓			
[149]		✓			✓		
[153]			✓		✓		
[154]		✓		✓			
• Distributed							
[127]	✓			✓			
[130]		✓		✓			
[136, 160, 162]			✓		✓		
[157]		✓				✓	
[158, 159, 161]			✓			✓	
[163]			✓	✓			

Chapter 3

Vehicle Modelling

3.1 Series Hybrid Electric Vehicle

The series HEVs play an important part in the transition from pure ICE vehicles to traffic electrification. Although there are a few series HEVs on the market in 2022, such as the family car Nissan Note E-Power [164] and the buses equipped with the series-E powertrain developed by BAE Systems [165], the optimal EM control solutions of series HEVs are also relevant to the EM control strategies of plug-in series HEVs, such as the BMW i3, Audi A1 e-tron and Leading Ideal One, which have advantages in a longer driving range and better energy economy [166, 167]. The series HEV model utilised in this thesis is described in [67]. In particular, the ICE and the electric machines are approximated by steady-state efficiency maps, while the power converter, inverter and transmission system are modelled by constant efficiency factors that take into account the possible energy losses. This vehicle model captures the essential physical characteristics of the powertrain components with relatively low dynamic order, thereby being widely applicable for HEV analysis and control design [168–170]. In the following part of this section, the powertrain system and the longitudinal dynamics of the series HEV are introduced.

The series HEV powertrain architecture is sketched in Fig. 3.1. As can be noticed, the power outputs from the primary source (PS) and the secondary source (SS) branches are combined electrically at the DC-link. Then, the total power is delivered to the driving wheels included in the propulsion load (PL) branch, which is an inverter driven electric motor/generator, mechanically connected to the wheels with a transmission system characterised by a fixed gear ratio g_r. The inverter and transmission are modelled as constant efficiency terms η_i, η_t, while the efficiency of the motor/generator, η_m, is described by a static efficiency map of the load torque and the angular speed, as shown in Fig. 3.2.

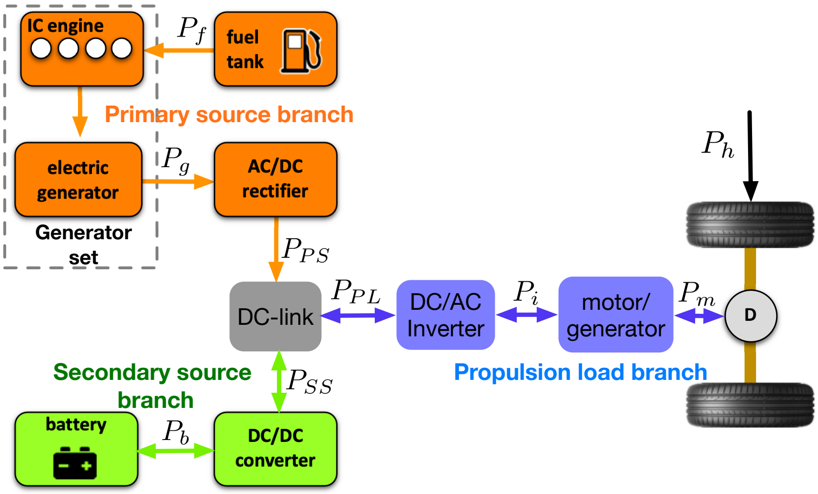

Fig. 3.1 Powertrain architecture of the series HEV.

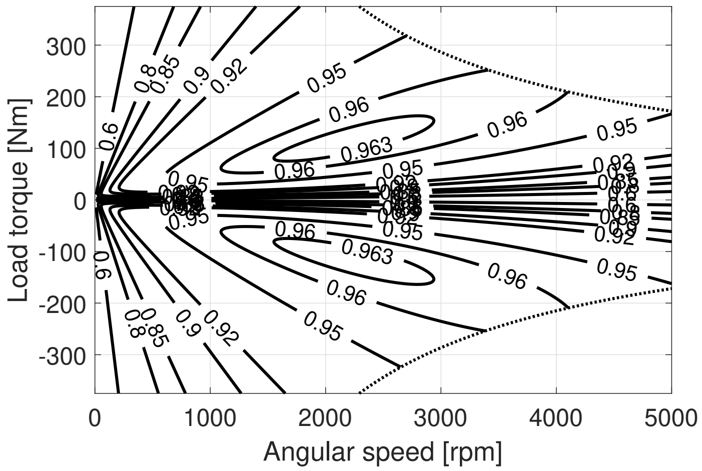

Fig. 3.2 Efficiency of the reversible motor/generator (generator = positive torque, motor = negative torque) [171]. The torque bounds (due to power limitation) are shown by dotted lines. The rated power of the machine is 95kW.

By virtue of the series architecture, it is reasonable to assume the load power P_{PL} is a known signal, as it is independent of the EM (power split) between the two energy sources [172]. Given a driving cycle and the steady state efficiencies η_i, η_t, η_m, P_{PL} may be determined by:

$$P_{PL} = \begin{cases} \dfrac{P_{drive}}{\eta_i \eta_m \eta_t}\,, & \forall P_{drive} \geq 0\,, \qquad (3.1a) \\ (P_{drive} - P_h)\eta_i \eta_m \eta_t\,, & \forall P_{drive} < 0\,, \qquad (3.1b) \end{cases}$$

where P_{drive} is the power at the driving wheels requested to follow the driving cycle, and P_h is the mechanical braking power directly applied to the wheels. Furthermore, P_{drive} can be evaluated by Newton's laws of the longitudinal motion, as follows:

$$P_{drive} = v\left(ma + F_r + F_d + mg\sin\theta\right), \tag{3.2}$$

where v, a and m are the speed, acceleration and mass of the vehicle respectively, $F_r = f_r mg$ and $F_d = f_d v^2$ are the resistance forces respectively with coefficients f_T and f_D due to rolling and aerodynamics drag, and θ is the road slope associated with the speed profile. By considering that the mechanical braking power is dissipated and $P_{SS_{\min}}$ is the maximum charging power of the SS, it is possible to always freely choose P_h such that P_{PL} in (3.1b) for $P_{drive} < 0$ is as follows

$$P_{PL} = \max\left(P_{drive}\eta_i\eta_m\eta_t, P_{SS_{\min}}\right), \forall P_{drive} < 0 \tag{3.3}$$

to maximise energy regeneration, and hence fuel economy.

Consequently, it is reasonable to decouple the EM problem of a series HEV into two steps: 1) compute P_{PL} requested by a driving cycle by (3.1a), (3.2) and (3.3) through a preview prediction of future behaviour by wireless communication technologies (see the scheme in Fig. 2.2) and 2) find an appropriate power split (for $P_{PL}(t) > 0$) between the two energy sources subject to the power balance at the DC-link:

$$P_{PL} = P_{PS} + P_{SS}, \tag{3.4}$$

where P_{PS} is the PS branch output power and P_{SS} is the SS branch output power.

3.1.1 Primary Source Branch

As shown in Fig. 3.1, the engine branch is formed by an ICE, a permanent magnet synchronous generator, and an AC-DC rectifier, which are connected in series. The overall efficiency of this branch is simply the product of individual component steady state efficiencies. The present work is based on the PS branch efficiency map shown in Fig. 3.3 [172]. Due to the mechanical separation between the primary source branch and the wheels, a requested power from ICE can be supplied by choosing the most efficient torque-speed operating points as denoted by the red dashed line in the left figure of Fig. 3.3. In such a case, the fuel mass rate q_f, as shown in Fig. 3.3, can be fitted approximately as a linear function of the branch output power P_{PS}. The fuel consumption model (FCM) of the fuel mass m_f is therefore given by,

$$\dot{m}_f = q_{f0} + \alpha_f P_{PS}, \tag{3.5}$$

where q_{f0} acts as the idling fuel mass rate, and α_f is the coefficient of power transformation.

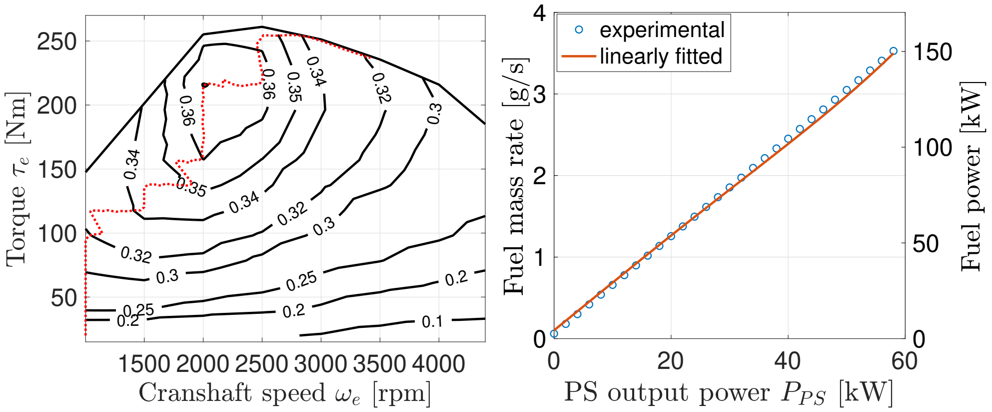

Fig. 3.3 Left: map of overall efficiency of the engine branch [172]. The torque-speed operating points for maximum engine branch efficiency at different output power values are shown by a dashed red curve. Right: fuel mass rate with PS power, when the most efficient torque-speed operating point is followed at each power value.

3.1.2 Secondary Source Branch

The battery is modelled as a series connection of an ideal voltage source and an ohmic resistance, therefore the battery voltage V_b is defined by $V_b = V_{oc} - i_b R_b$, where V_{oc} is the open circuit voltage of the battery, i_b is the battery current assumed positive during the discharge phase, and R_b is the internal resistance. By considering the battery output power $P_b = V_b i_b$, i_b can be solved with respect to V_{oc}, R_b and P_b, as follows:

$$i_b = \frac{V_{oc} - \sqrt{V_{oc}^2 - 4P_b R_b}}{2R_b}. \tag{3.6}$$

The battery state-of-charge (SOC) represents the only state variable, governed by $\dot{\text{SOC}} = -i_b/Q_{\max}$, where $Q_{\max}$ is the battery capacity. Instead of using a nonlinear mapping between SOC and the open circuit voltage, V_{oc} is reasonably approximated by a constant voltage, which is compatible with the usual aim of a charge sustaining (CS) battery management, by which the SOC is narrowly constrained. Furthermore, by combining the battery with the bidirectional DC/DC converter, the SS output power is obtained by:

$$P_{SS} = \eta_{dc}^{\text{sign}(P_{SS})} P_b, \tag{3.7}$$

where η_{dc} is the efficiency of the DC/DC converter. Substituting the algebraic solution of i_b (obtained by applying (3.7) in (3.6)), the dynamic behaviour of the SS can be described by the differential equation of SOC with respect to P_{SS} only as:

$$\dot{\mathrm{SOC}} = \frac{-V_{oc} + \sqrt{V_{oc}^2 - 4P_{SS}R_b/\eta_{dc}^{\mathrm{sign}(P_{SS})}}}{2R_b\,Q_{\max}}. \tag{3.8}$$

Moreover, the operation of both energy sources is subject to,

$$\mathrm{SOC}_{\min} \leq \mathrm{SOC} \leq \mathrm{SOC}_{\max}, \tag{3.9}$$

$$0 \leq P_{PS} \leq P_{PS_{\max}}, \tag{3.10}$$

$$P_{SS_{\min}} \leq P_{SS} \leq P_{SS_{\max}}, \tag{3.11}$$

where $\mathrm{SOC}_{\min}$ and $\mathrm{SOC}_{\max}$ are the SOC operational limits, and $P_{PS_{\max}}$ and $P_{SS_{\max}}$ are the maximum propulsive power PS and SS can deliver respectively.

3.2 Battery Electric Vehicle

The gross motion of the battery electric vehicles (BEV) utilised in this thesis is modelled by using the single-track, non-holonomic vehicle model [67]. In this context, the longitudinal dynamics are described by the following differential equation:

$$\frac{d}{dt}v = \frac{F_w - F_r - F_d}{m}, \tag{3.12}$$

where $v(t)$ is the linear (forward) velocity of the BEV, m is the vehicle mass, F_w is the powertrain driving or braking force acting on the wheels, while $F_r = f_r mg$ and $F_d = f_d v^2$ are the resistance forces of rolling and air drag, respectively, with f_r and f_d the coefficients of rolling and air drag resistance. Moreover, F_w can be broken down into two separate control inputs, the powertrain driving force F_t and the mechanical braking force $F_h < 0$, such that

$$F_w = F_t + F_h. \tag{3.13}$$

3.2.1 BEV Powertrain Model

As shown in Fig. 3.4, the powertrain of the BEV connected to the battery contains a DC/DC converter, an electric motor and a transmission set, where both the converter and the transmission are simply modelled by constant efficiency factors and the efficiency of the motor is modelled as a static efficiency map [67, 173]. Hence, the physical limits of the force

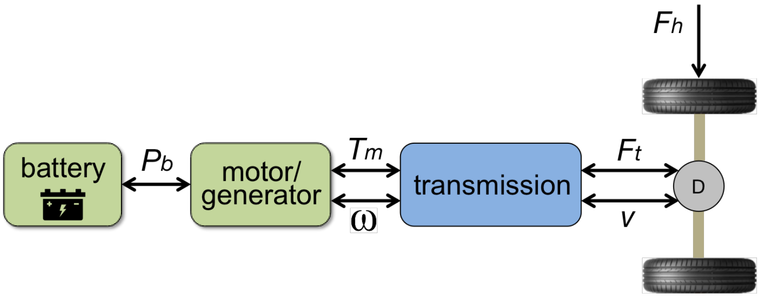

Fig. 3.4 Power flow scheme of a BEV powertrain.

on the wheels from the powertrain, F_w (see (3.13)), can be expressed as:

$$\frac{g_r}{r_w}T_{m,\min} = F_{t,\min} \leq F_t \leq F_{t,\max} = \frac{g_r}{r_w}T_{m,\max}, \tag{3.14a}$$

$$ma_{\min} - \frac{g_r}{r_w}T_{m,\min} = F_{b,\min} \leq F_h \leq F_{b,\max} = 0, \tag{3.14b}$$

$$ma_{\min} = F_{w,\min} \leq F_w \leq F_{w,\max} = \frac{g_r}{r_w}T_{m,\max}, \tag{3.14c}$$

where T_m is the motor torque constrained by $T_m \in [T_{m,\min}, T_{m,\max}]$, r_w is the wheel radius, g_r is the fixed transmission gear ratio, $a_{\min}$ is the peak deceleration during an emergency brake.

3.2.2 Battery Output Power Model

According to established literature, the input power (electric side) of the motor, P_b, can be represented as a quadratic function of motor force, F_t, and vehicle speed (equivalent to motor torque and angular speed respectively), given by [174]:

$$P_b = b_1 F_t^2 + b_2 F_t v, \tag{3.15}$$

where b_1 and b_2 are fitting parameters. Though the battery power is a nonlinear function of P_b due to the internal resistance losses, which are insignificant compared to other powertrain losses [175]. Hence, it is reasonable to neglect the influence of the battery internal resistance and to approximate the battery power by P_b, such that the battery energy usage of the BEV, J_b, can be evaluated based on the tank-to-wheel energy path of the vehicle , P_b, as follows:

$$J_b = \int_0^T P_{b,i}\, dt, \tag{3.16}$$

where T is the total time of the driving mission.

Part I

Optimal Energy Management for A Single CAV

Chapter 4

Optimal Energy Management of Series HEVs with Engine Start-Stop System

4.1 Introduction

This chapter focuses on the single-vehicle energy management problem based on a preview of traffic information through wireless communication technologies (i.e. V2I and GPS). The purpose of this chapter is to bridge the gap between rule-based and optimisation-based EM strategies in the more general context with the SSS considered, by proposing a novel heuristic strategy for EM control of series HEVs with SSS. The main contributions of the work in this chapter are summarised as follows:

a. Fundamental analysis with an HEV model without engine SSS that considers the main physics of the EM problem for series HEVs is conducted and feasible fundamental solutions of the optimal EM for series HEVs are found (this is a generalisation of the work in [176]).

b. Fundamental analysis with an HEV model with an ideal (lossless) engine SSS, which additionally to the model features in contribution a) captures the basic physics of the SSS, is conducted and feasible fundamental solutions of the optimal EM for series HEVs with SSS are found.

c. Fundamental analysis proves that CS operation is a necessary condition to reach globally optimal fuel economy in series HEVs.

d. By using simple and effective control rules that are inspired by the fundamental analysis and solutions of the optimal EM in contributions a) and b), as well as by the CS operation optimality result in contribution c), a novel heuristic strategy, HPTS, is proposed for the EM control of series HEVs with a more realistic SSS for which engine restarts are associated with a fuel penalty. An analytic solution of the optimal EM is not feasible in this case.

e. The performance of the HPTS is evaluated and benchmarked against DP solutions and a recently developed state-of-the-art rule-based method. Moreover, the impact of the penalty fuel for engine restarts is investigated by simulation.

The remainder of this chapter is structured as follows. Section 4.2 introduces the vehicle model and the formulation of the EM problem. A theoretical derivation of the optimal EM solutions is presented in Section 4.3, and from the analysis, the HPTS is proposed. Section 4.3 also includes the analysis that proves the optimality of CS operation. Simulation results and discussion are presented in Section 4.4. Finally, concluding remarks are given in Section 4.5. Note that Sections 4.2- 4.5 are taken from the author's publication [177].

4.2 Modelling and Problem Formulation

This section introduces the overall vehicle model with particular emphasis on the modelling of the engine start-stop system (SSS), which has not been considered sufficiently in the past. The vehicle model is developed based on the series HEV system (without the engine start-stop system) described in Section 3.1.

The SSS allows the ICE to be switched off without idling loss. However, some amount of fuel is consumed to turn on the ICE again. In this work, this penalty fuel usage is modelled by a constant term $m_p = Kq_{f0}\,\mathrm{kg}$, which is equivalent to the amount of fuel consumed by idling the ICE for K seconds. Moreover, the delay of restarting the engine is neglected as it mainly affects the driving comfort rather the than fuel economy.

To integrate the SSS dynamics into the fuel consumption model (3.5), let us introduce the binary engine off/on state $s_{eng} \in \{0,1\}$ and the jump set $\mathcal{S} \triangleq \{s_{eng} | s_{eng}^{+} \neq s_{eng}\}$, with s_{eng}^{+} the next value of the state. As such, ICE operation can be characterised in terms of s_{eng} and P_{PS}: 1) the engine is switched off when $s_{eng} = 0$, $P_{PS} = 0$, 2) the engine is idling when $s_{eng} = 1$, $P_{PS} = 0$, and 3) the engine produces propulsive power when $s_{eng} = 1$, $P_{PS} > 0$. Finally, the FCM in the presence of the SSS may be described by the following hybrid dynamical system:

$$\begin{cases} \dot{m}_f = q_{f0}\, s_{eng} + \alpha_f P_{PS}, & \text{if } s_{eng} \notin \mathcal{S}, \\ \dot{s}_{eng} = 0, & \end{cases} \tag{4.1}$$

and

$$\begin{cases} s_{eng}^{+} = s_{eng} + u_s, & \text{if } s_{eng} \in \mathcal{S}, \\ m_f^{+} = m_f + m_p(1 - s_{eng}), & \end{cases} \tag{4.2}$$

where $u_s \in \{-1, 1\}$ is the SSS control signal.

In view of (3.8), (4.1), and (4.2), the overall system dynamics are captured by the hybrid system given by:

$$\dot{\mathbf{x}} = \mathbf{f}(\mathbf{x},\mathbf{u}) = \begin{pmatrix} q_{f0} s_{eng} + \alpha_f P_{PS} \\ \dfrac{-V_{oc} + \sqrt{V_{oc}^2 - 4 P_{SS} R_b / \eta_{dc}^{\mathrm{sign}(P_{SS})}}}{2 R_b Q_{\max}} \\ 0 \end{pmatrix}, \tag{4.3}$$

if $s_{eng} \notin \mathcal{S}$, and if $s_{eng} \in \mathcal{S}$:

$$\mathbf{x}^+ = \mathbf{g}(\mathbf{x},\mathbf{u}) = \begin{pmatrix} m_f + m_p(1 - s_{eng}) \\ \mathrm{SOC} \\ s_{eng} + u_s \end{pmatrix}, \tag{4.4}$$

where $\mathbf{x} = [m_f, \mathrm{SOC}, s_{eng}]^\top$ and $\mathbf{u} \triangleq [P_{PS}, P_{SS}, u_s]^\top$ represent the state variables and control inputs, respectively.

The EM control aims to minimise the overall fuel consumption m_f by an appropriate power split between P_{PS} and P_{SS}, which satisfy the DC-link power balance:

$$P_{PL} = s_{eng} P_{PS} + P_{SS}, \tag{4.5}$$

where the P_{PL} in this single-vehicle energy management problem in this chapter can be determined by a preview of the future driving cycle through V2I communication or GPS (see the scheme in Fig. 2.2).

The main characteristic parameters of the series HEV model studied in this chapter are summarised in Table 4.1.

4.3 Energy Management Strategies

This section aims to provide a fundamental analysis to show the nature of optimal EM solutions using two variants of the presented vehicle model, both of which have been used for the design of EM strategies in the literature: 1) without engine SSS, and 2) with an ideal engine SSS ($m_p = 0$). The analytic solutions yield some fundamental principles that are used to go beyond the treatment of models 1) and 2) and construct a new heuristic control strategy, the HPTS, for the more realistic model (4.3)-(4.4). Further analysis is carried out to justify the optimality of the CS operation in terms of fuel efficiency, which is linked to the control design and results presented in this chapter.

Table 4.1 Main parameters of the series HEV model with SSS.

Description	Symbol	Value
Vehicle mass	m	1500 kg
Rolling resistance coefficient	f_T	0.01
Aerodynamics drag coefficient	f_D	0.47
Efficiency of the transmission	η_t	0.96
idling fuel mass rate	q_{f0}	0.12g/s
Power transformation factor	α_f	0.059 g/kW/s
Battery capacity	$Q_{\max}$	5 Ah
Battery internal resistance	R_b	0.2056 Ω
Battery open circuit voltage	V_{oc}	300 V
Efficiency of inverters	η_r, η_i	0.96
Efficiency of converter	η_{dc}	0.96
SS power limits	$P_{SS_{\min/\max}}$	$-15/30$kW
Battery SOC limits	$\mathrm{SOC}_{\min/\max}$	$0.5/0.8$
PS power limit	$P_{PS_{\max}}$	70kW

For the sake of further analysis, let us first introduce some useful notations and definitions for the upcoming analysis. Consider T the total time of the driving mission. Two sets of time intervals are considered, $\Phi \triangleq \{t|P_{PL}(t) \geq 0\}$ and $\Psi \triangleq \{t|P_{PL}(t) < 0\}$, such that $\Phi \cup \Psi$ is the full time horizon $\{t|0 \leq t \leq T\}$. The overall SOC variation over $[0,T]$ is defined as

$$\Delta\mathrm{SOC} \triangleq \mathrm{SOC}(0) - \mathrm{SOC}(T).$$

It is clear that,

$$\Delta\mathrm{SOC} = \Delta_\Phi\mathrm{SOC} + \Delta_\Psi\mathrm{SOC},$$

where

$$\Delta_\Phi\mathrm{SOC} \triangleq -\int_\Phi \frac{d\mathrm{SOC}}{dt}dt$$

and

$$\Delta_\Psi\mathrm{SOC} \triangleq -\int_\Psi \frac{d\mathrm{SOC}}{dt}dt \leq 0.$$

Moreover, Φ can be divided into 2 subsets as $\Phi = \Phi_d \cup \Phi_c$ with $\Phi_d \triangleq \{t|P_{PL}(t) \geq 0, i_b(t) \geq 0\}$, $\Phi_c \triangleq \{t|P_{PL}(t) \geq 0, i_b(t) < 0\}$. These subsets respectively collect the battery discharging and charging intervals for all $t \in \Phi$. Therefore,

$$\Delta\mathrm{SOC} = \Delta_{\Phi_d}\mathrm{SOC} + \Delta_{\Phi_c}\mathrm{SOC} + \Delta_\Psi\mathrm{SOC} \tag{4.6}$$

with $\Delta_{\Phi_c}\mathrm{SOC} < 0$ and $\Delta_{\Phi_d}\mathrm{SOC} \geq 0$. Finally, for brevity, the dependence of all variables on t is dropped in the following analysis.

4.3.1 Analysis for Series HEV Model without SSS

Let us start from analysing the powertrain system without the SSS, as the analytic solution is also instrumental for subsequently studying the optimal EM solution for the system with consideration of the SSS.

According to the power balance at the DC-link (4.5), the input power signal P_{PS} of the FCM (3.5) can be replaced by $P_{PS} = P_{PL} - P_{SS}$ (s_{eng} is substituted as 1). By considering (3.5), the fuel consumption minimisation problem can be rewritten as,

$$\min J = \int_0^T q_{f0}\, dt + \alpha_f \int_0^T P_{PL}\, dt - \alpha_f \int_0^T P_{SS}\, dt,$$

which is equivalent to

$$\min_{P_{SS}} J = -\alpha_f \int_0^T P_{SS}\, dt, \tag{4.7}$$

as $\int_0^T q_{f0}\, dt + \alpha_f \int_0^T P_{PL}\, dt$ is constant for a given driving cycle and independent of the EM control. The EM control problem of a series HEV is now formulated as an optimisation problem with only one dynamic state, SOC, and a single control input, P_{SS}, subject to the SOC operational limits (3.9) and the energy source power limits,

$$\max(P_{PL} - P_{PS_{\max}}, P_{SS_{\min}}) \leq P_{SS} \leq \min(P_{SS_{\max}}, P_{PL}), \tag{4.8}$$

where (4.8) is obtained by combining (3.10), (3.11) and (4.5). Based on the optimal solution for P_{SS}, the fuel usage, $m_f(T)$, can be evaluated a posteriori. To address this optimisation problem, constrained and unconstrained arcs need to be pieced together. Based on the state constraints (3.9), the optimal solution is the result of different combinations of the following possible arcs.

1) State Constraints not Active

Based on PMP, a candidate for an optimal control input P_{SS}^* for minimising (4.7) is found if P_{SS}^* minimises the Hamiltonian:

$$H = -\alpha_f P_{SS} + \begin{cases} \lambda \dfrac{-V_{oc} + \sqrt{V_{oc}^2 - 4P_{SS} R_b / \eta_{dc}}}{2R_b Q_{\max}}, & P_{SS} \geq 0, \\ \lambda \dfrac{-V_{oc} + \sqrt{V_{oc}^2 - 4P_{SS} R_b \eta_{dc}}}{2R_b Q_{\max}}, & P_{SS} < 0, \end{cases} \tag{4.9}$$

which includes the costate λ. The dynamics of the costate are described by

$$\dot{\lambda} = -\frac{\partial H}{\partial \mathrm{SOC}} = 0, \tag{4.10}$$

which implies the optimal costate λ is constant. By taking the partial derivative of H with respect to P_{SS}, we obtain:

$$\frac{\partial H}{\partial P_{SS}} = -\alpha_f - \begin{cases} \dfrac{\lambda}{\eta_{dc} Q_{\max} \sqrt{V_{oc}^2 - 4P_{SS}R_b/\eta_{dc}}}, & P_{SS} \geq 0, \\ \dfrac{\lambda \eta_{dc}}{Q_{\max} \sqrt{V_{oc}^2 - 4P_{SS}R_b\eta_{dc}}}, & P_{SS} < 0. \end{cases}$$

If $\lambda = 0$, $\partial H/\partial P_{SS} = -\alpha_f < 0$, which is independent of the input. Hence, the Hamiltonian is minimised at the maximum value of the input, as follows:

$$P_{SS}^* = P_{SS_{\max}}. \tag{4.11}$$

If $\lambda > 0$, it is immediate to show that $\partial H/\partial P_{SS} < 0$, $\forall P_{SS}$ (with $P_{SS_{\max}} < V_{oc}^2\eta_{dc}/(4R_b)$), and the optimal control input follows (4.11). If $\lambda < 0$, the second order derivative of H with respect to P_{SS},

$$\frac{\partial^2 H}{\partial P_{SS}^2} = \begin{cases} -\dfrac{2\lambda R_b}{\eta_{dc}^2 Q_{\max} \left(V_{oc}^2 - 4P_{SS}R_b/\eta_{dc}\right)^{3/2}}, & P_{SS} \geq 0 \\ -\dfrac{2\lambda \eta_{dc}^2 R_b}{Q_{\max} \left(V_{oc}^2 - 4P_{SS}R_b\eta_{dc}\right)^{3/2}}, & P_{SS} < 0 \end{cases}$$

is always positive. As such, H is formed by two convex segments continuous at $H(0) = 0$, and the global minimum of H depends on the minima of the functions representing both segments of H. By solving the algebraic equation $\partial H/\partial P_{SS} = 0$ for $P_{SS} \geq 0$ and $P_{SS} < 0$ respectively, we obtain,

$$P_{SS}^* = \frac{1}{4R_b}\left(\eta_{dc}V_{oc}^2 - \frac{\lambda^2}{\alpha_f^2 Q_{\max}^2 \eta_{dc}}\right), \text{ if } P_{SS} \geq 0, \tag{4.12a}$$

$$P_{SS}^* = \frac{1}{4R_b}\left(\frac{V_{oc}^2}{\eta_{dc}} - \frac{\lambda^2 \eta_{dc}}{\alpha_f^2 Q_{\max}^2}\right), \quad \text{if } P_{SS} < 0, \tag{4.12b}$$

at which the two quadratic functions reach their minima. If $\lambda \in (-\alpha_f Q_{\max}\eta_{dc}V_{oc}, 0)$, both optimal control inputs shown in (4.12a) and (4.12b) are positive, which implies the minimum of H within the domain $P_{SS} < 0$ is $H(0)$, and therefore, the global minimum of H is obtained at (4.12a). Similarly, for $\lambda \in (-\infty, -\alpha_f Q_{\max}V_{oc}/\eta_{dc})$, it can be inferred that both solutions shown in (4.12a) and (4.12b) are negative. Hence, the global minimum of H is obtained when P_{SS} follows (4.12b). Finally, if $\lambda \in \left[-\alpha_f Q_{\max}V_{oc}/\eta_{dc}, -\alpha_f Q_{\max}\eta_{dc}V_{oc}\right]$, the optimal control shown in (4.12a) is negative and in (4.12b) is positive. As such, H is monotonically increasing for $P_{SS} \geq 0$ and monotonically decreasing for $P_{SS} < 0$, which yields $P_{SS}^* = 0$. By including the control constraints (4.8), the optimal input P_{SS}^{*} is given as follows:

$$P_{SS}^{*}=\begin{cases} \min(P_{SS_{\max}}, P_{PL}), & \forall\lambda \in [0,\infty), \\ \min\left(P_{SS}^{*+}, P_{SS_{\max}}, P_{PL}\right), & \forall\lambda \in (-\alpha_f Q_{\max}\eta_{dc}V_{oc}, 0), \\ \min(0, P_{PL}), & \forall\lambda \in \left[-\dfrac{\alpha_f Q_{\max}V_{oc}}{\eta_{dc}}, -\alpha_f Q_{\max}\eta_{dc}V_{oc}\right], \\ \min\left(\max\left(P_{SS}^{*-}, P_{PL}-P_{PS_{\max}}, P_{SS_{\min}}\right), P_{PL}\right), & \forall\lambda \in \left(-\infty, -\dfrac{\alpha_f Q_{\max}V_{oc}}{\eta_{dc}}\right). \end{cases} \tag{4.13}$$

where, for brevity, we denote P_{SS}^{*+} and P_{SS}^{*-} the solutions given in (4.12a) and (4.12b), respectively. As it can be seen, there exist four possible optimal modes of operation depending on the value of λ. Given initial and terminal conditions $\mathrm{SOC}(0)$ and $\mathrm{SOC}(T)$ in conjunction with P_{PL} of a given driving cycle, the value of λ can be calculated by solving a boundary value problem through a simple parameter searching approach that ends when the $\mathrm{SOC}(T)$ is satisfied. As the costate λ is denoted as an equivalence factor, which represents the ratio of fuel consumption to electrical energy required when following a given P_{PL} profile, the finding of λ is equivalent to identifying the constant operating power of the SS. It is noteworthy that P_{SS}^{*} is constant unless a control constraint (see (4.8)) is reached. Moreover, when $P_{PL} < 0$ (i.e., $t \in \Psi$), it can be seen in all cases shown in (4.13) that the optimal input is simply expressed as,

$$P_{SS}^{*} = P_{PL} \tag{4.14}$$

unless $\max\left(P_{SS}^{*-}, P_{PL} - P_{PS_{\max}}, P_{SS_{\min}}\right) < P_{PL}$ (which is a special case of the fourth case in (4.13)), and in such a case,

$$P_{SS}^{*} = \max\left(P_{SS}^{*-}, P_{PL} - P_{PS_{\max}}, P_{SS_{\min}}\right). \tag{4.15}$$

The latter is a non typical case where significant battery charging is required, such that the ICE will be active even during the braking phase to boost the battery charging power.

2) State Constraints Active

By operating the SS at P_{SS}^{*}, the unconstrained optimal state trajectory, $\mathrm{SOC}^{*}(t, P_{SS}^{*})$, may violate the state constraint (3.9) during the operation. The optimal solution in such cases can be found by invoking a recursive scheme [178]. Suppose that at some time $t = t_p$, the state constraint is exceeded the most in the unconstrained optimal trajectory, the problem is then split in two subproblems with boundary conditions $\{\mathrm{SOC}(0), \mathrm{SOC}(t_p)\}$ and $\{\mathrm{SOC}(t_p), \mathrm{SOC}(T)\}$, respectively, with $\mathrm{SOC}(t_p) = \mathrm{SOC}_{\max}$ in the case the upper state constraint is exceeded, otherwise $\mathrm{SOC}(t_p) = \mathrm{SOC}_{\min}$. By following the same approach used for the unconstrained case, it is immediate to find the optimal costate and the associated control solution for both problems. From the jump conditions of the PMP, λ is discontinuous at t_p, and $\lambda(t_p^+) < \lambda(t_p^-)$ if the upper bound is reached, $\lambda(t_p^+) > \lambda(t_p^-)$ if the lower bound is reached. Once the solution for a subproblem is found, such properties can be utilised to facilitate the searching of λ for the other subproblem. If the constraint is still violated in any of the two subproblems, the procedure is repeated until all state constraints are met.

To illustrate the above recursive solution searching mechanism, a numerical example with HEV parameters given in Table 4.1 is demonstrated in Fig. 4.1. The HEV is requested to follow a segment (WL-L) of a standard driving cycle (that will be properly introduced later in Fig. 4.7) with the associated P_{PL} profile as shown in Fig. 4.1, and the boundary conditions of SOC set to $\text{SOC}(0) = 79.8\%, \text{SOC}(T) = 79.8\%$. As it can be noticed, in the unconstrained

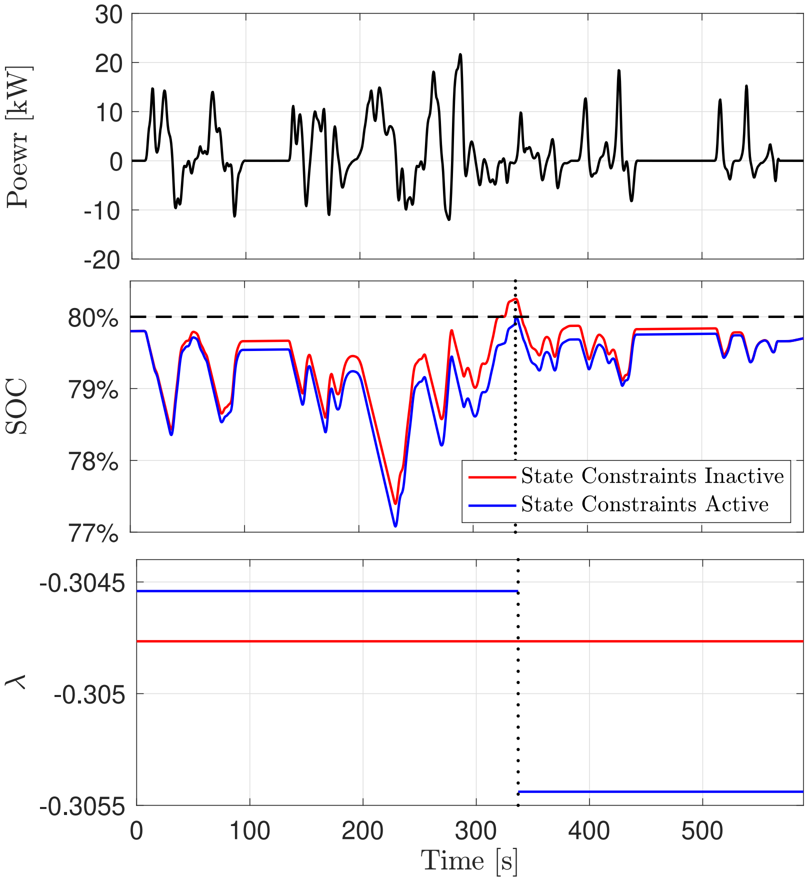

Fig. 4.1 Sketch of example optimal solution for a vehicle mission when a state (SOC) constraint is reached. Top: Mission shown as P_{PL} power profile results from the WL-L driving cycle. Middle: Optimal SOC trajectories for the unconstrained (red) and constrained (blue) cases. Bottom: Optimal costate, λ, for the unconstrained (red) and constrained (blue) cases.

optimal state (SOC) trajectory, the SOC constraint is exceeded the most at $t_p = 337\mathrm{s}$, where the boundary value problem is subsequently split into two subproblems. By repeating the global search of λ for both subproblems, a piecewise constant λ is found. Since the SOC constraint is fulfilled by the resulting state trajectories in both phases, the recursive algorithm ends and the optimal solution is found.

To further clarify the closed form control solution (4.13), another example is carried out by utilising a simple but representative P_{PL} profile. As it can be seen in Fig. 4.2, by following a simple P_{PL} profile the optimal power-split profiles are found by DP for vehicle parameters given in Table 4.1 with a fixed terminal $\mathrm{SOC}(T)$ at 0.65. To emulate different scenarios in (4.13), (last three Cases in (4.13) except Case 1 which is a sub-solution of Case 2) initial SOC cases are set to: 0.64, 0.5775, 0.54, which are associated with the three different cases of $\Delta_\Phi\mathrm{SOC} > 0$ (solution Case 2), $\Delta_\Phi\mathrm{SOC} = 0$ (solution Case 3) and $\Delta_\Phi\mathrm{SOC} < 0$ (solution Case 4), respectively. The subcase of Case 4 shown by (4.15) may occur if $\mathrm{SOC}(0)$ is set to a further lower value (more charge is required to meet the terminal SOC condition by the end of the mission). Under these circumstances, the SS is charged throughout the mission at a constant power below the negative P_{PL} value (this subcase is not shown in Fig. 4.2). The numerical (DP) results in Fig. 4.2 verify the closed form solution (4.13), indicating that for an optimal EM (during the propulsive phase Φ) the SS is operated at a load levelling fashion unless a control or a state limit is reached (for example, during the period $t \in [0,5]$ in Case 2). As a consequence, once the PS is active, its power output P_{PS} follows the trends of the P_{PL} profile but with a fixed power difference that is equal to P_{SS}^*.

4.3.2 Analysis for Series HEV Model with Lossless SSS

In this section, the SSS is integrated with no penalty fuel ($m_p = 0$), as commonly assumed in EM studies (see for example [14, 169, 179]). In such a case, the new Hamiltonian $\forall t$ is:

$$H = \begin{cases} H_1 = q_{f0} + \alpha_f(P_{PL} - P_{SS}) + \lambda \dfrac{-V_{oc} + \sqrt{V_{oc}^2 - 4P_{SS}R_b/\eta_{dc}^{\mathrm{sign}(P_{SS})}}}{2R_b\,Q_{\max}}, & P_{SS} < P_{PL}, \\ H_2 = \lambda \dfrac{-V_{oc} + \sqrt{V_{oc}^2 - 4P_{PL}R_b/\eta_{dc}^{\mathrm{sign}(P_{PL})}}}{2R_b\,Q_{\max}}, & P_{SS} = P_{PL}. \end{cases} \tag{4.16}$$

The dynamics of the costate remains the same as (4.10). The minimum of the Hamiltonian with respect to the control input P_{SS} can be found by identifying the minimum of the two candidates H_1 and H_2 of the piecewise Hamiltonian (4.16), and selecting the minimum between the two candidates [18, 179]. For the sake of further analysis, let H_1^* and H_2^* denote

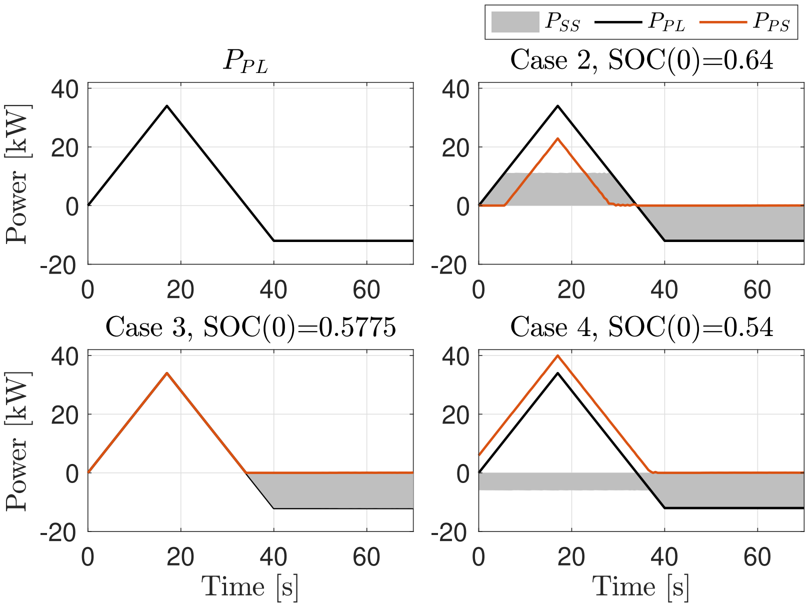

Fig. 4.2 Optimal power-split solutions found by DP for the case without SSS for an example power demand trajectory P_{PL} of 70 s, an $\mathrm{SOC}(T) = 0.65$ and three different cases of $\mathrm{SOC}(0)$. Each $\mathrm{SOC}(0)$ case is chosen to respectively actualise the last three of the closed-form solution cases in (4.13), associated with $\lambda = -0.2929$ for Case 2, $\lambda = -0.3448$ for Case 4 and $\lambda \in [-0.3361, -0.3097]$ for Case 3 (the control signal does not depend on λ), with the two λ transition points being $-\alpha_f Q_{\max} V_{oc}/\eta_{dc} = -0.3361$ and $-\alpha_f Q_{\max} \eta_{dc} V_{oc} = -0.3097$. Note that in Case 4 for an even lower $\mathrm{SOC}(0)$ (more demand on battery charging), during negative P_{PL} the optimal solution may request the engine to contribute to the charging of the battery, and therefore P_{PS} may become positive, instead of 0, while at the same time P_{SS} may become more negative than P_{PL}, instead of being equal to P_{PL}.

the optima of H_1 and H_2, respectively. The minimum for the second candidate H_2 is trivial,

$$H_2^* = H_2, \;\; P_{SS}^* = P_{PL}, \tag{4.17}$$

since the expression H_2 does not depend on the control variable P_{SS}. In accordance with the results (without the SSS) shown previously, the following analysis for the present case of SSS is carried out individually for all the four cases presented in (4.13).

a) $\lambda \in [0, \infty)$: Due to the fact that H_1 is monotonically decreasing as P_{SS} increases (for example, consider that $\frac{\partial H_1}{\partial P_{SS}} < 0$) and $P_{SS} < P_{PL}$, it can be inferred that $H_1 > H_2$ for all feasible P_{SS}. Therefore, the associated optimal control solution shown in (4.13) remains as the optimum under such circumstances, and the optimal Hamiltonian, H^*, is

$$H^*(P_{SS}^*) = \begin{cases} H_1^* = H_1(P_{SS_{\max}}), & \text{if } P_{PL} > P_{SS_{\max}}, \\ H_2^*, & \text{if } P_{SS_{\max}} \geq P_{PL}. \end{cases} \tag{4.18}$$

b) $\lambda \in (-\alpha_f Q_{\max}\eta_{dc}V_{oc}, 0)$: The minimum of H_1 by applying the unconstrained optimal control input P_{SS}^{*+} (defined in (4.12a)) is:

$$H_1^* = q_{f0} + \alpha_f P_{PL} - \frac{\alpha_f \eta_{dc} V_{oc}^2}{4R_b} - \frac{\lambda^2}{4R_b Q_{\max}^2 \alpha_f \eta_{dc}} - \lambda \frac{V_{oc}}{2R_b Q_{\max}}. \tag{4.19}$$

The minimum of the switching Hamiltonian H may be identified by assuming $\tilde{H} = H_1^* - H_2^*$, which is a quadratic and concave function with respect to P_{PL} ($H_1^*(P_{PL})$ is linear and $H_2^*(P_{PL})$ is convex). The maximum value of $\tilde{H}$, $\tilde{H}_{max}$, can be identified by first solving the equation $\partial \tilde{H}/\partial P_{PL} = 0$, yielding $P_{PL}^* = P_{SS}^{*+} > 0$ from which it is immediate to obtain $\tilde{H}_{max} = \tilde{H}(P_{PL}^*) = q_{f0} > 0$. Hence, the equation $\tilde{H} = 0$ has two real roots $P_{PL}^+(\lambda)$ and $P_{PL}^-(\lambda)$ (the superscript "$-$" stands for the smaller root while "$+''$ represents the greater one), which result in a power interval $\Sigma_1 = \{P_{PL} | P_{PL}^- < P_{PL} < P_{PL}^+\}$, and for $P_{PL} \in \Sigma_1$, it holds that

$$\tilde{H} > 0 \Rightarrow H_1^* > H_2^*. \tag{4.20}$$

Expression (4.20) gives the region where H_2^* is the minimum of the switching Hamiltonian. Otherwise, H_1^* is the minimum. A singularity may occur when P_{PL} equals P_{PL}^+ or P_{PL}^- as both minimum candidates adopt the same value. In this case, either H_1^* or H_2^* can be selected, and the preference could depend on the emphasis placed on other aspects, including NOx emissions, driver comfort, engine noise, and SSS cost (response lag and additional fuel required to restart the engine). The present work focuses on the fuel efficiency of energy management, which is directly influenced by the engine start fuel cost (as modelled in (4.1)-(4.2)). In this context, H_1^* should be chosen at the singularity to minimise the number of engine on/off switches.

If $P_{PL} > P_{SS_{\max}}$, it is straightforward to show that the Hamiltonian is minimised at H_1^*, as $H^* = H_2^*$ is valid only when $P_{PL} \leq P_{SS_{\max}}$ (see (4.18)). Let us now consider the case $P_{PL} \leq P_{SS_{\max}}$. When the unconstrained optimal control, P_{SS}^{*+}, is greater than P_{PL} (that is equivalent to $P_{PL} < P_{PL}^-$), P_{SS}^* will be saturated by P_{PL} such that $P_{SS}^* = P_{PL}$. Hence, the P_{PL} power region that yields $P_{SS}^* = P_{PL}$ (i.e., $H^* = H_2^*$, full electric mode) is $\mathcal{P}_{e,1} \triangleq \{P_{PL} | \Sigma_1 \cup P_{SS}^{*+} > P_{PL} \cap P_{PL} \leq P_{SS_{\max}}\}$. Therefore, the optimal solution for $\lambda \in (-\alpha_f Q_{\max}\eta_{dc}V_{oc}, 0)$, can be expressed as:

$$H^*(P_{SS}^*) = \begin{cases} H_2^*, & P_{PL} \in \mathcal{P}_{e,1}, \\ H_1^* = H_1(\min(P_{SS}^{*+}, P_{SS_{\max}})), & \text{otherwise.} \end{cases} \tag{4.21}$$

By following in this subsection the same steps conducted previously, it is straightforward to derive the P_{PL} regions where $H_1^* > H_2^*$ in the remaining two scenarios shown in (4.13): c) $\lambda \in \left[-\alpha_f Q_{\max}V_{oc}/\eta_{dc}, -\alpha_f Q_{\max}\eta_{dc}V_{oc}\right]$ and d) $\lambda \in \left(-\infty, -\alpha_f Q_{\max}V_{oc}/\eta_{dc}\right)$. Without loss of generality, let us assume the condition (4.20) is valid in case c) for $P_{PL} \in \mathcal{P}_{e,2}$, and in case d) for $P_{PL} \in \mathcal{P}_{e,3}$. Thus, the optimal solution in both scenarios can be expressed as:

c) $\lambda \in \left[-\alpha_f Q_{\max} V_{oc}/\eta_{dc}, -\alpha_f Q_{\max} \eta_{dc} V_{oc}\right]$:

$$H^*(P_{SS}^*) = \begin{cases} H_2^*, & P_{PL} \in \mathcal{P}_{e,2}\,, \\ H_1^* = H_1(0), & \text{otherwise}\,. \end{cases} \tag{4.22}$$

d) $\lambda \in \left(-\infty, -\alpha_f Q_{\max} V_{oc}/\eta_{dc}\right)$:

$$H^*(P_{SS}^*) = \begin{cases} H_2^*, & P_{PL} \in \mathcal{P}_{e,3}\,, \\ H_1^* = H_1\left(\max\left(P_{SS}^{*-}, P_{PL} - P_{PS_{\max}}, P_{SS_{\min}}\right)\right), & \text{otherwise}\,. \end{cases} \tag{4.23}$$

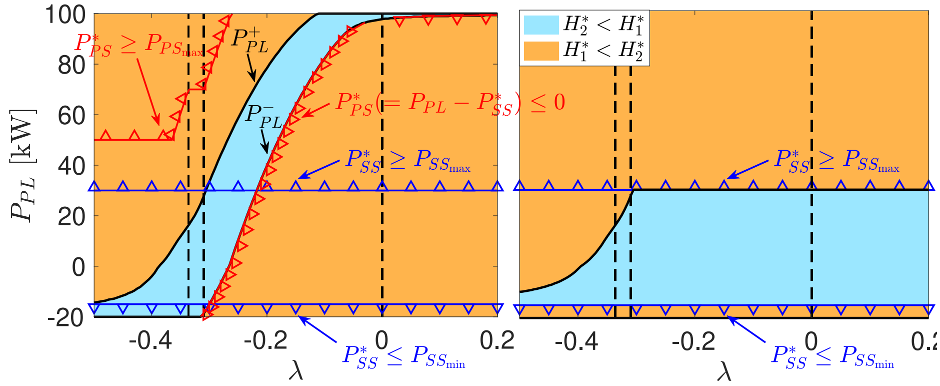

Fig. 4.3 A graphical representation of H^* for the HEV parameters given in Table 4.1. Orange colour represents regions where H_1^* is the minimum and blue colour represents regions where H_2^* is the minimum. The black solid lines represent the non-unicity solutions where $H_1^* = H_2^*$, while the vertical black dashed lines from left to right are $\lambda = -\alpha_f Q_{\max} V_{oc}/\eta_{dc}$, $\lambda = -\alpha_f Q_{\max} \eta_{dc} V_{oc}, \lambda = 0$, which define different costate regions. The left plot shows the solution without involving control constraints (4.8)(or (3.10)-(3.11)), although constraints are displayed as sawtooth lines. The sawtooth facing regions are invalid once the PS and SS power constraints are included. The right plot shows the minimum Hamiltonian solution combining the control constraints displayed in the left plot.

A graphical representation of the optimal solutions is illustrated in Fig. 4.3 for different values of costate λ (horizontal-axis) and load power P_{PL} (vertical-axis). As it can be seen, the optimum H^* selects the minimum among the two candidates, H_1^* and H_2^* (with the regions of different colour in Fig. 4.3 specifying where each candidate has the lowest value), and when $H_1^* = H_2^*$, H_1^* is selected under the provision of minimising ICE start-stop events. The left plot in Fig. 4.3 denotes the solution without including the control constraints on P_{SS} (and P_{PS} as a consequence). In this case the two solution regions are separated by two borders (shown as thick solid lines), on which $\tilde{H} = 0$ (singularity). In particular, for $\lambda \in (-\alpha_f Q_{\max} \eta_{dc} V_{oc}, 0)$, the upper and lower borders respectively denote $P_{PL} = P_{PL}^{+}$ and $P_{PL} = P_{PL}^{-}$ as they have been previously defined in Section 4.3.2-b). The left plot in Fig. 4.3 is also overlaid with lines that show the control constraints (obtained by (3.10)-(3.11) or (4.8)). By including these control constraints in the problem, the practical solution is shown in the right plot of Fig. 4.3, which verifies the closed form solution described by (4.18), (4.21), (4.22) and (4.23).

In conclusion, the optimal solution P_{SS}^{*} that minimises the piecewise Hamiltonian (4.16) is formed by the four segments, as shown in (4.18), (4.21), (4.22) and (4.23). Each segment is a piecewise function that merges a section of (4.13), obtained in absence of the SSS, with $P_{SS}^{*} = P_{PL}$ (except for $\lambda \geq 0$ where the control law is unique(see the first line of (4.13) and (4.18)). Depending on the PL branch power demand P_{PL}, the optimal control policy may switch between the two pieces of the solution within one segment. As with the previous no SSS case, the unconstrained closed form solution can be found explicitly by numerically identifying λ, which determines the switching threshold and the optimal SS operating power. If a state constraint is violated in the unconstrained solution, the recursive algorithm described in Section 4.3.1 can be utilised to iteratively find the optimal solution.

Similarly to the previous case without the SSS in Fig. 4.2, example DP solutions for the present case are illustrated in Fig. 4.4 for the same P_{PL} profile, vehicle parameters and

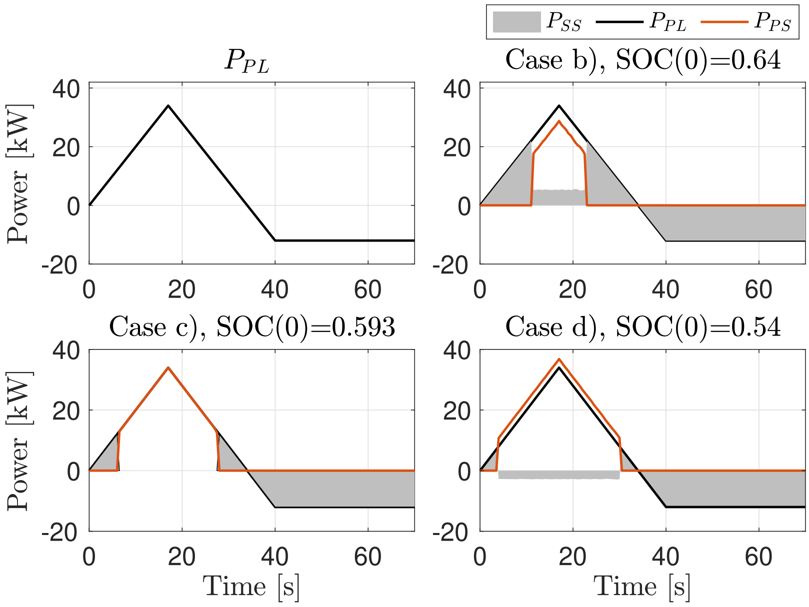

Fig. 4.4 Optimal power-split solutions found by DP for the case with the lossless SSS for an example power demand trajectory P_{PL} of 70 s, an $\mathrm{SOC}(T) = 0.65$ and three different cases of $\mathrm{SOC}(0)$. Each $\mathrm{SOC}(0)$ case is chosen to respectively actualize the closed-form solution cases in (4.21)-(4.23). The power interval where the powertrain is operated in full electric mode for each solution is $\Sigma_1 = [0, 21.98]$ kW, $\Sigma_2 = [0, 12.47]$ kW and $\Sigma_3 = [0, 6.987]$ kW, respectively.

target SOC(T) at 0.65. Fig. 4.4 shows that the three representative analytic solutions cases (4.21)-(4.23) ((4.18) is not shown since it is a sub-solution of (4.21)) are precisely followed. The optimal power profiles indicate that during the propulsive phase Φ the powertrain is operated in pure electric mode at low load requirements. Once P_{PL} reaches the switching threshold, the PS is activated and the powertrain is operated in ICE only or hybrid mode with the SS being charged/discharged at a constant power as with the behaviour in no SSS case.

The presence of the switching threshold therefore represents a fundamental difference of the present case solution to the solution of the case with no SSS, derived in Section 4.3.1. With no SSS, only one parameter is needed to reconstruct the solution, the constant power at which the SS power levels off once the ICE is on; for example, in Cases 2, 3, and 4 in Fig. 4.2, it levels off respectively at a positive value, zero, and a negative value; see also the parameter $P_{SS,th}$ in the context of Case 2 in [176]. In contrast, with the SSS present, two parameters are required to reconstruct the solution, the constant power at which the SS power levels off once the ICE is on, as before, and the switching threshold.

4.3.3 Hysteresis Power Threshold Strategy (HPTS)

By using insights gained from the preceding solutions presented in Sections 4.3.1 and 4.3.2, the HPTS is developed in this section to address the most realistic case, where the penalty fuel for the engine reactivation is involved, and for which analytic solutions are not feasible.

When engine start fuel cost, m_p is enabled, $m_p{=}Kq_{f0}$ is added to the base fuel consumption as long as the transition $\mathcal{S}_{0\to 1} \triangleq \{s_{eng}|s_{eng}=0,\, s_{eng}^{+}=1\}$ is detected. Application of the optimal EM solution derived for a lossless SSS to this case may result in fast engine on/off switching dynamics when P_{PL} fluctuates around switching power thresholds, thus leading to a significant increase of fuel usage. The HPTS attempts to address this issue and to approximate the global optimal solution with consideration of m_p by combining the control policies extracted from the analytic solutions obtained previously with a newly designed switching logic for ICE on/off control. The overall control scheme is graphically shown in Fig. 4.5.

As it can be noticed, the principles of HPTS are defined based on a 2-dimensional map of the SOC and P_{PL}, which is partitioned into several zones by the SOC limits and power load thresholds. Similarly to the analytic solutions derived based on the lossless SSS, P_{PL} is followed by P_{SS} only at low power loads (including negative P_{PL}) and the PS is activated, in hybrid or PS-only mode, at higher load requirements. More specifically, when the ICE is activated, it is operated at $P_{PS} = P_{PL} + \Delta P_{PS}$ with ΔP_{PS} a tuneable constant parameter, thus the SS is always operated at a constant power $-\Delta P_{PS}$ when the ICE is active. This operation

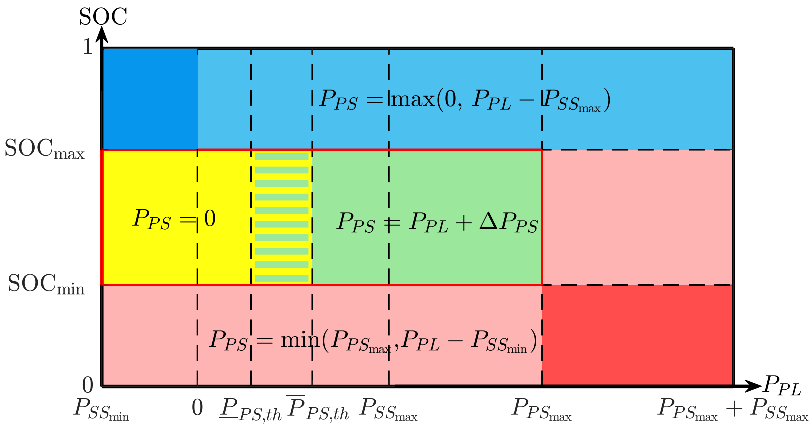

Fig. 4.5 The operation scheme of the HPTS with different operating stages classified based on the given SOC and P_{PL}. The primary operation mode is active in the region where the coordinates (on the P_{PL}-SOC map) satisfy $\mathrm{SOC}_{\min} < \mathrm{SOC} < \mathrm{SOC}_{\max}$ and $P_{SS_{\min}} \leq P_{PL} \leq P_{PS_{\max}}$, which give rise to a rectangular area designated by a red solid frame. ΔP_{PS} is a tuneable parameter. The hysteresis zone is shown by the mixture of yellow and green colours. Red and blue zones represent emergency handling operations[1].

is inspired by the analytic solution (4.13), (4.21)-(4.23) (in which ΔP_{PS} is in fact a constant that depends on ΔSOC and is found analytically), and it introduces an additional degree of freedom (the tuneable parameter ΔP_{PS}) as compared to the conventional load following (exclusive operation) strategy ($\Delta P_{PS} = 0$) used in [12]. Depending on the sign and value of ΔP_{PS}, when the ICE is activated the SS may be discharged to cover the unfulfilled power demand ($\Delta P_{PS} < 0$), charged by the PS to absorb the excess PS power ($\Delta P_{PS} > 0$), or idling ($\Delta P_{PS} = 0$ and the mode falls into the PS-only mode).

In order to reduce the incidence of ICE on/off transitions, a hysteresis switching scheme for ICE on/off control is also developed, as illustrated in Fig. 4.6. The hysteresis dynamics are assigned in relation to the engine on/off state s_{eng}, giving,

$$P_{SS} = (1 - s_{eng})P_{PL} - s_{eng}\Delta P_{PS},\ P_{PS} = s_{eng}(P_{PL} + \Delta P_{PS}), \tag{4.24}$$

and

$$s_{eng} = \begin{cases} 0, & \text{if } P_{PL} \leq \underline{P}_{PS,th} \\ 1, & \text{if } P_{PL} > \overline{P}_{PS,th} \\ s_{eng}(t^{-}), & \text{otherwise,} \end{cases}$$

---

[1] Operation in the lower right and upper left corners, shaded as red and blue regions, by the defined rules is only possible in transient conditions (short time) to avoid draining or overflowing the SOC. The latter can be naturally avoided by assigning more mechanical brakes so that, for example, $P_{PL} = 0$ (see (3.1b)).

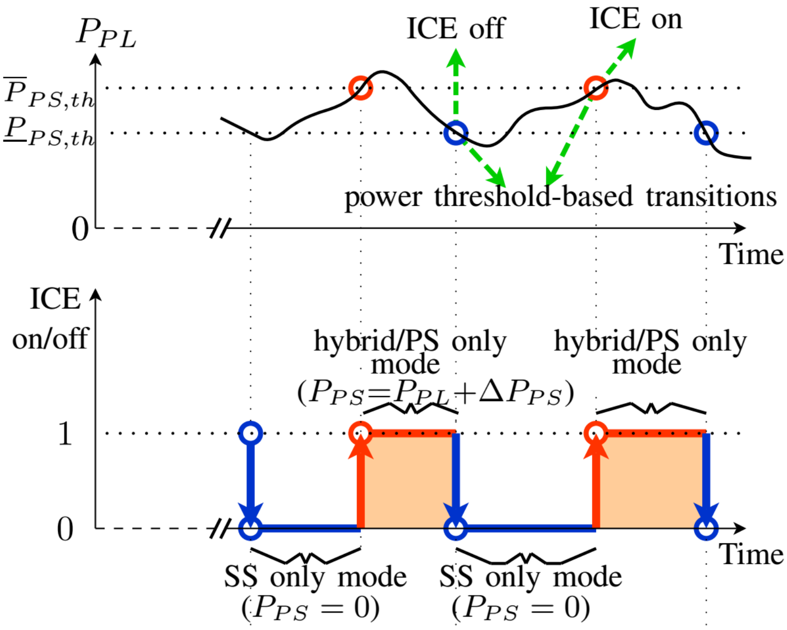

Fig. 4.6 Hysteresis switching scheme for ICE on/off control.

where t^- represents the time instant before t, and $\underline{P}_{PS,th}$ and $\overline{P}_{PS,th}$ are two separate tuneable power thresholds. The hysteresis dynamics dictate the operation in the hysteresis zone in Fig. 4.5, while it is clear that outside the hysteresis zone the P_{SS} and P_{PS} expressions in (4.24) fall back respectively to those in the yellow and green zones in Fig. 4.5.

Operation outside the primary region triggers the emergency rules, which aim to prevent the SOC constraints violation (which may happen in practice due to control discretization) and also define the power split for extremely large power demand ($P_{PL} > P_{PS,\max}$). More specifically, when SOC reaches or goes beyond its limits ($\mathrm{SOC} \geq \mathrm{SOC}_{\max} \vee \mathrm{SOC} \leq \mathrm{SOC}_{\min}$), the SS power is set to maximum ($\min(P_{SS_{\max}}, P_{PL})$) or minimum ($\max(P_{PL} - P_{PS_{\max}}, P_{SS_{\min}})$) operating power, respectively, to force the SOC immediately back into the main operational zone, as inspired by the PMP analysis in Section 4.3.1 and Fig. 4.1. In particular, with the operational policy for $\mathrm{SOC} \leq \mathrm{SOC}_{\min}$, the PS can be triggered on (enabling the hybrid mode) even during braking.

The design of the HPTS amounts to finding optimally tuned values for $\underline{P}_{PS,th}$, $\overline{P}_{PS,th}$ and ΔP_{PS} that minimise the fuel cost m_f while maintaining the CS condition:

$$\Delta \mathrm{SOC} = 0. \tag{4.25}$$

Condition (4.25) is sought because it is naturally optimal as will be shown next in Section 4.3.4, which is also a major contribution of this chapter. The global tuning nature of the control requires access to the whole driving cycle in advance (as is the case with

DP and ECMS) so that the tunable parameters can be tuned separately for each driving cycle. This allows for the rules of the HPTS to be tailored for all driving cycles rather than having compromised control policies that may excel on some driving cycles but behave less well on others. Thus, HPTS can be used to obtain benchmark solutions, and also it can be implemented in practice when the driving profile is known or can be estimated.

4.3.4 Fuel Economy Evaluation

The equivalent fuel consumption (EFC) is a measure of the fuel economy that has been widely used in the literature for evaluating overall fuel economy. It allows the comparison of the overall fuel economy by considering the actual fuel consumption as well as the shortage/surplus of final SOC. In this subsection we prove that the optimal EFC of a driving mission is achieved for CS operation, which provides additional justification beyond practical reasons about why CS operation should be sought. The definition of the EFC is [16]:

$$m_{efc}=\begin{cases} m_f+S_{d,efc}\Delta\mathrm{SOC}\dfrac{Q_{\max}V_{oc}}{q_{HV}}, & \Delta\mathrm{SOC}\geq 0, \\ m_f+S_{c,efc}\Delta\mathrm{SOC}\dfrac{Q_{\max}V_{oc}}{q_{HV}}, & \Delta\mathrm{SOC}<0, \end{cases} \tag{4.26}$$

where the two equivalence factors $S_{d,efc}$ and $S_{c,efc}$ (for battery discharging and charging respectively) represent the correlation of the electrical energy and the fuel chemical energy required when following a driving cycle, q_{HV} is the gasoline lower heating value. Hence, to proceed with the assessment of an energy management system (EMS), $S_{d,efc}$ and $S_{c,efc}$ have to be identified a priori for each driving cycle and for each vehicle model. In brief, the identification method proposed in [16] requires a sweep of the power sharing factor $u_{efc} \triangleq P_{PS}/P_{PL}$, $\forall t \in \Phi$ within the range $[1-\Delta u_{efc}, 1+\Delta u_{efc}]$, with Δu_{efc} selected such that either the upper or the lower bound for the SOC is not violated during the operation. The overall electrical and fuel energy consumption for a specific value of u_{efc} while undergoing a given drive cycle are respectively computed by

$$E_e \triangleq \int_0^T i_b V_{oc} dt \quad \text{and} \quad E_f \triangleq \int_0^T q_{HV}\dot{m}_f dt,$$

where i_b is the battery current as defined in (3.6), and E_e and E_f are plotted against each other for different values of u_{efc}. Such a plot is separated into two segments intersecting at $u_{efc}=1$, at which the propulsion power is purely provided by the ICE. The slopes of straight lines that fit the (E_e, E_f) data of these two segments are identified as the negative values of $S_{d,efc}$ and $S_{c,efc}$ respectively. It will now be shown that the EFC definition inherently drives the optimal EFC solutions (of an EMS) to be strictly CS as in (4.25).

As the hybrid mode is enabled only during an emergency when $P_{PL} < 0$, it is reasonable to assume $P_{SS} = P_{PL}, \forall t \in \Psi$. As such, the fuel consumption at the end of the driving mission, in light of (4.3), (4.4) and (4.5), is expressed as:

$$m_f = q_{f0} \int_0^T s_{eng}\, dt + \alpha_f \int_\Phi P_{PL} dt - \alpha_f \int_\Phi P_{SS}\, dt + N_r m_p, \tag{4.27}$$

where N_r is the number of engine restarts during the mission and $\alpha_f \int_\Phi P_{PL} dt$ is fixed for a given driving cycle and independent of the EM control. The fuel energy for a given driving cycle is $E_f = q_{HV} m_f$. In terms of the electrical energy E_e, when $u_{efc} \geq 1$ it means that E_e is never used for propulsion, that is $\Phi_d = \emptyset$, $\Phi = \Phi_c$, and when $u_{efc} < 1$ it is clear that $\Phi_c = \emptyset$, $\Phi = \Phi_d$. Therefore, E_e can be rewritten as,

$$E_e = \begin{cases} \displaystyle\int_{\Phi_d} \frac{P_{SS} V_{oc}}{\eta_{dc} V_b} dt + E_{e,\Psi}, & \text{if } u_{efc} < 1, \\ \displaystyle\int_{\Phi_c} \frac{P_{SS} \eta_{dc} V_{oc}}{V_b} dt + E_{e,\Psi}, & \text{if } u_{efc} \geq 1, \end{cases}$$

where $E_{e,\Psi} = \Delta_\Psi \mathrm{SOC}\, Q_{\max} V_{oc}$ only depends on P_{PL}. Consider two arbitrary values of $u_{efc} \geq 1$ within the admissible set $[1, 1 + \Delta u_{efc}]$. It is obvious that N_r and s are invariant between the two scenarios. Then, the slope corresponding to $S_{d,efc}$ is evaluated by,

$$\begin{aligned} S_{d,efc} = -\frac{\Delta E_f}{\Delta E_e} &= \frac{q_{HV} \alpha_f \int_{\Phi_c} (P_{SS,1} - P_{SS,2}) dt}{\eta_{dc} V_{oc} \int_{\Phi_c} \left(\frac{P_{SS,1}}{V_{b,1}} - \frac{P_{SS,2}}{V_{b,2}} \right) dt} \\ &= \frac{q_{HV} \alpha_f \int_{\Phi_c} ((i_{b,1} - i_{b,2})(V_{oc} - R_b(i_{b,1} + i_{b,2}))) dt}{V_{oc} \eta_{dc}^2 \int_{\Phi_c} \left(i_{b,1} - i_{b,2} \right) dt}, \end{aligned}$$

where the subscripts 1 and 2 indicate the two scenarios driven by the two distinct u_{efc} values. Since $V_{oc} - R_b(i_{b,1} + i_{b,2}) \geq V_{oc}, \forall t \in \Phi_c$, it is obtained that:

$$S_{d,efc} > \frac{1}{\eta_{dc}^2} q_{HV} \alpha_f. \tag{4.28}$$

Similarly, $S_{c,efc}$ is evaluated as follows, with respect to two arbitrary values of $u_{efc} < 1$ within the admissible set $[1 - \Delta u_{efc}, 1)$:

$$S_{c,efc} = \frac{q_{HV} \alpha_f \eta_{dc}^2 \int_{\Phi_d} ((i_{b,3} - i_{b,4})(V_{oc} - R_b(i_{b,3} + i_{b,4}))) dt}{V_{oc} \int_{\Phi_d} \left(i_{b,3} - i_{b,4} \right) dt} < q_{HV} \alpha_f \eta_{dc}^2. \tag{4.29}$$

Turning to the steps required for the calculation of m_{efc} and by applying (3.7) to (4.27), it holds that,

$$m_f = q_{f0}\int_0^T s_{eng}\,dt + \alpha_f\int_\Phi P_{PL}dt - \alpha_f\int_\Phi \eta_{dc}^{\mathrm{sign}(P_b)}P_b\,dt + N_r m_p, \tag{4.30}$$

where the term $\alpha_f\int_\Phi \eta_{dc}^{\mathrm{sign}(P_b)}P_b\,dt$ can be expanded by using the definitions of Φ_d and Φ_c, as follows:

$$\alpha_f\int_\Phi \eta_{dc}^{\mathrm{sign}(P_b)}P_b\,dt = \alpha_f\left(\int_{\Phi_d}\eta_{dc}P_b dt + \int_{\Phi_c}\frac{1}{\eta_{dc}}P_b dt\right). \tag{4.31}$$

In relation to the charging and discharging intervals, let us define,

$$\begin{aligned} V_{b,d} &\triangleq V_{oc} - R_b\,i_b \le V_{oc}, \quad \forall t \in \Phi_d\,,\\ V_{b,c} &\triangleq V_{oc} - R_b\,i_b > V_{oc}, \quad \forall t \in \Phi_c\,. \end{aligned} \tag{4.32}$$

Then, (4.31) can be expressed as,

$$\begin{aligned} &\alpha_f\left(\int_{\Phi_d}\eta_{dc}P_b dt + \int_{\Phi_c}\frac{1}{\eta_{dc}}P_b dt\right)\\ &= -Q_{\max}\alpha_f\left(\eta_{dc}\int_{\Phi_d}V_{b,d}\frac{d\mathrm{SOC}}{dt}dt + \frac{1}{\eta_{dc}}\int_{\Phi_c}V_{b,c}\frac{d\mathrm{SOC}}{dt}dt\right), \end{aligned} \tag{4.33}$$

where $i_b = -Q_{\max}\frac{d\mathrm{SOC}}{dt}$ is applied. Owing to the mean value theorem, there exist two time instants $t_d \in \Phi_d$ and $t_c \in \Phi_c$, such that:

$$\begin{aligned} \int_{\Phi_d}V_{b,d}\frac{d\mathrm{SOC}}{dt}dt &= V_{b,d}(t_d)\int_{\Phi_d}\frac{d\mathrm{SOC}}{dt}dt = -V_{b,d}(t_d)\Delta_{\Phi_d}\mathrm{SOC}\\ \int_{\Phi_c}V_{b,c}\frac{d\mathrm{SOC}}{dt}dt &= V_{b,c}(t_c)\int_{\Phi_c}\frac{d\mathrm{SOC}}{dt}dt = -V_{b,c}(t_c)\Delta_{\Phi_c}\mathrm{SOC}. \end{aligned} \tag{4.34}$$

By substituting (4.30) in (4.26) and applying (4.33) and (4.34), it is immediate to obtain the explicit expression of m_{efc}, as follows:

$$m_{efc} = \begin{cases} m_{f0} - \left(\eta_{dc}V_{b,d}(t_d)\Delta_{\Phi_d}\mathrm{SOC} + \frac{1}{\eta_{dc}}V_{b,c}(t_c)\Delta_{\Phi_c}\mathrm{SOC}\right) \\ \qquad \times Q_{\max}\alpha_f + S_{d,efc}\Delta\mathrm{SOC}\frac{Q_{\max}V_{oc}}{q_{HV}}, \ \Delta\mathrm{SOC} \ge 0\,, \\ m_{f0} - \left(\eta_{dc}V_{b,d}(t_d)\Delta_{\Phi_d}\mathrm{SOC} + \frac{1}{\eta_{dc}}V_{b,c}(t_c)\Delta_{\Phi_c}\mathrm{SOC}\right) \\ \qquad \times Q_{\max}\alpha_f + S_{c,efc}\Delta\mathrm{SOC}\frac{Q_{\max}V_{oc}}{q_{HV}}, \ \Delta\mathrm{SOC} < 0\,, \end{cases} \tag{4.35}$$

where, $m_{f0} = q_{f0}\int_0^T s_{eng}\,dt + N_r m_p + \alpha_f\int_\Phi P_{PL}\,dt$, and the piecewise function (4.35) is continuous at $\Delta\mathrm{SOC} = 0$.

By using (4.6), (4.35) can be rearranged into (4.36).

$$m_{efc}=\begin{cases} \frac{Q_{\max}V_{oc}}{q_{HV}}\left(S_{d,efc}-\eta_{dc}\alpha_f q_{HV}\frac{V_{b,d}(t_d)}{V_{oc}}\right)\Delta_{\Phi_d}\mathrm{SOC}+q_{f0}\int_0^T s_{eng}\,dt+N_r m_p & \\ \quad +\frac{Q_{\max}V_{oc}}{q_{HV}}\left(S_{d,efc}-\frac{1}{\eta_{dc}}\alpha_f q_{HV}\frac{V_{b,c}(t_c)}{V_{oc}}\right)\Delta_{\Phi_c}\mathrm{SOC} & \\ \quad +\alpha_f\int_{\Phi} P_{PL}\,dt+S_{d,efc}\Delta_{\Psi}\mathrm{SOC}\frac{Q_{\max}V_{oc}}{q_{HV}}, & \Delta\mathrm{SOC}\geq 0, \\ \frac{Q_{\max}V_{oc}}{q_{HV}}\left(S_{c,efc}-\eta_{dc}\alpha_f q_{HV}\frac{V_{b,d}(t_d)}{V_{oc}}\right)\Delta_{\Phi_d}\mathrm{SOC}++q_{f0}\int_0^T s_{eng}\,dt+N_r m_p & \\ \quad +\frac{Q_{\max}V_{oc}}{q_{HV}}\left(S_{c,efc}-\frac{1}{\eta_{dc}}\alpha_f q_{HV}\frac{V_{b,c}(t_c)}{V_{oc}}\right)\Delta_{\Phi_c}\mathrm{SOC} & \\ \quad +\alpha_f\int_{\Phi} P_{PL}\,dt+S_{c,efc}\Delta_{\Psi}\mathrm{SOC}\frac{Q_{\max}V_{oc}}{q_{HV}}, & \Delta\mathrm{SOC}<0. \end{cases} \tag{4.36}$$

As it can be seen, (4.36) is a piecewise bilinear function of $V_{b,d}(t_d)$, $V_{b,c}(t_c)$, $\Delta_{\Phi_c}\mathrm{SOC}$, $\Delta_{\Phi_d}\mathrm{SOC}$, s and N_r, which are all influenced by the EM strategy through P_{SS}. On the other hand, the last two terms of each part in (4.36) are independent of the EM and only depend on P_{PL}, and therefore they are constants for a given P_{PL} profile. As a consequence, $\Delta_{\Phi}\mathrm{SOC}$ is determined once a pair of boundary conditions of SOC $(\mathrm{SOC}(0),\mathrm{SOC}(T))$ is given (that determine $\Delta\mathrm{SOC}$). The P_{SS} profile that meets the the desired $\Delta_{\Phi}\mathrm{SOC}$ is not unique, and it is possible to find some P_{SS} profile that sets $V_{b,d}, V_{b,c}$ independently of each other to some desirable profiles, and as a result, $\Delta_{\Phi_d}\mathrm{SOC}$, $\Delta_{\Phi_c}\mathrm{SOC}$, s and N_r (that are respectively determined by $V_{b,d}, V_{b,c}$) can be independently assigned to desired values. By considering the inequality conditions (4.28) and (4.29), as well as (4.32) and that $\eta_{dc}\leq 1$, it can be inferred that:

$$S_{d,efc}-\eta_{dc}\alpha_f q_{HV}\frac{V_{b,d}(t_d)}{V_{oc}}>0, \tag{4.37}$$

$$S_{c,efc}-\frac{1}{\eta_{dc}}\alpha_f q_{HV}\frac{V_{b,c}(t_c)}{V_{oc}}<0. \tag{4.38}$$

By referring to the $\Delta\mathrm{SOC}\geq 0$ case in (4.36) it can be easily inferred that m_{efc} is minimised when $\Delta_{\Phi_d}\mathrm{SOC}$ is minimised, since (4.37) is true. By further taking into account (4.6), it can be concluded that $\Delta\mathrm{SOC}=0$ is necessary when m_{efc} is minimum. Similarly, when $\Delta\mathrm{SOC}<0$ in (4.36), m_{efc} is minimised when $\Delta_{\Phi_c}\mathrm{SOC}$ is maximised, since (4.38) is true. Therefore, by referring to (4.6) the necessary condition to minimise m_{efc} in this case is also $\Delta\mathrm{SOC}=0$ (owing to the continuity of (4.36) at $\Delta\mathrm{SOC}=0$). Hence, the strictly CS condition (4.25) is a *necessary* condition overall for EFC minimisation.

4.4 Numerical Results

The EM control strategies considered and developed in this work are tested by simulations in which the vehicle follows predefined driving cycles. The WLTP (worldwide harmonized light vehicles test procedure) corresponds to the latest test procedure adopted by industry and it is therefore utilised in the present work. As shown in Fig. 4.7, the WLTP profile is a single driving cycle with four stages, defined by their average speed: low (WL-L), medium (WL-M), high (WL-H) and extra high (WL-E). Each of the stages can be considered on their own as independent driving cycles.

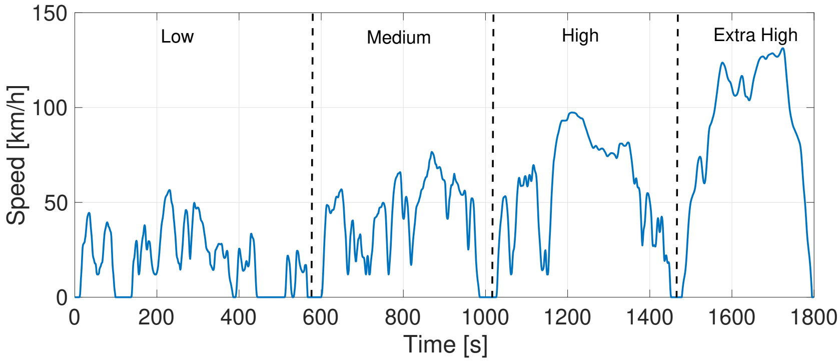

Fig. 4.7 Speed profile of WLTP with four individual stages classified by their average speed.

In addition to the WLTP, an experimental speed profile (shown in Fig. 4.8) is also adopted for performance and robustness assessment purposes. This time history data, that is recorded by a newly built data acquisition device [180], exhibits realistic driving behaviour on a rural road. As compared to standard test cycles, this experimental speed pattern contains particular features that better reflect real-world driving, such as the influences of legal speed limits and road grades, and the driving style of the human driver who is inclined to apply higher values of acceleration and deceleration than in the WLTP.

The proposed HPTS is individually applied to the four segments of the WLTP speed profile, and the solutions are benchmarked against DP [181] and XOS [12] in the context of both linear FCM (3.5) and experimental (quasilinear) FCM (dotted line in the right plot of Fig. 3.3) for robustness verification purposes. It is noteworthy that ECMS, which is one of the popular EM control strategies in the literature, breaks down for the problem addressed in this chapter, and therefore not used for comparison. The reason is briefly explained as follows. ECMS finds the optimal power split to minimise an equivalent fuel consumption,

Fig. 4.8 Top: 12.1km rural route selected as a real-world vehicle driving mission https://t.ly/n2wL. Bottom: Experimental driving speed profile for the mission above.

defined as

$$\dot{m}_{eq} = \begin{cases} \dot{m}_f(P_{PS}) + S_d \dfrac{P_{SS}}{q_{HV}}, & P_{SS} \geq 0, \\ \dot{m}_f(P_{PS}) + S_c \dfrac{P_{SS}}{q_{HV}}, & P_{SS} < 0, \end{cases} \tag{4.39}$$

where the two constants S_d and S_c are equivalence factors that translate the energy discharged/charged by the SS into a corresponding amount of fuel consumed/stored. Due to the linear/quasilinear FCM for a series HEV, (4.39) becomes a linear/quasilinear combination of P_{PS} and P_{SS} with individual gradients depending on α_f, q_{HV}, S_d and S_c. Hence, the ECMS simply operates P_{PS} always at its maximum or always at its minimum throughout a mission, irrespective of the power demand, and with the choice of (always) maximum or minimum P_{PS} depending on the sign of the gradients, unless SOC limits are reached. For a fair comparison and also to satisfy the necessary condition of fuel consumption optimality, the same SOC CS boundary condition $\mathrm{SOC}(0) = \mathrm{SOC}(T) = 0.65$ is imposed for all methods. The penalty fuel coefficient for engine restarts is set to $K = 0.8$ in the first instance, while an investigation of its influence on the comparative results is also carried out.

Given a driving cycle, the proposed HPTS is applied by tuning the design parameters $\underline{P}_{PS,th}$, $\overline{P}_{PS,th}$ and ΔP_{PS}, while also aiming to satisfy the CS condition as mentioned. Thus, the tuning process involves finding the combination of the three parameters, among all combinations that lead to CS operation, that minimises the fuel consumption; the EFC is now equal to the fuel consumption due to the CS condition. Fig. 4.9 presents an example of the tuning graph for the WL-M cycle with the linear FCM model (3.5). The surface in Fig. 4.9 denotes the control solutions satisfying $\Delta \mathrm{SOC} = 0$, and the optimal solution in terms of fuel consumption is identified approximately at $\overline{P}_{PS,th} = 18.5\,\mathrm{kW}$, $\underline{P}_{PS,th} = 6.5\,\mathrm{kW}$ and $\Delta P_{PS} = 9.5\,\mathrm{kW}$.

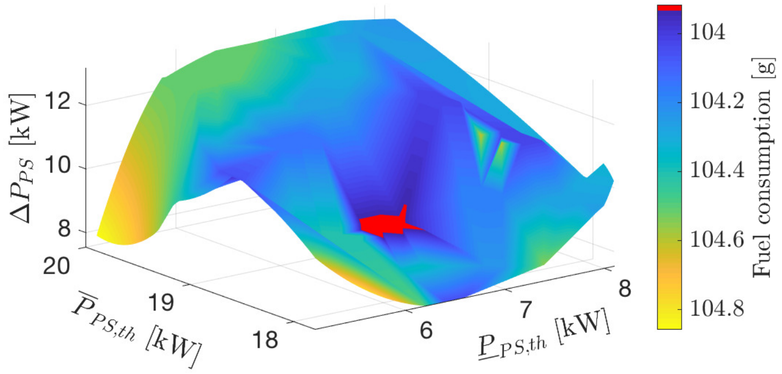

Fig. 4.9 HPTS optimal solutions obtained by tuning $\overline{P}_{PS,th}$, $\underline{P}_{PS,th}$ and ΔP_{PS}, when the linear FCM model (3.5) is employed and while satisfying charge sustaining operation.

Fig. 4.10 presents the power profiles and the associated engine on/off states determined by these control methods when the WL-M cycle is simulated. Compared to the XOS, both DP and the HPTS can reduce the engine restarts by manipulating the operation of the PS and SS. In particular, when the ICE is activated in cases of DP and HPTS, the powertrain is operated in hybrid mode, in which the battery is charged by the ICE at a constant SS power, and therefore additional engine breaks are allowed to prevent the engine status from being changed too frequently, as can be found in the control solution of XOS (for example, around 50 s and 250 s in Fig. 4.10). Further comparing the solutions of HPTS and DP, the HPTS is more sluggish in its response to a PS power request (a phase delay can be observed in Fig. 4.10 by comparing their PS profiles) due to the impact of the hysteresis switching mechanism. Moreover, the PS operating power of HPTS is higher than DP, which also yields more battery charge during $s_{eng} = 1$ and further reduced ICE on/off transitions. As a consequence, the battery SOC of HPTS has more noticeable variations than the profiles generated by the other two methods, as shown in Fig. 4.11. For example, the battery in the case of HPTS is charged intensively from 180s to 220s, thereby allowing the ICE to be

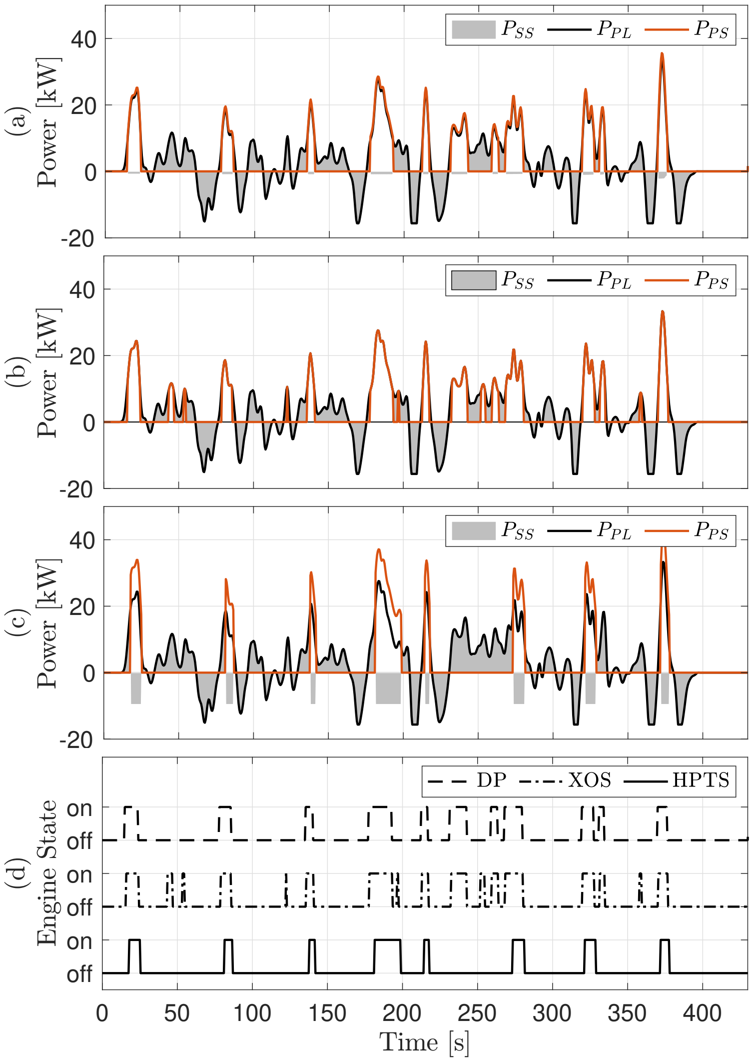

Fig. 4.10 Power ((a): DP, (b): XOS, (c): HPTS) and engine state $s_{eng}(t)$ (plot (d)) profiles when WL-M is simulated with the linear FCM model (3.5) and CS condition $\Delta\text{SOC} = 0$.

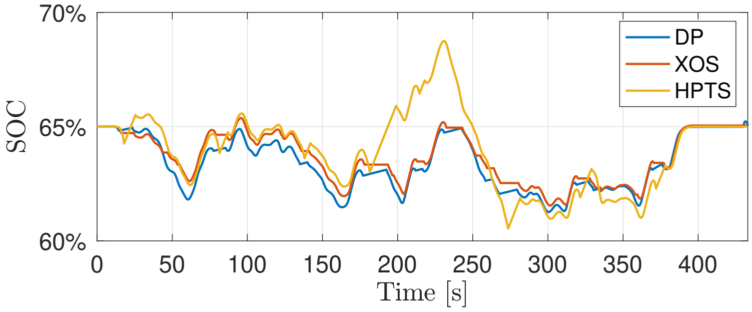

Fig. 4.11 Battery SOC profiles when WL-M is simulated with the linear FCM model (3.5). CS condition $\Delta\text{SOC} = 0$ is achieved in all cases.

Table 4.2 Fuel consumption $[g]$ with the linear FCM model and percentage fuel increase compared to DP solutions.

	DP	XOS	HPTS
WL-L	54.5	61.3 (12.5%)	57.8 (6.06%)
WL-M	99.5	106.5 (7.04%)	104.2 (4.72%)
WL-H	175.1	183.3 (4.68%)	179.8 (2.68%)
WL-E	311.1	313.4 (0.74%)	312.6 (0.48%)
Experimental	251.2	273.6 (8.92%)	261.1 (3.49%)

switched off for the next 50s. Although the SOC in the case of XOS performs closely to the DP solution, it will be shown later that the fuel economy of XOS is significantly impaired by the unnecessary ICE switches (which incur additional fuel usage). The fuel consumption of all the methods is compared in Table 4.2.

The solutions of the HPTS are much closer to the results of DP as compared to the XOS for all cases. Approximately, there is 0.48%-6.06% more fuel usage by HPTS than the DP for WLTP cycles, and the gap decreases from WL-L to WL-E. This can be understood that more fuel saving is expected by an optimally controlled SSS during urban driving rather than driving on the motorway, where the SSS is rarely engaged. In the context of the real-world experimental driving cycle that involves mixed traffic conditions, the HPTS solution is only 3.49% behind the DP and can save about 5.4% more fuel as compared to the XOS. The results verify the capability of HPTS in dealing with general driving scenarios.

The performance of the HPTS is further examined by employing the experimental FCM shown in Fig. 3.3. Similarly to the linear FCM case, the optimal selection of the design parameters is identified by a global tuning process. As shown in Fig. 4.12, the

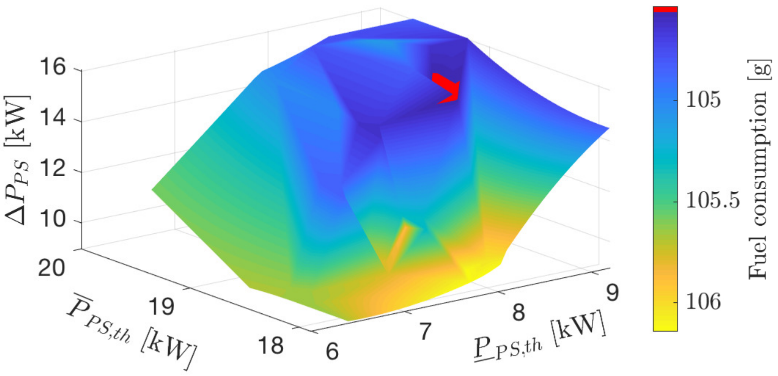

Fig. 4.12 HPTS optimal solutions obtained by tuning $\overline{P}_{PS,th}$, $\underline{P}_{PS,th}$ and ΔP_{PS}, when the nonlinear experimental FCM (see Fig. 3.3) is employed and while satisfying charge sustaining operation.

optimal parameter selection for the nonlinear FCM is $\overline{P}_{PS,th} = 18.72\,\mathrm{kW}$, $\underline{P}_{PS,th} = 8.5\,\mathrm{kW}$ and $\Delta P_{PS} = 15.0\,\mathrm{kW}$. The power and engine switching profiles of the three control methods are shown in Fig. 4.13. As it can be seen, the HPTS is able to emulate the power profiles solved by DP while XOS remains at the same operation as shown in Fig. 4.10. The engine switching profiles further confirm the findings; it is notable that once again both DP and HPTS reduce significantly the engine on/off events compared to the XOS. The SOC profiles reported in Fig. 4.14 show that, in this case, the HPTS can produce a profile closer to the DP solution as compared to the XOS. The control solutions of the three methods for the experimental driving cycle are also demonstrated in Fig. 4.15 to provide further evidence of

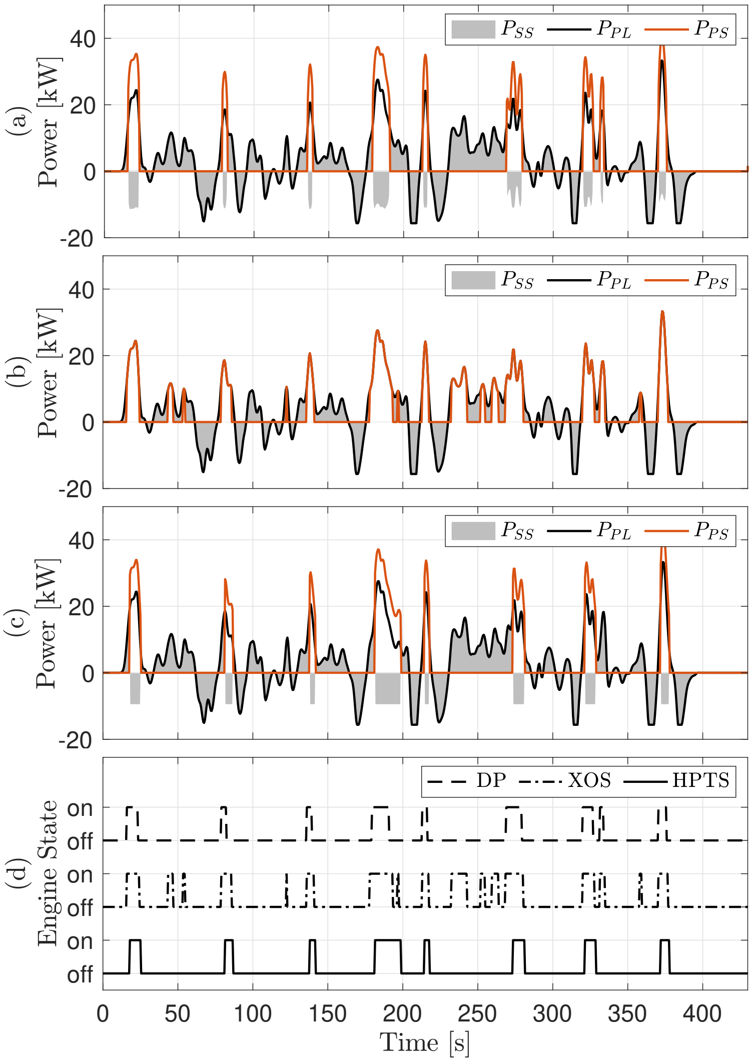

Fig. 4.13 Power profiles and engine switching profile when WL-M is simulated with the nonlinear experimental FCM and CS condition $\Delta\mathrm{SOC} = 0$. (a): DP. (b): XOS. (c): HPTS. (d): engine state $s_{eng}(t)$.

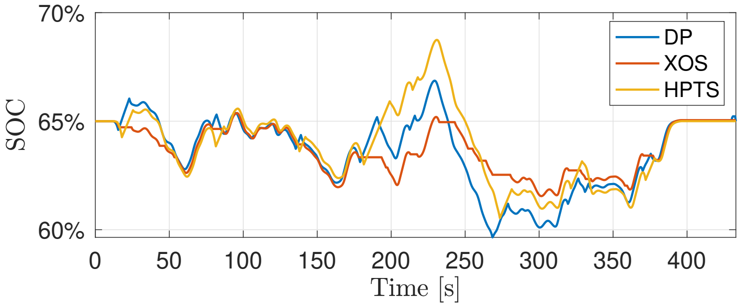

Fig. 4.14 Battery SOC profiles when WL-M is simulated with the nonlinear experimental FCM. CS condition ΔSOC$=$0 is achieved in all cases.

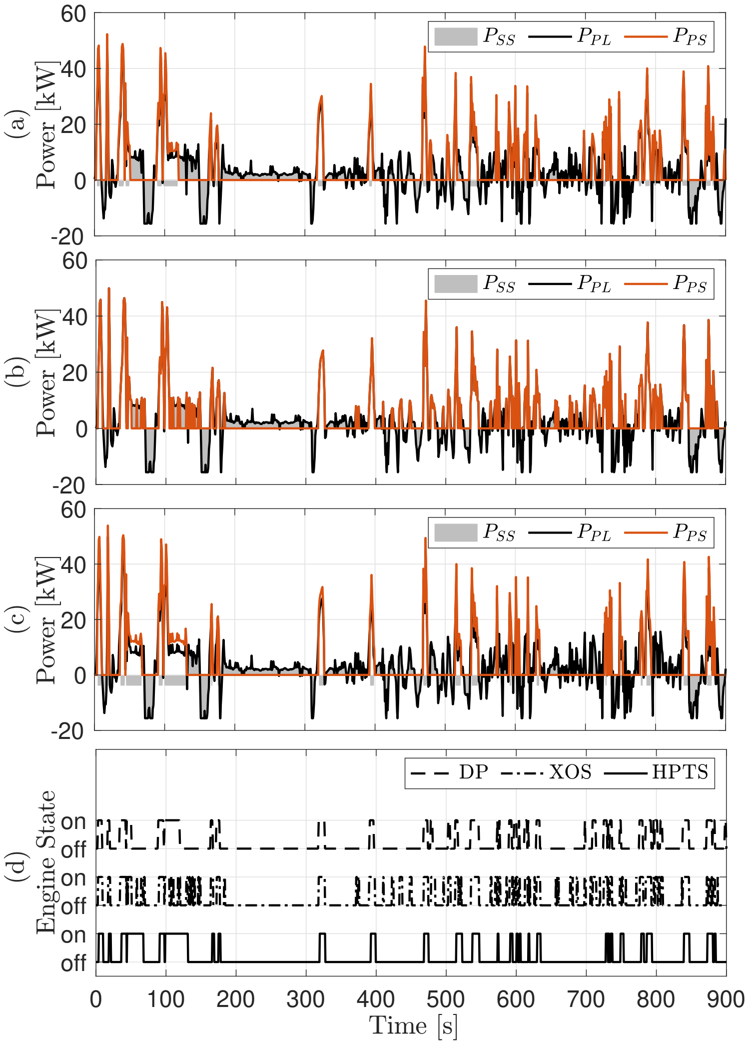

Fig. 4.15 Power profiles and engine switching profile when the experimental driving cycle is simulated with the nonlinear experimental FCM and CS condition ΔSOC$=$0. (a): DP. (b): XOS. (c): HPTS. (d): engine state $s_{eng}(t)$.

Table 4.3 Fuel consumption $[g]$ with the nonlinear experimental FCM and percentage fuel increase compared to DP solutions.

	DP	XOS	HPTS
WL-L	55.0	68.1 (23.8%)	59.0 (7.27%)
WL-M	99.7	113 (13.3%)	105.8 (6.12%)
WL-H	174.8	192.1 (9.90%)	181.0 (3.55%)
WL-E	307.1	312.3 (1.69%)	309.8 (0.88%)
Experimental	249.4	286.1 (14.72%)	259.9 (4.21%)

the resemblance between DP and the HPTS. As it can be seen, both the DP and HPTS have similar power profiles while the XOS entails much more engine switching operations, which incur additional fuel usage. The fuel consumption results of all the methods in the case of experimental FCM are presented in Table 4.3. By comparing the results with the previous solutions solved for the linear FCM model in Table 4.2, it can be observed that the optimality (percentage fuel increase) of the XOS degrades considerably, while the HPTS is more robust against the model nonlinearity, with the optimality decreased by only 0.4%-1.4% for each cycle as compared to the linear case. It is noteworthy that for the experimental driving cycle the fuel increase for the HPTS is only 0.04% as compared to its counterpart with the linear FCM, and furthermore the HPTS achieves an astonishing 10% less fuel consumption as compared to the XOS.

To gain more insight into the effect of the penalty fuel for the engine reactivation, a further investigation is carried out to compare the solutions of the three control methods using different penalty fuel coefficient K. For $K \in [0,2]$, the total fuel consumption of the three methods for the experimental FCM is depicted in Fig. 4.16. As it can be noticed, the

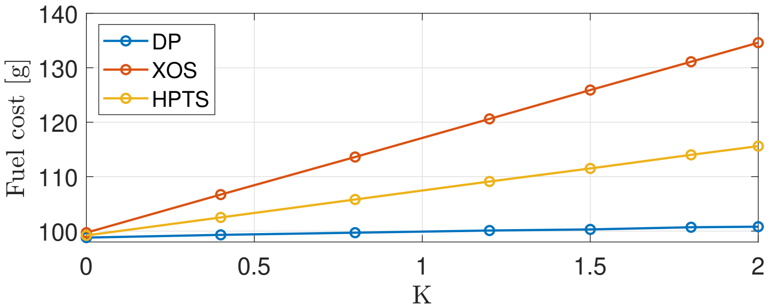

Fig. 4.16 Fuel consumption cost with varied penalty fuel coefficient K using the nonlinear experimental FCM and CS condition $\Delta\text{SOC} = 0$ when WL-M is simulated.

HPTS is found to outperform the XOS for all studied K with up to 16.44% improvement in terms of fuel consumption. Moreover, the fuel usage is linearly dependent on the penalty fuel coefficient K for all the three control cases, and the differences between each solution of the tested methods decrease as K decreases, which is expected with the further improvement of the SSS efficiency. When $K = 0$, the HPTS highly resembles the global optimal solution delivered by DP, with only 0.4% fuel increment, whereas the XOS lags the HPTS by another 0.5%.

The global tuning (by repetitive simulation for a batch of parameter combinations) of HPTS and the running time of DP required for the solutions reported in Table 4.3 are further compared in Table 4.4. The evaluation of both methods is performed in Matlab & Simulink environment on an Intel i5 2.9 GHz CPU with 8 GB of memory. As it can be seen, the proposed HPTS is more computationally efficient than DP, while the benefit is expected to become more significant for a more complex powertrain model as the computational burden of DP increases exponentially with the number of system states (eventually DP becomes unusable even for moderately complex models). It is not difficult to see that the tuning effort depends on the size of the power interval of searching, which is usually identified empirically. With the tuning results obtained for more tested cycles, more accurate searching intervals can be identified when a new driving cycle is investigated based on the nature of the cycle (for example, urban, rural or motorway driving), and therefore the tuning effort can be further reduced. Moreover, HPTS acts entirely on the three tunable control parameters, as opposed to classic optimal control (DP) that acts on a state input. This is another salient feature that allows the globally tuned HPTS parameters for any test cycles (predetermined and available in the database, such as WLTP) to be directly applied to any unknown cycle based on the speed forecast, such as the predicted average speed from a navigation system and classification against the test cycles. In such a case, the tuning effort is negligible.

Table 4.4 Comparison of tuning (HPTS) and running time (DP) [minutes] required by HPTS and DP for the results in Table 4.3.

	WL-L	WL-M	WL-H	WL-E	Experimental
DP	61.81	43.89	47.44	34.12	93.02
HPTS	17.09	15.50	15.70	14.77	18.58

Herein, a simple adaptive scheme is further implemented to show the robustness of an adaptive HPTS in real-world driving scenarios, where global parameter tuning is not feasible. It is assumed that the optimal control parameters for the four segments of WLTP are pre-determined and saved in a database. Given a new driving mission where the speed profile is unknown, the driving condition within a short prediction horizon can be forecast and classified in line with the individual segments of WLTP according to the estimated average speed (readily available from an onboard navigation system) with high accuracy. Then the associated control parameters from WLTP are applied straightforwardly. Such a classification scheme is not vulnerable to uncertainties in the speed forecast as it relies only on the four WLPT segments that are characterized by considerably different average speeds. This simple adaptive scheme is tested for the experimental driving speed shown in Fig. 4.8 in comparison with DP, globally tuned HPTS and XOS. The results are reported in Fig. 4.17 and Table 4.5. As it can be seen, the experimental driving profile is partitioned into nine segments of 100 s, each representing a prediction horizon matched to an individual WLTP component based on the average speed for that horizon. The resulting SOC profile of the adaptive HPTS shows that the battery remains near CS (SOC$(T) = 64.3\%$). For a fair comparison with the three benchmark solutions obtained under strict CS condition, the EFC (4.26) of the adaptive HPTS solution is calculated (261.7 g) to take into account the small SOC deviation from SOC$(0) = 65\%$. It is found that the adaptive HPTS solution only lags the DP by 4.93% with only marginal differences as compared to its globally tuned counterpart (4.21% behind the DP), which reflects the robustness of the proposed algorithm.

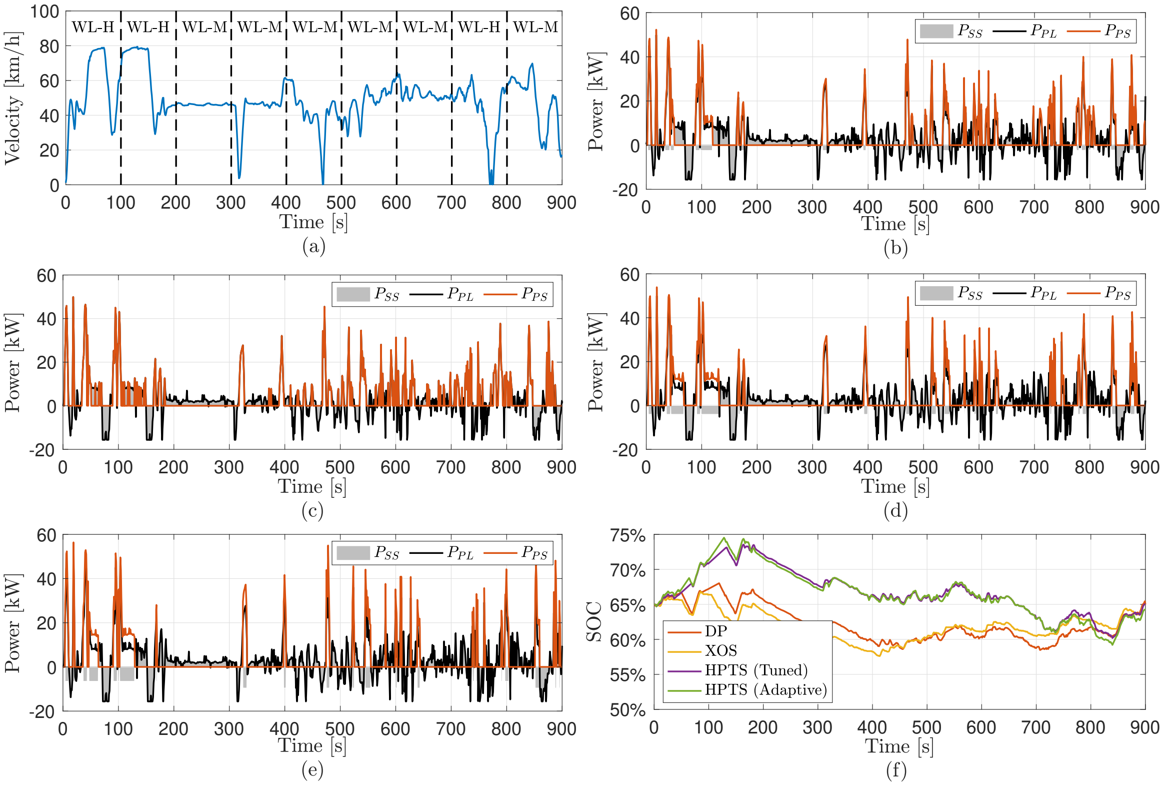

Fig. 4.17 (a): Experimental speed profile partitioned every 100 s with each segment matched to the WLTP segments based on its average speed, while the WLTP control parameters are applied to each segment accordingly. (b)-(f) Power profiles (of DP, XOS, HPTS globally tuned, and HPTS adaptive, respectively) and SOC profile when the rural London experimental driving cycle is simulated with the nonlinear FCM model.

Table 4.5 Comparison of equivalent fuel consumption $[g]$ and percentage fuel increase compared to DP solutions.

DP	XOS	HPTS (Globally tuned)	HPTS (Adaptive)
249.4	286.1 (14.72%)	259.9 (4.21%)	261.7 (4.93%)

4.5 Conclusions

This chapter proposes a novel rule-based EM control strategy, HPTS, for series HEVs with the engine SSS. The principal mechanisms of the HPTS are developed with inspiration from the closed-form solutions of the optimal energy source power split derived in this chapter. In particular, the mathematical analysis is carried out for two model cases: 1) without SSS, 2) with the lossless SSS where the fuel usage for engine restarts is ignored, thus yielding two fundamental optimisation solutions that can be represented by simple control rules. The HPTS further extends these rules with consideration of a more realistic SSS model that incorporates penalty fuel for engine restarts. The HPTS essentially combines two operational modes: battery-only mode and hybrid/engine-only mode, with the latter mode depending on a tuneable power offset. The two modes are separated by a hysteresis switching algorithm parameterised by a pair of thresholds. As such, a minimum duration is ensured for each mode, which naturally prevents fast engine on/off switching that is detrimental to fuel usage. The two thresholds and the offset are regulated based on the information of different HEV model (or real vehicle) parameters and driving cycles by a systematic tuning process, targeting charge sustaining operation that is proven in this chapter to be optimal in the context of the equivalent fuel consumption.

DP simulation results verify the analytic solutions obtained for the two simple vehicle models. As such, the globally optimal solutions for these models can be simply produced without referring to DP, which usually involves heavy computation effort. The control performance of the HPTS is evaluated and benchmarked against DP and a recently proposed rule-based method, XOS, in simulations with a realistic SSS that involves a fuel penalty for engine switch on. It is demonstrated that the proposed HPTS outperforms the XOS for all studied driving cycles, especially for the profiles that emulate urban driving. Moreover, the simple nature of the HPTS also makes it a potential benchmarking strategy for high-fidelity vehicle models, where DP is no longer applicable.

Part II

Energy-Optimal Strategy for Vehicle Following Scenario

Chapter 5

NN-Based NMPC Framework for Vehicle Following Strategy of Series HEVs

5.1 Introduction

This chapter proposes an energy-optimal control strategy, EACC, to address the vehicle following problem, where the speed and EM of the ego vehicle are optimally controlled with consideration of the interaction with the vehicle ahead. The fundamental concept of EACC is the NMPC, which optimises the velocity and power split over a sliding time window. To forecast the future uncertain speed of the preceding vehicle, the NN predictor introduced in [115] is applied in the NMPC framework. The focus of the chapter is on the series HEV powertrain architecture. However, the ideas that are presented also have relevance to other HEV architectures. The main contributions of this chapter are summarised as follows:

a. Compared to the very recent work on the car following EM [113], the presented chapter addresses a more realistic car following scenario, where the influence of the following distance on the air drag losses is modelled. As such, the ego vehicle can make use of the drafting technique to reduce aerodynamic energy losses.

b. The vehicle jerk is modelled to ensure smooth control, and therefore it improves driving comfort and avoids unrealistic jerky manoeuvre.

c. The performance of the proposed EACC is evaluated by comparing it with two benchmark methods: 1) the solution of optimal control problem (OCP) is solved globally with a precise speed profile of the lead vehicle, and 2) a practical ACC method that is also based on NMPC, whereas a constant and close following distance is targeted to enjoy the drafting effect.

d. The impact of the prediction horizon length on the overall optimality is investigated.

This chapter is organised as follows. Section 5.2 introduces the car following scheme and the powertrain model of the series HEV. The proposed method is described in Section 5.3, together with two benchmark methods. Simulation examples and comparative studies are illustrated in Section 5.4, followed by the concluding remarks in Section 5.5. Note that Sections 5.2- 5.5 are taken from the author's publication [182].

5.2 Model Description

The car following model considered in this work is illustrated in Fig. 5.1, where the vehicle in front is identified as an uncontrolled reference vehicle, followed by a controlled ego vehicle. Moreover, it is assumed that the lead vehicle is travelling at a speed v_{ref}, and the past status of the lead vehicle, including the speed and travelled space, (v_{ref}, s_{ref}) can be shared with the ego vehicle by proper communication systems without any delay.

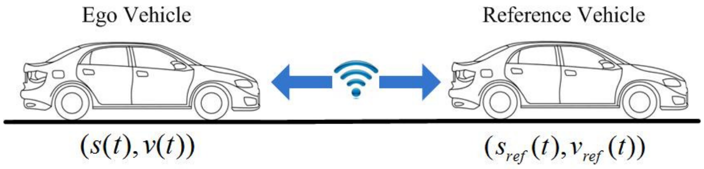

Fig. 5.1 Vehicle following scheme with V2V communication considered.

Consider (s, v) respectively the distance and speed of the ego vehicle. The inter-vehicular distance, d, between the two vehicles is defined by $d \triangleq s_{ref} - s$. To main a safe vehicle following scheme, the gap between the two vehicles is constrained by:

$$d_{\min} \leq d \leq d_{\max} , \tag{5.1}$$

where $d_{\min}$ is the minimum distance to avoid rear-end collision and $d_{\max}$ is the maximum value to maintain the car following mode. The selections of $d_{\min}$ and $d_{\max}$ depend on the road type, the vehicle travelling speed, the traffic flow, the driver preference, and the V2V communication range [113, 183–185].

The ego vehicle motion is given in terms of speed and travelled space by the following differential equations:

$$\frac{d}{dt} s = v , \tag{5.2a}$$

$$m \frac{d}{dt} v = F_w + F_h - f_r m g - f_d(d)\, v^2 , \tag{5.2b}$$

where m is the vehicle mass, F_h is the braking force, f_r is the coefficient of tyre rolling resistance, and $f_d(d)$ is the aerodynamic drag coefficient, modelled as a function of the distance to the lead vehicle [174, 186]. Besides, F_w is the powertrain driving force at the wheels, and the powertrain model of the ego vehicle is developed based on the series HEV system described in Section 3.1.

For an HEV with energy recovery system, $F_w > 0$ in driving condition (energy transfer from the powertrain to the vehicle) and $F_w \leq 0$ during energy recovery. As commonly assumed in EM studies [187], the regenerate braking is not restricted by the braking distribution between front and rear axles, such that all the braking power is recoverable and it is only restricted by the battery power charging limit.

The present work adopts the nonlinear air drag model [174] that is able to capture the influence of inter-vehicular distance on the drag coefficient in the context of a passenger car. The behaviour of the model is illustrated in Fig. 5.2. As it can be seen, the air drag coefficient (the aerodynamic losses) can be effectively reduced by travelling close to the reference vehicle due to the drafting effect.

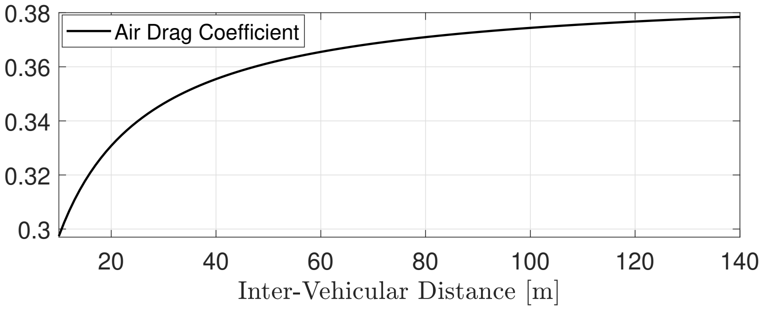

Fig. 5.2 Air drag coefficient of a passenger car, modelled as a function of inter-vehicular distance [174].

In view of the series HEV model, as shown in Fig. 3.1 presented in Section 3.1, the series HEV has three independent sources of power P_{SS}, P_{PS} and P_h, which are freely controlled to obtain the desired values of vehicle speed and acceleration. Then, the overall vehicle model, $\frac{d}{dt}x = f(x,u,t)$ that collects (5.2), (3.5), (3.8) and the dynamics of the forces, is expressed as:

$$\frac{d}{dt}\begin{pmatrix} m_f \\ \mathrm{SOC} \\ v \\ s \\ F_{PS} \\ F_{SS} \\ F_h \end{pmatrix} = \begin{pmatrix} q_{f0} + \alpha_f (P_{PL} - P_{SS}) \\ \dfrac{-V_{oc} + \sqrt{V_{oc}^2 - 4P_{SS}R_b/\eta_{dc}^{\mathrm{sign}(P_{SS})}}}{2R_b\,Q_{\max}} \\ \dfrac{1}{m}\left(F_w + F_h - f_r m g - f_d(d)\,v^2\right) \\ v \\ m j_{PS} \\ m j_{SS} \\ m j_h \end{pmatrix} \tag{5.3}$$

where $x \triangleq [m_f, \mathrm{SOC}, v, s, F_{PS}, F_{SS}, F_h]^\top$ are the state variables, $u \triangleq [j_{PS}, j_{SS}, j_h]$ are the control inputs, and j_{PS}, j_{SS}, j_h are the jerk variables of the associated forces, $F_{PS} = P_{PS}/v$, $F_{SS} = P_{SS}/v$, and $F_h = P_h/v$, which are introduced to indirectly control the power variables and ensure the smoothness of the control. Furthermore, following inequality constraints are also imposed due to physical and operational limits:

$$0 \le P_{PS} \le P_{PS_{\max}}\,, \tag{5.4a}$$

$$P_h \le 0\,, \tag{5.4b}$$

$$P_{SS_{\min}} \le P_{SS} \le P_{SS_{\max}}\,, \tag{5.4c}$$

$$\mathrm{SOC}_{\min} \le \mathrm{SOC} \le \mathrm{SOC}_{\max}\,, \tag{5.4d}$$

$$0 \le v \le v_{\max}\,, \tag{5.4e}$$

$$j_{PS},\, j_{SS},\, j_h \in [j_{\min}, j_{\max}]\,. \tag{5.4f}$$

The main characteristic parameters of the vehicle model are summarised in Table 5.1, where the power limits are chosen to emulate the energy sources for a medium-sized passenger car with a series hybrid powertrain.

Table 5.1 Main parameters of the series HEV model

description	symbol	value
vehicle mass	m	1500 kg
rolling resistance coefficient	f_r	0.01
efficiency of the transmission	η_t	0.96
idling fuel mass rate	q_{f0}	0.061 g/s
power transformation factor	α_f	0.059 g/kW/s
battery capacity	$Q_{\max}$	5 Ah
battery internal resistance	R_b	0.2056 Ω
battery open circuit voltage	V_{oc}	300 V
efficiency of inverters	η_r, η_i	0.96
efficiency of converter	η_{dc}	0.96
SS power limits	$P_{SS_{\min/\max}}$	$-15/30$ kW
battery SOC limits	$\mathrm{SOC}_{\min/\max}$	$0.5/0.8$
PS power limit	$P_{PS_{\max}}$	70 kW

5.3 Problem Formulation

The main objective is to optimise the speed and EM of the ego vehicle over a specified time-horizon $[0, T]$, such that its fuel consumption $m_f(T)$ is minimised and the battery is charge sustained at the end of the mission (i.e., $\mathrm{SOC}(0) \approx \mathrm{SOC}(T)$), subject to state and control constraints as well as the constraint on the inter-vehicular distance. To address the optimisation problem online, this section proposes the EACC which combines MPC control with an NN-based speed predictor. Prior to the introduction of the novel scheme, benchmark strategies are introduced next.

5.3.1 Optimal Control Problem (OCP) Method

By assuming that the reference speed profile v_{ref} is available for all $t \in [0,T]$, it is immediate to obtain s_{ref} by integration with $s_{ref}(0)=d_0$, where d_0 is the initial distance between the two vehicles. Then the control problem can be formulated as an OCP. The objective function is designed as:

$$J_{oc} = W_1 m_f(T) + W_2 \left(\mathrm{SOC}(T) - \mathrm{SOC}(0)\right)^2 \tag{5.5}$$

where W_1, W_2 are two constant weights, tuned to balance the control performance in both aspects. The objective J_{oc} is minimised subject to system differential equations (5.3) and the inequality constraints (5.1) and (5.4). Finally, the problem is completed by imposing following boundary conditions:

$$\begin{aligned}
&s(0) = s_{ref}(0) - d_0 = 0,\, s(T) = s_{ref}(T) - d_0,\\
&v(0) = v_{ref}(0),\, v(T) = v_{ref}(T),\\
&F_{PS}(0) = F_{SS}(0) = F_h(0) = 0,\, m_f(0) = 0,\\
&\mathrm{SOC}(0) = 0.65,\, \mathrm{SOC}(t_0) = 0.65,
\end{aligned}$$

where SOC is initialised at the middle of the allowed SOC range, and the control forces and other states are initialised at 0. Furthermore, the terminal condition on s ensures the space travelled by the ego vehicle is identical to that travelled by the reference vehicle.

5.3.2 Adaptive Cruise Control (ACC) Strategy

During real-world driving, v_{ref} is usually unknown a priori. This promotes the development of ACC strategies for driver assistance. Similarly to most of the available ACC systems [188], the benchmark ACC considered in this chapter aims to maintain a fixed distance from the vehicle ahead by adaptively adjusting the velocity of the ego vehicle. Additionally, to further improve the fuel efficiency of the ACC, and consequently to enable effective comparison with the proposed approach, it is also assumed that the benchmark ACC enforces the ego vehicle to stay closely behind the lead vehicle so that it can benefit from drafting.

The ACC is designed based on an NMPC framework in discrete time with sampling time T_s,

$$\min_{\mathbf{u}} J_{k,\mathrm{ACC}}\,, k = 1,2,\dots,T/T_s \tag{5.6a}$$

$$\textbf{s.t.:}\quad x(t_k|t_k) = x_0, \tag{5.6b}$$

$$x(t_{k+j+1}|t_k) = f(x(t_{k+j}|t_k), u(t_{k+j}|t_k)),\ j = 0,\dots,N_p - 1, \tag{5.6c}$$

$$\boldsymbol{g}(x(t_{k+j}|t_k), u(t_{k+j}|t_k), \hat{x}_r(t_{k+j}|t_k)) \le 0,\ j = 0,\dots,N_p - 1, \tag{5.6d}$$

where $\mathbf{u} = [u(t_k|t_k), u(t_{k+1}|t_k), \dots, u(t_{k+N_p-1}|t_k)]$, N_p is the dimension of the prediction horizon, x_0 is the initial condition for each iteration, and $\hat{x}_r \triangleq [\hat{v}_{ref}, \hat{s}_{ref}]$ represents the predicted reference velocity and space. The ACC assumes that the reference vehicle keeps its speed constant within a prediction horizon:

$$\hat{v}_{ref}(t_{k+j}|t_k) = v_{ref}(t_1|t_k), \quad j = 0,1,\dots N_p\,, \tag{5.7}$$

and

$$\hat{s}_{ref}(t_{k+j}|t_k) = \hat{s}_{ref}(t_k|t_k) + T_s \sum_{h=0}^{j} \hat{v}_{ref}(t_{k+h}|t_k)\,,\ j = 0,\dots,N_p \tag{5.8}$$

with $\hat{s}_{ref}(t_1|t_k) = d_0$. The speed forecasting method (5.7) represents an elementary but widely applicable algorithm [188] that enables the ACC to be implemented in real-time for benchmarking purposes. The following terminal cost is used for the ACC:

$$J_{k,\mathrm{ACC}} = W_1 m_f(t_{N_p}|t_k) + W_2 \left(\mathrm{SOC}(t_{N_p}|t_k) - \mathrm{SOC}(0)\right)^2 + W_3 \sum_{j=0}^{N_p} \left(\hat{d}(t_{k+j}|t_k) - d_{ACC}\right)^2, \tag{5.9}$$

where $k = 1,2\dots,T/T_s$, W_1, W_2, W_3 are constant weights, $\hat{d} = \hat{s}_{ref} - s$ is the anticipated inter-vehicular distance and d_{ACC} is the desired following distance. As such, in addition to the fuel usage and SOC variations (first two terms), the third term in (5.9) represents a running cost penalising also the variation in the headway distance.

Within each finite horizon, $J_{k,\mathrm{ACC}}$ is minimised subject to various constraints and boundary conditions (5.6c)-(5.6d). More specifically, the dynamic constraints (5.6c) represent the discretised version of vehicle system (5.3), with the initial condition x_0 for each iteration. x_0 is the same as used in the OC case at $t = 0$, and it is updated iteratively based on the system states at $t = t_k$, $k = 1,2,\dots,T/T_s$. The $\boldsymbol{g}(\cdot)$ inequality constraints (5.6d) incorporate (5.1) and (5.4), which are identical to the OC case.

5.3.3 Enhanced Adaptive Cruise Control (EACC) Strategy

The EACC strategy, which is developed in this section, aims to further improve the fuel economy performance of the ACC without losing the real-time control property.

Terminal cost design

Similarly to the ACC, the EACC is also formulated as an NMPC problem (5.6), subject to identical constraints and initial conditions to those of the ACC. However, the terminal cost is redesigned to allow adjustable following distance:

$$J_{k,\text{EACC}} = W_1 m_f(t_{N_p}|t_k) + W_2 \left(\text{SOC}(t_{N_p}|t_k) - \text{SOC}(0)\right)^2 + W_3(\hat{v}_{ref}(t_{N_p}|t_k) - v(t_{N_p}|t_k))^2, \tag{5.10}$$

where $k = 1, 2, \ldots, T/T_s$, and the last term penalises the difference between the terminal speed of both vehicles, as opposed to the ACC that keeps the headway distance fixed. As a consequence, the ego vehicle is able to make use of the inter-vehicular distance variation within an NMPC horizon for fuel economy improvement, while keeping up with the reference speed at the end of the horizon at each iteration. Thus, the terminal cost avoids the sub-optimal solution where the ego vehicle maintains the maximum following distance at the end of the horizon at each iteration that minimises the ego vehicle travelled distance and hence its fuel usage, regardless of the terminal position and velocity of the reference vehicle.

Reference velocity forecasting

In addition to the novel objective function (5.10), the proposed EACC further incorporates a neural network to provide a more effective reference vehicle velocity prediction, $\hat{v}_{ref}(t_{k+j}|t_k)$ with $j = 0, 1, \ldots N_p$ and associated $\hat{s}_{ref}$ by (5.8), within each NMPC horizon, as compared to the corresponding constant velocity prediction in the ACC shown in (5.7).

Neural networks are widely used for time series forecasting as they can be trained to establish a nonlinear mapping relationship between input and output data. For velocity prediction purposes, usually historical velocity sequences are considered as the input of the NN, and the outputs are predicted horizon velocity sequences. Each input-output pattern is composed of a moving window of fixed length, which can be expressed as:

$$[v_k, v_{k+1}, \ldots, v_{k+N_p}] = f_{NN}(v_{k-N_h}, \ldots, v_{k-1}, v_k),$$

where N_h is the dimension of the input historical velocity sequence, and f_{NN} represents the nonlinear map of the NN predictor, which is obtained by offline training.

In this work, a radial basis function neural network (RBF-NN) is applied for speed forecasting of the EACC. The advantages of the RBF-NN have been examined in [115], where the RBF-NN shows better convergence speed and precision in the context of velocity prediction of ground vehicles, as compared to a few other types of network structures. The framework of the RBF-NN is shown in Fig. 5.3. After the input sequences v_h are received and rearranged, the pre-trained Gaussian function-based hidden layer establish the nonlinear relationship between input and output. Then, the output layer yields output patterns v_p, which are linear combinations of the hidden layer outputs. The number of the neurons in the output layer is identical to the size of output v_p, while that in the hidden layer is tunable and predefined, which determines the precision of the prediction with proper selection of the neuron numbers.

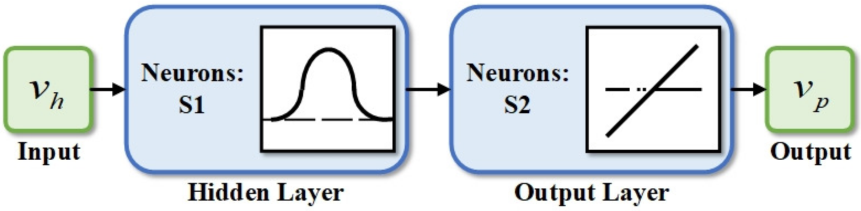

Fig. 5.3 Scheme of RBF-NN predictor with historical velocity sequences v_h as the input, followed by a Gaussian function-based hidden layer that depicts the nonlinear relationship between input and output, and then the output layer yields the predicted velocity sequences v_p. S_1 and S_2 are the numbers of neurons respectively for the hidden and output layers.

5.4 Numerical Results

This section provides a comprehensive comparative analysis of the three car following control strategies described in Section 5.3. All the optimisation problems are addressed by the ACADO toolkit, which provides a general framework for efficiently solving optimal control and model predictive control problems based on direct optimal control methods [189]. The sampling time of the solver is kept the same for all cases at T_s=0.5 s, which provides an appropriate balance between numerical accuracy and computational complexity. Prior to showing the comparative results, a test driving profile of the reference vehicle v_{ref} is introduced next, together with prediction examples of this profile by the RBF-NN.

5.4.1 Reference Velocity and Prediction

To evaluate the performance of the NMPC methods (ACC and EACC), the urban/suburban cycle JP-15 is selected as the reference velocity, v_{ref}, in this work to emulate a mixed urban/suburban driving environment. Moreover, the training set for the RBF-NN predictor is formed by the four individual components of the WLTP cycle.

Fig. 5.4 illustrates a prediction example by the RBF-NN utilised in the EACC, for $N_h = 40$ and $N_p = 20$. In other words, it shows 10-second-ahead prediction for the JP-15 cycle based on v_{ref} during the past 20 seconds. As it can be seen, the RBF-NN predictor is able to achieve accurate prediction within a short horizon.

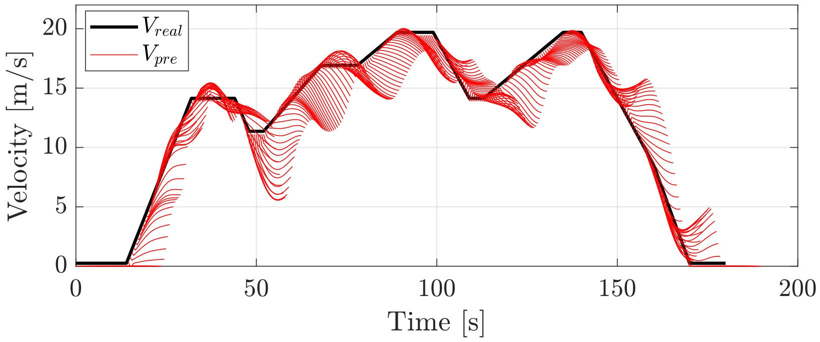

Fig. 5.4 Reference velocity (JP-15) and the 20-step-ahead ($N_p = 20$) velocity prediction by the RBF-NN driven by the past 40 steps ($N_h = 40$) reference speed data.

5.4.2 Comparative Results of the Control Strategies

In order to achieve a fair comparison, all the approaches are tuned to be battery charge sustaining with negligible differences in the terminal SOC values. Thus, the fuel consumption of each method can be compared without the need to refer to the equivalent fuel, which evaluates the fuel and battery charge consumption under a single paradigm [13]. The inter-vehicular distance limits are set to avoid both rear-end collision and the disruption of car following scenario. For simplicity, constant limits are employed in this study. Similarly to [113], the inter-vehicular distance limits are defined as a linear function of speed, $d_{\min} = b_0 + b_1 v_{\min}$, $d_{\max} = b_0 + b_1 v_{\max}$ where b_0 and b_1 are coefficients, which are set to 5m and 3s, respectively. As the velocity of JP-15 is bounded within $[0,20]$ m/s, following distance limits are adopted: $d_{\min} = 5\text{m}$, $d_{\max} = 65\text{m}$. The desired headway distance of the ACC is set to 15m, which is close to the lower distance limit to enable drafting, while leaving enough distance for tolerance to cope with the imprecise speed prediction. The other two methods, OCP and EACC, as well as the ACC, are initialised with the same distance value for consistency: $d_0 = d_{ACC} = 15\,\text{m}$. Moreover, the influence of the prediction horizon is investigated by comparing solutions with different horizon lengths ($N_p = 10$, $N_p = 20$, and $N_p = 30$), to provide further insight into the design of the NMPC-based EACC.

The first case considered is with a prediction horizon for EACC set to $N_p = 10$, which enables accurate velocity forecasts. The optimal ego vehicle speed profile as well as the resulting inter-vehicular distance profile solved by EACC is compared in Fig. 5.5 with the solutions of OCP and ACC with the same horizon length. As it can be seen, both OCP and

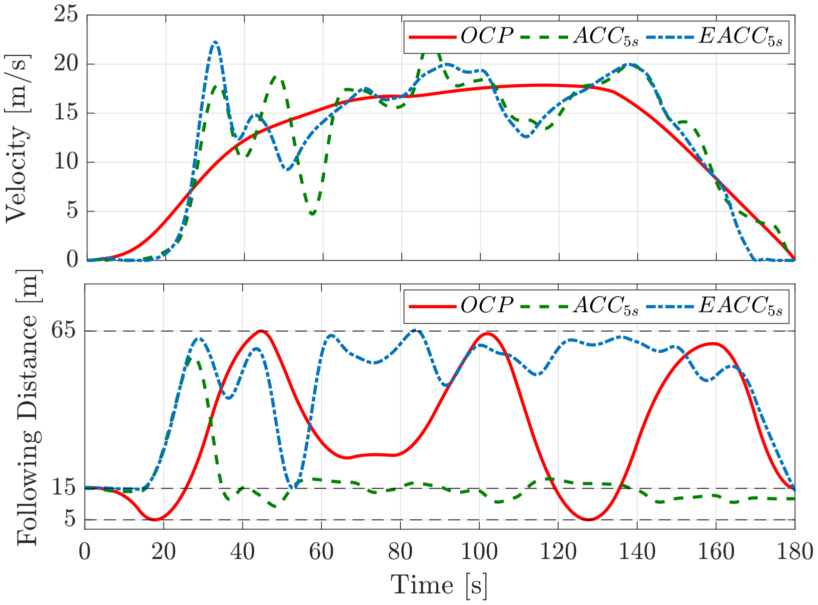

Fig. 5.5 Optimal ego vehicle driving speeds and the inter-vehicular distances solved by OCP, and the two NMPC methods, ACC and EACC with a 10-step (5 s) prediction ahead. The following distance of the ACC has a large overshoot at the beginning due to the transient response to the acceleration of the leading vehicle.

EACC exploit the inter-vehicular distance variation rather than staying closely behind the reference vehicle. This allows OCP and EACC to yield smoother speed profiles, and hence lower accelerations, which are expected to be more energy efficient in terms of powertrain operation.

The energy source and other friction energy losses for the whole mission are evaluated for each method, which reinforces some of the earlier observations and conclusions. The histogram in Fig. 5.6 shows the various power losses for each control strategy. It is clear that the biggest component of losses in all simulated cases corresponds to the PS branch power losses, which is expected since the most inefficient component of the powertrain is the ICE, and the reference vehicle follows a low average-speed profile whereby the air drag losses are not significant. The rolling resistance losses of all three strategies are the same as a fixed distance is travelled in each case. By driving smoothly, OCP substantially reduces the energy losses from the PS branch, PL branch and mechanical brakes, and results in the least overall energy losses. Although EACC incurs more PS branch and mechanical braking

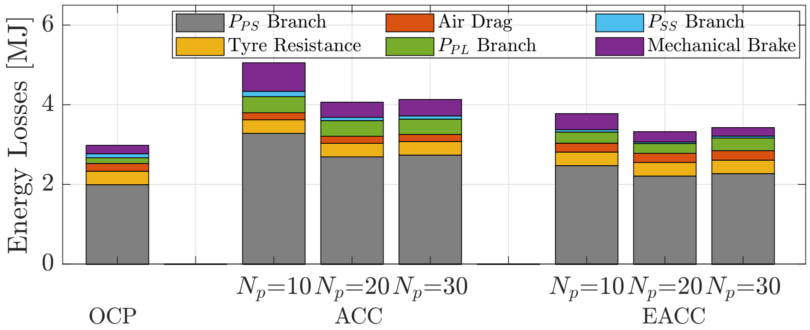

Fig. 5.6 Energy losses breakdown for the optimal solutions solved by the three strategies (OCP, ACC and EACC) for the JP-15 driving cycle as the reference velocity.

energy losses than OCP, it reduces the aforementioned energy losses as compared to ACC. In addition, ACC also produces more SS branch energy losses as its driving profile (see Fig. 5.5) demands high power output from both energy sources to perform larger acceleration, and high battery charge rate for larger deceleration. Although ACC is able to cut aerodynamic drag losses by closing the gap between the two vehicles (i.e., drafting), it ends up with the largest overall energy losses because of the more significant losses from the other aspects.

Fig. 5.7 shows the comparative results of fuel consumption and computation time. The performances of ACC and EACC are compared by using the OCP solution as the benchmark. For the prediction horizon of 5 s ($N_p = 10$), the EACC proposed in this work consumes 26.7% more fuel than OCP, which is a remarkable improvement as compared to the result of the ACC, which leads to 71.6% more fuel consumption. Both NMPC methods are developed for real-time implementation and thereby they are much more computationally efficient than OCP. In comparison with ACC, the additional running time requested by EACC mainly comes from the more advanced speed forecasting approach. The length of the prediction horizon is one of the most crucial factors that influences the performance of NPMC methods. In this context, the horizon length of the ACC and EACC is further increased to $N_p = 20$ and $N_p = 30$ to investigate its impact. As shown in Figs. 5.6-5.7, extending the prediction horizon increases the computational burden, but it also enhances the ability to anticipate future behaviour of the reference vehicle. Therefore, both the ACC and the EACC benefit from the change of the horizon window from 10 to 20 time steps. However, when N_p is further increased, the optimality of both algorithms starts degrading, since the accuracy of the velocity prediction also drops. The best performing EACC with $N_p = 20$ lags the OCP solution by 12.1%. By comparing this EACC case with the best behaved ACC that consumes 38.8% more fuel than the OCP, the fuel saved by the EACC is approximately 26%.

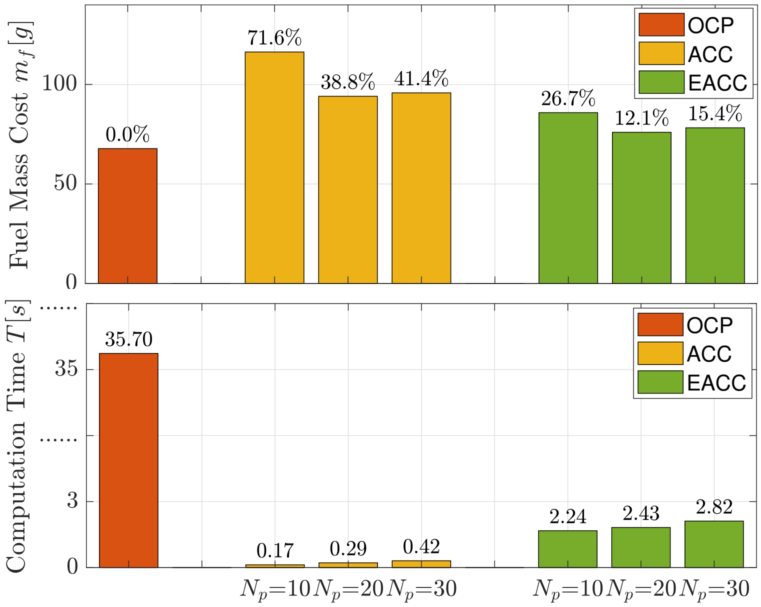

Fig. 5.7 Fuel consumption and computation time of three control strategies (OCP, ACC and EACC). The fuel percentage increase as compared to the OCP for each NMPC case is indicated in the top plot.

5.5 Conclusions

This chapter proposes the novel control strategy EACC for energy management and velocity control of series hybrid electric vehicles in car-following scenarios. This method is developed based on an NMPC framework, in which the velocity of the lead vehicle is predicted by a radial basis function neural network speed forecasting approach.

In contrast with the conventional ACC that aims for a fixed following distance, EACC encourages the ego vehicle to exploit the inter-vehicular distance variation, especially when the vehicle ahead is driven inefficiently. The control performance of the EACC is benchmarked against the full-horizon solutions solved by an OCP and a suitably designed ACC. The simulation examples based on a typical reference vehicle driving cycle confirm the improvement of EACC over ACC in terms of fuel economy at the expense of the slightly increased computational complexity. Moreover, the fuel economy of the EACC solution is shown to be relatively close to that of the OCP solution with a remarkable reduction in the running time.

Chapter 6

LMI-based RMPC Framework for Vehicle Following Scenario of BEVs

6.1 Introduction

This chapter proposes an LMI-based RMPC method that aims to find the energy-efficient following velocity of an ego BEV and to guarantee a safe rear-end distance in the presence of external disturbances and modelling errors. Considering the nonlinearity of the vehicle longitudinal and powertrain dynamics involved in the eco-ACC problem, most of the existing MPC-based control strategies are still computationally demanding for onboard processing units of modern vehicles, particularly the nonlinear MPC approaches [112, 190, 191]. Therefore, in this chapter, the optimisation problem is formulated in the space domain so that the overall problem can be convexified in the form of a semi-definite program, which ensures a rapid solving speed and a unique solution. The contribution of the chapter is threefold:

a. A convex eco-ACC modelling framework for an electric vehicle with consideration of various disturbances and uncertainties is developed. A rigorous proof of the equivalence between the convexified and the original non-convex problem is also provided to complete the framework.

b. A LMI-based RMPC algorithm is designed for the ACC problem with SDPR to formulate the control problem into LMIs.

c. Numerical comparisons between the robust and a nominal MPC are carried out to verify the effectiveness of the RMPC method.

The rest of this chapter begins with a description of the vehicle following model and a convex problem formulation in Section 6.2, and it is followed by Section 6.3, which introduces the SDPR RMPC algorithm. Simulation results are illustrated and discussed in Section 6.4. Finally, conclusions are provided and a future work plan is suggested in Section 6.5. Note that Sections 6.2- 6.5 are taken from the author's publication [192].

6.1.1 Notation and Preliminary:

Let $\mathbb{R}$ and $\mathbb{N}$ denote the real and natural numbers, respectively. For $r_1 \in \mathbb{R}$ and $n_1, n_2 \in \mathbb{N}$, $\mathbb{R}_{\geq r_1}$, $\mathbb{R}_{>r_1}$, $\mathbb{N}_{>n_1}$, and $\mathbb{N}_{[n_1,n_2]}$ denote sets $\{r \in \mathbb{R} | r \geq r_1\}$, $\{r \in \mathbb{R} | r > r_1\}$, $\{n \in \mathbb{N} | n > n_1\}$, and $\{n \in \mathbb{N} | n_1 \leq n \leq n_2\}$, respectively. For $m \in \mathbb{N}_{>0}$, $X \in \mathbb{R}^m$ and $Y \in \mathbb{N}^m$ denote vectors with m rows and all the elements being real and natural numbers, respectively. For $m, n \in \mathbb{N}_{>0}$, $X \in \mathbb{R}^{m \times n}$ and $Y \in \mathbb{N}^{m \times n}$ denote matrix with m rows and n columns and all the elements being real and natural numbers, respectively.

Definition 6.1. *Let M be a symmetric matrix, and $M^\top$ denotes the transpose of the M such that $M = M^\top$. The following statements are equivalent for the symmetric matrix $M \in \mathbb{R}^{n \times n}$:*

a. The symmetric matrix M is (semi-)positive definite, $M > 0$ ($M \geq 0$).

b. For all $\alpha \in \mathbb{R}$, there exists $\alpha^\top M \alpha \geq 0$ ($\alpha^\top M \alpha > 0$).

c. All the eigenvalues of M are positive (non-negative), $\lambda_i(M) > 0$ ($\lambda_i(M) \geq 0$).

Definition 6.2. *A convex optimisation problem is one of the form*

$$\begin{aligned} \min_{\mathbf{x}} \quad & f(x) \\ \textbf{\textit{s.t.}}: & g_i(x) \leq 0, \quad i = 1, \dots, h \\ & a_i^T x = b_i, \quad i = 1, \dots, p \end{aligned} \tag{6.1}$$

where the equality constraint functions $a_i^T x = b_i$ are affine, the objective function and inequality constraint functions $f(x), g_1(x), g_2(x), \dots, g_h(x)$ are convex functions, i.e., satisfy

$$f(\alpha x + \beta y) \leq \alpha f(x) + \beta f(y)$$

for all $x, y \in \mathbb{R}^n$, and $\alpha, \beta \in \mathbb{R}$ with $\alpha + \beta = 1, \alpha \geq 0, \beta \geq 0$.

6.2 Model Description and Convexification

6.2.1 Vehicle Following Model

This work considers the vehicle following scenario, where an ego vehicle (controlled vehicle) follows a lead vehicle (reference vehicle) with a safety inter-vehicular time gap. The space domain modelling approach is utilised to facilitate problem convexification [193]; the convexification process will be presented later in Section 6.2.2. Let s denote the variable of travelled distance. The transformation from time to space domain is achieved by changing the independent variable of time t to s via $\frac{d}{ds} = \frac{1}{v}\frac{d}{dt}$. It is convenient to use as a state variable the kinetic energy $E(s) = \frac{1}{2}mv^2(s)$ in the space domain instead of the variable $v(s)$, the linear (forward) velocity of the controlled vehicle.

Fig. 6.1 shows the scheme of the vehicle following problem with the V2V communication system and the implementation of RMPC. Past information containing kinetic energy $E_{ref}(s)$

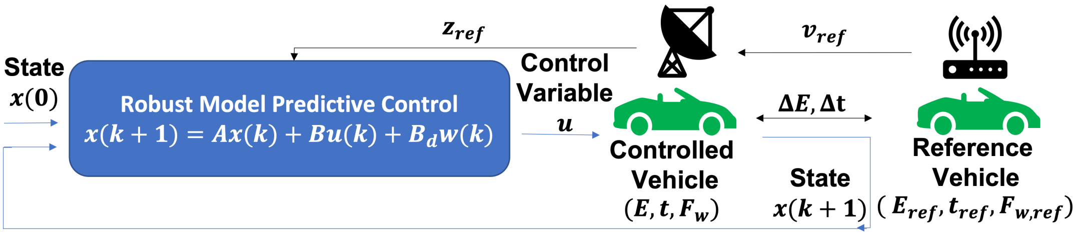

Fig. 6.1 Scheme of the RMPC-based eco-ACC.

and travelled time $t_{ref}(s)$ of the reference vehicle are shared with the controlled vehicle. Note that the communication through the V2V system in this work is assumed to be ideal with no delays. For safety purposes and the feasibility of the V2V communication range, the following constraint is imposed:

$$\frac{\Delta v(s)}{|a_{\min}|} + T_\sigma \leq \Delta t(s) \leq \Delta t_{max} \tag{6.2}$$

where $\Delta t(s) = t(s) - t_{ref}(s)$ is the time gap between the two vehicles at distance s, $\Delta v(s) = v(s) - v_{ref}(s)$ is the corresponding velocity difference with $v(s) = \sqrt{2E(s)/m}$, $v_{ref}(s) = \sqrt{2E_{ref}(s)/m_{ref}}$, and m and m_{ref} are the masses of the ego and the reference vehicle, respectively. Moreover, $a_{\min} = \frac{F_{w,\min}}{m}$ is the maximum allowed deceleration, with $F_{w,\min}$ the maximum braking force (it has a negative value), such that the force acting on the wheels (driving or braking), $F_w \geq F_{w,\min}$. T_σ is the braking response time of the vehicle braking system (lag between driver braking command and braking system response) [193]. As such, the left hand side of (6.2) is the time-to-collision (TTC) constraint designed for the controlled vehicle to avoid a potential rear-end collision. The right hand side of (6.2) is a designed upper bound of $\Delta t(s)$ where its value is determined by considering the traffic flow rate [185], the driver preference [183], as well as the V2V communication range [184].

Instead of utilising the state of the controlled vehicle $(E(s), t(s))$ to construct the control problem, this work considers $(\Delta E(s), \Delta t(s))$ as states for the convenience of integrating the information of the leading vehicle in a nominal system:

$$\frac{d}{ds}\Delta E(s) = F_w(s) - F_r - 2\frac{f_d}{m}E(s) - F_{ref}(s)\,, \tag{6.3a}$$

$$\frac{d}{ds}\Delta t(s) = \frac{1}{v(s)} - \frac{1}{v_{ref}}, \tag{6.3b}$$

where $\Delta E(s) = E(s) - E_{ref}(s)$ is the difference of the kinetic energies of the two vehicles, $F_r = f_r mg$ is the tyre resistance force with f_r the rolling resistance coefficient, f_d is air drag resistance coefficient [182], and $F_{ref}(s) = \frac{d}{ds}E_{ref}(s)$ is the total force of the reference vehicle. Furthermore the sampling interval $\Delta s \in \mathbb{R}_{>0}$. The difference of the kinetic energies $\Delta E(s)$ and driving force $F_w(s)$ of the controlled vehicle are constrained, respectively, by permissible limits:

$$\frac{1}{2}mv_{\min}^2 - E_{ref}(s) \leq \Delta E(s) \leq \frac{1}{2}mv_{\max}^2 - E_{ref}(s), \tag{6.4a}$$

$$F_{w,\min} \leq F_w(s) \leq F_{w,\max}, \tag{6.4b}$$

where $v_{\min}$ and $v_{\max}$ are minimum and maximum speed limits, in which $v_{\max}$ is determined based on infrastructure requirements and traffic regulations and $v_{\min}$ is set as a sufficiently small positive value to avoid the singularity issue in (6.3b). Moreover, $F_{w,\max}$ is the maximum force that the powertrain is capable of delivering to the wheels.

In this work, we consider the controlled vehicle as a BEV, of which the powertrain model is developed based on the BEV system described in Section 3.2 with an static motor efficiency map [67]. As such, the total force acting on the wheels $F_w(s)$ can be divided into two separate parts, the powertrain driving force $F_t(s)$ and the mechanical braking force $F_b(s) \leq 0$, such that

$$F_w(s) = F_t(s) + F_b(s) \tag{6.5}$$

where the physical limit constraints of $F_w(s)$, $F_t(s)$ and $F_b(s)$ are introduced in (3.14).

Based on the (3.15), the battery energy consumption is modelled in an ideal lossless form [67] for a convenience of convex optimisation formulation as shown later in Section 6.2.2:

$$J_b = \int_0^{s_f} F_t(s)ds, \tag{6.6}$$

where $F_t(s) \geq 0$ indicates discharge of the battery and $F_t(s) < 0$ corresponds to braking energy recovered by the powertrain.

Assumption 6.1. *The friction brake F_b is inactive, such that $F_b(s) = 0$ over the range $s \in [0, s_f]$.*

Assumption 6.1 holds in most cases by the fact that regenerative braking is naturally maximised in order to promote eco-driving, which targets minimum energy usage. The case when the assumption does not hold is analysed in Remark 6.3 later in this section.

Under Assumption 6.1, the battery energy cost J_b in (6.6) is equivalent to

$$J_w = \int_0^{s_f} F_w(s) ds, \tag{6.7}$$

The objective of the vehicle following problem in this work is to find the optimal wheel force, $F_w(s)$, that minimises a multi-objective function of the controlled vehicle, achieving driving speed and energy optimisation over the range $[0, s_f]$, expressed as follows:

$$V = W_1 \int_0^{s_f} (E(s) - \frac{1}{2} m\bar{v}^2(s))^2 ds + W_2 J_w + W_3 \left(t(s_f) - t(0)\right), \tag{6.8}$$

where $W_1, W_2 \in \mathbb{R}_{>0}$ are weighting factors. The first term in (6.8) is designed for the controlled vehicle to follow a constant cruise speed $\bar{v}$, whose value is determined based on various road conditions (such as highway or urban road) and the legal speed limit, and the second and third term aims to minimise the battery energy cost (6.7) and the travelled time over the entire horizon, respectively.

6.2.2 Model Convexification

Despite the complexity introduced in the time difference constraint (6.2) and the dynamics system of the vehicle following model in space domain (6.3), this work formulates the eco-ACC problem as a convex optimisation problem by suitable approximations, to take advantage of computational efficiency and guarantee of a unique optimal solution of convex optimisation. The approximation made in this work ensures that the approximated problem is consistent and feasible to the original problem. To convexify the nonlinearity in the state dynamics of the time difference $\Delta t(s)$ (see (6.3b)), an auxiliary optimisation variable $\zeta(s)$ is introduced to relax the derivative of the travelled time of the controlled vehicle $\frac{d}{ds} t(s) = \frac{1}{v(s)}$:

$$\frac{d}{ds} \Delta t(s) = \zeta(s) - 1/v_{ref}, \tag{6.9a}$$

$$\zeta(s) \geq 1/\sqrt{2E(s)/m}, \tag{6.9b}$$

such that (6.3b) is relaxed as a linear dynamic (6.9a) and a convex path constraint (6.9b). With the introduction of $\zeta(s)$, the objective function (6.8) can be rewritten in a convex form with a convex function $J(s)$:

$$V = \int_0^{s_f} J(s) ds = \int_0^{s_f} W_1 \left(E(s) - \frac{m\bar{v}^2(s)}{2} \right)^2 + W_2 F_w(s) + W_3 \zeta(s) ds, \tag{6.10}$$

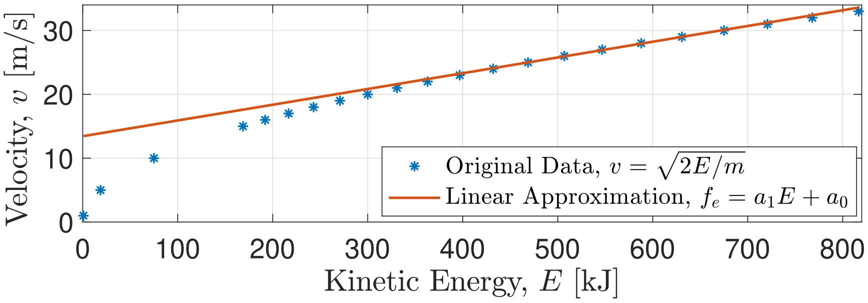

Fig. 6.2 Linearised approximation relationship between kinetic energy E and velocity v.

where the third term is replaced by an integral of ζ over distance s. The minimisation on ζ can not only minimise the travelled time but also encourages (6.9b) to hold the equality, which indirectly guarantees the feasibility and conservativeness of the convex solutions. Further verification of the validity of (6.9b) is performed in Proposition 6.1 as shown later in Section 6.2.3

In terms of the left hand side of (6.2), the nonlinearity existing in the representation of the velocity of the controlled vehicle, $v(s)=\sqrt{2E(s)/m}$, can be approximated by a conservative linear relationship $f_e(E(s))=a_1E(s)+a_0$ [193], as shown in Fig. 6.2. Hence, the constraint of Δt can be rewritten in a convex form:

$$T_\sigma + \frac{f_e(E(s)) - v_{ref}(s)}{|a_{\min}|} \leq \Delta t(s) \leq \Delta t_{\max}\,, \forall E(s) \in [\frac{1}{2}mv_{\min}^2, \frac{1}{2}mv_{\max}^2] \tag{6.11}$$

where $f_e(E(s))=a_1E(s)+a_0$ with a_0 and a_1 as the fitting parameters.

6.2.3 Optimisation Formulation

Suppose a sampling distance interval $\Delta s \in \mathbb{R}_{>0}$, and without loss of generality, it is assumed that $s_f = k_f \Delta s$ with $k_f \in \mathbb{N}_{>0}$. Thus, the convex optimisation problem with the system state $x(k) = [\Delta E(k), \Delta t(k)]^\top$ and the control input $u(k) = [F_w(k), \zeta(k)]^\top$ for any $k \in \mathbb{N}_{[0,k_f]}$ is formulated to find the optimal control input $u(k)$ at each step k, that minimises the objective function in discretised-form:

$$\min_{\mathbf{u}} V = \sum_{k=0}^{k_f} J(k)\Delta s\,, \tag{6.12a}$$

$$\textbf{s.t.} \quad x(k+1) = Ax(k) + Bu(k) + B_cC(k)\,, \tag{6.12b}$$

$$\underline{f}(k) \leq f(x(k), u(k), \omega(k)) \leq \overline{f}(k)\,, \tag{6.12c}$$

$$-\zeta(k) + 1/\sqrt{2E(k)/m} \leq 0\,, \tag{6.12d}$$

$$x(0) = \begin{bmatrix} \Delta E(0) \\ \Delta t(0) \end{bmatrix}, x(k_f) = \begin{bmatrix} \Delta E(k_f) \\ \Delta t(k_f) \end{bmatrix}, \tag{6.12e}$$

where (6.12d) is a convex inequality constraint, (6.12e) are the boundary conditions, and the convex function $J(k)$ in (6.12a) is the rearrangement based on the definition of (6.10) in a state-space form:

$$\begin{aligned} & J(k) = (z(k) - \bar{z}(k))^\top Q^\top Q(z(k) - \bar{z}(k)) + Pz(k) + z(k)^\top P^\top, \\ & z(k) = C_z x(k) + D_{zu} u(k), \\ & C_z = \begin{bmatrix} 1 & 0 & 0 \\ 0 & 0 & 0 \end{bmatrix}^\top, \quad D_{zu} = \begin{bmatrix} 0 & 0 & 1 \\ 0 & 1 & 0 \end{bmatrix}^\top, \end{aligned} \tag{6.13}$$

where $Q = \mathrm{diag}\{\sqrt{W_1}, 0, 0\} \succeq 0$, $P = [0, W_2/2, W_3/2] \succeq 0$, $z(k) = [\Delta E(k), F_w(k), \zeta(k)]^\top$ and $\bar{z}(k) = [\frac{1}{2}m\bar{v}^2 - E_{ref}(k), 0, 0]^\top$.

The discretised dynamic equation (6.12b) collects the differences of kinetic energy ΔE (6.3a) and travelled time Δt (6.9a), which is specified as below:

$$\begin{aligned} & x(k+1) = Ax(k) + Bu(k) + B_c C(k), \\ & A = \begin{bmatrix} 1 - \frac{2f_d}{m}\Delta s & 0 \\ 0 & 1 \end{bmatrix}, B = \begin{bmatrix} \Delta s & 0 \\ 0 & \Delta s \end{bmatrix}, \\ & B_c = \begin{bmatrix} \Delta s & 0 \\ 0 & \Delta s \end{bmatrix}, C = \begin{bmatrix} -F_{tyre} - \frac{2f_d}{m}E_{ref}(k) - F_{ref}(k) \\ -\frac{1}{\sqrt{2E_{ref}(k)/m}} \end{bmatrix}. \end{aligned} \tag{6.14}$$

The inequality constraints (6.12c) summarises linear constraints (6.2) and (6.4) within a state-space form:

$$\begin{aligned} & f(k) = C_f x(k) + D_{fu} u(k), \\ & C_f = \begin{bmatrix} 1 & 0 \\ 0 & 1 \\ 0 & 0 \end{bmatrix}, \quad D_{fu} = \begin{bmatrix} 0 & 0 \\ 0 & 0 \\ 1 & 0 \end{bmatrix}, \end{aligned} \tag{6.15}$$

where $f(k) = [\Delta E(k), \Delta t(k), F_w(k)]^\top$ with a lower bound $\underline{f}(k) = [\frac{1}{2}v_{\min}^2 - E_{ref}(k), \frac{\Delta v(s)}{|a_{\min}|} + T_\sigma, F_{w,\min}]^\top$ and an upper bound $\overline{f}(k) = [\frac{1}{2}v_{\max} - E_{ref}(k), \Delta t_{\max}, F_{w,\max}]^\top$.

Proposition 6.1. *Under Assumption 6.1 and a necessary condition* $(-W_1 m\bar{v}^2 + 2W_2 f_d/m) > 0$, *if there exists feasible solution of OCP* (6.12)*, the globally optimal solution of OCP* (6.12) *always finds the equality condition of* (6.9b)*, and therefore the solution of the relaxed convex problem OCP* (6.12) *is valid.*

Proof. See in Appendix I-A.

Remark 6.1. *Given the inter-vehicular distance constraint* (6.2)*, there might be a case where the ego vehicle cannot catch up with the reference vehicle such that the violation of the upper-bound happens. In this circumstance, a feasible solution can be derived with the control action to enforce the velocity of the ego vehicle to reach and maintain at* $v_{\max}$*. Once* (6.2) *is valid again, the control action is derived by solving the convex optimisation problem* (6.12)*.*

Lemma 6.1. *Under Remark 6.1, if there is no violation of the upper-bound of* (6.2)*, there always exists a sufficiently small constant* $\sigma \geq 0$ *and let* $v_{\min} = \sigma$*, then a feasible solution can be found.*

Proof. See in Appendix I-B.

Remark 6.2. *Given the convex optimisation problem* (6.12)*, there might be a case where no valid solution can be found due to the discrepancy between the convexfied and the actual systems. This can be addressed by Lemma 6.1 and Remark 6.1.*

Remark 6.3 (Active friction brakes)**.** *Solving OCP* (6.12) *may yield a solution trajectory where* $F_w(k) < \frac{g_r}{r_w} T_{\min}(k)$ *for some* k *(regenerated braking power is saturated). In this circumstance, friction brake is invoked to meet the total force demand at the wheels,* $F_w(k) = \frac{g_r}{r_w} T_{\min}(k) + F_b(k)$*. As such, the equivalence between* (6.6) *and* (6.7) *is no longer guaranteed due to the discrepancy between the energy costs in both objective functions (regeneration of friction brakes is assumed in* (6.7)*), and therefore, the optimality of OCP* (6.12) *may be compromised in such a case. Nevertheless, the equality of* (6.9b) *holds invariably (as inferred from the proof in Appendix I-A), which, in turn, ensures the feasibility of the convex optimisation solution.*

6.3 Robust Model Predictive Controller

In this work, we propose an LMI-based RMPC scheme to counter the impact of the disturbance $w(s)$, as shown in Fig. 6.1, using SDPR [194, 195], following a similar methodology to a computationally efficient and verified scheme in non-automotive industrial applications [196]. First of all, we consider the discretised dynamic equation (6.14) with an external disturbance $\omega(k)$ is given as below:

$$x(k+1) = Ax(k) + Bu(k) + B_c C(k) + B_d \omega(k) \tag{6.16}$$

where $B_d = [\Delta s, 0]^\top$, $\omega(k) \leq f_\omega(\overline{v_\omega})$ is an external disturbance caused by various reasons such as V2V communication noises, modelling mismatches and prediction errors, where $f_\omega(\overline{v_\omega}) = \frac{1}{2} m \overline{v_\omega}^2 / \Delta s$ is defined in terms of the disturbance limits on the reference vehicle speed $\overline{v_\omega} \in \mathbb{R}_{>0}$.

In order to formulate the control problem into a LMI-based RMPC scheme, let us first define the following stack vectors:

$$\mathbf{x}=\begin{bmatrix} x(0) \\ x(1) \\ \vdots \\ x(N_p) \end{bmatrix},\mathbf{f}=\begin{bmatrix} f(0) \\ f(1) \\ \vdots \\ f(N_p) \end{bmatrix},\mathbf{z}=\begin{bmatrix} z(0) \\ z(1) \\ \vdots \\ z(N_p) \end{bmatrix},\boldsymbol{\omega}=\begin{bmatrix} \omega(0) \\ \omega(1) \\ \vdots \\ \omega(N_p-1) \end{bmatrix} \tag{6.17}$$

and $\mathbf{C}=[C(0),\ldots,C(N_p-1)]^\top$, where $N_p \in \mathbb{N}_{>0}$ is the prediction horizon.

Using the above stacked matrix definition, the system dynamic (6.16) over the prediction horizon N_p can be expressed as:

$$\mathbf{x}=\widetilde{A}x(0)+\widetilde{B}\mathbf{u}+\widetilde{B}_c\mathbf{C}+\widetilde{B}_d\boldsymbol{\omega}, \tag{6.18}$$

where $\widetilde{A}$, $\widetilde{B}$, $\widetilde{B}_c$ and $\widetilde{B}_d$ are stacked coefficient matrices and are readily obtained from iterating the dynamics in (6.16). Moreover, the stacked vector $\mathbf{u}=[u(0),\ldots,u(N_p-1)]^\top$ represents the input signal over the prediction horizon N_p. Lastly, $x(0)$ represents the initial state defined in (6.12e). By substituting the stack vectors defined in (6.17) and repeating recursive steps in (6.15), stacked coefficient matrices $\widetilde{C}_f$ and $\widetilde{D}_{fu}$ are obtained, and hence the corresponding stacked format of the signal response function of constraints is:

$$\mathbf{f}=\widetilde{C}_f x(0)+\widetilde{D}_{fu}\mathbf{u}+\widetilde{D}_{fd}\boldsymbol{w}. \tag{6.19}$$

where $\widetilde{D}_{fd}$ is a stacked matrix of $[0, 0, 0]^\top$. By using analogous methods, the stacked form of the response function of $z(k)$ in the convex function $J(k)$, which is defined in (6.13), can be expressed by:

$$\mathbf{z}=\widetilde{C}_z x(0)+\widetilde{D}_{zu}\mathbf{u}+\widetilde{D}_{zd}\boldsymbol{w}, \tag{6.20}$$

where $\widetilde{C}_z$ and $\widetilde{D}_{zu}$ are stacked coefficient matrices after iterating the $z(k)$ equation in (6.13), and $\widetilde{D}_{zd}$ is a stacked matrix of $[0, 0, 0]^\top$. By substituting (6.13) and (6.20) in (6.12a), (6.12a) becomes:

$$\begin{aligned}\min_{\mathbf{u}} V=&(\widetilde{C}_z x_0+\widetilde{D}_{zu}\mathbf{u}+\widetilde{D}_{zd}\boldsymbol{\omega}-\mathbf{z}_{ref})^\top\mathbf{Q}^\top\mathbf{Q}(\widetilde{C}_z x_0+\widetilde{D}_{zu}\mathbf{u}+\widetilde{D}_{zd}\boldsymbol{\omega}-\mathbf{z}_{ref})\\ &+\mathbf{P}(\widetilde{C}_z x_0+\widetilde{D}_{zu}\mathbf{u}+\widetilde{D}_{zd}\boldsymbol{\omega})+(\widetilde{C}_z x_0+\widetilde{D}_{zu}\mathbf{u}+\widetilde{D}_{zd}\boldsymbol{\omega})^\top\mathbf{P}^\top,\end{aligned} \tag{6.21}$$

where $\mathbf{Q}$, $\mathbf{P}$ are stack matrices of the weighting matrices Q and P, respectively, and $\mathbf{z}_{ref}$ is a stacked vector of vector $\bar{z}$. Next, an auxiliary variable $\overline{\gamma}$ is defined as the upper boundary of the cost function $V \leq \overline{\gamma}$ such that

$$V-\overline{\gamma}\leq 0. \tag{6.22}$$

The SDPR is applied to the left hand side (LHS) of the inequality in (6.22):

$$LHS = -(\boldsymbol{\omega} - \underline{\boldsymbol{\omega}})^\top D(\overline{\boldsymbol{\omega}} - \boldsymbol{\omega}) - [\boldsymbol{\omega}^\top \ 1] L(\mathbf{u}, D, \overline{\gamma}) \begin{bmatrix} \boldsymbol{\omega} \\ 1 \end{bmatrix}, \tag{6.23}$$

with LMI: $L(\mathbf{u}, D, \overline{\gamma}) =$

$$\begin{bmatrix} -\widetilde{D}_{zd}^\top \mathbf{Q}^\top \mathbf{Q} \widetilde{D}_{zd} + D & -D\frac{\underline{\boldsymbol{\omega}}+\overline{\boldsymbol{\omega}}}{2} - bd \\ * & \underline{\boldsymbol{\omega}}^\top D \overline{\boldsymbol{\omega}} - cd - \mathbf{u}^\top \widetilde{D}_{zu}^\top \mathbf{Q}^\top \mathbf{Q} \widetilde{D}_{zu} \mathbf{u} + \overline{\gamma} \end{bmatrix},$$

$$\begin{aligned} bd &= \widetilde{D}_{zd}^\top \mathbf{Q}^\top \mathbf{Q} \widetilde{C}_z x_0 + \widetilde{D}_{zd}^\top \mathbf{Q}^\top \mathbf{Q} \widetilde{D}_{zu} \mathbf{u} - \widetilde{D}_{zd}^\top \mathbf{Q}^\top \mathbf{Q} \mathbf{z}_{ref} + \widetilde{D}_{zd}^\top \mathbf{P}^\top, \\ cd &= x_0^\top \widetilde{C}_z^\top \mathbf{Q}^\top \mathbf{Q} \widetilde{C}_z x_0 + x_0^\top \widetilde{C}_z^\top \mathbf{Q}^\top \mathbf{Q} \widetilde{D}_{zu} \mathbf{u} + \mathbf{u}^\top \widetilde{D}_{zu}^\top \mathbf{Q}^\top \mathbf{Q} \widetilde{C}_z x_0 \\ &\quad - x_0^\top \widetilde{C}_z^\top \mathbf{Q}^\top \mathbf{Q} \mathbf{z}_{ref} - \mathbf{z}_{ref}^\top \mathbf{Q}^\top \mathbf{Q} \widetilde{C}_z x_0 - \mathbf{u}^\top \widetilde{D}_{zu}^\top \mathbf{Q}^\top \mathbf{Q} \mathbf{z}_{ref} \\ &\quad - \mathbf{z}_{ref}^\top \mathbf{Q}^\top \mathbf{Q} \widetilde{D}_{zu} \mathbf{u} + \mathbf{z}_{ref}^\top \mathbf{Q}^\top \mathbf{Q} \mathbf{z}_{ref} + \mathbf{P}(\widetilde{C}_z x_0 + \widetilde{D}_{zu} \mathbf{u}) + (\widetilde{C}_z x_0 + \widetilde{D}_{zu} \mathbf{u})^\top \mathbf{P}^\top, \end{aligned}$$

where $*$ denotes the symmetry element of the corresponding matrix, D is a positive semi-definite diagonal matrix ($0 \preceq D \in \mathbb{R}^{N_p \times N_p}$), and $\underline{\boldsymbol{\omega}}$ and $\overline{\boldsymbol{\omega}}$ are stacked vectors of the lower boundary $-|f_w(\overline{v_w})|$ and upper boundary $|f_w(\overline{v_w})|$ of the disturbance $w(s)$. In the matrix $L(\mathbf{u}, D, \overline{\gamma})$, $\mathbf{u}$ is the optimal control sequence that is expected to be computed by the RMPC. However, the term $\mathbf{u}^\top \widetilde{D}_{zu}^\top \mathbf{Q}^\top \mathbf{Q} \widetilde{D}_{zu} \mathbf{u}$ is a quadratic nonlinear term, which cannot be applied in LMI optimisation. In order to eliminate the nonlinearity in $L(\mathbf{u}, D, \overline{\gamma})$, Schur Complement is applied and thus, $L(\mathbf{u}, D, \overline{\gamma})$ becomes:

$$L(\mathbf{u}, D, \overline{\gamma}) = \begin{bmatrix} -\widetilde{D}_{zd}^\top \mathbf{Q}^\top \mathbf{Q} \widetilde{D}_{zd} + D & -D\frac{\underline{\boldsymbol{\omega}}+\overline{\boldsymbol{\omega}}}{2} - bd & 0 \\ * & \underline{\boldsymbol{\omega}}^\top D \overline{\boldsymbol{\omega}} - cd + \overline{\gamma} & \mathbf{u}^\top \widetilde{D}_{zu}^\top \mathbf{Q}^\top \\ * & * & I \end{bmatrix}, \tag{6.24}$$

where $I \in \mathbb{R}^{((N_p+1)\times 3)\times((N_p+1)\times 3)}$ is an identity matrix. Since $-(\boldsymbol{\omega} - \underline{\boldsymbol{\omega}})^\top D(\overline{\boldsymbol{\omega}} - \boldsymbol{\omega})$ is negative, (6.22) is satisfied if and only if matrix $L(\mathbf{u}, D, \overline{\gamma})$ is positive semi-definite:

$$L(\mathbf{u}, D, \overline{\gamma}) \succeq 0. \tag{6.25}$$

Moreover, the linear inequality constraints (6.12c) are also stacked and processed by the SDPR method in a similar manner shown above. Let us define stacked vectors of upper and lower boundaries of (6.19) such that $\underline{\mathbf{f}} \leq \mathbf{f} \leq \bar{\mathbf{f}}$. Then, taking the upper boundary as an example:

$$\widetilde{C}_f x_0 + \widetilde{D}_{fu} \mathbf{u} + \widetilde{D}_{fd} \boldsymbol{\omega} \leq \bar{\mathbf{f}}. \tag{6.26}$$

The subtraction between the linear constraint (6.12c) and the upper bound (6.19) are described as follows:

$$e_i^\top \mathbf{f} - e_i^\top \bar{\mathbf{f}} = e_i^\top \widetilde{C}_f x_0 + e_i^\top \widetilde{D}_{fu}\mathbf{u} + e_i^\top \widetilde{D}_{fd}\boldsymbol{\omega} - e_i^\top \bar{\mathbf{f}} \leq 0, \tag{6.27}$$

where e_i is a vector whose ith element equals to 1 and the rest of the elements are assigned to zero, and $i \in \{1, 2, \ldots, N_p+1\}$.

By applying the SDPR method on (6.27), the LMI of linear constraint (6.12c) with respect to the upper bound (6.19) can be found as $L_u(\mathbf{u}, D_{u,i})$ through a subtraction between $\mathbf{f}$ and $\bar{\mathbf{f}}$:

$$e_i^\top \mathbf{f} - e_i^\top \bar{\mathbf{f}} = -(\boldsymbol{\omega} - \underline{\boldsymbol{\omega}})^\top D_{u,i}(\overline{\boldsymbol{\omega}} - \boldsymbol{\omega}) - \begin{bmatrix} \boldsymbol{\omega}^\top & 1 \end{bmatrix} L_u(\mathbf{u}, D_{u,i}) \begin{bmatrix} \boldsymbol{\omega} \\ 1 \end{bmatrix}, \tag{6.28}$$

and

$$L_u(\mathbf{u}, D_{u,i}) = \begin{bmatrix} D_{u,i} & -D_{u,i}\frac{\underline{\boldsymbol{\omega}}+\overline{\boldsymbol{\omega}}}{2} - \frac{\widetilde{D}_{fd}^\top e_i}{2} \\ * & \underline{\boldsymbol{\omega}}^\top D_{u,i}\overline{\boldsymbol{\omega}} - e_i^\top \widetilde{C}_f x_0 - e_i^\top \widetilde{D}_{fu}\mathbf{u} + e_i^\top \bar{\mathbf{f}} \end{bmatrix} \tag{6.29}$$

where $D_{u,i}$ is a positive semi-definite diagonal matrix ($0 \preceq D_{u,i} \in \mathbb{R}^{N_p \times N_p}$). Since $-(\boldsymbol{\omega} - \underline{\boldsymbol{\omega}})^\top D_{u,i}(\overline{\boldsymbol{\omega}} - \boldsymbol{\omega})$ is negative, $e_i^\top \mathbf{f} - e_i^\top \bar{\mathbf{f}} \leq 0$ is satisfied if and only if matrix $L_u(\mathbf{u}, D_{u,i})$ is positive semi-definite:

$$L_u(\mathbf{u}, D_{u,i}) \succeq 0. \tag{6.30}$$

Similarly to the deduction of $L_u(\mathbf{u}, D_{u,i})$, the LMI of (6.12c) with respect to the lower bound can also be determined by a subtraction between $\mathbf{f}$ and $\underline{\mathbf{f}}$:

$$e_i^\top \mathbf{f} - e_i^\top \underline{\mathbf{f}} = -(\boldsymbol{\omega} - \underline{\boldsymbol{\omega}})^\top D_{l,i}(\overline{\boldsymbol{\omega}} - \boldsymbol{\omega}) - \begin{bmatrix} \boldsymbol{\omega}^\top & 1 \end{bmatrix} L_l(\mathbf{u}, D_{l,i}) \begin{bmatrix} \boldsymbol{w} \\ 1 \end{bmatrix}, \tag{6.31}$$

and

$$L_l(\mathbf{u}, D_{l,i}) = \begin{bmatrix} D_{l,i} & -D_{l,i}\frac{\underline{\boldsymbol{\omega}}+\overline{\boldsymbol{\omega}}}{2} - \frac{\widetilde{D}_{fd}^\top e_i}{2} \\ * & \underline{\boldsymbol{\omega}}^\top D_{u,i}\overline{\boldsymbol{\omega}} - e_i^\top \widetilde{C}_f x_0 - e_i^\top \widetilde{D}_{fu}\mathbf{u} + e_i^\top \underline{\mathbf{f}} \end{bmatrix} \tag{6.32}$$

where $D_{l,i}$ is a negative semi-definite diagonal matrix ($0 \succeq D_{l,i} \in \mathbb{R}^{N_p \times N_p}$). Since $-(\boldsymbol{\omega} - \underline{\boldsymbol{\omega}})^\top D_{l,i}(\overline{\boldsymbol{\omega}} - \boldsymbol{\omega})$ is positive, $e_i^\top \mathbf{f} - e_i^\top \underline{\mathbf{f}} \geq 0$ is satisfied if and only if matrix $L_l(\mathbf{u}, D_{l,i})$ is negative semi-definite:

$$L_l(\mathbf{u}, D_{l,i}) \preceq 0 \tag{6.33}$$

To summarise, the LMI-based RMPC problem can be expressed as a convex optimisation subject to the convex path constraint (6.12d) and three LMIs $L(\mathbf{u}, D, \bar{\gamma}) \succeq 0$, $L_u(\mathbf{u}, D_{u,i}) \succeq 0$, $L_l(\mathbf{u}, D_{l,i}) \preceq 0$, as follows:

$$\min_{\mathbf{u}} \ \bar{\gamma} \tag{6.34a}$$

$$\textbf{s.t. } (6.12\text{d}), (6.25), (6.30), (6.33) \tag{6.34b}$$

$$\textbf{given: } x(0) = [\delta E(0), \Delta t(0)]^\top \tag{6.34c}$$

$$0 \preceq D \in \mathbb{R}^{N_p \times N_p}, 0 \preceq D_{u,i} \in \mathbb{R}^{N_p \times N_p}, 0 \succeq D_{l,i} \in \mathbb{R}^{N_p \times N_p}. \tag{6.34d}$$

The main characteristic parameters of the BEV model are summarised in Table. 6.1.

Table 6.1 Main parameters of the BEV model parameters.

description	symbols	values
controlled/reference vehicle mass	m/m_{ref}	1500 kg
tyre rolling resistance coefficient	f_T	0.01
air drag coefficient	f_d	0.36
minimum/maximum velocity	$v_{\min}/v_{\max}$	1/33 m/s
braking response time	T_σ	2 s
maximum time difference	$\Delta t_{\max}$	11 s
minimum/maximum force on wheels	$F_{w,\min}/F_{w,max}$	-4500/4500 N

6.4 Numerical Results

The performance of the proposed LMI-based RMPC on the vehicle following scenario is evaluated in this section. The speed profile of the reference vehicle in the following adopts the extra high stage of the worldwide harmonised light vehicles test cycles (WLTP) to emulate high-way driving, with its average speed set as the cruise speed $\bar{v}$ (see Fig. 6.3).

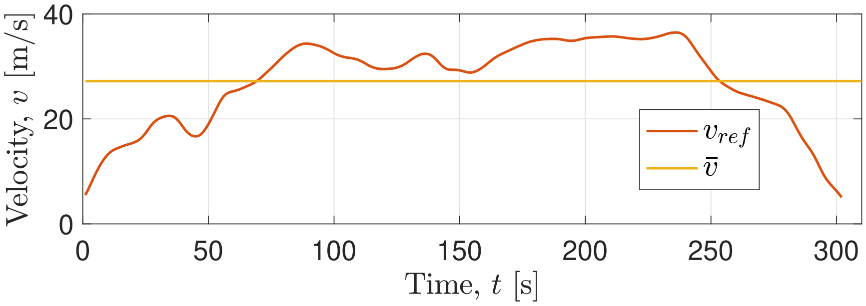

Fig. 6.3 Velocity profile of the reference vehicle (WLTP extra high), v_{ref}, and the constant cruise velocity, $\bar{v}$.

The numerical evaluation of the proposed RMPC method is performed in two steps: 1) a comparison between the RMPC and a nominal MPC method with the same vehicle dynamics model and the cost function under the same initial conditions and disturbance; 2) an investigation on the impact of the horizon length and the amplitude of the disturbance.

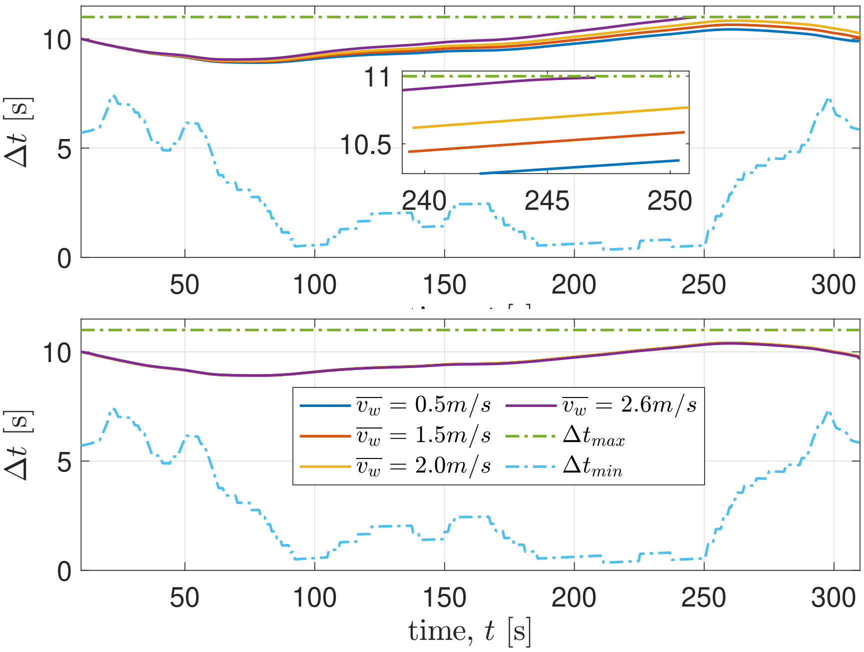

Fig. 6.4 Comparisons of the optimal inter-vehicular time gap Δt between the nominal MPC (top) and RMPC (bottom) with a prediction horizon $N = 5$.

All the convex optimisation problems are solved by the CVX toolkit with MOSEK solver in the Matlab environment on a 1.6 GHz Dual-Core Intel Core i5 processor with 8 GB memory. The sampling interval of the solver is kept the same for all cases at $\Delta s = 40$ m, which strikes a balance between numerical accuracy and computation burden.

The first case considered is with a prediction horizon set to $N = 5$. The optimal inter-vehicular time gap, Δt, solved by the RMPC method is compared in Fig. 6.4, with the solutions of the nominal MPC. As it can be seen, when there is a small disturbance ($\overline{v_w} = 0.5\ m/s$), both nominal and robust controllers can maintain a safe Δt over the entire simulation. As the amplitude of the disturbance increases to $\overline{v_w} = 2.0\ m/s$, the time gap of the nominal MPC is still within the desired safety gap due to some inherent robustness because of the feedback-loop in the MPC framework. However, further increase on the disturbance to $\overline{v_w} = 2.6\ m/s$ eventually makes the nominal MPC infeasible while the RMPC framework is able to counter the impact of the external disturbance. Time gap plots of different disturbances managed by the RMPC are on top of each other, which is shown in the bottom of Fig 6.4. Further simulations (not shown here) demonstrate that the RMPC controller can tolerate disturbances at least as high as $\overline{v_w} = 3.9\ m/s$, thus validating its additional robustness as compared to nominal MPC.

To further investigate the performance of the RMPC, the energy consumption is evaluated with different prediction horizon lengths ($N_p = 3$ to $N_p = 12$) and disturbance limits ($\overline{v_w} =$

0.5 m/s to $\overline{v_w} = 2.5\ m/s$). It can be seen in Fig. 6.5 that when $N_p = 5$ there are significant energy savings for four disturbance limit cases at roughly 40%, as compared to the result with $N_p = 3$. This can be understood that extending the prediction horizon initially enhances the ability to anticipate future behaviour of the reference vehicle, which leads to more optimal solutions. However, when N_p is further increased, the optimality of the RMPC with small disturbance limit $\overline{v_w} = 0.5\ m/s$ has trivial improvement, while the rest of the disturbance cases have worse optimality in terms of energy cost or infeasible solutions (for example, the $\overline{v_w} = 2.5\ m/s$ at $N_p = 10$ is infeasible) due to the decreased accuracy of the reference vehicle velocity prediction and aggregated impact of the external disturbances. Although extending the prediction horizon length could improve the energy savings in some cases, as described just above, the computational burden is also increased, as shown in Table 6.2. As we can see, as compared to the result with $N_p = 3$, the computational time of the optimal solution with $N_p = 5$ is increased by 34% but with a 40% reduction in energy cost (see Fig. 6.5). Further extension of the horizon length can barely improve the energy saving while instead the computational burden is increased up to 202% in the case of $N_p = 12$. Thus, by carefully selecting the prediction horizon length N_p, the energy consumption can be significantly reduced and the computational burden can still be within an acceptable range for potential implementation.

Table 6.2 Average computational time of various RMPC horizon length from $N_p = 3$ to $N_p = 12$, with the same disturbance limit $\overline{v_w} = 0.5\,m/s$.

Prediction horizon length, N_p	3	5	8	10	12
Average computational time [s]	1.02	1.37	1.93	2.45	3.09

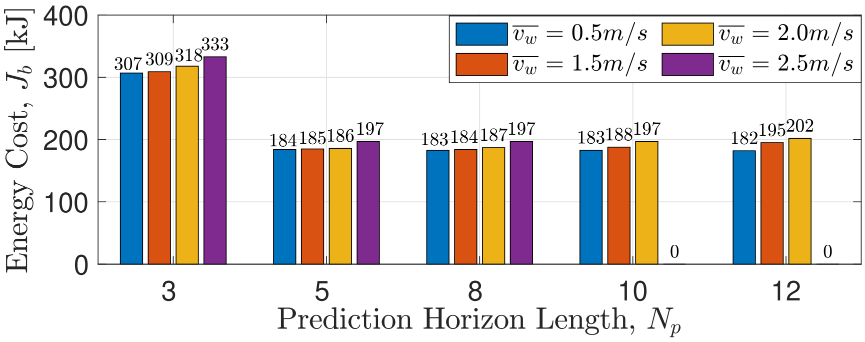

Fig. 6.5 Comparisons of energy consumption solved by the RMPC with different N_p and $\overline{v_w}$.

6.5 Conclusions

This chapter proposes a convex LMI-based RMPC with SDPR method to optimise energy efficiency in a vehicle following problem. Minimisation of controlled vehicle energy consumption as well as of the difference between the controlled vehicle speed and a constant cruise speed in traffic, subject to relevant constraints, are guaranteed under the influence of external disturbances.

Moreover, a comparison between the proposed LMI-based RMPC and a nominal MPC is conducted to demonstrate the robustness of the RMPC in dealing with the impact of external disturbances. A further investigation of different RMPC prediction horizon lengths reveals that the energy consumption can be improved by roughly 40% by carefully selecting the prediction horizon length. Finally, an analysis of the computational time suggests the implementation potential of the proposed RMPC.

Part III

Optimal Control for CAVs at Signal-Free Intersections

Chapter 7

A Centralised Convex Framework for CAVs at Signal-Free Intersections

7.1 Introduction

Cooperative vehicle management emerges as a promising solution to improve road traffic safety and efficiency. This chapter addresses the speed planning problem for a group of electric CAVs at an unsignalised intersection with the consideration of turning manoeuvres. In more detail, the contribution of this chapter is listed as below:

a. The proposed coordination scheme optimises in a hierarchical fashion the crossing order and the corresponding velocity trajectories, involving turning manoeuvres, within the entire intersection area without invoking restrictive assumptions on 1) the crossing order (e.g., FIFO) or 2) the actual or average vehicle speed at any point within the intersection or its centre, which was the case in many existing works, such as [135, 145, 154]. This new and more challenging control paradigm can lead to a further optimised solution.

b. Efficient solutions for the formulated coordinated scheme are proposed by suitably relaxing the nonconvex constraints and reformulating both upper (crossing order optimisation) and lower (velocity trajectory optimisation) level nonconvex OCPs into convex SOCPs using a space-domain modelling approach. A rigorous proof of the equivalence between the convexified and the original non-convex problem is also provided to complete the framework.

c. The optimality of the proposed coordination scheme (with a relaxed SOCP solution) is demonstrated by comparison with a valid lower bounding optimal solution with expanded feasibility. Moreover, the benefit over traditional approaches is investigated by comparison with a benchmark solution that is obtained by following the FIFO policy.

The rest of this chapter is organised as follows. Section 7.2 introduces the modelling framework of an autonomous intersection crossing problem, with consideration of the electric powertrain model of each CAV. The associated OCP for energy cost and travel time minimisation is also formulated in Section 7.2 , while the hierarchical coordination scheme is introduced in Section 7.3 and the SOCP reformulation of the original OCP is performed in Section 7.4. Simulation results and discussion are presented in Section 7.5. Finally, concluding remarks are given in Section 7.6. Note that Sections 7.2- 7.6 are taken from the author's publication [197].

7.1.1 Notation and Preliminary:

Definition 7.1. *A second-order cone program (SOCP) is a convex optimisation problem of the form:*

$$\begin{aligned} &\min_x f^\top x \\ &\textbf{\textit{s.t.}} : ||A_i x + b_i|| \leq c_i^T x + d_i,\, i = 1, \dots, M \end{aligned} \tag{7.1}$$

where $x \in \mathbb{R}^m$ *is the optimisation variable and* f, A_i, b_i, c_i, d_i *are problem parameters.* $||\cdot||$ *is the standard Euclidean norm, i.e.,* $||u|| = (u^\top u)^{1/2}$, *and the associated constraint,*

$$||A_i x + b_i||_2 \leq c_i^T x + d_i\,,$$

is called a second-order cone constraint.

7.2 Problem Statement

7.2.1 Intersection Model

The present work considers a scenario where multiple homogeneous CAVs approach an unsignalised intersection and need to be regulated to ensure safe, smooth and energy efficient flow of traffic. As illustrated in Fig. 7.1, the intersection contains four branches coming from the north, south, east and west. For simplicity, it is assumed that all the roads in the intersection are flat with two lanes per perpendicular road (one lane per branch), while lane changes and road slopes are not considered in the present framework.

The centre of the intersection is the MZ, *Merging Zone*, where vehicles merge from different directions, and therefore, it is the area of potential lateral collisions. The area of the MZ is considered to be a square of sides S. CAVs are allowed to go straight through, or turn left or right in the MZ, while U-turns are not allowed. The intersection has a central traffic

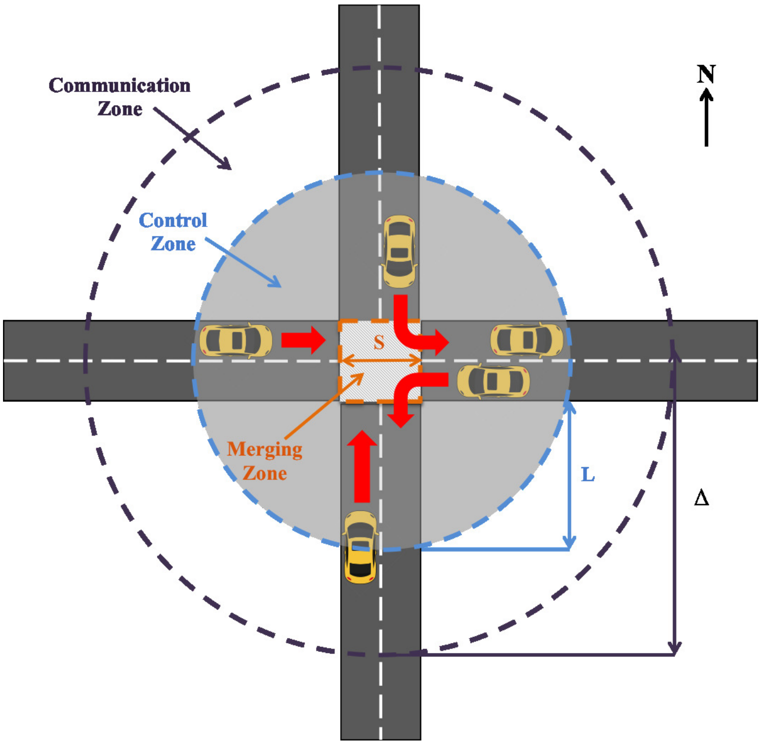

Fig. 7.1 Autonomous intersection with connected and autonomous vehicles.

coordinator, called *Intersection Controller* (IC). Vehicles approaching the intersection will first enter a *Communication Zone* (ComZ), where the IC can communicate with each CAV. The radius of the ComZ, Δ, depends on the communication range capability of modern V2I technology. Moving forward towards the intersection, the CAVs will enter from the ComZ to the more compact CZ, *Control Zone*, inside which the motion of each CAV is fully controlled by the IC. The distance from the entry of the CZ to the entry of the MZ is L, with $\Delta > L > S$ as the sensing range is usually much greater than the physical length of the MZ and the CZ.

At each time, only the vehicles that are running within the annuluses between the boundaries of ComZ and CZ will be considered for trajectory planning by the IC. Let us denote $N \in \mathbb{N}_{>0}$ the total number of CAVs arriving at the ComZ and remain inside the annulus within a fixed time-interval $T \in \mathbb{R}_{>0}$, and $\mathcal{N} = \{1, 2, \ldots, N\} \in \mathbb{Z}^N$ the set to designate the agreed order in which the vehicles will cross the intersection. The determination of the crossing order will be elaborated in Section 7.3 as part of the coordination scheme. Furthermore, all CAVs are considered as identical BEVs. The length of each vehicle equals to l_i, $(l_i < S, i \in \mathcal{N})$. These assumptions are relatively straightforward to relax as long as the vehicle lengths and powertrain models are known to the central coordinator. The control target is to optimise the total electric energy and time consumption of all N CAVs by determining their speed trajectories (in a centralised manner) from the entry of the CZ to the exit point of the CZ, which depends on the turning decision of a CAV made at the MZ. In the subsequent part of this chapter, the decision of the ith CAV at the intersection is denoted by $d_i \in \{-1,0,1\}$, wherein $d_i = 0$ indicates going straight, while $d_i = -1$ and $d_i = 1$ indicate a left turn and a right turn, respectively.

The gross motion of CAVs is modelled by using the single-track, non-holonomic electric vehicle model with details presented in Section 3.2. In this context, the longitudinal dynamics are described by the following differential equation:

$$\frac{d}{dt}v_i(t) = \frac{F_{w,i}(t) - F_{r,i} - F_{d,i}(t)}{m_i},\ i \in \mathcal{N}, \tag{7.2}$$

where $v_i(t)$ is the linear (forward) velocity of the ith CAV, m_i is the vehicle mass, $F_{w,i}(t)$ is the powertrain driving or braking force acting on the wheels, while $F_{r,i} = f_{r,i}m_i g$ and $F_{d,i}(t) = f_{d,i}v_i^2(t)$ are the resistance forces of rolling and air drag, respectively, with $f_{r,i}$ and $f_{d,i}$ the coefficients of rolling and air drag resistance. Moreover, $F_{w,i}(t)$ can be broken down into two separate control inputs, the powertrain driving force $F_{t,i}(t)$ and the mechanical braking force $F_{b,i} \leq 0$, such that

$$F_{w,i}(t) = F_{t,i}(t) + F_{b,i}(t), \tag{7.3}$$

where $F_{t,i}(t)$, $F_{b,i}(t)$, and $F_{w,i}(t)$ are constrained by their physical limitations as defined in (3.14), respectively.

It is considered that the traffic follows the *left-hand driving system* and all vehicles travel along the centreline of their lane. The path of a turning CAV at the intersection can be modelled as a 90° arc with turning radius $R_l = S/4$ for the left turn and $R_r = 3S/4$ for the right turn. As such, the driving distance of CAV i inside the MZ is:

$$\delta(d_i) = \begin{cases} S, & d_i = 0, \\ \frac{1}{8}\pi S, & d_i = -1, \\ \frac{3}{8}\pi S, & d_i = 1. \end{cases} \tag{7.4}$$

Considering that the mission starts when the front of the vehicle enters the CZ and ends when its front reaches the exit of the CZ, the total travel distance of each CAV within the CZ is $2L + \delta(d_i)$.

Instead of formulating the problem in the time domain, which is the common approach used in existing works, this chapter defines the intersection problem in the space domain, which is beneficial for acquiring the vehicle arrival times at any given position inside the CZ. This fact turns out to be very useful in establishing time-dependent constraints and obtaining the travel time of each CAV required to cross the intersection. The latter aspect greatly facilitates the joint optimisation formulation of energy and travel time costs rather than requiring additional steps to tackle the free end-time problem that appears if the problem is formulated in the time domain [135]. The use of the space domain also allows the overall intersection management problem to be formulated as an SOCP, which offers a rapid and unique solution search as compared to nonconvex counterparts, as will be shown later in Section 7.4.

Let s denote the variable of travelled distance. By changing the independent variable t to s via $\frac{d}{ds} = \frac{1}{v_i}\frac{d}{dt}$, the differential equation (7.2) describing the vehicle longitudinal dynamics can be rewritten as:

$$\frac{d}{ds}v_i(s) = \frac{F_{w,i}(s) - F_{r,i} - F_{d,i}(s)}{m_i v_i(s)},\ i \in \mathcal{N}, \tag{7.5}$$

for all $s \in [0, 2L + \delta(d_i)]$. As the model is formulated in the space domain, the individual travel time t_i of each CAV is introduced as a system state, with its dynamics expressed by:

$$\frac{d}{ds}t_i(s) = \frac{1}{v_i(s)},\ i \in \mathcal{N}, \tag{7.6}$$

from which the required travel time of each CAV to traverse the CZ can be expressed as,

$$J_{t,i} = t_i(2L + \delta(d_i)) - t_i(0), \tag{7.7}$$

where $t_i(0)$ is the entry time of CAV i in the CZ. The velocity of each CAV is constrained by:

$$v_{\min} \leq v_i \leq v_{\max,i}(s), \tag{7.8}$$

where $v_{\min}$ is set to a sufficiently small positive constant to avoid singularity issues in (7.6) without sacrificing the generality of the formulation, and $v_{\max,i}(s)$ is set for safety and comfort purposes and depends on the vehicle turning decision and the position at the intersection. More specifically, the upper speed limit $v_{\max,i}(s)$ is defined as a piecewise constant function, which is $v_{\max,i}(s) = v^f_{\max,i}$, $\forall s \in [0, L) \cup (L + \delta(d_i), 2L + \delta(d_i)]$ whereas for $s \in [L, L + \delta(d_i)]$ in the MZ, it follows:

$$v_{\max,i}(s) = \begin{cases} v^f_{\max,i}, & \text{straight travelling,} \\ v^l_{\max,i}, & \text{left turn,} \\ v^r_{\max,i}, & \text{right turn,} \end{cases} \tag{7.9}$$

with $v^l_{\max,i} < v^r_{\max,i} < v^f_{\max,i}$. In this work, speed limits for cornering, $v^l_{\max}$, $v^r_{\max}$, are estimated by utilising the acceleration diamond [67] that represents a constraint for ordinary drivers on longitudinal and lateral accelerations for comfortable driving (away from the limits of tire adherence on the road):

$$\left|\frac{F_{w,i}/m_i}{a_{x,max}}\right| + \left|\frac{v_i\Omega_i}{a_{y,max}}\right| \leq 1\,, \tag{7.10}$$

where Ω_i is the vehicle yaw rate, defined by,

$$\Omega_i = \begin{cases} v_i/R_l, & \text{left turn,} \\ v_i/R_r, & \text{right turn,} \end{cases} \tag{7.11}$$

and the physical limits of the longitudinal and lateral accelerations, $a_{x,max}$ and $a_{y,max}$ respectively, are chosen to be the nominal gravitational acceleration g. Note that $F_{w,i}/m_i$ represents a good approximation of the longitudinal acceleration (by ignoring the subtle influence of resistive forces $F_{r,i}$ and $F_{d,i}$) and $v_i\Omega_i$ corresponds to the lateral acceleration. The acceleration diamond conforming to (7.10) is illustrated in Fig. 7.2. As it can be seen, the longitudinal deceleration/acceleration of each BEV is bounded by $[F_{w,\min}/m_i,\, F_{w,\max}/m_i]$, where $F_{w,\max} = \max\{\frac{g_{r,i}}{r_{w,i}} T_{\max,i}\}$ and $F_{w,\min} = \min\{m_i a_{\min,i}\}$ represent the maximum and minimum available driving force acting on the wheels, respectively. $r_{w,i}$ is the wheel radius and $g_{r,i}$ is the transmission gear ratio. Note that the value of $F_{w,\max}$ is defined on the basis of the motor efficiency map and associated motor torque limits shown in Fig. 3.2, and $F_{w,\min}$ is chosen such that $a_{\min,i} = F_{w,\min}/m_i$ be the peak deceleration for braking, which provides a reasonable margin to the limit of tire adhesion. In order to streamline the modelling framework, under cornering the admissible zone for operation is taken as the rectangular dark grey area shown in Fig. 7.2, which corresponds to the uniformed longitudinal acceleration limits, $[-F_{w,\max}/m_i,\, F_{w,\max}/m_i]$. Operation within this region can be provided entirely by the powertrain driving force $F_{t,i}$, where any amount of braking can be fully regenerated, and which is compatible with the target of eco-driving sought in the present work. Note that under straight running conditions, it is further allowed to operate a CAV in the light gray area below the mentioned dark grey area, however, in that case additional mechanical braking, $F_{b,i}$, would be required. As the feasible dark grey region also defines the maximum permissible lateral acceleration (i.e., $v_i\Omega_i$), which is realised at the four corners of the rectangular dark grey area, the maximum permissible speed for left and right turns, respectively, can consequently be derived from (7.10) and (7.11) as follows:

$$v^l_{\max,i} = \sqrt{\left(1 - \frac{F_{w,\max}/m_i}{a_{x,\max}}\right) a_{y,\max} R_l}\,, \tag{7.12a}$$

$$v^r_{\max,i} = \sqrt{\left(1 - \frac{F_{w,\max}/m_i}{a_{x,\max}}\right) a_{y,\max} R_r}\,. \tag{7.12b}$$

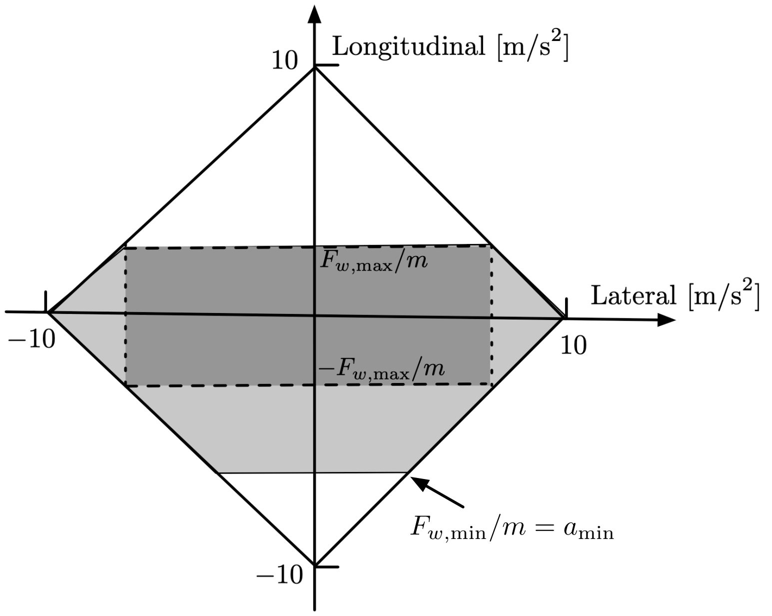

Fig. 7.2 Theoretical driving comfort limits represented by an acceleration diamond [67] (thick solid lines) and the theoretical performance envelope of the BEV (light grey area). For simplicity of implementation, a practical performance region of the BEV (dark grey area) under cornering conditions is assumed to be enveloped by longitudinal acceleration saturated at $\pm F_{w,\max}/m_i$ (horizontal dashed lines) and conservative lateral acceleration limits (vertical dotted lines). $F_{w,\max}$ is calculated based on the BEV motor torque limits (±300 Nm) as given in [173] and $a_{\min,i}$ is given in Table 7.1.

Additional constraints, the collision avoidance constraints, are designed to address further safety challenges of the unsignalised intersection coordination problem. Note that, given an arbitrary CAV $h \in \mathcal{N}$ and $s \in [0,L]$, any CAV $i \in \mathcal{N}$ must belong to one of the following subsets of $\mathcal{N}$: 1) $\mathcal{C}_h$ collects vehicles travelling in the same direction as the ith vehicle; 2) $\mathcal{O}_h$ collects vehicles travelling in the opposite direction to the ith vehicle; 3) $\mathcal{P}_{L,h}$ and $\mathcal{P}_{R,h}$ collect vehicles travelling in the perpendicular directions to the ith vehicle from its left and right hand sides, respectively.

Assuming CAV k is immediately ahead of CAV i with $i \in \mathcal{C}_k$, the following constraint on the time gap, $t_i(s) - t_k(s+l_k)$, is imposed to ensure the absence of rear-end collisions

$$t_i(s) - t_k(s+l_k) > \max\left(\frac{v_i(s) - v_k(s+l_k)}{|a_{\min,i}|}, t_\delta\right) \tag{7.13}$$

where the first term in the max function of the inequality represents the time-to-collision [198], and t_δ is a small time constant to enforce a safety margin invariably.

The rear-end collision avoidance constraint (7.13) is enforced over the entire space horizon $[0, 2L + \delta(d_i)]$ if $d_i = d_k$. However, when $d_i \neq d_k$, (7.13) is needed only for $s \in [0, L]$

whereas for the rest of the mission, $s \in [L, 2L + \delta(d_i)]$, only the following constraint is imposed:

$$t_k(L + \delta(d_k) + l_k) \leq t_i(L),\ i \in \mathcal{C}_k \tag{7.14}$$

which prevents rear-end collisions between CAVs i and k within the MZ as it does not allow them to travel inside the MZ at the same time.

For any CAV $i \notin \mathcal{C}_j, i > j$, it is clear that a collision can only arise after they enter the MZ, for $s \in [L, 2L + \delta(d_i)]$. In order to discuss collision threats (including side and rear-end collisions) in this context, let us further define subsets of $\mathcal{O}_j$, $\mathcal{P}_{L,j}$ and $\mathcal{P}_{R,j}$ in relation to the intention d_i of vehicle i, as follows:

$$\mathcal{O}_j = \mathcal{O}^l_j \cup \mathcal{O}^s_j \cup \mathcal{O}^r_j \tag{7.15}$$

$$\mathcal{P}_{L,j} = \mathcal{P}^l_{L,j} \cup \mathcal{P}^s_{L,j} \cup \mathcal{P}^r_{L,j} \tag{7.16}$$

$$\mathcal{P}_{R,j} = \mathcal{P}^l_{R,j} \cup \mathcal{P}^s_{R,j} \cup \mathcal{P}^r_{R,j} \tag{7.17}$$

where the superscripts l, s, r denote left turn, going straight and right turn of the ith vehicle, respectively. Potential collisions between CAVs i and j may occur if CAV i belongs to:

$$\mathcal{L}_j \triangleq \begin{cases} \mathcal{O}^r_j \cup \mathcal{P}_{L,j} \cup \mathcal{P}^s_{R,j} \cup \mathcal{P}^r_{R,j}, & \text{if } d_i = 0, \\ \mathcal{O}^r_j \cup \mathcal{P}^s_{R,j} \cup \mathcal{P}^r_{R,j}, & \text{if } d_i = -1, \\ \mathcal{O}_j \cup \mathcal{P}_{L,j} \cup \mathcal{P}^s_{R,j} \cup \mathcal{P}^r_{R,j}, & \text{if } d_i = 1, \end{cases} \tag{7.18}$$

which is influenced by the decision d_j of the lead CAV j at the MZ. An illustration of these collision models are given in Fig. 7.3. To prevent such collisions inside the MZ between vehicles j and $i \in \mathcal{L}_j$, the IC simply follows the rule that the ith CAV enters the MZ only after

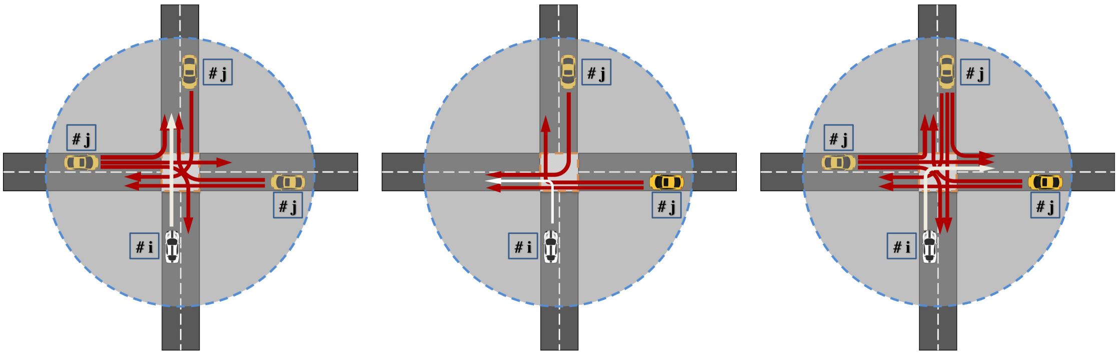

(a) $\mathcal{O}^r_j \cup \mathcal{P}_{L,j} \cup \mathcal{P}^s_{R,j} \cup \mathcal{P}^r_{R,j}$, if $d_i = 0$. (b) $\mathcal{O}^r_j \cup \mathcal{P}^s_{R,j} \cup \mathcal{P}^r_{R,j}$, if $d_i = -1$. (c) $\mathcal{O}_j \cup \mathcal{P}_{L,j} \cup \mathcal{P}^s_{R,j} \cup \mathcal{P}^r_{R,j}$, if $d_i = 1$.

Fig. 7.3 Illustration of potential collisions (7.18) between CAVs i (white vehicle) and j (yellow vehicles) at the MZ with $i > j$.

CAV j has left the MZ, and once again (7.14) is applicable. If vehicle i further belongs to $\mathcal{D}_j$ that is a subset of $\mathcal{L}_j$, defined by:

$$\mathcal{D}_j \triangleq \begin{cases} \mathcal{P}^l_{L,j} \cup \mathcal{P}^r_{R,j}, & \text{if } d_i = 0, \\ \mathcal{O}^r_j \cup \mathcal{P}^s_{R,j}, & \text{if } d_i = -1, \\ \mathcal{O}^l_j \cup \mathcal{P}^s_{L,j}, & \text{if } d_i = 1, \end{cases} \tag{7.19}$$

both CAVs i and j merge into the same lanes after the MZ. As such, the rear-end collision avoidance constraint (7.13) is once again required for $s \in [L + \delta(d_i), 2L + \delta(d_i)]$ so as to avoid potential rear-end collision between these vehicles. Otherwise, when $i \in \mathcal{L}_j \backslash \mathcal{D}_j$, then both vehicles travel towards different directions after leaving the MZ, which excludes the possibility of collisions outside the MZ. The above characterisation of the potential collisions (7.19) after the MZ is a novelty of the present work and extremely important when turns are allowed, as vehicles may travel in the same direction after leaving the MZ, but with a noticeable difference in speed, which could lead to a rear-end collision immediately after the MZ; for example, a left-turning vehicle travelling at low speed followed by a straight driving vehicle travelling at high speed in a perpendicular direction. The treatment of these scenarios has not been addressed in the literature as it is only permitted with the extended control horizon that spans the whole CZ, including the section after the MZ, which is one of the important contributions of this chapter.

Finally, for any CAV $i \notin \mathcal{L}_h \cup \mathcal{C}_h$, there is no interference between CAV h and i inside the MZ. Hence, only the following constraint is required:

$$t_i(L + \delta(d_i)) \geq t_h(L + \delta(d_i)), \; i > h. \tag{7.20}$$

As opposed to the more restrictive constraint (7.14), constraint (7.20) allows multiple CAVs in and to exit the MZ at the same time.

7.2.2 Powertrain System and Energy Consumption Model

In this subsection, the powertrain system and energy consumption models are developed based on the BEV system described in Section 3.2. Hence, the battery energy usage of a single CAV based on the efficiency map of the electric motor as given in [173] with constant torque limits can be found by integrating $P_{b,i}$ in the space domain as follows:

$$J_{b,i} = \int_0^{2L+\delta(d_i)} \frac{P_{b,i}(s)}{v_i(s)} \, ds. \tag{7.21}$$

The following assumptions are imposed to complete the modelling framework described above.

Assumption 7.1. *All the vehicle information (e.g., position, velocity, acceleration) can be measured precisely, and the data can be transferred between each CAV and the IC without errors and delays.*

Assumption 7.2. *After entering the CZ, all CAVs are capable of precisely following the trajectories provided by the IC with no deviations, e.g. due to modeling and measurement errors.*

Assumption 7.3. *The decision of each vehicle on whether a turn is to be made at the MZ and their arrival time and speed at the CZ are known upon its entry at the ComZ.*

Assumption 7.4. *For each CAV i, constraints* (7.8), (7.13) *and* (3.14) *are inactive at* $t_i(0)$.

Assumption 7.5. *All the CAVs leave the CZ at the same terminal speed* $v_f \in [v_{\min}, v_{\max}]$, *such that*

$$v_i(2L+\delta(d_i)) = v_f,\ \forall i \in \mathcal{N} \tag{7.22}$$

Assumption 7.1-7.2 may be not valid for practical vehicular networks. On that occasion, it can be relaxed by using a worst-case analysis as long as the measurement and communication uncertainties are bounded. More conservative safety constraints can be formulated by incorporating the upper bounds on the uncertainties (e.g., measurement noise, communication delay, etc). Assumption 7.3 is essential to implement the centralised optimal control scheme. The feasibility of this assumption can be justified if CAVs are managed to enter the CZ at a predefined speed and time. Relaxation of the assumption can be accomplished by using a model predictive control framework. Assumption 7.4 is needed to ensure that all CAVs arriving at the CZ have feasible initial states and initial control inputs. The Assumption (7.22) is intended to streamline the framework and to allow solutions in different scenarios to be compared. Further relaxation of (7.22) (non-uniform $v_i(2L+\delta(d_i))$) can be made easily, if necessary.

7.2.3 Optimal Control Problem Formulation

The central IC aims to find the crossing order and speed trajectories of all CAVs which minimises a weighted sum of the aggregate battery electric energy, $J_{b,i}$ as defined in (7.21), and travelling time, $J_{t,i}$ as defined in (7.7), subjected to the aforementioned constraints related to vehicle physical limits and safety regulations. For a specific crossing order $\mathcal{N}$, this optimal control problem can be formulated as:

OCP 7.1.

$$\min_{\mathbf{u}} \quad J(\mathbf{x},\mathbf{u}) = \sum_{i=1}^{N} W_1 J_{t,i} + W_2 J_{b,i} \tag{7.23a}$$

$$\textit{s.t.}: \quad \frac{d}{ds}\mathbf{x} = \mathbf{f}(\mathbf{x},\mathbf{u},s) \tag{7.23b}$$

$$\boldsymbol{\psi}(\mathbf{x},\mathbf{u},s) \leq \mathbf{0} \tag{7.23c}$$

$$\boldsymbol{\phi}\left(\mathbf{x}(0),\mathbf{x}(2L+\delta(d_i))\right) = \mathbf{0}, \tag{7.23d}$$

where

$$\begin{aligned} \mathbf{x} &= [v_1, v_2, \ldots, v_N, t_1, t_2, \ldots, t_N]^\top, \\ \mathbf{u} &= [F_{t,1}, F_{t,2}, \ldots, F_{t,N}, F_{b,1}, F_{b,2}, \ldots, F_{b,N}]^\top, \end{aligned} \tag{7.24}$$

represent the system state and control variables, respectively. W_1, W_2 are the weighting factors tuned to balance the trade-off between the two objectives. The state vector $\mathbf{x}$ evolves according to the dynamic system (7.23b) that encompasses (7.5) and (7.6). The inequality constraints (3.14), (7.8), (7.13), (7.14) and (7.20) are taken into account by (7.23c). The boundary conditions (7.23d) specify the initial and terminal conditions of the states, which fulfil the conditions imposed in Assumptions 7.4 and 7.5. To find the global optimum, OCP 7.1 has to be solved for all possible crossing orders. For a scenario with N vehicles, there are potentially $N!$ different orders under which the vehicles can cross the intersection. Therefore, the problem becomes intractable for practical problem sizes.

7.3 The Hierarchical Centralised Coordination Scheme

In this section we present an efficient control-based coordination strategy, which circumvents the complexity issue introduced in Section 7.2.3, and yet it provides close-to-optimal solutions. The control framework is composed of two levels, a crossing order scheduler and a trajectory optimiser, deployed in a hierarchical manner. In particular, the upper-level scheduler determines an optimal crossing order $\mathcal{N}$ whereas the lower-level optimiser solves the optimal trajectories of all CAVs so that collision avoidance is guaranteed for the given order. Each scheme involves solving an individual coordination problem in a centralised fashion. Next, we specify the two steps of our approach.

7.3.1 Crossing Order Scheduler

Considering the single lane road depicted in Fig. 7.1, CAVs approaching the intersection from the same direction will enter and leave the MZ in the same order they arrive at the CZ.

Therefore, the major challenge stems from the collision avoidance and prioritising constraints for CAVs merging from different directions, i.e., (7.14) and (7.20), which depend on the crossing order. To determine an optimal crossing order without invoking an exhaustive search, we define a virtual coordination problem in the form of OCP 7.1:

OCP 7.2.

$$\min_{\mathbf{u}} \quad J(\mathbf{x},\mathbf{u}) \tag{7.25a}$$

$$\textit{s.t.}: \quad (3.14),(7.5),(7.6),(7.8),(7.13)\ \textit{and}\ (7.22) \tag{7.25b}$$

where (7.14) and (7.20) are not imposed.

Solving OCP 7.2 yields a set of optimal (non-conservative) CAV trajectories from which the IC can determine the crossing order for the lower-level coordinator. The main idea is motivated, as see in (7.14) and (7.20), by the fact that vehicles with intersected trajectories within the MZ should follow a crossing order based on their optimised entry times at the MZ. Otherwise, for those vehicles with no intersection between their trajectories in the MZ, their orders are determined by their MZ exit times. As such, the implementation steps after solving OCP 7.2 are performed as follows.

Step 1: Sort CAVs based on their optimised entry times at the MZ, and let $\mathcal{N}_i$ denote the resulting order and denote with $(\mathcal{N}_i)^k$ the k-th element in the order.

Step 2: Label successive CAVs, i.e. $(\mathcal{N}_i)^k$ and $(\mathcal{N}_i)^{k+1}, \forall k = 0,\cdots,N-1$, with “with collision potentials” or “no collision potentials”, depending on their entry positions and intentions.

Step 3: Sort CAVs based on their MZ exit times, and let $\mathcal{N}_o$ denote the resulting order.

Step 4: Swap the orders of $(\mathcal{N}_i)^k$ and $(\mathcal{N}_i)^{k+1}, \forall k=0,\cdots,N-1$ in $\mathcal{N}_i$, if they have reversed orders in $\mathcal{N}_o$ ($(\mathcal{N}_i)^{k+1}$ leaves the MZ ahead of $(\mathcal{N}_i)^k$) and they are labelled “no collision potentials”.

Step 5: By repeating Step 4 for all successive CAV pairs in $\mathcal{N}_i$ with regard to $\mathcal{N}_o$, the crossing order $\mathcal{N}$ is obtained.

7.3.2 Trajectory Optimiser

Given the intersection crossing order obtained from OCP 7.2, the trajectory of each CAV can be optimised by solving OCP 7.1 but with (7.14), (7.20) enforced based on the new agreed order $\mathcal{N}$.

OCP 7.3.

$$\min_{\mathbf{u}} \quad J(\mathbf{x},\mathbf{u}) \tag{7.26a}$$

$$\textit{s.t.}: \quad (3.14),(7.5),(7.6),(7.8),(7.13),(7.14),(7.20)\ \textit{and}\ (7.22) \tag{7.26b}$$

It is noteworthy that OCP 7.2 and OCP 7.3 are difficult to tackle due to the presence of the nonconvex electric energy consumption model (7.21), and the nonlinear vehicle longitudinal model (7.5) and (7.6). In this regard, the convex reformulation of OCP 7.2 and OCP 7.3 is discussed in the next Section.

Remark 7.1. *Given a crossing order obtained in the upper-level, there might be a case where no feasible solution can be found in the lower-level due to the discrepancy between the upper and lower optimisation problems. This can be addressed by recursively solving the lower-level problem with continuously reducing* $v_{\min}$*, which then terminates when a valid feasible solution is found.*

7.4 Convex Problem Formulation and Benchmark Solutions

In this Section, a convex approximation that yields a feasible upper-bound solution of (7.23) is introduced, and then a lower-bound solution and a conventional baseline solution (obtained from the simple lossless model in the literature) are also defined for benchmarking purposes. As the differences of OCP 7.2 and OCP 7.3 only consist in two linear constraints (7.14), (7.20) that are independent of the convexification, we will use OCP 7.2 as a representative example for the analysis; the same analysis also applies for OCP 7.3.

7.4.1 Proposed solution (SOCP-UB)

The SOCP formulation of OCP 7.2 is carried out in three steps: 1) reformulation of the objective function, 2) state transformation to linearise the longitudinal dynamics of each CAV, and 3) reformulation of the nonconvex state constants resulting from 2). Certain approximations are applied in 1)-3) under the condition that the approximated problem is feasible to the original problem.

a) Step 1 After the substitution in (7.21), the electric power defined in (3.15) becomes a nonconvex model for battery energy usage due to the presence of $F_{t,i}^2(s)/v_i(s)$. This chapter proposes an immediate solution to convexify the resulting battery energy model by replacing the power model (3.15) with:

$$\overline{P}_{b,i} = \overline{b}_2 F_{t,i}^2 v_i + \overline{b}_1 F_{t,i} v_i + \overline{b}_0 v_i, \tag{7.27}$$

that can be made to fit tangentially from above (as shown in the top plot in Fig. 7.4) the results

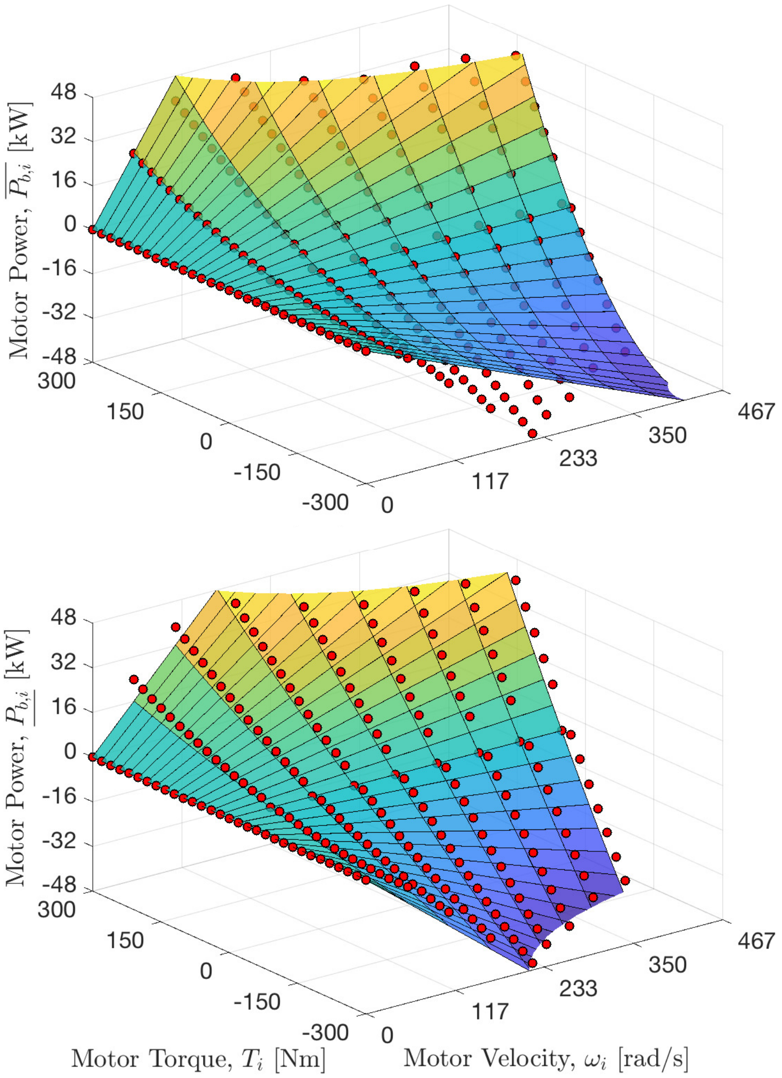

Fig. 7.4 Nonlinear regression of the motor power data (red dots, calculated based on the efficiency map as given in [173] using (3.15)) by using upper (Top) and lower tangential fitting (Bottom) for SOCP-UB and SOCP-LB, respectively. The R-square fit for upper case is 94.33% and 95.13% for the lower case, respectively.

of the battery power according to (3.15) calculated based on the efficiency map as given in [173]. The fitting parameters $\overline{b}_2$, $\overline{b}_1$, $\overline{b}_0$ are obtained by solving the following constrained optimisation problem:

$$\min_{\overline{b}_2\overline{b}_1\overline{b}_0} \left\|\overline{P}_{b,i}(v_i,F_{t,i}) - P_{b,i}(v_i,F_{t,i})\right\|_2 \tag{7.28a}$$

$$\textbf{s.t.:} \quad \overline{P}_{b,i}(v_i,F_{t,i}) - P_{b,i}(v_i,F_{t,i}) \geq 0\,. \tag{7.28b}$$

which ensures $\overline{P}_{b,i}(v_i,F_{t,i})$ is an upper bound to the optimal power of the original problem OCP 7.2. By substituting (7.27) into (7.21), the battery energy usage integral of a single CAV for the SOCP-UB problem can be rewritten in a convex quadratic form:

$$\overline{J}_{b,i} = \int_0^{2L+\delta(d_i)} \overline{b}_2 F_{t,i}(s)^2 + \overline{b}_1 F_{t,i}(s) + \overline{b}_0\, ds. \tag{7.29}$$

Assumption 7.6. *The regression model* (7.29) *can find an accurate fitting of* $\overline{P}_{b,i}$ *by* $\overline{b}_1$ *and* $\overline{b}_2$ *that comply with the condition*

$$\overline{b}_1 + 2\overline{b}_2 F_{w,\min} > 0, \forall i \in \mathcal{N}, \tag{7.30}$$

Assumption 7.7. *The friction brake* $F_{b,i}$ *is inactive, such that* $F_{b,i}(s) = 0, \forall i \in \mathcal{N}, \forall s \in [0, 2L + \delta(d_i)]$.

Assumption 7.6 implies that $\overline{b}_1$ has sufficiently large positive value compared to $\overline{b}_2$. This is consistent with the magnitude of the terms of the fitting model (7.29) based on their physical interpretation, where the fitting term involving $\overline{b}_1$ is found to be the dominant one when the model (7.29) is fitted to data. Assumption 7.7 holds in most cases by the fact that regenerative braking is naturally maximised in order to promote eco-driving, which targets minimum energy usage. The case when the assumption does not hold is analysed in Remark 7.2 later in this section. Under Assumption 7.7, energy cost $\overline{J}_{b,i}$ in (7.29) is equivalent to

$$\overline{J}_{w,i} = \int_0^{2L+\delta(d_i)} \left(\overline{b}_2 F_{w,i}^2(s) + \overline{b}_1 F_{w,i}(s) + \overline{b}_0\right) ds. \tag{7.31}$$

b) Step 2 To linearise the nonlinear dynamics (7.5) and (7.6), a change of variable is performed, $v_i \to E_i$, where $E_i(s)$ is the kinetic energy of CAV i defined by $E_i(s) = \frac{1}{2} m_i v_i^2(s)$. As such, (7.5) and (7.6) can be rewritten as:

$$\frac{d}{ds} E_i(s) = F_{t,i}(s) + F_{b,i}(s) - F_{r,i} - 2\frac{f_d}{m_i} E_i(s)\,, \tag{7.32a}$$

$$\frac{d}{ds} t_i(s) = \frac{1}{\sqrt{2E_i(s)/m_i}}, \quad i \in \mathcal{N}, \tag{7.32b}$$

where (7.32a) becomes linear with respect to the transformed state $E_i(s)$ whereas the dynamics of $t_i(s)$ remain nonlinear. Due to the convexity of (7.32b), it is reasonable to relax the dynamic equation of $t_i(s)$ into a linear differential equation along with a convex inequality constraint and a penalised cost function of (7.23a), described as follows:

$$\frac{d}{ds}t_i(s) = \zeta_i(s), \tag{7.33a}$$

$$\zeta_i(s) \geq \frac{1}{\sqrt{2E_i(s)/m_i}}, \tag{7.33b}$$

$$\min_{\mathbf{u},\boldsymbol{\zeta}} \; J(\mathbf{x},\mathbf{u},\boldsymbol{\zeta}) = \sum_{i=1}^{N} W_1\tilde{J}_{t,i} + W_2\bar{J}_{b,i} \tag{7.33c}$$

where $\boldsymbol{\zeta} = [\zeta_1, \zeta_2, \dots, \zeta_N]^\top$ is a vector of auxiliary control variables $\zeta_i(s)$, and $\tilde{J}_{t,i}$ is the travel time estimated by ζ_i:

$$\tilde{J}_{t,i} = \int_0^{2L+\delta(d_i)} \zeta_i(s)ds. \tag{7.34}$$

With $\tilde{J}_{t,i}$ minimised, the control variable $\zeta_i(s)$ intends to find its minimum boundaries as solutions (i.e. $\zeta_i(s) = 1/\sqrt{2E_i(s)/m_i}$), which can be proved through Proposition 7.1 (as presented later in this section) based on the Assumptions 7.6-7.7.

c) Step 3 To deal with the square root in the non-quadratic constraint (7.33b), both sides of the constraint are squared yielding,

$$\zeta_i(s)^2 E_i(s) \geq m_i/2 \tag{7.35}$$

which is equivalent to [199]:

$$E_i(s) \geq \rho_{1,i}^2(s) \tag{7.36a}$$

$$\zeta_i(s) \geq \rho_{2,i}(s) \tag{7.36b}$$

$$\rho_{1,i}(s)\rho_{2,i}(s) \geq \sqrt{(m_i/2)} \tag{7.36c}$$

$$\rho_{1,i}(s) \geq 0, \quad \rho_{2,i}(s) \geq 0 \tag{7.36d}$$

with $\rho_{1,i}(s)$ and $\rho_{2,i}(s)$ auxiliary control variables. The kinetic energies E_i are bounded due to the boundedness of the permissible speed limits (7.8):

$$E_{\min,i} \leq E_i(s) \leq E_{\max,i}, \; i \in \mathcal{N}, \tag{7.37}$$

where $E_{\min,i} = \frac{1}{2}m_i v_{\min}^2$ and $E_{\max,i} = \frac{1}{2}m_i v_{\max,i}(s)^2$ are respectively determined by the velocity limits $v_{\min}$ and $v_{\max,i}(s)$.

d) Step 4 After replacing $v_i(s)$ with $E_i(s)$, the rear-end collision avoidance constraint (7.13) becomes:

$$t_i(s) - t_k(s+l_k) > \max\left(\frac{\sqrt{2E_i(s)/m_i}}{|a_{\min,i}|} - \frac{\sqrt{2E_k(s+l_k)/m_k}}{|a_{\min,i}|}, t_\delta\right), \tag{7.38}$$

which is equivalent to

$$t_i(s)-t_k(s+l_k) > t_\sigma \tag{7.39a}$$

$$t_i(s)-t_k(s+l_k) > \frac{\sqrt{2E_i(s)/m_i}}{|a_{\min}|} - \frac{\sqrt{2E_k(s+l_k)/m_k}}{|a_{\min}|} \tag{7.39b}$$

As it can be noticed, (7.39b) yields a noncovex feasible set. An immediate and effective solution to convexify the feasible region is to linearise the nonlinearity induced by the term $\sqrt{2E_i(s)/m_i}$ (see Fig. 7.5). Let us consider $f(E_i(s))$ a linear approximation of the velocity $v_i(s) = \sqrt{2E_i(s)/m_i}$, such that,

$$f(E_i(s)) = a_0 + a_1 E_i(s) \quad \forall E_i(s) \in [E_{\min,i}, E_{\max,i}], \tag{7.40}$$

where a_0 and a_1 are obtained through a constrained least-squares optimisation for $E_i \in [E_{\min,i}, E_{\max,i}]$:

$$\min_{a_0,a_1} \left\| f(E_i) - \sqrt{2E_i/m_i} \right\|_2 \tag{7.41a}$$

$$\textbf{s.t.:} \quad f(E_i) - \sqrt{2E_i/m_i} \geq 0\,. \tag{7.41b}$$

which is formed to maximise feasibility while preserving convexity. The problem (7.41) is a simple linear regression problem that can be solved effortlessly. It is noteworthy that there exists a unique solution $f^*(E_i(s)) = a_0^* + a_1^* E_i(s)$ that is tangential to $\sqrt{2E_i(s)/m_i}$. As such, the feasibility is confined to a convex set with the boundary $f^*(E_i(s))$ rather than $\sqrt{2E_i(s)/m_i}$, as shown in Fig. 7.5.

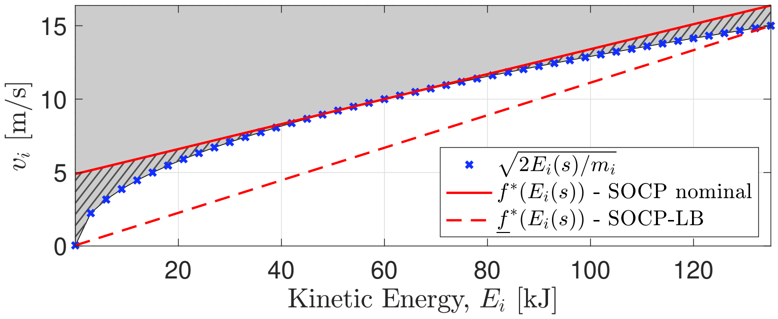

Fig. 7.5 The solid line shows the linearly approximated relationship between kinetic energy and velocity. The grey region denotes the feasible set and the shaded grey areas indicate the sacrificed feasibility due to the artificial conservativeness. The dashed line shows a nonconservative envelope approximation, which allows to generate a lower bound solution for benchmarking purposes.

Considering the linearisation performed by (7.41), the constraint (7.39b) can be converted to a convex inequality, as follows:

$$t_i(s) - t_k(s+l_k) > \frac{a_0^* + a_1^* E_i(s) - \sqrt{2E_k(s+l_k)/m_k}}{|a_{\min,i}|} \tag{7.42}$$

which is a relaxed and conservative (see the shaded grey areas in Fig. 7.5) constraint with a larger tolerance on the car-following safety distance, particularly during the low and high speed ranges. Note that the nonlinear term of E_k is retained as the linearisation of E_i is sufficient to ensure the convexity of the problem. As such, it avoids extra conservativeness that would be introduced if it was also approximated. To preserve more feasibility, one may use a successive convexification algorithm, which is more computationally demanding due to a recursive project-and-linearise procedure [200]. Despite using a simple linearisation, the proposed algorithm is shown to yield close-to-optimal results as will be verified by a non-conservative lower bounding solution defined in Section 7.4.2.

Next, it is shown that the non-quadratic constraint (7.42) can be reformulated in a quadratic form. By rearranging (7.42), it holds that:

$$\gamma_k(s) > -\frac{\sqrt{2E_k(s+l_k)/m_k}}{|a_{\min,i}|}, \tag{7.43}$$

where

$$\gamma_k(s) = t_i(s) - t_k(s+l_k) - \frac{a_0^* + a_1^* E_i(s)}{|a_{\min,i}|} \tag{7.44}$$

is a linear combination of state variables. If $\gamma_k(s) \geq 0$ (which indicates the time gap between two consecutive vehicles is sufficiently large for the following vehicle i to fully stop without collision), the inequality (7.43) holds naturally as $-\sqrt{2E_k(s+l)/m_k}/|a_{\min,i}|$ is always negative. On the other hand, if $\gamma_k(s) < 0$, it yields,

$$\frac{\sqrt{2E_k(s+l_k)/m_k}}{|a_{\min,i}|} > -\gamma_k(s)(>0),$$

which, by squaring both sides, is equivalent to,

$$\frac{2E_k(s+l_k)/m_k}{a_{\min,i}^2} > \gamma_k(s)^2.$$

After rearrangement, it yields:

$$2E_k(s+l) > m a_{\min,i}^2 \gamma_k(s)^2, \tag{7.45}$$

which is the quadratic counterpart of (7.42).

Thus, OCP 7.2 can be transformed into the following optimisation problem:

OCP 7.4.

$$\min_{\tilde{\mathbf{u}}} \tilde{J} = \sum_{i=1}^{N} W_1 \tilde{J}_{t,i} + W_2 \bar{J}_{w,i} \tag{7.46a}$$

$$\textbf{\textit{s.t.:}} \quad \frac{d}{ds}\mathbf{x}(s) = f(\mathbf{x}, \tilde{\mathbf{u}}, s)\,, \tag{7.46b}$$

$$\boldsymbol{\psi}(\mathbf{x}(s), \tilde{\mathbf{u}}(s)) \leq 0\,, \tag{7.46c}$$

$$\boldsymbol{\phi}(\mathbf{x}(0), \mathbf{x}(2L + \delta(d_i))) = 0\,, \tag{7.46d}$$

where $\tilde{\mathbf{u}} \triangleq [\mathbf{u}, \boldsymbol{\zeta}, \boldsymbol{\rho}]^\top$, $\boldsymbol{\rho} \triangleq [\rho_{1,1}, \dots, \rho_{1,N}, \rho_{2,1}, \dots, \rho_{2,N}]^\top$, and$\tilde{J}$ is expressed in quadratic form with $\tilde{J}_{w,i}$ and $\tilde{J}_{t,i}$ defined in (7.31) and (7.34), respectively. The dynamic constraints (7.46b) are formed by (7.32a) and (7.33a). The inequality constraints (7.46c) include the state constraints (7.37), (7.39a), (7.45) (whereas the reformulated OCP 7.3 also involves the two linear constraints (7.14), (7.20)) and the control limits (3.14), (7.36). Finally, the problem is completed by the boundary condition:

$$E_i(2L + \delta(d_i)) = \frac{1}{2} m_i v_f^2, \ \forall i \in \mathcal{N}$$

that is inferred from (7.22). Since the objective function and constraints are quadratic, this problem can be immediately turned into an SOCP [199].

Proposition 7.1. *Under Assumption 7.6 and Assumption 7.7, if there exist a feaible solution of OCP 7.4, the globally optimal solution of OCP 7.4 always finds the equality condition of* (7.33b)*, and therefore the solution of the relaxed convex OCP 7.4 is valid.*

Proof. See in Appendix II-A.

Note that Proposition 7.1 only valid if feasible solutions exist. To ensure the existence of the feasible solutions, let us introduce the following Lemma 7.1.

Lemma 7.1. *There always exists a sufficiently small constant $\sigma \geq 0$ and let $v_{\min} = \sigma$, then a feasible solution can be found.*

Proof. See in Appendix II-B.

From Lemma 7.1, by solving the convex optimisation problem with continually reduced lower bound of the speed limit to $v_{min} = \sigma$, there always exists a σ and a corresponding feasible solution with $E_i^*(s) = \frac{1}{2} m \sigma^2$ that allows any vehicle i, which has a potential collision with vehicle $h < i$, to operate at an almost static condition such that collision avoidance constraints can be satisfied, and therefore the equality condition of (7.33b) hold.

Remark 7.2 (Active friction brakes)**.** *Solving OCP 7.4 may yield a solution trajectory where $F_{w,i}(s) < \frac{g_r}{r_w} T_{\min,i}(s)$ for some s (regenerated braking power is saturated). In this circumstance, friction brake is invoked to meet the total force demand at the wheels, $F_{w,i}(s) = \frac{g_r}{r_w} T_{\min,i}(s) + F_{b,i}(s)$. As such, the equivalence between* (7.29) *and* (7.31) *is no longer guaranteed due to the discrepancy between the energy costs in both objective functions (regeneration of friction brakes is assumed in* (7.31)*), and therefore, the optimality of OCP 7.4 may be compromised in such a case. Nevertheless, the equality of* (7.33b) *holds invariably (as inferred from the proof in Appendix II-A), which, in turn, ensures the feasibility of the convex optimization solution.*

7.4.2 Benchmark solutions

To provide an indication of and therefore evaluate how far a solution is from the true optimal, it is important to develop a lower bounding formulation of OCP (7.23). In addition, a baseline solution with the FIFO policy is also solved for further comparison.

a) Lower bounding SOCP (SOCP-LB) Note that the solution of OCP 7.2 yields a lower bound on the objective function value compared to the global optimum of OCP 7.1. It is proper to consider SOCP-LB as the solution of OCP 7.2. To preserve its non-conservativeness, convexification of OCP 7.2 in such a case requires tight approximations from below of the root term $\sqrt{2E_i(s)/m_i}$ in (7.38) and of the battery power relationship in (3.15). An immediate solution for the former approximations to connect the two end points $\sqrt{2E_{\min,i}/m_i}$ and $\sqrt{2E_{\max,i}/m_i}$ of the trajectory of $\sqrt{2E_i(s)/m_i}, \forall E_i \in [E_{\min,i}, E_{\max,i}]$, yielding a straight line $\underline{f}^*(E_i(s))$ as shown in Fig 7.5. In this context, the problem is solved over the entire feasible set plus a small portion of infeasible set whereby the solution (possibly infeasible) guarantees the same or smaller objective function values compared to the true optimal of OCP (7.23).

For the latter approximation, a lower tangential fitting to the battery power is performed (see Fig. 7.4) to obtain:

$$\underline{P}_{b,i} = \underline{b}_2 F_{t,i}(s)^2 v_i + \underline{b}_1 F_{t,i} v_i + \underline{b}_0 v_i,$$

where $\underline{b}_2$, $\underline{b}_1$, $\underline{b}_0$ can be obtained analogously to (7.28).

Following the same steps in the SOCP-UB introduced in Section 7.4.1, it is straightforward to formulate SOCP-LB simply by replacing a_0^* and a_1^* in (7.42) with the coefficients of the straight line $\underline{f}^*(E_i(s))$, and by substituting $\overline{P}_{b,i}(s)$ in (7.31) with $\underline{P}_{b,i}(s)$, as follows:

$$\underline{J}_{w,i} = \int_0^{2L+\delta(d_i)} \underline{b}_2 F_{w,i}(s)^2(s) + \underline{b}_1 F_{w,i}(s) + \underline{b}_0(s)\, ds. \tag{7.47}$$

b) Baseline solution (SOCP-Baseline) The baseline solution consist in solving OCP 7.3 by following the SOCP framework proposed in Section 7.4.1 with the constraints (7.14) and (7.20) set in line with the FIFO protocol, as with the approaches widely used in the literature [151, 135]

7.4.3 Energy Consumption Evaluation

For a fair comparison between different methodologies, the battery energy consumption for all methods is evaluated using the nominal motor efficiency map as given in [173]. For a single CAV i, it follows $E^*_{\text{Bat},i} = \int_0^{2L+\delta(d_i)} F^*_{\text{Bat},i}(s)\,ds$, where

$$F^*_{\text{Bat},i}(s) = \begin{cases} \dfrac{F^*_{t,i}(s)}{\eta_m(F^*_{t,i}(s), E^*_i(s))}, & \forall F_{t,i}(s) \geq 0, \\ (F^*_{t,i}(s) - F^*_{b,i}(s))\eta_m(F^*_{t,i}(s), E^*_i(s)), & \forall F_{t,i}(s) < 0. \end{cases} \tag{7.48}$$

$E^*_{\text{Bat},i}(s)$ is the actual battery energy consumption obtained by following the optimal control actions $F^*_{t,i}(s)$, $F^*_{b,i}(s)$ and the corresponding optimal state $E^*_i(s)$ solved in each case, and $\eta_m(F^*_{t,i}(s), v^*_i(s))$ is the powertrain efficiency (a look-up table) as given in [173].

7.5 Numerical Results

The evaluation of the proposed method is fourfold: 1) the SOCP-UB (7.46) is solved for different weighting combinations $\{W_1, W_2\}$ of (7.46a) under a series of different arrival rates to show the trade-off between energy cost and travel time as well as the impact of the traffic density on the overall optimality; 2) the relationship between the safety margin between the vehicles and energy consumption is examined by solving SOCP-UB for different arrival rates subject to a fixed average travel time; 3) the tightness of the relaxation bounds involved in SOCP-UB is investigated by benchmarking SOCP-UB against SOCP-LB; 4) the performance of the SOCP-UB is compared to the SOCP-Baseline to show the benefit of the proposed coordination scheme over the FIFO policy in terms of optimality.

For the sake of simplicity, the simulation in this work assumes all CAVs to be identical, with the main characteristic parameters of each vehicle model summarised in Table 7.1.

Table 7.1 Main parameters of the BEV model.

description	symbol	value
vehicle mass	m_i	1200 kg
vehicle body length	l_i	4 m
wheel radius	$r_{w,i}$	0.3 m
transmission gear ratio	$g_{r,i}$	3.5
rolling resistance coefficient	$f_{r,i}$	0.01
air drag resistance coefficient	$f_{d,i}$	0.47
minimum velocity	$v_{\min}$	0.1 m/s
maximum forward velocity	$v^f_{\max,i}$	15 m/s
vehicle maximum deceleration	$a_{\min,i}$	−6.5 m/s^2

In the following case studies, we consider an intersection following the layout in Fig. 7.1, with $L = 150$ m and $S = 10$ m. Given the size of the MZ, the turning radii can be calculated as $R_l = 2.50$ m and $R_r = 7.50$ m, and from (7.12), $v^l_{\max,i}$ and $v^r_{\max,i}$ are determined as $v^l_{\max,i} = 4.16$ m/s and $v^r_{\max,i} = 7.19$ m/s. $v_{\min} = 0.1$ m/s and $v^f_{\max,i} = 15$ m/s are also applied. All the vehicles are assumed to leave the intersection at the same terminal speed $v_f = 10\,\text{m/s}$. In (7.13), the time safety margin is set to $t_\delta = \Delta s / v_{\max,i} = 0.13\,\text{s}$ with $\Delta s = 2\,\text{m}$ the sampling space, to accommodate the rapid velocity changes within a sampling space interval. Without loss of generality, the control problem is initialised with randomised initial conditions $v_i(0)$ and $t_i(0)$ for all CAVs subject to the constraints imposed in Assumptions 7.4. In particular, CAVs' initial speeds follow a uniform distribution within $[v_{\min}, v_{\max}]$, while their arrival times, $t_i(0)$, follow a Poisson distribution. Moreover, the entry direction and turning decision, d_i of each CAV are also randomly generated. The SOCP is solved using the convex solver CVX with MOSEK [201] in Matlab on a personal computer with Intel Core i5 2.9 GHz and 8 GB of RAM. Table. 7.2 shows that the average running time for 20 vehicles is less than 3 s, and it is less than 8 s when the vehicle number is increased to 60. To present a general traffic flow scenario, the vehicle number in the following cases is set to $N = 60$.

Table 7.2 Average, minimum & maximum computation time of 100 simulation trials with randomised initial conditions for the proposed hierarchical centralised coordination scheme.

Vehicle number, N	20	60
Average Computational time [s]	2.71	7.52
Minimum Computational time [s]	2.59	7.30
Maximum Computational time [s]	2.86	7.89

In the first instance, the SOCP-UB is solved at an arrival rate of 750 veh/h (vehicles per hour) per lane, which is ordinary for practical intersections. The weighting factors are set to emphasise more on the travel time term in the objective function. For illustration purposes, the travelled distance and velocity profiles of only the first 20 CAVs are shown as the rest of the vehicle exhibit similar patterns of distance and speed profiles. Fig. 7.6 shows the traveled distance profiles. As can be observed, the cooperatively assigned crossing order $\mathcal{N}$ is distinct from the arriving order at the CZ owing to the upper-level scheduling mechanism. Given order $\mathcal{N}$ defined in the upper-level, the lower-level controller schedules the CAVs such that no CAV violates the rear-end and lateral collision constraints, which verifies the validity of the optimal solution. More specifically, if two vehicles have a potential collision inside the MZ, the following one will not be allowed to enter the MZ until the vehicle ahead has left (see (7.14)), such as vehicles #19 and #20, where the number with # denotes the vehicle order in $\mathcal{N}$. Conversely, if the paths of two or more vehicles do not intersect, they are allowed to travel inside the MZ at the same time, such as vehicles #4 and #5. Moreover, the effectiveness

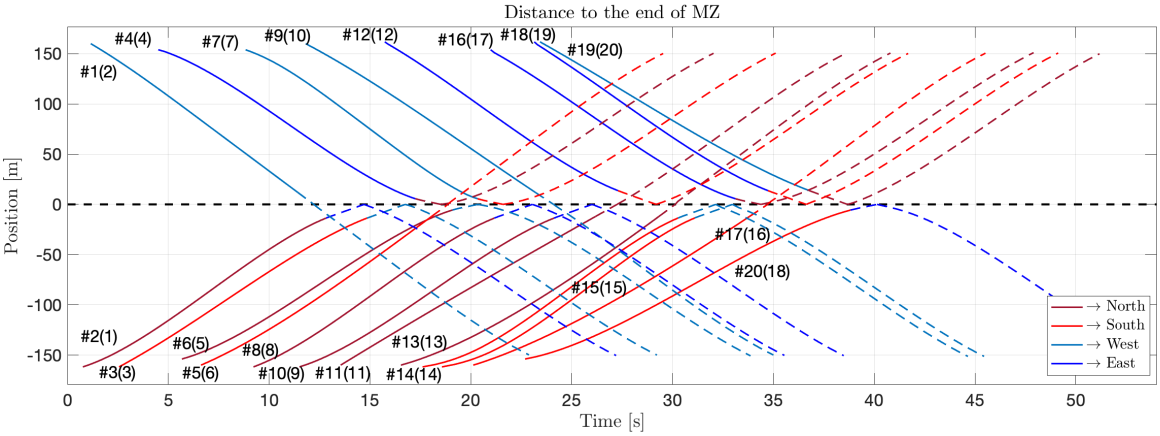

Fig. 7.6 Travelled distance trajectories of the first 20 CAVs among 60 CAVs by solving the SOCP-UB with $N=60$ CAVs at an arrival rate of 750 veh/h per lane. The dashed black line represents the end of the MZ. The dash-coloured trajectories correspond to trajectories of all CAVs passing the entry of the MZ. The four vehicle heading directions are denoted with different colours. The numbers with # denote the crossing order $\mathcal{N}$ and the numbers in the brackets are the arriving order at the CZ. The upper-level scheduler sorts the vehicles in order of $\mathcal{N}=\{2,1,3,4,6,5,7,8,10,9,11,12,13,14,15,17,16,19,20,18\}$.

of rear-end collision avoidance can be identified as the solution has no intersections between trajectories of the same colour throughout the CZ.

The optimal speed trajectories of the first 20 vehicles are shown in Fig. 7.7, where the profiles are grouped based on the entering direction at the CZ. As it can be seen, the speed trajectory of a CAV highly depends on its decision d_i at the intersection, which can be inferred by the change of colour between the solid and dashed parts of the lines depicting the speed profiles. If $d_i=0$, the path of the vehicle within the CZ is a straight line, and in this context, the CAV accelerates to a cruising speed value and stays at this speed until the exit of the CZ approaches. On the other hand, if a turn is made at the intersection, that is $d_i=\{-1,1\}$, the optimal speed profiles involve two separate phases, joined by a short period of cruising at the speed limits for cornering inside the MZ (e.g., vehicles #1 and #2). In some cases, the speed may not follow the foregoing trajectories due to the compromise on safety requirements. For example, vehicle #17 exhibits relatively lower acceleration at the beginning compared to others, and vehicle #11 decelerates its speed until it enters the MZ. Vehicle #7 applies additional braking before entering the MZ in order to leave enough space margin to allow the vehicle ahead, #6, to complete its turn. Such a compromise is more noticeable when the arrival times of two consecutive vehicles are close to each other, for example under high traffic density conditions. Moreover, as electric vehicles have recuperative brakes, all CAVs intend to follow a regular profile that involves acceleration to a cruise speed value,

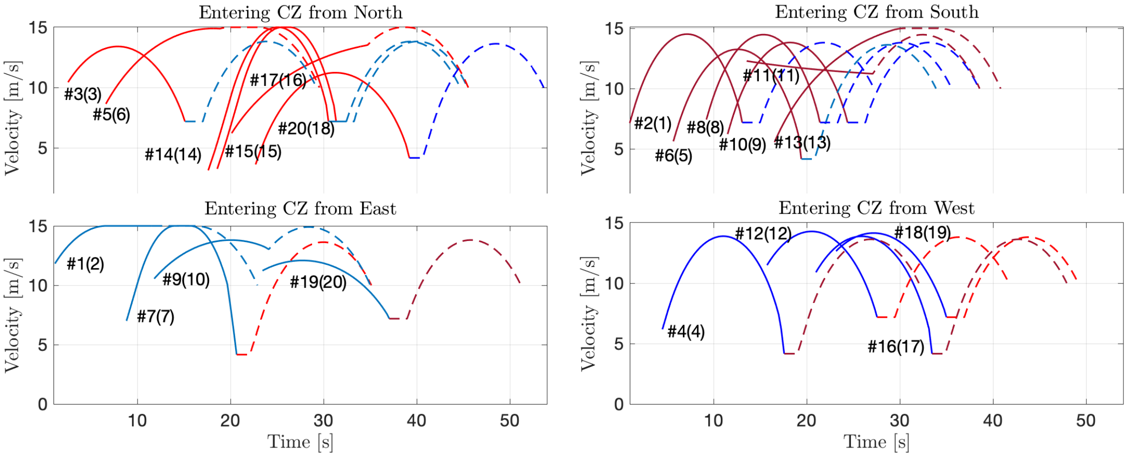

Fig. 7.7 Optimal speed profiles for the first 20 CAVs among 60 CAVs by solving the SOCP-UB at an arrival rate of 750 veh/h per lane with the peak speed limit at 15 m/s. The solid lines represent the trajectories before the vehicle enters the MZ, while after the vehicle enters the MZ the speed profiles are shown by dashed lines. The numbers with # denote the crossing order $\mathcal{N}$ and the numbers in the brackets are the arriving order at the CZ.

followed by a period of constant speed cruising until the exist of CZ (for straight running) or the entry of MZ (if turning is required) approaches, so as to reduce total electric energy consumption [172]. A visual demonstration of the optimal solutions can be found at the link https://youtu.be/Xmh6pOzlSe0.

In order to investigate the impact of traffic density and the trade-off between energy consumption and travel time, the optimal solutions for a series of combinations of the weight factors, W_1 and W_2, (under the same initial conditions) and for different arrival rates are presented in Fig. 7.8. As it can be seen, the Pareto front results for four different arrival rates indicate that an increase in travel time of approximately 20% can lead to an average fuel consumption reduction of 41.7%, while further increase in travel time can eventually yield up to 55.6% fuel consumption reduction. These results point out the importance of examining the energy-time trade-off, as a small sacrifice in travel time can significantly affect the energy efficiency. The comparison among four arrival rates indicates that the overall optimality deteriorates as the arrival rate increases. The reason is that a higher arrival rate implies a higher traffic density condition, where the motions of vehicles are more restrained by the surrounding vehicles, and therefore, the optimal solution tends to be compromised by collision avoidance requirements. Furthermore, the influence of the arrival rate is more apparent when the average travel time is small. This can be understood that with an emphasis on the travel time minimisation, the optimisation encourages the CAVs to travel at maximum speed, which yields more restrictive solutions due to the tougher

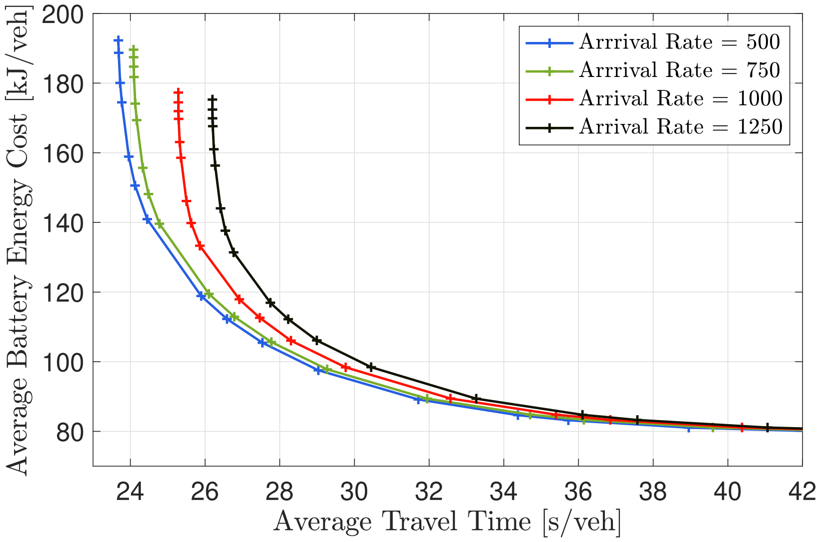

Fig. 7.8 Trade-off between average battery energy consumption and average travel time for arrival rates from 500 veh/h per lane to 1250 veh/h per lane and for a range of (W_1, W_2) pairs.

collision avoidance constraints in such cases, and the restrictiveness rises as the arrival rate increases. Finally, it has been found that further decrease in the arrival rate below 500 veh/h makes negligible impact on the optimality, as the traffic is sufficiently sparse to allow free optimisation of each velocity trajectory without concession to other vehicles.

To examine the relationship between the safety margin and energy consumption, a comparison of the average time gap and energy consumption is made among cases of different arrival rates while keeping the average travel time fixed. Note that the time gap is defined in (7.13) and the average is taken only for the subset of vehicles with potential for rear-end collision ($\mathcal{C}_h$ set). Table 7.3 presents the results for the case of a fixed average travelled time of 26.77 s, which is representative of cases where arrival rate changes have an influence on energy consumption (see Fig. 7.8). As it can be seen, there is an upward trend

Table 7.3 Average time gap at different arrival rates with a fixed average travelled time 26.77 s with $t_\delta = \Delta s / v_{\max} = 0.13$ s.

Arrival Rate [veh/h]	500	750	1000	1250
Energy Cost [kJ]	110.93	112.97	119.95	131.34
Average time gap [s]	7.14	4.90	4.11	3.74
Minimum time gap [s]	0.17	0.15	0.14	0.13
Maximum time gap [s]	20.46	14.32	13.02	12.41

in the energy cost from 111.43 kJ to 119.95 kJ as the arrival rate increases from 500 veh/h to 1000 veh/h. Meanwhile, the average time gap decreases from 7.14 s to 4.11 s for the same arrival rate change. This can be understood that increased traffic density could result in severe congestion and more acceleration/deceleration behaviour, and therefore reduced time gap and higher energy consumption. When the arrival rate is 1250 veh/h, the energy consumption is steeply compromised to 131.34 kJ, as also shown in Fig. 7.8, which is influenced by the higher number of activation of the limiting time gap (see t_δ in (7.13) and also observe that the minimum time gap for this arrival rate in Table 7.3 reaches $t_\delta = 0.13$ s).

The optimality of the SOCP-UB is investigated by comparing its performance with SOCP-LB and SOCP-Baseline introduced in Section 7.4.2. As shown in Fig. 7.9, the solutions of the SOCP-UB are close to the SOCP-LB, which implies the tightness of the linearly approximated bound shown in Fig. 7.5 and the battery power shown in Fig. 7.4. Owing to the increased feasibility in terms of following distance, the SOCP-LB as compared to the SOCP-UB can reach a more time-efficient solution, which, however, is potentially unsafe (infeasible). As an example, when the average energy cost is 147 kJ/veh, the average travel time is increased by only 1.6% for the SOCP-UB as compared to SOCP-LB. It can also be observed that when $W_1 \gg W_2$, the energy cost becomes negligible in the objective function, thus the optimal speed trajectories derived by the two schemes (SOCP-LB and SOCP-UB) are pushed to the upper speed limits, and the optimality gap is further increased to 2.3% at an average energy cost of 189.5 kJ/veh. On the other hand, the Pareto front of the SOCP-UB is always below that of the SOCP-Baseline with a maximum optimality gap at 2.4% at the same average energy cost of 189.5 kJ/veh, which highlights the benefits of using a planning-based scheduling method instead of the FIFO policy. In particular, when the

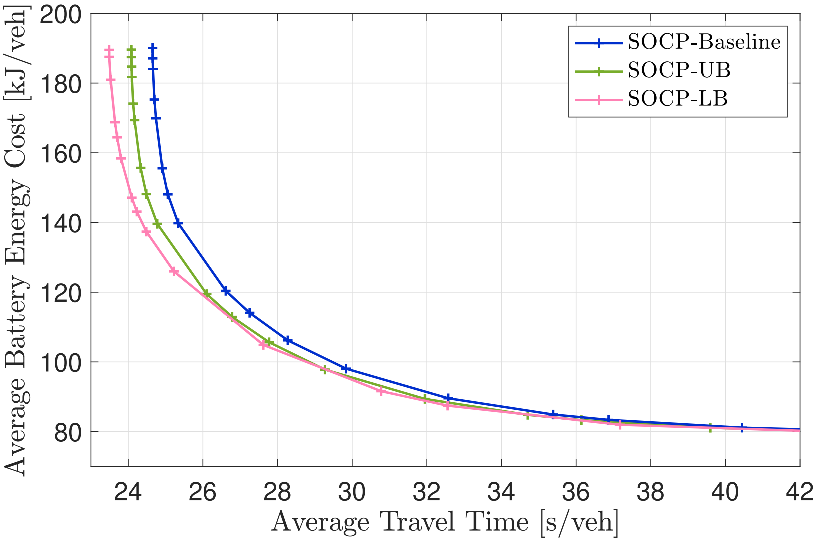

Fig. 7.9 Comparison of the energy-time cost trade-off between the SOCP-UB and the benchmark solutions at an arrival rate of 750 veh/h per lane.

average travel time is 24.74 s, the SOCP-UB can save up to 21.8% energy consumption with respect to the SOCP-Baseline. As the energy cost weight, W_2, is gradually increased, the optimality gap among the three schemes becomes negligible. This can be understood by the fact that the CAVs are encouraged to travel at a lower average speed when the emphasise is on the energy consumption, resulting in large enough time gaps between CAVs so that their speed trajectories can be freely optimised without being limited by the safety enforcement constraints.

7.6 Conclusions

In this chapter, the traffic coordination problem at signal-free traffic intersections is addressed for connected and autonomous vehicles. The dynamics of each vehicle are modelled by a realistic longitudinal model in conjunction with an explicitly formulated electric powertrain system, which allows the energy consumption to be accurately estimated. The problem is approached by a hierarchical centralised coordination scheme that aims to minimise a weighted sum of the aggregate electric energy consumption and travelling time required to drive through the junction by sequentially optimising the passing order and explicit velocity trajectories in two stages. The overall problem is formulated in the space domain, and in this context, the resulting OCPs in both stages can be respectively suitably relaxed as convex SOCP problems, which can be solved to optimality efficiently using a standard optimisation solver.

Simulation results verify the validity and computational efficiency of the solution obtained by the proposed control scheme, which enables the method to be implemented using current technologies. To illustrate the trade-off between energy consumption and travel time, a range of cases with different weighting on these two costs are examined and the Pareto front corresponding to different combinations of the two costs is produced. The investigation of the Pareto solutions emphasises the importance of optimising their trade-off, as a compromise of 20% in travel time could lead to up to 41.7% in energy savings. According to the comparison with a valid lower bounding solution of the full original problem, the presented approximation OCP algorithm is able to achieve feasible solutions close to this bounding solution, which further demonstrates the tightness of the convex relaxation employed in the proposed OCP. Finally, the method proposed in this paper is compared to a benchmark solution commonly employed in the literature, obtained using a simple FIFO policy. The proposed technique is found to outperform the benchmark solution with up to an impressive 21.8% improvement in terms of energy-saving when travel time in both cases is equalised, and furthermore, with the same energy consumption, the method can save up to 2.4% travel time.

Chapter 8

A Robust Control Strategy for Decentralised Signal-free Intersection Management

8.1 Introduction

This chapter proposes a hierarchical robust control strategy, HRCS for autonomous intersection crossing in a decentralised coordination framework, where the optimisation problem is formulated in the space domain to avoid the end-time free problem (thus more straightforward to employ an MPC) and utilise a convex optimisation framework. Moreover, both modelling and measurement uncertainties are considered in the state-space model and addressed by the developed hierarchical control framework. This formulation enables the consideration of state-independent unmodelled longitudinal nonlinearities (e.g. gradient resistance caused by road slopes), and measurement noises of locations and velocities caused by sensors and environmental disturbances. In particular, the hierarchical strategy involves an upper and lower level optimisation, in which the crossing order is optimised in the upper level by solving an OCP, which then guides the lower level controller to derive optimal solutions in real-time. To address the aforementioned uncertainties, a tube-based RMPC is designed for the lower level coordination based on the robust invariant set centred along the nominal trajectory. In summary, this chapter makes the following contributions:

- This Chapter introduces a novel robust and decentralised optimisation-based autonomous intersection coordination framework, which takes into account vehicle modelling uncertainties and measurement noise.
- In addition to velocity trajectory optimisation, the proposed scheme also finds the crossing order of the CAVs based on the local trajectory optimisation and heuristic

rules. This leads to significantly better solutions compared to most of the existing works, where a predefined non-optimised (e.g., FIFO) crossing policy is enforced.

- Inspired by the authors' prior work on centralised intersection coordination in Chapter 7, computationally efficient solutions for the formulated decentralised coordinated scheme are derived by suitably relaxing the non-convex constraints and reformulating the associated optimisation problems into convex SOCPs. A rigorous proof of the equivalence between the convexified and the original non-convex problem is also provided to complete the framework, which also implies the robust satisfaction of the safety and operational constraints.

The rest of this chapter is organised as follows. Section 8.2 introduces a convex modelling framework of autonomous intersection crossing that includes the powertrain model of the CAV. The formulation of the decentralised HRCS is given in Section 8.3. Simulation results and discussion are presented in Section 8.4. Finally, concluding remarks are given in Section 8.5. Note that Sections 8.2- 8.5 are taken from the author's publication [202].

8.1.1 Notation and Preliminary:

Given sets $\mathbb{W}$, $\mathbb{V}$, the Minkowski sum of sets $\mathbb{W}$, $\mathbb{V}$ is $\mathbb{W} \oplus \mathbb{V} = \{x + y | x \in \mathbb{W}, y \in \mathbb{V}\}$ and the Minkowski difference of sets $\mathbb{W}, \mathbb{V}$ is $\mathbb{W} \ominus \mathbb{V} = \{x \in \mathbb{E} | V + x \in \mathbb{W}\}$.

8.2 Problem Statement

8.2.1 System Modeling and General Problem Setup

The intersection coordination problem studied in the chapter consists of a group of vehicles approaching a signal-free intersection, as shown in Fig. 8.1, where lane changes and turning manoeuvres are not allowed. All vehicles are assumed to be autonomous and connected, and there are no other non-autonomous road users (e.g. human driven vehicles, cyclist and pedestrians). As it can be seen, the intersection is formed by two perpendicular roads with two lanes per road. Vehicles approaching the intersection will first enter a CZ, *Control Zone*. The centre of the intersection is the MZ, *Merging Zone*, where vehicles merge from different directions, and therefore lateral collision may occur. As it can be seen, the area of the MZ is considered as a square of side S and the distance from the entry of the CZ to the entry of the MZ is L, with $L > S$. The intersection also has a coordinator that facilitates exchange of information among the CAVs inside the CZ. Hence, in practice L is determined by the communication range capability of the CAVs and the coordinator. Note

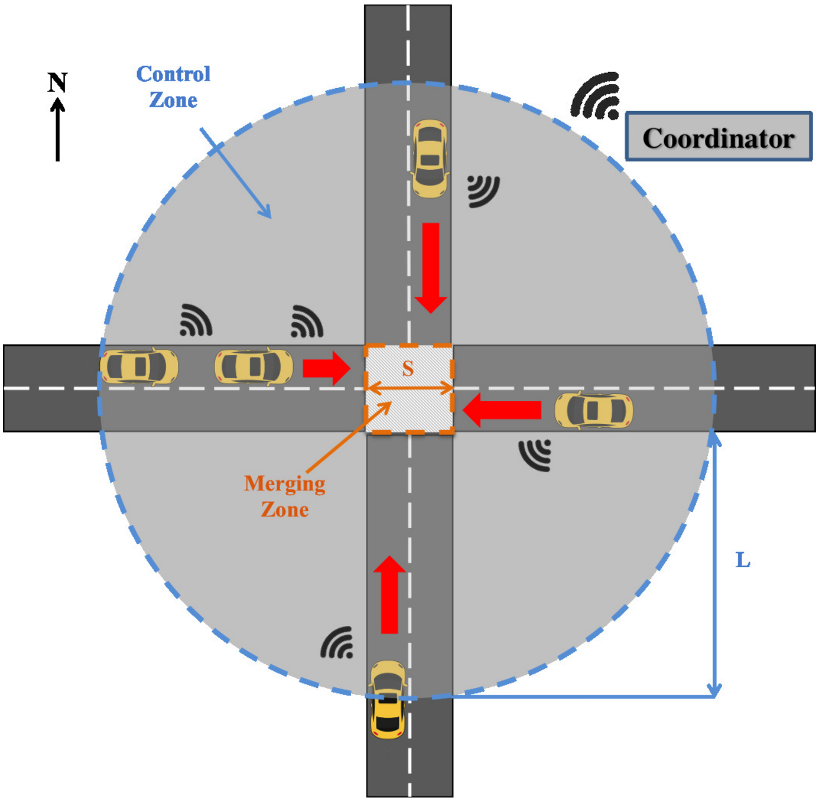

Fig. 8.1 The system architecture of autonomous intersection crossing problem.

that the intersection coordinator is only used to streamline the communication process for the decentralised control scheme, and it is not involved in making control decisions. The decentralised control scheme will be specified in Section 8.3.

Let us denote by $N(t) \in \mathbb{N}_{>0}$ the total number of CAVs within the CZ at a given time $t \in \mathbb{R}_{>0}$ and the set $\mathcal{N}(t) \subseteq \mathbb{N}^{N(t)}$ to designate the crossing order in which the vehicles will enter the MZ. The determination of the crossing order will be elaborated in Section 8.3.1 The control target is to minimise the average energy consumption and travel time of $N(t)$ CAVs by finding in a decentralised manner the optimal sequence $\mathcal{N}(t)$ and the optimal speed trajectory for each vehicle from the entry of the CZ to the exit of the MZ. For notational convenience, we consider that $\mathcal{N}$ and N are identical to $\mathcal{N}(t)$ and $N(t)$ in the rest of this paper, respectively.

Definition 8.1. *Given an arbitrary CAV $h \in \mathcal{N}$, any CAV $i \in \mathcal{N}$, $i \neq h$ can be categorized into one of the following subsets of $\mathcal{N}$ based on its physical location inside the CZ: 1) $\mathcal{C}_h$ collects vehicles traveling in the same direction as the ith vehicle; 2) $\mathcal{L}_h$ collects vehicles traveling in the perpendicular directions to the ith vehicle; 3) $\mathcal{O}_h$ collects vehicles traveling in the opposite direction to the ith vehicle.*

This research focuses on developing a coordination scheme in the space domain, which leads to the following two advantages: (a) the free end-time optimisation problem in the time domain is avoided, and (b) the problem can be formulated using similar convex programs techniques as shown in Chapter 7 [197]. Let s denote the variable of travelled distance and $v_i(s)$ denote the velocity of the ith vehicle. The transformation from time to space domain is achieved by changing the independent variable t to s via $\frac{d}{ds}=\frac{1}{v}\frac{d}{dt}$. Thus, in the space domain, the distance travelled for each CAV is constant and equals to $L+S+l_i$, $i\in\mathcal{N}$, and the travel time of each CAV can be readily obtained as a state variable,

$$\frac{d}{ds}t_i=\frac{1}{v_i}=\frac{1}{\sqrt{2E_i/m_i}}, \tag{8.1}$$

where $E_i(s)=\frac{1}{2}m_iv_i^2(s)$ is the kinetic energy, and m_i is the mass of the ith vehicle. As such, the required travel time of the ith CAV to cross the intersection is:

$$J_{t,i}=t_i(L+S+l_i)-t_i(0), \tag{8.2}$$

where $t_i(0)$ is the arrival time of CAV i at the CZ. Hereafter, $E_i(s)$ is introduced instead of v_i for modelling the motion dynamics to cancel the nonlinearity due to the air drag. Considering $E_i(s)$ and vehicle longitudinal dynamics, the motion of vehicle i can be described by,

$$\frac{d}{ds}E_i(s)=F_{w,i}(s)-F_{r,i}-\frac{2f_{d,i}}{m_i}E_i(s), \tag{8.3}$$

where $F_{w,i}(s)=F_{t,i}(s)+F_{b,i}(s)$ is the total force acting on the wheels with $F_{t,i}(s)$ and $F_{b,i}(s)$ being the powertrain driving force and the friction brake force acting on the wheels, respectively. $F_{r,i}=f_{r,i}m_ig$ is the rolling resistance force of CAV i with coefficient $f_{r,i}$, and $f_{d,i}$ is the coefficient of air drag resistance of the ith CAV. It is further assumed that all vehicles are equipped with electric drives, and subject to constraints in (3.14).

The energy cost of each CAV, $J_{b,i}$, is evaluated based on the tank-to-wheel energy path of the vehicle, which can be represented as a time integral of $P_{b,i}(F_{t,i},v_i)$, a function of vehicle force and speed (which correspond to motor torque and speed). As such, the energy usage in the space domain of each CAV is: $J_{b,i}=\int_0^{L+S+l_i}\frac{P_{b,i}(F_{t,i},v_i)}{v_i(s)}ds$. By analogy to the common quadratic battery power model [203], the following fitting model is chosen for $P_{b,i}$:

$$P_{b,i}(F_{t,i},v_i)=b_2F_{t,i}^2v_i+b_1F_{t,i}v_i+b_0v_i, \tag{8.4}$$

where b_0, b_1, b_2 are fitting parameters obtained on the basis of a motor map. As such, the battery energy usage in the space domain of each CAV is:

$$J_{b,i}=\int_0^{L+S+l_i}\left(b_2F_{t,i}(s)^2+b_1F_{t,i}(s)+b_0\right)ds. \tag{8.5}$$

For safety purposes, rear-end and lateral collision avoidance constraints and speed limits are required:

$$t_i(s) - t_h(s + l_h) \geq t_\delta,\ \forall i \in \mathcal{C}_h, \tag{8.6}$$

$$t_i(L) \geq t_h(L + S + l_h)\,,\ \forall i \in \mathcal{L}_h\,, \tag{8.7}$$

$$\frac{1}{2} m_i v_{\min}^2 \leq E_i(s) \leq \frac{1}{2} m_i v_{\max}^2\,, \tag{8.8}$$

where t_δ is a minimum time gap enforced to prevent rear-end collision between vehicle i and the vehicle immediately ahead, $v_{\min}$ is set to a sufficiently small positive constant to avoid singularity issues that would appear in (8.1) when v_i=0, and $v_{\max}$ is determined based on the infrastructure constraints and traffic regulations [150].

Lateral collision constraint (8.7) guarantees that the ith vehicle enters the MZ only after the hth vehicle leaves the MZ. For any CAV $i \in \mathcal{O}_h$, there is no interference between CAVs h and i inside the CZ. Hence, only the following constraint

$$t_i(L+S) > t_h(L+S),\ \forall i \in \mathcal{O}_h\,, \tag{8.9}$$

is required to fulfil the crossing order.

The following assumptions are also needed to complete the modelling framework described above:

Assumption 8.1. *All vehicle information (e.g., position, velocity, acceleration) can be measured through sensors, and the data can be transferred between each CAV and the coordinator without delays.*

Assumption 8.2. *For each CAV i, constraints* (8.6)*,* (3.14a)*, and* (8.8) *are inactive at* $t_i(0)$.

Assumption 8.1 may not be valid for practical vehicular networks. On that occasion, it can be relaxed by using a worst case analysis as long as the measurement and communication delays are bounded. Assumption 8.2 is needed to ensure that all CAVs arriving at the CZ have feasible initial states and initial control inputs.

Based on the above Assumption 8.1-8.2 and equations (8.1)-(8.9), the autonomous coordination problem can be formulated as an OCP. Taking into account a crossing order $\mathcal{N}$ and the objective of minimising the travel time (8.2) and energy consumption (8.5), the OCP is defined as

OCP 8.1.

$$\min_{\mathbf{u}_{\text{nonlinear}}} \quad W_1 \sum_{i=1}^{N} J_{t,i} + W_2 \sum_{i=1}^{N} J_{b,i} \tag{8.10a}$$

$$\textbf{s.t.}: (3.14\text{a}), (3.14\text{b}), (8.1), (8.3), (8.6), (8.7), (8.8), (8.9), \tag{8.10b}$$

where

$$\mathbf{u}_{\text{nonlinear}} = [F_{t,1}(s), F_{t,2}(s), \cdots, F_{t,N}(s), F_{b,1}(s), F_{b,2}(s), \cdots, F_{b,N}(s)]^\top \in \mathbb{R}^{2N},$$

and $W_1, W_2 \in \mathbb{R}_{>0}$ are weighting factors. Note that the crossing order $\mathcal{N}$ is determined by another OCP that is introduced later in Section 8.3.1.

8.2.2 Convex Modelling Approach

OCP 8.1 is a non-convex optimisation problem because of the non-affine equality dynamics (8.1). Subsequently, we show that OCP 8.1 can be convexified such that under certain assumptions the solution of the relaxed, convex problem is identical to the solution of the original non-convex OCP 8.1.

Toward this direction, the dynamics of t_i are rewritten as

$$\frac{d}{ds} t_i(s) = \zeta_i(s), \tag{8.11}$$

$$\zeta_i(s) \geq \frac{1}{\sqrt{2E_i(s)/m_i}}, \tag{8.12}$$

which relax the original nonlinear differential equation into a linear differential equation and a convex constraint of the auxiliary control variable $\zeta_i(s)$.

The following Assumption 8.3-8.4 are needed to proceed with the proof of Proposition 8.1 defined later in this section.

Assumption 8.3. *The regression model* (8.4) *can find an accurate fitting of* $P_{b,i}$ *by* b_1 *and* b_2 *that comply with the condition*

$$b_1 + 2b_2 F_{w,\min} > 0, \forall i \in \mathcal{N}, \tag{8.13}$$

where $F_{w,\min} = \min\{m_i a_{\min,i}\} < 0, \forall i \in \mathcal{N}$ *representing the maximum available braking force of all CAVs.*

Assumption 8.3 implies that b_1 is sufficient large positive value compared to b_2. This is consistent with the magnitude of the terms of the fitting model (8.4) based on their physical interpretation, where the fitting term involving b_1 is found to be the dominant one when the model (8.4) is fitted to data.

According to Assumption 8.3, it is immediate to determine the fitting parameters b_0, b_1, b_2 by solving the following constrained optimisation problem:

$$\min_{b_0, b_1, b_2 \in \mathbb{R}_{>0}} \quad ||P_{b,i}(F_{t,i}, v_i) - P^*_{b,i}||_2 \tag{8.14a}$$

$$\textbf{s.t.}: (8.13), \tag{8.14b}$$

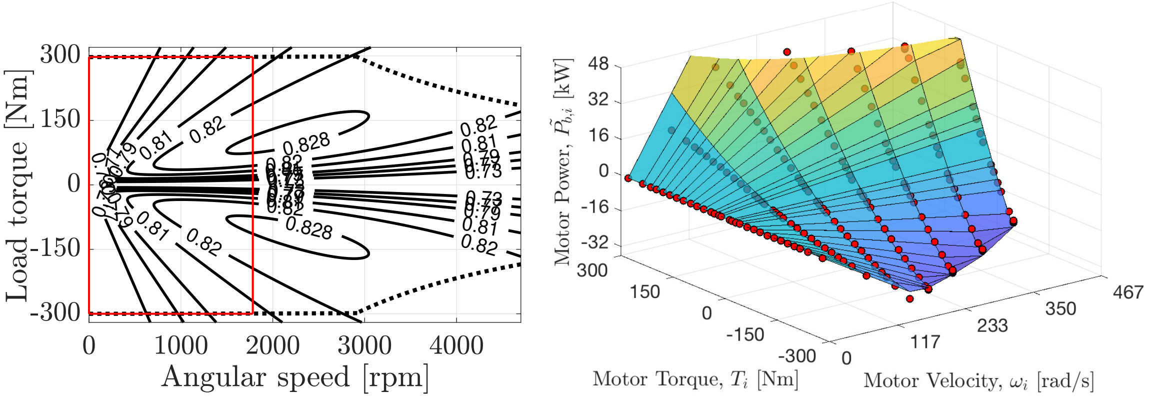

Fig. 8.2 Left: efficiency map of the electric motor (positive torque indicates battery discharging and negative torque represents battery charging) with operational bounds (dotted lines). The area surrounded by red lines denotes the operational region for the feasible vehicle speed specified by (8.8). Right: nonlinear regression of the battery output power data (red dots, calculated based on the efficiency map shown in the left figure of Fig. 8.2) by solving (8.14) with an R-square fit of 99.25% whereas the result of unconstrained fitting (without (8.14b)) is 99.53%.

with $P^*_{b,i}$ the experimental battery output power data subject to certain motor torque and speed combinations. A representative example of the fitting (8.4) on the basis of the motor map given in [67] is given Fig. 8.2, which verifies the accuracy of the fitting model.

Assumption 8.4. *The friction brake $F_{b,i}$ is inactive, such that $F_{b,i}(s) = 0, \forall i \in \mathcal{N}, \forall s \in [0, L+S+l_i]$.*

Assumption 8.4 holds in most cases by the fact that regenerative braking is naturally maximised in order to promote eco-driving, which targets minimum energy usage. The case when the assumption does not hold is analysed in Remark 8.1 later in this section.

Under Assumption 8.4, energy cost $J_{b,i}$ in (8.5) is equivalent to

$$J_{w,i} = \int_0^{L+S+l_i} \left(b_2 F^2_{w,i}(s) + b_1 F_{w,i}(s) + b_0\right) ds. \tag{8.15}$$

Now, we have all ingredients to reformulate the non-convex problem OCP 8.1 as a convex SOCP problem:

OCP 8.2.

$$\min_{\mathbf{u}} \quad W_1 \sum_{i=1}^{N} J_{t,i} + W_2 \sum_{i=1}^{N} J_{w,i} \tag{8.16a}$$

$$\textbf{\textit{s.t.}} : (3.14c), (8.3), (8.6), (8.7), (8.8), (8.9), (8.11), (8.12), \tag{8.16b}$$

where $\mathbf{u} = [F_{w,1}(s), \cdots, F_{w,N}(s), \zeta_1(s), \cdots, \zeta_N(s)]^\top \in \mathbb{R}^{2N}$.

It is worth noting that the validity of the solution of OCP 8.1 relies on the tightness of (8.12), which is addressed by Proposition 8.1.

Proposition 8.1. *Under Assumption 8.3 and Assumption 8.4, the globally optimal solution of OCP 8.2 always finds the equality condition of* (8.12)*, and therefore the solution of the relaxed, nonlinear convex problem OCP 8.2 is identical to the solution of the non-convex problem OCP 8.1.*

Proof. See in Appendix III-A.

Note that Proposition 1 only valid if feasible solutions exist. To ensure the existence of the feasible solutions, let us introduce the following Lemma 8.1.

Lemma 8.1. *There always exists a sufficiently small constant* $\sigma > 0$ *and let* $v_{\min} = \sigma$*, then a feasible solution can be found.*

Proof. See in Appendix III-B.

From Lemma 8.1, by solving the convex optimisation problem with continually reduced lower bound of the speed, there always exists a σ and a corresponding feasible solution with $E_i^*(s) = \frac{1}{2}m\sigma^2$ that allows vehicle i to operate at an almost static condition such that collision avoidance constraints can be satisfied, and therefore the equality condition (8.12) holds.

Remark 8.1 (Active friction brakes)**.** *Solving OCP 8.2 may yield a solution trajectory where* $F_{w,i}(s) < \frac{g_{r,i}}{r_{w,i}} T_{\min,i}(s)$ *for some s (regenerated braking power is saturated). In this circumstance, friction brake is invoked to meet the total force demand at the wheels,* $F_{w,i}(s) = \frac{g_{r,i}}{r_{w,i}} T_{\min,i}(s) + F_{b,i}(s)$*. As such, the equivalence between OCP 8.1 and OCP 8.2 (see OCP 8.1) is no longer guaranteed due to the discrepancy between the energy costs in both OCPs (regeneration of friction brakes is assumed in OCP 8.2), and therefore, the optimality of OCP 8.2 may be compromised in such a case. Nevertheless, the equality of* (8.12) *holds invariably (as inferred from the proof in Appendix II-A), which, in turn, ensures the feasibility of the convex optimization solution.*

8.3 Hierarchical Robust Control Strategy

This section introduces the novel decentralised control strategy (i.e., HRCS), where the convex problem formulated in OCP 8.2 plays a key role for its formulation. The optimisation scheme in this work is composed of an upper-level crossing order scheduler and a lower-level trajectory optimiser RMPC, deployed in a hierarchical and decentralised manner. Every time a new vehicle i arrives at the entry point of the CZ, its local controller determines the optimal passing order $\mathcal{N}_i$ by solving an OCP 8.3 as will be described in Section 8.3.1. The tube-based RMPC embedded in each CAV finds its individual optimal trajectory to cross the signal-free intersection.Note that the intersection coordinator works as an information relay without making any control decisions. Specifically, the coordinator will collect the new crossing order $\mathcal{N}_i$ and transmit it all vehicles inside the CZ such that their lower-level controller will update the collision avoidance constraints in the lower-level optimisation problem based on an updated crossing order.

Prior to the introduction of the individual algorithms in the two layers, let us first introduce some preliminaries that are used across the two layers. Considering a sampling distance interval $\Delta s \in \mathbb{R}_{>0}$, and without loss of generality it is assumed that $L+S+l_i = \alpha\Delta s$, $L = \alpha_1\Delta s$, $S = \alpha_2\Delta s$, $l_i = \alpha_3\Delta s$, $\alpha, \alpha_1, \alpha_2, \alpha_3 \in \mathbb{N}_{>0}, \alpha = \alpha_1 + \alpha_2, \alpha_1 > \alpha_2$.

The objective function in a discretised form for vehicle i is formulated based on (8.16a) as

$$J_{d,i} = \sum_{k=0}^{\alpha-1} [W_1(b_2F_{w,i}^2(k) + b_1F_{w,i}(k) + b_0) + W_2\zeta_i(k)]\Delta s, \tag{8.17}$$

The discretised system equations (8.3) and (8.11), and the related constraints can be rewritten as:

$$x_i(k+1) = A_ix_i(k) + B_iu_i(k) + \omega_i(k), \tag{8.18a}$$

$$y_i(k) = C_ix_i(k) + \nu_i(k), \tag{8.18b}$$

$$x_i = \begin{bmatrix} E_i \\ t_i \end{bmatrix}, \quad u_i = \begin{bmatrix} F_{w,i} - F_{r,i} \\ \zeta_i \end{bmatrix}, \quad A_i = \begin{bmatrix} \mathrm{e}^{\frac{-2f_{d,i}\Delta s}{m_i}} & 0 \\ 0 & 1 \end{bmatrix},$$

$$B_i = \begin{bmatrix} -\frac{m_i(\mathrm{e}^{-\frac{2f_{d,i}\Delta s}{m_i}} - 1)}{2f_{d,i}} & 0 \\ 0 & \Delta s \end{bmatrix}, \quad C_i = \begin{bmatrix} 1 & 0 \\ 0 & 1 \end{bmatrix},$$

where $k = 0, 1, \ldots, \alpha-1$, $\omega_i(k) = [\omega_{E,i}(k),\, 0]^\top$ with a closed convex set bounding on process noise $\mathbb{W}_i = \{\omega_{E,i}(k) \in \mathbb{R} : ||\omega_{E,i}(k)|| \le \overline{\omega}_{E,i}\}$ and $\overline{\omega}_{E,i} \in \mathbb{R}_{>0}$, $\nu_i(k) = [\nu_{E,i}(k),\, \nu_{t,i}(k)]^\top$ with a closed convex set bounding on measurement noise $\mathbb{V}_i = \{\nu_i(k) \in \mathbb{R}^2 : ||\nu_i(k)|| \le \overline{\nu}_i\}$ and $\overline{\nu}_i \in \mathbb{R}_{>0}$, and y_i is the measured signal of the ith vehicle's status, obtained by onboard sensors. The consideration of ω_i and ν_i involves, respectively, the state-independent unmodelled vehicle longitudinal dynamics (e.g. gradient resistance caused by road slopes), and the measurement noises from the sensors and environment disturbances. Moreover, the nominal system of the actual dynamics system (8.18a) embedded in the designed RMPC controller can be written as:

$$\bar{x}_i(k+1) = A_i\bar{x}_i(k) + B_i\bar{u}_i(k), \tag{8.19}$$

where the disturbance term ω_i is neglected, $\bar{x}_i(k)$ is the nominal state, and $\bar{u}_i(k)$ is the nominal control input.

In the decentralised framework, the coordinator assigns a unique identity to each CAV when the vehicle enters the CZ of the intersection based on the vehicle's arrival time and its entering direction. The identity that the coordinator assigns to each vehicle that arrives at the CZ is defined as $(i, d_i, \mathcal{I}_i(k))$, where $i \in \mathcal{N}(t_i(0))$ is the optimal crossing order of vehicle i to enter the MZ as will be described in OCP 8.3, d_i is an index denoting the travelling direction (north, south, east and west), and $\mathcal{I}_i(k)$ is the information set generated by the coordinator at step k by collecting the past optimal nominal state sequence of vehicle i:

$$\mathcal{I}_i(k) = [\bar{\mathbf{x}}_i(0), \bar{\mathbf{x}}_i(1), \cdots, \bar{\mathbf{x}}_i(k)] \in \mathbb{R}^{(N_p+1)\times 2k}, \tag{8.20}$$

where $\bar{\mathbf{x}}_i(k) = [\bar{\mathbf{E}}_i(k), \bar{\mathbf{t}}_i(k)] \in \mathbb{R}^{(N_p+1)\times 2}$ is the optimal nominal state sequence computed by the local controller on vehicle i at step k within a predefined receding horizon N_p, and

$$\begin{aligned}\bar{\mathbf{E}}_i(k) &= [\bar{E}_i(k|k), \bar{E}_i(k+1|k), \ldots, \bar{E}_i(k+N_p|k)]^\top,\\ \bar{\mathbf{t}}_i(k) &= [\bar{t}_i(k|k), \bar{t}_i(k+1|k), \ldots, \bar{t}_i(k+N_p|k)]^\top.\end{aligned}$$

8.3.1 Crossing Order Scheduler

Considering the single lane road depicted in Fig. 8.1, CAVs approaching the intersection from the same direction will enter and leave the MZ in the same order they arrive at the CZ. Therefore, the major challenge stems from the collision avoidance and prioritising constraints for CAVs merging from different directions, i.e., (8.7) and (8.9), which depends on the crossing order. To determine an optimal crossing order without an invoking exhaustive search, we define a virtual coordination problem in the discrete-time form:

OCP 8.3.

$$\min_{\bar{\mathbf{u}}_\mathbf{i}} \quad J_{d,i}(\bar{\mathbf{x}}_i, \bar{\mathbf{u}}_i) \tag{8.21a}$$

$$\textbf{\textit{s.t.}} : \bar{x}_i(0) = \hat{x}_i(0), \tag{8.21b}$$

$$\bar{x}_i(k+1) = A_i \bar{x}_i(k) + B_i \bar{u}_i(k), \tag{8.21c}$$

$$(3.14c), (8.3), (8.6), (8.8), (8.11), (8.12), \; k = 0, 1, \ldots, \alpha - 1, \tag{8.21d}$$

where $\bar{\mathbf{x}}_i = [\bar{x}_i(0), \bar{x}_i(1), \ldots, \bar{x}_i(\alpha)]^\top \in \mathbb{R}^{(\alpha+1)\times 2}$, $\bar{\mathbf{u}}_i = [\bar{u}_i(0), \bar{u}_i(1), \ldots, \bar{u}_i(\alpha-1)]^\top \in \mathbb{R}^{\alpha\times 2}$, (8.21c) collects the nominal dynamics (8.19), and the initial value of the nominal state $\bar{x}_i(0)$ takes the value of the actual initial condition $x_i(0)$ since the disturbances are ignored.

Each vehicle needs to find the ideal (non-conservative) MZ entry and exit times, $t_{i,in}$ and $t_{i,out}$ by solving OCP 8.3 at the entry point of the CZ. Without considering the lateral collision avoidance constraints. The main idea is that for those vehicles that have potential lateral collisions, their crossing orders are based on their entry times at the MZ, while if there is no interference between the CAVs, their orders are based on their exit times at the MZ. As such, the implementation steps are performed as follows.

Step 1: Given $t_{i,in}$ and $t_{i,out}$ for vehicle $i \in \mathcal{A}_i$ with $\mathcal{A}_i = \{1,2,3\cdots,i\}$ the arrival order at the CZ, and a previously designated crossing order $\mathcal{N}_{i-1} \in \mathbb{N}^{(i-1)}$ (i.e., $\mathcal{N}_{i-1} = \mathcal{N}(t), \forall t \in [t_{i-1}(0), t_i(0))$), which is a permutation of $\mathcal{A}_{i-1}$. For the sake of further discussion, let us consider N_{i-1}^{k} the kth element in $\mathcal{N}_{i-1}$.

Step 2: The ith arriving vehicle receives the entry position and intention of the last vehicle, N_{i-1}^{i-1} in $\mathcal{N}_{i-1}$ from the IC, and then determines if there is lateral collision potential or not.

Step 3: (i) If there exists “lateral collision potential", the new crossing order $\mathcal{N}_i$ is determined at vehicle i by evaluating the ideal entry time of the ith arriving vehicle and the vehicle $N_{i-1}^{i-1} \in \mathcal{N}_{i-1}$ at the MZ:

$$\mathcal{N}_i = \begin{cases} \{N_{i-1}^{1}, \dots, N_{i-1}^{i-2}, N_{i-1}^{i-1}, i\}, \; t_{i,in} \geq t_{N_{i-1}^{i-1},in}, \\ \{N_{i-1}^{1}, \dots, N_{i-1}^{i-2}, i, N_{i-1}^{i-1}\}, \; t_{i,in} < t_{N_{i-1}^{i-1},in}, \end{cases}$$

(ii) If there exists “no lateral collision potential", the new crossing order $\mathcal{N}_i$ is determined at vehicle i by evaluating the exit time of the ith arriving vehicle and the vehicle $N_{i-1}^{i-1} \in \mathcal{N}_{i-1}$ at the MZ:

$$\mathcal{N}_i = \begin{cases} \{N_{i-1}^{1}, \dots, N_{i-1}^{i-2}, N_{i-1}^{i-1}, i\}, \; t_{i,out} \geq t_{N_{i-1}^{i-1},out}, \\ \{N_{i-1}^{1}, \dots, N_{i-1}^{i-2}, i, N_{i-1}^{i-1}\}, \; t_{i,out} < t_{N_{i-1}^{i-1},out}, \end{cases}$$

Step 4: The IC receives $\mathcal{N}_i$ from vehicle i and if $\mathcal{N}_i \neq \{\mathcal{N}_{i-1}, i\}$, $\mathcal{N}_i$ is transmitted to vehicle $N_{i-1}^{i-1} \in \mathcal{N}_{i-1}$ and $(i+1)$th arriving vehicle. Otherwise, $\mathcal{N}_i$ is transmitted to $(i+1)$th arriving vehicle only.

Given the crossing order, $\mathcal{N}_i$, the lateral collision avoidance constraints in the lower-level optimisation are set up correspondingly to ensure safety.

8.3.2 Trajectory Optimiser

Before the description of the lower-level controller, some preliminaries that are utilised to construct the collision constraints during the receding horizon windows are introduced first. Based on the identity $(i, d_i, \mathcal{I}_i(k))$, the coordinator exchanges the information set $\mathcal{I}_i(k)$ with the associated vehicles (see below) to enable collision avoidance constraints to be established for each local controller according to (8.6) (8.7) and (8.9). Depending on the crossing order of the CAV i, the information it requires from the coordinator to enable local control is defined as follows:

a. no information is required, if $i = 1$,

b. $\mathcal{I}_{i-1}(k_{i-1})$, if $i \in \mathcal{C}_{i-1}$,

c. $\mathcal{I}_{i-1}(k_{i-1})$ and $\mathcal{I}_h(k_h)$ with $h < i$, where h stands for the CAV immediately ahead of CAV i, if $i \notin \mathcal{C}_{i-1}$ and $i \in \mathcal{C}_h$,

where k_{i-1} and k_h are the corresponding distance step of CAV $i-1$ and h, respectively, when the ith CAV is at step k, that are $t_h(k_h\Delta s) = t_{i-1}(k_{i-1}\Delta s) = t_i(k\Delta s)$. If $i \in \mathcal{C}_h$, the rear-end collision constraint (8.6) is reformatted for the RMPC-based decentralised HRCS as follows:

$$t_i(k+j+1|k) - \bar{t}_h((k-\alpha_3)+j+1|k-\alpha_3) > t_\delta, \tag{8.22}$$

where $j = 0, 1, \cdots, N_p - 1$, and $\bar{t}_h((k-\alpha_3)+j+1|k-\alpha_3)$ is the historical information stored in $\mathcal{I}_h(k_h)$. In addition to the rear-end collision avoidance constraint, the constraints concerning about the lateral collision avoidance and prioritisation for CAV $i \in \{\mathcal{L}_h, \mathcal{O}_h\}$, i.e., (8.7) and (8.9), will be reformatted and described latter in (8.36)-(8.41) in this section.

After obtaining the optimal crossing order $\mathcal{N}(t_i(0))$ from OCP 8.3, the trajectory of CAV i can be optimized by solving an RMPC problem that replaces the objective function (8.21a) with the later defined objective function (8.36)-(8.38) to satisfy conditions (8.7) and (8.9), and to cope with the additive disturbance ω_i and ν_i in the actual system (8.18). This work adopts an RMPC with output feedback and robust invariant tubes based on the nominal system (8.19). An observer is firstly deigned to measure the state of each vehicle. Then, we design robust invariant tubes based on the nominal system (8.19) to bound the nominal state and input. As such, by applying the optimal nominal input solved in each step k, the actual vehicle dynamics constraints $\{x_i \in \mathbb{X}_i, u_i \in \mathbb{U}_i, (x_i, u_i) \in \mathbb{X}_i \times \mathbb{U}_i\}$ can always be satisfied even with the effects of the admissible disturbance sequences w_i and ν_i. The set $\mathbb{X}_i$ collects constraints (8.8) (8.22) as well as lateral collision avoidance and prioritisation constraints (8.40)-(8.41) as described latter in this section, and the set $\mathbb{U}_i$ collects (3.14c), and the set $\mathbb{X}_i \times \mathbb{U}_i$ collects mixed state and input constraint (8.12).

The states of the system (8.18a) are estimated by a Luenberger observer with dynamics described by:

$$\begin{aligned} \hat{x}_i(k+1) &= A_i\hat{x}_i(k) + B_i u_i(k) + L_{c,i}(y_i(k) - \hat{y}_i(k)), \\ \hat{y}_i(k) &= C_i\hat{x}_i(k), \end{aligned} \tag{8.23}$$

where $\hat{x}_i$ and $\hat{y}_i$ are the estimations of state and output, respectively, and $L_{c,i}$ is the observer gain such that the eigenvalues of $A_{L,i}(\triangleq A_i - L_{c,i}C_i)$ satisfy the condition $\lambda(A_{L_i}) < 1$. Considering the estimation error

$$\tilde{x}_i(k) = x_i(k) - \hat{x}_i(k)\,, \tag{8.24}$$

it can be readily shown that its dynamics are governed by

$$\tilde{x}_i(k+1) = A_{L,i}\tilde{x}_i(k) + \tilde{\delta}_i(k)\,, \tag{8.25}$$

where $\tilde{\delta}_i(k) = \omega_i(k) - L_{c,i}\nu_i(k)$. From the bounds of the disturbances, it follows that

$$\tilde{\delta}_i(k) \in \tilde{\Delta}_i \triangleq \mathbb{W}_i \ominus L_{c,i}\mathbb{V}_i\,. \tag{8.26}$$

Since $A_{L,i}$ is stable, a robust invariant tube $\tilde{\mathbb{S}}_i$ can be found such that if $\tilde{x}_i(0) \in \tilde{\mathbb{S}}_i$, $\tilde{x}_i(k)$ remain in the tube for all $\tilde{\delta}_i(k)$. In view of (8.25), it holds that $A_{L,i}\tilde{\mathbb{S}}_i \oplus \tilde{\Delta}_i \subseteq \tilde{\mathbb{S}}_i$ and for the observer gain $L_{c,i}$, the robust invariant tube $\tilde{\mathbb{S}}_i$ that includes the effects of $\tilde{\delta}_i(k) \in \tilde{\Delta}_i$ can be computed as:

$$\tilde{\mathbb{S}}_i = (1 - \mu_{L,i})^{-1} \bigoplus_{j=0}^{n_{L,i}-1} A_{L,i}^{j}\tilde{\Delta}_i\,,$$

where $n_{L,i} \in \mathbb{N}_{>0}$ is a finite integer and $\mu_{L,i} \in [0,1)$ such that $A_{L,i}^{n_{L,i}}\tilde{\Delta}_i \subseteq \mu_{L,i}\tilde{\Delta}_i$ [204].

Moreover, the following relationship can be inferred from (8.24)

$$x_i(k) \in \hat{x}_i(k) \oplus \tilde{\mathbb{S}}_i\,, \tag{8.27}$$

which yields a steady state assumption $\tilde{x}_i(0) \in \tilde{\mathbb{S}}_i$ because if the state estimation $\hat{x}_i$ lies in the tightened constraint set $\mathbb{X}_i \ominus \tilde{\mathbb{S}}_i$, the original state x_i is guaranteed to lie in $\mathbb{X}_i$.

In this paper, the robust control policy is formed by an open-loop control solved by an optimisation problem with nominal dynamics given by (8.19) and tightened constraints, and ancillary feedback control based on the observation of the state (from (8.23)). The feedback controller is defined as:

$$u_i(k) = \bar{u}_i(k) + K_i e_i(k)\,, \tag{8.28}$$

where K_i is the gain of the feedback controller such that $A_{K,i}(\triangleq A_i + B_iK_i)$ meets the condition $\lambda(A_{K,i}) < 1$. e_i is the tracking error between the observer state and the nominal system, defined as:

$$e_i(k) \triangleq \hat{x}_i(k) - \bar{x}_i(k)\,. \tag{8.29}$$

With the control action (8.28), the closed-loop observer state satisfies:

$$\begin{aligned} \hat{x}_i(k+1) =& A_i\hat{x}_i(k)+B_i\bar{u}_i(k)+B_iKe_i(k) \\ &+L_{c,i}C_i\tilde{x}_i(k)+L_{c,i}\nu_i(k)\,, \end{aligned} \tag{8.30}$$

and the dynamics of the tracking error $e_i(k)$ are:

$$\begin{aligned} e_i(k+1) &= A_{K,i}e_i(k)+\bar{\delta}_i(k)\,, \\ \bar{\delta}_i(k) &= L_{c,i}C_i\tilde{x}_i(k)+L_{c,i}\nu_i(k)\,, \\ \bar{\delta}_i(k) &\in \bar{\Delta}_i \triangleq L_{c,i}C_i\tilde{\mathbb{S}}_i \oplus L_{c,i}\mathbb{V}_i\,. \end{aligned} \tag{8.31}$$

By analogy to the robust invariant tube for the observation error $\tilde{x}_i(k)$, the following conditions hold for the $e_i(k)$:

$$\begin{aligned} &e_i(k) \in \bar{\mathbb{S}}_i, \forall k\,, \\ &\hat{x}_i(k) \in \bar{x}_i(k) \oplus \bar{\mathbb{S}}_i \end{aligned} \tag{8.32}$$

with the robust invariant tube for $e_i(k)$, $\bar{\mathbb{S}}_i = (1-\mu_{K,i})^{-1} \oplus_{j=0}^{n_{K,i}-1} A_{K,i}^{j}\bar{\Delta}_i$, where a finite integer $n_{K,i} \in \mathbb{N}_{>0}$ and a scalar $\mu_{K,i} \in [0,1)$ satisfy $A_{K,i}^{n_{K,i}}\bar{\Delta}_i \subseteq \mu_{K,i}\bar{\Delta}_i$ [204], and $A_{K,i}\bar{\mathbb{S}}_i \oplus \bar{\Delta}_i \subseteq \bar{\mathbb{S}}_i$.

Based on the definition of the estimation error (8.24) and the tracking error (8.29), the actual state can be achieved by:

$$x_i(k) = \bar{x}(k)+e_i(k)+\tilde{x}_i(k)\,. \tag{8.33}$$

The bound on the nominal state can be derived by combining the actual state and input constraints (8.18) and the feedback control policy (8.28),

$$\begin{aligned} &\bar{x}_i(k) \in \bar{\mathbb{X}}_i\,, && (8.34a) \\ &\bar{u}_i(k) \in \bar{\mathbb{U}}_i\,, && (8.34b) \\ &\bar{\mathbb{X}}_i \triangleq \begin{cases} \mathbb{X}_i \ominus \mathbb{S}_i, \text{ if } i=1\,, \\ \mathbb{X}_i \ominus \mathbb{S}_i \ominus \mathbb{S}_h, \text{ if } i>1\,, \end{cases} \\ &\bar{\mathbb{U}}_i \triangleq \mathbb{U}_i \ominus (K_i\bar{\mathbb{S}}_i)\,, \end{aligned}$$

where $\mathbb{S}_i \triangleq \tilde{\mathbb{S}}_i \oplus \bar{\mathbb{S}}_i$, $\mathbb{S}_h \triangleq \tilde{\mathbb{S}}_h \oplus \bar{\mathbb{S}}_h$, and $\tilde{\mathbb{S}}_h$ and $\bar{\mathbb{S}}_h$ are the estimation error and tracking error derived invariant tubes of $\mathbb{X}_h$, respectively, which are generated to cope with the disturbance in the exchange information $\mathcal{I}(k_h)$ of the vehicle h ($h \in \mathbb{N}(t_i(0))$, $h<i$, and $i \in \mathcal{C}_h \cup \mathcal{L}_h$). Moreover the following assumptions are imposed to guarantee the feasibility of (8.34):

$$\mathbb{S}_i \subset \mathbb{X}_i, \quad K_i\bar{\mathbb{S}}_i \subset \mathbb{U}_i\,.$$

The assumptions above ensure the existence of tightened sets for the nominal state $\bar{x}_i(k)$ and input $\bar{u}_i(k)$ such that the actual state $x_i(k)$ and input $u_i(k)$ of the controlled system $x_i(k+1)=A_i x_i(k)+B_i u_i(k)+\omega_i(k)$ with feedback-loop $u_i(k)=\bar{u}_i(k)+K_i(\hat{x}_i(k)-\bar{x}_i(k))$ satisfy the original constraints $x_i(k) \in \mathbb{X}_i$ and $u_i(k) \in \mathbb{U}_i$ for all admissible disturbances $\omega_i(k)$ and $\nu_i(k)$.

Therefore, this work proposes an RMPC-based HRCS designed based on the nominal system (8.21c). At an update instant k, the tube-based RMPC in the lower-level finds the optimal control sequence $\bar{\mathbf{u}}_i^*(k)=\{\bar{u}_i^*(k|k),\bar{u}_i^*(k+1|k),\ldots,\bar{u}_i^*(k+N_p-1|k)\}$ and the optimal state sequence $\bar{\mathbf{x}}_i^*(k)=\{\bar{x}_i^*(k|k),\bar{x}_i^*(k+1|k),\ldots,\bar{x}_i^*(k+N_p|k)\}$ by solving the following convex RMPC problem:

OCP 8.4.

$$\min_{\bar{\mathbf{u}}_i(k)} \ \bar{J}_{d,i}(\bar{\mathbf{x}}_i(k),\bar{\mathbf{u}}_i(k)) \tag{8.35a}$$

$$\textbf{\textit{s.t.}} \ \bar{x}_i(k|k)=\hat{x}(k) \tag{8.35b}$$

$$\bar{x}_i(k+j+1|k)=A_i\bar{x}_i(k+j|k)+B_i\bar{u}_i(k+j|k) \tag{8.35c}$$

$$\bar{u}_i(k+j|k)\in\bar{\mathbb{U}}_i \tag{8.35d}$$

$$\bar{x}_i(k+j|k)\in\bar{\mathbb{X}}_i, \quad j=0,1,\cdots,N_p-1 \tag{8.35e}$$

$$\textbf{\textit{given}}: \hat{x}_i(0)\in\begin{cases}\mathbb{X}_i\ominus\mathbb{S}_i, \ \textit{if}\ i=1\\ \mathbb{X}_i\ominus\mathbb{S}_i\ominus\mathbb{S}_h, \ \textit{if}\ i>1\end{cases} \tag{8.35f}$$

where $\bar{\mathbf{x}}_i(k)\in\mathbb{R}^{(N_p+1)\times 2}$, $\bar{\mathbf{u}}_i(k)\in\mathbb{R}^{N_p\times 2}$, $k=0,1,\ldots,\alpha$, $\hat{x}(k)$ is obtained by the observer (8.30) at the instant k, and the given and bounded $\hat{x}(0)$ is the measured initial state (entry state at CZ) satisfying Assumptions 8.2. Moreover, $\bar{J}_{d,i}(\bar{\mathbf{x}}_i(k),\bar{\mathbf{u}}_i(k))$ is the augmented objective function of (8.17), which will be designed next.

Due to the receding horizon nature of MPC, there is a potential infeasibility issue when vehicles reach the MZ from perpendicular or opposite directions and the constraints related to MZ are not initially considered. To prevent the infeasibility, the objective function (8.17) in the lower-level RMPC of HRCS for vehicle $i\in\{\mathcal{L}_h,\mathcal{O}_h\}$ is augmented by relaxing constraints (8.7) and (8.9) as follows:

$$\bar{J}_{d,i}=J_{d,i}+W_3\left(\max\{0,\Delta t_i^{\mathcal{L}}-\Gamma_i^{\mathcal{L}}\}\right)^2+W_4\left(\max\{0,\Delta t_i^{\mathcal{O}}-\Gamma_i^{\mathcal{O}}\}\right)^2, \tag{8.36}$$

where $\Delta t_i^{\mathcal{L}}, \Delta t_i^{\mathcal{O}}\in\mathbb{R}_{>0}$ are predefined tuneable parameters, and $\Gamma_i^{\mathcal{L}}$ and $\Gamma_i^{\mathcal{O}}$ are the time difference of the constraints (8.7) and (8.9),

$$\Gamma_i^{\mathcal{L}}=t_i^{\mathcal{L}}-\hat{t}_h^{\mathcal{L}}, \tag{8.37}$$

$$\Gamma_i^{\mathcal{O}}=t_i^{\mathcal{O}}-\hat{t}_h^{\mathcal{O}}. \tag{8.38}$$

Tuneable parameters $\Delta t_i^{\mathcal{L}}$ and $\Delta t_i^{\mathcal{O}}$ of a similar nature have been introduced in [26], but in a rather simpler non-robust framework for autonomous intersection management with a limited number of vehicles, simple vehicle modelling, and a different shrinking MPC horizon technique. Thus, if the time difference between vehicle i and h is large enough ($\Gamma_i^{\mathcal{L}} > \Delta t_i^{\mathcal{L}}$ and $\Gamma_i^{\mathcal{O}} > \Delta t_i^{\mathcal{O}}$), for $i \in \mathcal{L}_h \cup \mathcal{O}_h$ the augmented objective function (8.36) is identical to the original objective function (8.17). On the other hand, the augmented terms in (8.36) encourage the ith vehicle to gradually accelerate or decelerate in advance to maintain a time gap equal to the predefined parameters from the hth vehicle over the entire mission ($\Gamma_i^{\mathcal{L}} = \Delta t_i^{\mathcal{L}}$ and $\Gamma_i^{\mathcal{O}} = \Delta t_i^{\mathcal{O}}$). In this way, the hard braking to satisfy the constraints (8.7) and (8.9) can be avoided when the ith vehicle enters the MZ. Taking $\Gamma_i^{\mathcal{L}}$ as an example, it is specified as below:

$$
\begin{aligned}
&1)\ \text{if } k+N_p < \alpha_1 \wedge k_h - k \leq \alpha_2 + \alpha_3 \\
&t_i^{\mathcal{L}} = t_i(k+N_p|k) \\
&\hat{t}_h^{\mathcal{L}} = \begin{cases} \bar{t}_h(k_h+l+1|k_h), & \text{if } l<N_p,\ k_h+l+1=k+\alpha_2+\alpha_3, \\ \bar{t}_h(k_h+N_p|k_h)+\dfrac{[k+\alpha_2+\alpha_3-(k_h+N_p)]\Delta s}{\bar{v}_h(k_h+N_p|k_h)}, & \text{if } k_h+N_p < k+\alpha_2+\alpha_3, \end{cases}
\end{aligned}
\tag{8.39a}
$$

$$
\begin{aligned}
&2)\ \text{if } k+N_p \geq \alpha_1 \wedge k < \alpha_1 \\
&t_i^{\mathcal{L}} = t_i(k+j+1|k),\ k+j+1 = \alpha_1 \\
&\hat{t}_h^{\mathcal{L}} = \begin{cases} \bar{t}_h(k_h+l+1|k_h), & \text{if } l<N_p,\ k_h+l+1=\alpha, \\ \bar{t}_h(k_h+N_p|k_h)+\displaystyle\sum_{\beta=1}^{\alpha-(k_h+N_p)}\frac{\Delta s}{\hat{v}(\beta)}, & \text{if } k_h+N_p < \alpha, \end{cases}
\end{aligned}
\tag{8.39b}
$$

where $l \in \mathbb{N}_{[0,N_p-1]}$, and k_h, similarly to the earlier definition, stands for the associated step of the hth CAV such that $t_h(k_h\Delta s) = t_i(k\Delta s)$. The first case activates when the ith and the hth vehicles have a similar remaining distance to the entry of the MZ. The formulation encourages the ith vehicle to preserve a predefined time gap $\Delta t_i^{\mathcal{L}}$ for $\alpha_2+\alpha_3$ step-ahead space (equivalent to distance length $S+l_h$) to the hth vehicle before entering the MZ. As such, the effect of the lateral collision constraint (8.7) is considered from the start of the mission, and eventually the potential infeasibility issue in MPC framework when the ith vehicle and the hth vehicle reach the MZ at a similar time can be avoided. In the second case, as reflected by (8.39b), the lateral collision avoidance constraint (8.7) should still remain, and in discretised format it is described as follows:

$$
t_i^{\mathcal{L}} - \hat{t}_h^{\mathcal{L}} \geq 0, \quad \text{if } k+N_p \geq \alpha_1 \wedge k < \alpha_1, \tag{8.40}
$$

where the upper part of $\hat{t}_h^{\mathcal{L}}$ in (8.39b) implies that the time of the hth vehicle at the position $(L+S+l_h)$ can be obtained straightforwardly in the present space window. If the desired time at the position $(L+S+l_h)$ is unavailable, the lower part of $\hat{t}_h^{\mathcal{L}}$ in (8.39b) provides an estimation method, where the hth CAV will finish the rest of the mission at a conservatively (the slowest) estimated speed $\hat{v}(\beta)$, which is calculated based on the terminal speed of the present horizon and the minimum deceleration of the kinetic energy as below:

$$\hat{v}(\beta)=\max\left\{\sqrt{2\left(\bar{E}_h(k_h+N_p|k_h)-\beta\left.\frac{dE_h(s)}{ds}\right|_{\min}\right)/m_i}, v_{\min}\right\}$$

with

$$\left.\frac{dE_h(s)}{ds}\right|_{\min}=F_{w,\min}-F_{r,i}-f_{d,i}v_{\max}^2 \text{ is a constant.}$$

Note that the estimated speed $\hat{v}(\beta)$ and the index $\beta\in[1,\alpha-(k_h+N_p)]$ can be predetermined before the optimization. By analogy to the definition (8.39) of $\Gamma_i^{\mathcal{L}}$, the definition and estimation of $\Gamma_i^{\mathcal{O}}$ can also be obtained. The prioritisation constraint (8.9) in discretised form is then written as follows:

$$t_i^{\mathcal{O}}-\hat{t}_h^{\mathcal{O}}\geq 0,\quad \text{if } k+N_p\geq\alpha_1\wedge k<\alpha_1. \tag{8.41}$$

Corollary 8.1. *By finely tuning the parameters $\Delta t_i^{\mathcal{L}}$ and $\Delta t_i^{\mathcal{O}}$, the solution of the MPC problem always satisfies condition* (8.12) *with equality, and therefore the solution of the MPC problem is valid under Proposition 8.1.*

Proof. See in Appendix III-C.

Remark 8.2. *The convex tightened sets $\bar{\mathbb{U}}_i$ and $\bar{\mathbb{X}}_i$ in* (8.34) *for each vehicle i can be computed offline in a decentralised manner to increase computational efficiency.*

Remark 8.3. *Given a crossing order obtained in the upper level of the HRCS, there might be a case where no valid solution can be found in the lower level due to the discrepancy appearing between the upper and lower optimisation problems. This can be addressed by recursively solving the lower-level problem with continually reducing $v_{\min}$, and it terminates when a valid solution is found.*

8.4 Numerical Results

The evaluation of the proposed HRCS is listed below: 1) the effectiveness of the proposed convexified HRCS is verified and compared with benchmark solutions obtained by a nominal MPC-based strategy under the same initial conditions; 2) a comparison between the HRCS and a benchmark using the same tube-based MPC algorithm but following the FIFO policy to show the better performance of the designed upper-level crossing order scheduler; 3) the lower-level tube-based RMPC (8.35) is solved for different weighting combinations $\{W_1, W_2\}$ of (8.36) under fixed values of $\{W_3, W_4\}$ and a series of different arrival rates to show the trade-off between energy cost and travel time as well as the impact of the traffic density on the overall optimality; 4) the trade-offs between the robustness and the optimality are investigated; 5) the computational time with respect to the size of the sampling interval is investigated to show the validity of the method in potential practical application.

For the sake of fair comparison, a terminal speed condition is imposed for all CAVs:

$$\frac{1}{2}mv_f^2 - \gamma_i \leq E_i(L+S+l_i) \leq \frac{1}{2}mv_f^2 + \gamma_i \tag{8.42}$$

where $v_f \in [v_{\min}, v_{\max}]$ is a predefined terminal speed, and $\gamma_i \in \mathbb{R}_{>0}$ is an auxiliary optimisation variable, which is introduced to avoid potential feasibility issues caused by additive disturbances (i.e. process noise ω_i and measurement noise ν_i). The terminal condition (8.42) encourages all CAVs to reach the same terminal speed when leaving the MZ by minimising γ_i in the objective function, $\bar{J}_{i,k} + W_5 \cdot \gamma$. Note that it is straightforward to relax (8.42) with non-uniform terminal speeds.

Moreover, for the sake of simplicity, the simulation in this work assumes all CAVs to be identical, with the main characteristic parameters of each vehicle model are summarised in Table 8.1. In the following case studies, the parameters of the intersection are $L = 150$ m and $S = 10$ m with sampling interval $\Delta s = 2$ m. The bounds of the external disturbances ω_i and ν_i are $\overline{\omega}_{E,i} = \frac{1}{2}m\overline{\omega}_{v,i}^2$, $\overline{\nu}_i = [\frac{1}{2}m\overline{\nu}_{v,i}^2, \overline{\nu}_{t,i}]^\top$ where $\overline{\omega}_{v,i} = \overline{\nu}_{v,i} = 0.1\ m/s$ and $\overline{\nu}_{t,i} = 0.1\ s$. The values of the tuneable parameters in (8.36) are predefined to be $\Delta t_i^{\mathcal{L}} = \Delta t_i^{\mathcal{O}} = 0.4$ s based on consideration of the intersection dimensions. The minimum allowed time gap in (8.6) is set to $t_\delta = 1$ s, which is chosen as such due to the expectation that CAVs can cope safely

Table 8.1 Electric vehicle model parameters

description	symbol	value
vehicle mass	m_i	1200 kg
vehicle body length	l_i	4 m
wheel radius	$r_{w,i}$	0.3 m
transmission gear ratio	$g_{r,i}$	3.5
rolling resistance coefficient	$f_{r,i}$	0.01
air drag resistance coefficient	$f_{d,i}$	0.47
minimum velocity	$v_{\min}$	0.1 m/s
maximum velocity	$v_{\max}$	15 m/s
minimum acceleration	$a_{\min,i}$	-6.5 m·s^{-2}

with further reduced headway distances than human-driven vehicles. For illustrative and comparative purposes, let us consider a case with $N = 20$ CAVs all of which are assumed to leave the intersection (the MZ) at the same terminal speed $v_f = 10$ m/s. Without loss of generality, the control problem is initialised with randomised initial conditions $v_i(0)$ and $t_i(0)$ for all CAVs subject to the constraints imposed in Assumptions 8.2. In particular, CAVs' initial speeds follow a uniform distribution within $[v_{\min}, v_{\max}]$, while their arrival times, $t_i(0)$, follow a Poisson distribution. Moreover, the entry direction of each CAV is also randomly generated. The proposed HRCS is solved by using YALMIP and MOSEK [205] in Matlab on a personal computer with Intel Core i5 2.9 GHz and 8 GB of RAM.

In the first instance, the proposed method is solved with prediction horizon length $N_p = 15$ at an arrival rate of 800 veh/h (vehicles per hour) per lane, which is ordinary for practical intersections. The weighting factors are set to emphasise more on the travel time rather than energy consumption in the objective function. Fig. 8.3 presents the optimal travelled distance profile subject to an average travel time 12.31 s. As it can be seen, by giving the order $\mathcal{N}$ defined in the upper-level, the lower-level RMPC coordinates the CAVs such that no CAVs violate the rear-end and lateral collision constraints, which verifies the validity of the optimal solution. An example of lateral collision avoidance can be found in vehicle 12 and vehicle 13, where vehicle 13 will not be allowed to enter the MZ until the ahead vehicle 12 has left.

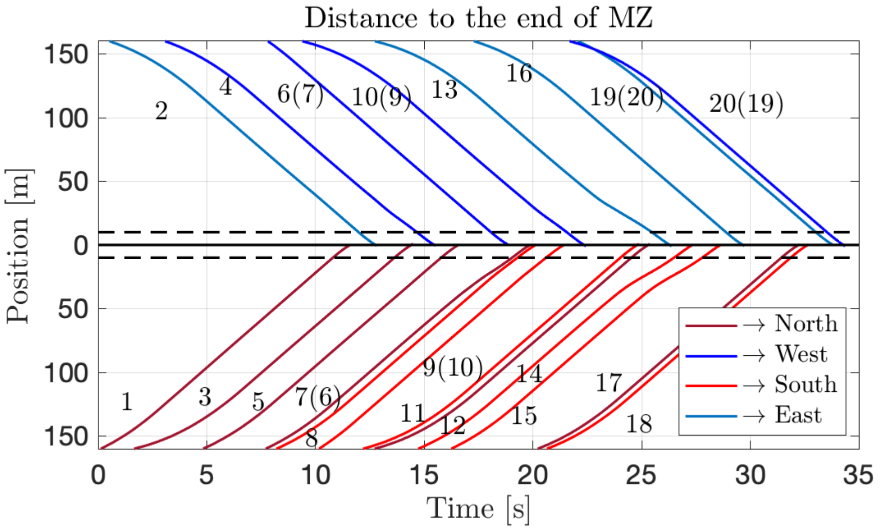

Fig. 8.3 Travelled distance trajectories (distance to the end of MZ) by solving the HRCS subject to an average travel time 12.31 s at an arrival rate of 800 veh/h per lane and with prediction horizon length $N_p = 15$. The horizontal dashed lines correspond to the entry of the MZ, while the horizontal continuous black line denotes the end of the MZ. The four vehicle heading directions are denoted using different colours. Note that the numbers in the brackets highlight the arriving orders of the vehicles at the CZ, which are different from their order entering the MZ. The upper-level scheduler sorts the vehicles in order of $\mathcal{N} = \{1, 2, 3, 4, 5, 7, 6, 8, 10, 9, 11, 12, 13, 14, 15, 16, 17, 18, 20, 19\}$.

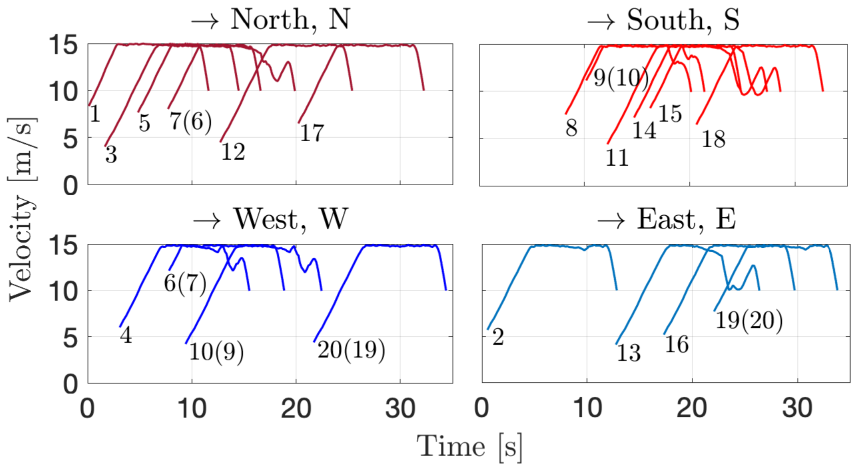

Fig. 8.4 Optimal speed profiles by solving the HRCS subject to an average travel time 12.31 s for all CAVs at an arrival rate of 800 veh/h per lane. Note that the numbers in the brackets highlight the arriving orders of the vehicles at the CZ, which are different from their order entering the MZ.

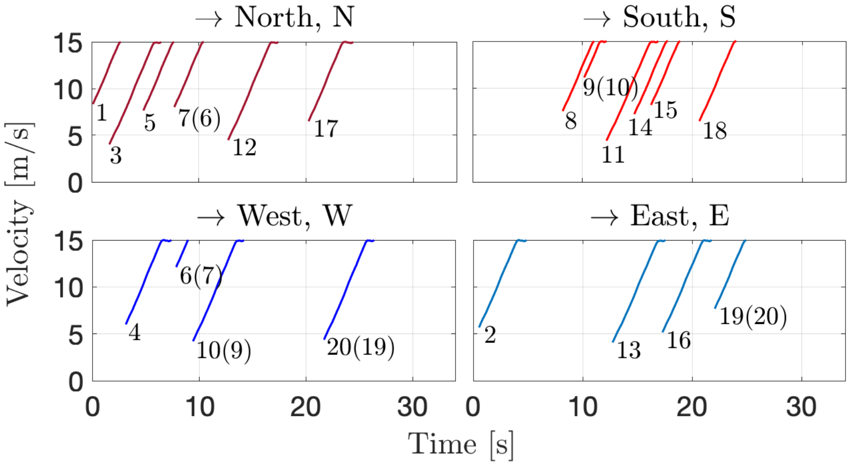

Fig. 8.5 Optimal speed profiles by solving the nominal MPC-based strategy under the same initial conditions as the results in Fig. 8.4. Note that the numbers in the brackets highlight the arriving orders of the vehicles at the CZ, which are different from their order entering the MZ.

The effectiveness of rear-end collision avoidance can be identified as the solution has no intersections between trajectories of the same colour throughout the CZ.

To verify the robustness of the proposed method, a comparison of the optimal speed trajectories with benchmark solutions obtained by a nominal MPC-based strategy under the same initial conditions and an average travel time 12.31 s can be found in Fig. 8.4 and Fig. 8.5, respectively, where the speed profiles in both scenarios are grouped based on the heading directions for illustration purposes. As it can be seen in Fig. 8.4, the velocity profiles of most CAVs solved by the proposed robust method tend to cruise at a constant speed and apply more intensive braking when approaching the exit of the MZ, which is due to the energy recovery in the powertrain of the battery electric vehicles. In some cases, if two vehicles have a potential collision inside the MZ and reach the MZ at a close time, the speed may not follow the foregoing trajectories due to the introduction of the augmented objective function (8.36). For example, the speed profiles of CAV 7 and CAV 13 exhibit early deceleration when approaching the MZ to preserve enough time gaps for lateral collision avoidance. To deal with the impact of external disturbances, the robust invariant tubes in HRCS prevent the peak speed from reaching the maximum allowed velocity by a margin even though in this case the emphasis is more on travel time than energy consumption. However, the peak speed in the nominal MPC-based strategy case (see in Fig. 8.5) remains at the constant value at $v_{\max} = 15$ m/s, which leads to fragile feasibility when it comes to disturbances. As a result, infeasible solutions are yielded by the nominal MPC-based strategy, which violate the speed constraints.

The optimality of the proposed method is firstly investigated by comparing with a benchmark solution using the same decentralised tube-based MPC algorithm for the lower-level trajectory optimisation but following the FIFO policy. As it can be seen in Fig. 8.6, owing to the proposed upper-level crossing scheduler, the HRCS as compared to the benchmark can reach a more energy-time efficient solution. In particular, when the average travel time is 12.72 s, the proposed method can save up to 16.35% energy consumption over the benchmark.

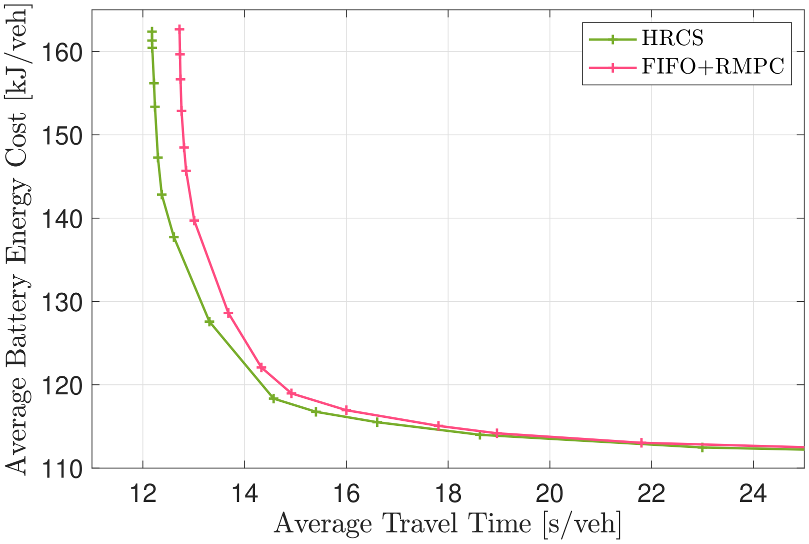

Fig. 8.6 Comparison of the energy-time cost trade-off between the proposed method and a benchmark using the same tube-based MPC following the FIFO policy with prediction horizon length $N_p = 15$ at an arrival rate of 800 veh/h per lane.

In order to investigate the impact of the prediction horizon length and the traffic density in HRCS, the trade-off between travel time and energy consumption for a series of combinations of the weight factors, W_1 and W_2, (under the same initial conditions and fixed W_3, W_4 and W_5) and for different prediction horizon lengths and arrival rates, are presented in Fig. 8.7 and Fig. 8.8, respectively. For both cases, the Pareto front results point out the importance of examining the energy-time trade-off, as a small change in the travel time can significantly affect the energy efficiency. For example, when the proposed HRCS method is used with prediction horizon length $N_p = 15$ under the arrival rate of 800 vehicle per hour per lane,

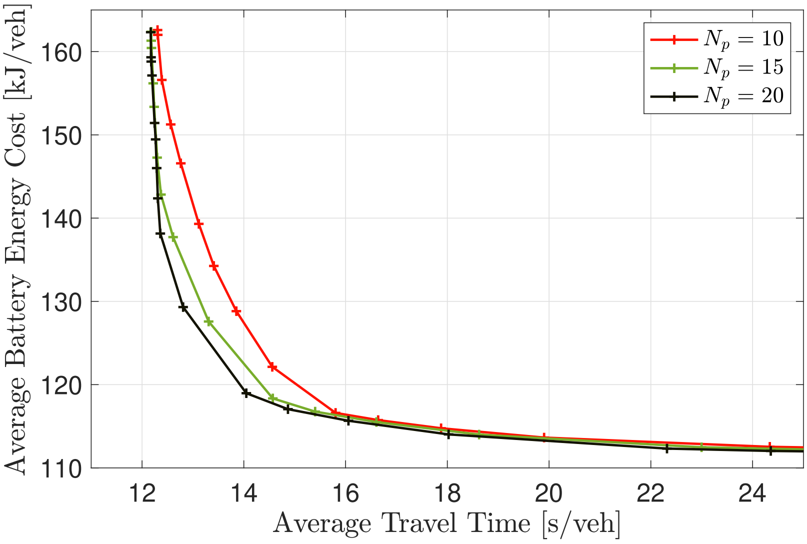

Fig. 8.7 The trade-offs between average battery energy consumption and average travel time at the arrival rate of 800 veh/h per lane for the decentralised HRCS with varied prediction horizon length $N_p = \{10, 15, 20\}$.

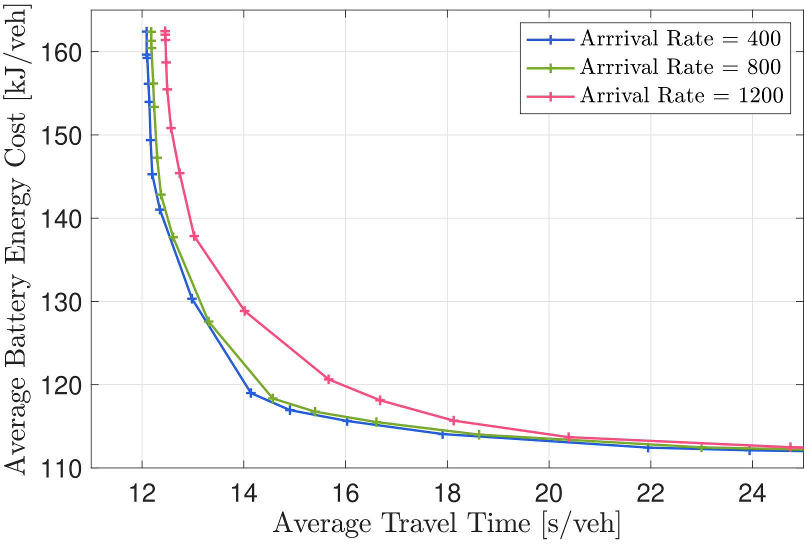

Fig. 8.8 The trade-offs between average battery energy consumption and average travel time with prediction horizon length $N_p = 15$ at different arrival rates from 400 to 1200 veh/h per lane for the decentralised HRCS.

an increase of 20% in travel time (from 12.18 s to 14.6 s) can lead to an average energy consumption reduction of 26.71%, while further increase in travel time can eventually yield up to 30.43% energy consumption reduction. In Fig. 8.7, the comparison among the three prediction horizon lengths indicates that the overall optimality increases as the N_p increases. The reason is that increasing the horizon tends to enhance the ability to anticipate the future behaviour of each CAV to satisfy the collision constraints, at a price of higher computational burden. However, the improvement in terms of energy consumption optimality from $N_p = 15$ to 20 is less than 6.1% for most cases, and therefore, the subsequent studies in this paper adopt $N_p = 15$ in the lower-level RMPC of the proposed HRCS.

Moreover, by comparing the results at different arrival rates from 400 to 1200 veh/h per lane, it can be observed in Fig.8.8 that the overall optimality deteriorates as the traffic density increases. The reason is that a higher arrival rate implies a higher traffic density condition, where the motions of vehicles are more restrained by the surrounding vehicles, and therefore, the optimal solution tends to be compromised by collision avoidance requirements. When most weight is placed on the travel time term ($W_2 \gg W_1$), an optimality gap can be observed between the cases with arrival rate of 800 and 1200 veh/h per lane, which indicates that with an emphasis on the travel time minimisation, the optimisation encourages the CAVs to travel at maximum speed, which yields more restrictive solutions due to the tougher collision avoidance constraints in such cases, and the restrictiveness rises as the arrival rate increases. As the weight W_1 for the energy cost is gradually increased, the optimality deteriorates, resulting in a maximum gap of 12.4% for the case with arrival rate of 800 veh/h per lane as compared to the case with arrival rate of 1200 veh/h per lane when the average travelled time is 12.45 s, and after this time the gap gets closer and gradually becomes negligible. The reason is that when the travel time is relaxed, there exists more room for speed optimisation, and optimal solutions in terms of energy consumption become similar. Finally, it has been found that further decrease in the arrival rate below 400 veh/h makes negligible impact on the optimality, as the traffic is sufficiently sparse to allow free optimisation of each velocity trajectory without concession to other vehicles.

To construct the relationship between the average time gap and energy consumption, an example case of the solutions caused by tougher collision constraints (with more emphasis on the travelled time) is investigated. Table. 8.2 presents the average time gap at different arrival rates with a fixed average traveled time 12.51 s. As it can be seen, there is an upward trend from left to right (as the arrival rate increases from 400 veh/h to 1200 veh/h) in the energy cost from 139.1 kJ to 164.48 kJ. Meanwhile, the average time gap decreases from 9.29 s to 1.69 s as the arrival rate increases from 400 veh/h to 1200 veh/h. This can be understood that

Table 8.2 Average time gap at different arrival rates with a fixed average travel time 12.51 s with $t_\delta = 1$ s.

Arrival Rate [veh/h]	400	800	1200
Average Energy Cost [kJ]	139.10	139.40	164.48
Average Time Gap [s]	5.44	2.57	1.69
Minimum Time Gap [s]	3.30	1.26	1.10
Maximum Time Gap [s]	9.29	4.56	2.98

Table 8.3 Average travel time and time gap with a fixed average energy cost 146.55 kJ and $t_\delta = 1$ s for different RMPC designs.

$\{\bar{\omega}_{v,i}, \bar{v}_{v,i}, \bar{v}_{t,i}\}$	$\{0.1, 0.1, 0.1\}$	$\{0.2, 0.2, 0.2\}$	$\{0.3, 0.3, 0.3\}$
Average Travel Time [s]	12.3‘	12.89	13.63
Average Time Gap [s]	2.56	2.57	2.60
Minimum Time Gap [s]	1.26	1.52	1.73
Maximum Time Gap [s]	4.56	4.56	4.56

increased traffic density could result in severe congestion and more acceleration/deceleration behavior, and therefore reduced time gap and higher energy consumption.

To further investigate the trade-off between robustness and optimality, further simulation trials are carried out, where disturbance bounds are conservatively used in the design of RMPC due to the lack of precise knowledge of the disturbances (commonly encountered in the practice). Recalling the disturbance bounds given in Section 8.4 (identical for all disturbance sources $\overline{\omega}_{v,i} = \overline{v}_{v,i} = 0.1\ m/s$ and $\overline{v}_{t,i} = 0.1\ s$), under the same initial conditions and disturbances, two additional RMPCs are designed and simulated with more conservative bounds of 0.2 and 0.3, respectively. The comparative results are shown in Table 8.3. As it can be seen, when the average energy cost is fixed at 146.55 kJ, doubling the bound in the RPMC design can increase the travel time by 4.72%, and the figure goes up to 10.8% when the bound is tripled. The results can be understood that the greater disturbance bound leads to the more conservative RMPC design in terms of the constraints tightening (reduced feasibility), which is reflected in the minimum time gaps show in the Table 8.3. Nevertheless, the maximum time gaps are not affected as no upper limit is imposed for the time gap between CAVs.

The proposed HRCS computational time of a single CAV i at every step with the sampling interval $\Delta s = 2\,\mathrm{m}$ is shown in Fig. 8.9. The dashed line denotes the estimated permissible computational time at every interval distance Δs in the space domain, obtained by $\Delta s / v_i(k)$. As it can be seen, the computational time of vehicle i is strictly below the maximum allowed time, which validates the implementation potential of the proposed HRCS approach.

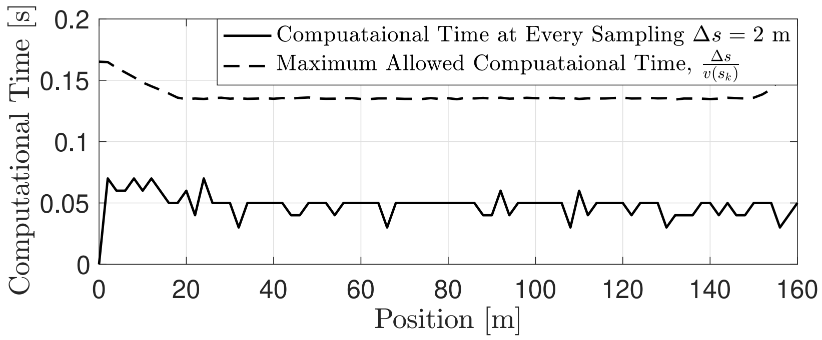

Fig. 8.9 Computational time of an example CAV i and the corresponding maximum allowed computational time $\Delta s/v_i(k)$ with sampling $\Delta s = 2\,\mathrm{m}$ by solving the decentralised HRCS problem.

8.5 Conclusions

This chapter proposes a new hierarchical robust control strategy, HRCS for decentralised autonomous intersection coordination of connected and autonomous electric vehicles. The HRCS determines the optimal crossing order and velocity trajectories successively using an optimal control method and a tube-based RMPC in a decentralised traffic coordination scheme. In particular, the RMPC can cope with the additive disturbances and modelling uncertainties entailed in the vehicle dynamic model and onboard sensor measurements, and therefore, it is the key to securing safety in reality. The optimisation problems entailed in the control framework are solved as convex SOCPs with a suitable relaxation and spatial modelling approach, which can guarantee a fast and unique solution. The equivalence between the relaxed and the original problems is validated.

Numerical examples verify the effectiveness and robustness of the proposed HRCS by comparisons against a nominal MPC-based strategy. The energy-time trade-off is examined for different prediction horizon lengths and arrival rates by finding the Pareto front of optimal solutions. The Pareto front shows an increase of 20% in travel time can lead to an average energy consumption reduction of about 24% at an arrival rate of 800 veh/h per lane with prediction horizon length $N_p = 15$. Finally, the computational efficiency of the convex HRCS is examined for a distance interval $\Delta s = 2$ m and the results show the practical potential of the proposed scheme.

Part IV

Conclusions and Appendixes

Chapter 9

Conclusions and Future Prospects

9.1 Concluding Remarks

CAVs are considered as a crucial transportation tool in the near future to improve traffic conditions (efficiency, safety, ecology and passenger comfort), and significant research efforts have been made on designing controllers for CAVs to optimise their performance within safe operating conditions. This thesis first of all provides a thorough review of the optimal control strategies for CAVs in three different driving scenarios, i.e. optimal EM of a single CAV (single-vehicle), energy-optimal strategy for the vehicle following scenario (two-vehicle), and optimal autonomous intersection management for CAVs (multi-vehicle), followed by a description of vehicle dynamics and powertrain model in terms of HEVs and BEVs. The control strategies proposed in this thesis are then categorised into three parts based on the above classification of driving scenarios. A summary of these strategies is listed below:

Optimal EM for a Single vehicle: Part I of the thesis addresses the EM problems of a single automated series HEV with consideration of engine SSS and battery charge sustaining operation. A novel rule-based EM control strategy, HPTS, is proposed for a series HEV to optimise its fuel economy with engine SSS associated with extra penalty fuel for engine restarts. The HPTS combines two operation modes, battery-only mode and hybrid/engine-only mode, of which the switch mechanism is determined by a tuneable power offset and two power thresholds. The simulation results verify the effectiveness of the proposed method with consideration of the SSS by benchmarking the solutions against the results solved by DP and another rule-based method, the XOS. Moreover, the overall performance of HPTS can be optimised for different vehicle parameters and driving cycles through a systematic tuning process.

Energy-Optimal Strategy for Vehicle Following Scenario: Part II proposes two energy-optimal control strategies via MPC framework to cope with the uncertainties existing in the vehicle following paradigm. To forecast the velocity of the preceding vehicle, an EACC method is designed with the incorporation of an NN velocity predictor. By benchmarking against the full-horizon solutions solved by an OCP and a suitably designed ACC, the performance of EACC is able to save more energy consumption than that of the ACC and a remarkable reduction in computational burden can be found as compared to that of OCP. The second control strategy considers the uncertainties existing in the V2V communication and the modelling error. As such, a convex LMI-based RMPC is designed for the ACC problem with SDPR to formulate the control problem into LMIs so as to optimise the energy efficiency of the controlled vehicle. A comparison between the RMPC and a nominal MPC under the same initial conditions verifies the robustness of the RMPC method. Further investigations on the prediction horizon length and computational time illustrate the importance of optimising the trade-off between energy consumption and computational burden, as a small compromise in computational time can significantly reduce the energy cost.

Optimal Autonomous Intersection Management for CAVs: In Part III, the signal-free intersection crossing problem for electric CAVs is addressed by two hierarchical cooperative vehicle management control strategies formulated in the space domain. As such, the OCPs can be respectively suitably relaxed as convex SOCP problems, which ensures a rapid search for solutions. The equivalency between the relaxed and the original problems is characterised by rigorous mathematical proof. The hierarchical scheme is designed to minimise a weighted sum of the aggregate electric energy consumption and travelling time required to drive through the junction by sequentially optimising the passing order and explicit velocity trajectories of the CAVs in two stages. The Pareto solutions emphasise the importance of optimising their trade-off, as a compromise in travel time could lead to a significant decrease in energy cost. By comparing the optimal solutions to those of a benchmarking method using FIFO, the proposed hierarchical scheme outperforms it in both energy and time savings. In particular, the first developed strategy focuses on a centralised coordination scheme with turning manoeuvres considered. Simulation results verify the validity and computational efficiency of the centralised hierarchical SOCP problem. Further investigation on the optimality shows the approximated convex SOCP is able to achieve feasible solutions close to a valid lower bounding solution of the original problem. The second developed strategy aims to improve the computational efficiency and counter the potential additive disturbances and modelling uncertainties entailed in the vehicle dynamic model and onboard sensor measurements, and therefore, a decentralised robust control strategy, HRCS, is proposed. The robustness is enhanced by a tube-based RMPC. Numerical examples verify the effectiveness and robustness of the proposed method by comparing it against a nominal MPC. Further investigation on the computational efficiency and the trade-off between robustness and optimality show the potential of HRCS for practical implementation.

9.2 Future Work

This section is devoted to highlighting possible extensions of the presented methodologies. These extensions are also explored for three different scenarios. In terms of the methodologies for the EM in a single automated vehicle case, future work can focus on the integration of additional modelling details and real-time implementation. For instance, the proposed HPTS can be extended by incorporating driving speed prediction and joint optimisation of both engine-out emissions and fuel consumption via the MPC technique or data-driven optimisation method. Moreover, robust optimisation schemes are necessary to be developed to cope with the uncertainty in model and decision parameters.

In terms of the other two scenarios, vehicle following strategy and autonomous intersection management, future direction focuses on more realistic vehicle dynamics and realistic traffic scenarios. The lateral dynamics of the controlled vehicle will be considered such that overtaking action can be included in the modelling framework, where a Boolean control variable could be used to represent the overtaking decision, and the OCP becomes a mixed-integer programming problem. The mathematical models of the autonomous intersection crossing problems in this thesis have only two lanes per road and lane changes are not allowed. Therefore, it is worth establishing a more realistic intersection model to emulate the real-world traffic scenario, where multiple lanes with waiting zones of turning and roundabouts can be included. Moreover, mixed traffic with human-driven vehicles is another direction. As such, the mathematical model of human driving vehicles and the traffic signals are required to be established. Besides, reinforcement learning can be utilised to predict the future state of the traffic environments, such as the traffic density at peak time, and the behaviour of the surrounding vehicles to enhance the performance of control strategies.

References

[1] A. Sharma and Z. Zheng, "Connected and automated vehicles: Opportunities and challenges for transportation systems, smart cities, and societies," *Automating Cities*, pp. 273–296, 2021.

[2] Q. Guo, L. Li, and X. J. Ban, "Urban traffic signal control with connected and automated vehicles: A survey," *Transportation Research Part C: Emerging Technologies*, vol. 101, pp. 313–334, 2019.

[3] J. Shuttleworth, "SAE Standards News: J3016 automated-driving graphic update," *SAE International*, 2019.

[4] K. Yang, Y. Huang, Y. Qin, C. Hu, and X. Tang, "Potential and challenges to improve vehicle energy efficiency via V2X: Literature review," *International Journal of Vehicle Performance*, vol. 7, no. 3-4, pp. 244–265, 2021.

[5] E. Farsimadan, F. Palmieri, L. Moradi, D. Conte, and B. Paternoster, "Vehicle-to-everything (V2X) communication scenarios for vehicular ad-hoc networking (VANET): An overview," in *Proceedings of the International Conference on Computational Science and Its Applications*. Springer, 2021, pp. 15–30.

[6] J. Guanetti, Y. Kim, and F. Borrelli, "Control of connected and automated vehicles: State of the art and future challenges," *Annual Reviews in Control*, vol. 45, pp. 18–40, 2018.

[7] The European Automobile Manufacturers' Association (ACEA), "New car registrations by fuel type, european union," https://www.acea.auto/files/20230201_PRPC-fuel_Q4-2022_FINAL-1.pdf, 2022, access date: 30 Apr. 2023.

[8] Goldman Sachs, "Electric vehicles: What's next VII: Confronting greenflation," *Global Automobiles, Equity Research, Goldman Sachs*, 2022.

[9] GOV.UK, "Decarbonising uk transport: technology roadmaps," https://www.gov.uk/government/publications/decarbonising-uk-transport-technology-roadmaps, 2021, access date: 30 Apr. 2023.

[10] G. Pasini, G. Lutzemberger, and L. Ferrari, "Renewable electricity for decarbonisation of road transport: Batteries or e-fuels?" *Batteries*, vol. 9, no. 2, p. 135, 2023.

[11] M. R. Wahid, B. A. Budiman, E. Joelianto, and M. Aziz, "A review on drive train technologies for passenger electric vehicles," *Energies*, vol. 14, no. 20, p. 6742, 2021.

[12] W. Shabbir and S. A. Evangelou, “Exclusive operation strategy for the supervisory control of series hybrid electric vehicles,” *IEEE Transactions on Control Systems Technology*, vol. 24, no. 6, pp. 2190–2198, 2016.

[13] ——, “Threshold-changing control strategy for series hybrid electric vehicles,” *Applied Energy*, vol. 235, pp. 761–775, 2019.

[14] S. Uebel, N. Murgovski, C. Tempelhahn, and B. Bäker, “Optimal energy management and velocity control of hybrid electric vehicles,” *IEEE Transactions on Vehicular Technology*, vol. 67, no. 1, pp. 327–337, 2018.

[15] R. Schmid, J. Bürger, and N. Bajcinca, “Efficient optimal control of plug-in-hybrid electric vehicles including explicit engine on/off decisions,” in *Proceedings of the 2018 European Control Conference (ECC)*. IEEE, 2018, pp. 596–601.

[16] A. Sciarretta, M. Back, and L. Guzzella, “Optimal control of parallel hybrid electric vehicles,” *IEEE Transactions on Control Systems Technology*, vol. 12, no. 3, pp. 352–363, 2004.

[17] T. Nüesch, P. Elbert, M. Flankl, C. Onder, and L. Guzzella, “Convex optimization for the energy management of hybrid electric vehicles considering engine start and gearshift costs,” *Energies*, vol. 7, no. 2, pp. 834–856, 2014.

[18] M. S. Schori, “Solution of optimal control problems for switched systems: Algorithms and applications for hybrid vehicles,” Ph.D. dissertation, Universiät Rostock. Fakultät für Informatik und Elektrotechnik, 2016.

[19] G. Gunter, C. Janssen, W. Barbour, R. E. Stern, and D. B. Work, “Model-based string stability of adaptive cruise control systems using field data,” *IEEE Transactions on Intelligent Vehicles*, vol. 5, no. 1, pp. 90–99, 2020.

[20] X. Lin and D. Görges, “Robust model predictive control of linear systems with predictable disturbance with application to multiobjective adaptive cruise control,” *IEEE Transactions on Control Systems Technology*, vol. 28, no. 4, pp. 1460–1475, 2020.

[21] B. Sakhdari and N. L. Azad, “Adaptive tube-based nonlinear MPC for economic autonomous cruise control of plug-in hybrid electric vehicles,” *IEEE Transactions on Vehicular Technology*, vol. 67, no. 12, pp. 11 390–11 401, 2018.

[22] S. Feng, H. Sun, Y. Zhang, J. Zheng, H. X. Liu, and L. Li, “Tube-based discrete controller design for vehicle platoons subject to disturbances and saturation constraints,” *IEEE Transactions on Control Systems Technology*, vol. 28, no. 3, pp. 1066–1073, 2020.

[23] Z. Zhong, M. Nejad, and E. E. Lee, “Autonomous and semiautonomous intersection management: A survey,” *IEEE Intelligent Transportation Systems Magazine*, vol. 13, no. 2, pp. 53–70, 2021.

[24] A. Gholamhosseinian and J. Seitz, “A comprehensive survey on cooperative intersection management for heterogeneous connected vehicles,” *IEEE Access*, vol. 10, pp. 7937–7972, 2022.

[25] Y. Bichiou and H. A. Rakha, “Real-time optimal intersection control system for automated/cooperative vehicles,” *International Journal of Transportation Science and Technology*, vol. 8, no. 1, pp. 1–12, 2019.

[26] L. Riegger, M. Carlander, N. Lidander, N. Murgovski, and J. Sjöberg, “Centralized MPC for autonomous intersection crossing,” in *Proceedings of the 2016 IEEE 19th International Conference on Intelligent Transportation Systems (ITSC).* IEEE, 2016, pp. 1372–1377.

[27] N. Chohan, M. A. Nazari, H. Wymeersch, and T. Charalambous, “Robust trajectory planning of autonomous vehicles at intersections with communication impairments,” in *Proceedings of the 2019 57th Annual Allerton Conference on Communication, Control, and Computing (Allerton).* IEEE, 2019, pp. 832–839.

[28] M. Khayatian, M. Mehrabian, and A. Shrivastava, “RIM: Robust intersection management for connected autonomous vehicles,” in *Proceedings of the 2018 IEEE Real-Time Systems Symposium (RTSS).* IEEE, 2018, pp. 35–44.

[29] C. Vitale, P. Kolios, and G. Ellinas, “Autonomous intersection crossing with vehicle location uncertainty,” *IEEE Transactions on Intelligent Transportation Systems*, vol. 23, no. 10, pp. 17 546–17 561, 2022.

[30] B. Chalaki and A. A. Malikopoulos, “A priority-aware replanning and resequencing framework for coordination of connected and automated vehicles,” *IEEE Control Systems Letters*, vol. 6, pp. 1772–1777, 2022.

[31] B. Chalaki and A. A. Malikopoulos, “Robust learning-based trajectory planning for emerging mobility systems,” in *Proceedings of the 2022 American Control Conference (ACC).* IEEE, 2022, pp. 2154–2159.

[32] L. Guzzella, A. Sciarretta *et al.*, *Vehicle propulsion systems.* Springer, 2007, vol. 1.

[33] C. M. Martinez, X. Hu, D. Cao, E. Velenis, B. Gao, and M. Wellers, “Energy management in plug-in hybrid electric vehicles: Recent progress and a connected vehicles perspective,” *IEEE Transactions on Vehicular Technology*, vol. 66, no. 6, pp. 4534–4549, 2017.

[34] D.-D. Tran, M. Vafaeipour, M. El Baghdadi, R. Barrero, J. Van Mierlo, and O. Hegazy, “Thorough state-of-the-art analysis of electric and hybrid vehicle powertrains: Topologies and integrated energy management strategies,” *Renewable and Sustainable Energy Reviews*, vol. 119, p. 109596, 2020.

[35] C. Yang, M. Zha, W. Wang, K. Liu, and C. Xiang, “Efficient energy management strategy for hybrid electric vehicles/plug-in hybrid electric vehicles: Review and recent advances under intelligent transportation system,” *IET Intelligent Transport Systems*, vol. 14, no. 7, pp. 702–711, 2020.

[36] B. Chen, X. Li, and S. Evangelou, “Comparative study of hybrid powertrain architectures from a fuel economy perspective,” in *Proceedings of the 14th International Symposium on Advanced Vehicle Control*, vol. 14. AVEC, 2018.

[37] A. Biswas and A. Emadi, "Energy management systems for electrified powertrains: State-of-the-art review and future trends," *IEEE Transactions on Vehicular Technology*, vol. 68, no. 7, pp. 6453–6467, 2019.

[38] F. Zhang, L. Wang, S. Coskun, H. Pang, Y. Cui, and J. Xi, "Energy management strategies for hybrid electric vehicles: Review, classification, comparison, and outlook," *Energies*, vol. 13, no. 13, p. 3352, 2020.

[39] F. Zhang, X. Hu, R. Langari, and D. Cao, "Energy management strategies of connected HEVs and PHEVs: Recent progress and outlook," *Progress in Energy and Combustion Science*, vol. 73, pp. 235–256, 2019.

[40] H. U. Ahmed, Y. Huang, and P. Lu, "A review of car-following models and modeling tools for human and autonomous-ready driving behaviors in micro-simulation," *Smart Cities*, vol. 4, no. 1, pp. 314–335, 2021.

[41] L. Xiao and F. Gao, "A comprehensive review of the development of adaptive cruise control systems," *Vehicle System Dynamics*, vol. 48, no. 10, pp. 1167–1192, 2010.

[42] S. P. Sathiyan, S. S. Kumar, and A. I. Selvakumar, "A comprehensive review on cruise control for intelligent vehicles," *International Journal of Innovative Technology and Exploring Engineering*, vol. 2, no. 5, pp. 89–96, 2013.

[43] J. Han, H. Shi, L. Chen, H. Li, and X. Wang, "The car-following model and its applications in the V2X environment: A historical review," *Future Internet*, vol. 14, no. 1, p. 14, 2021.

[44] J. Rios-Torres and A. A. Malikopoulos, "A survey on the coordination of connected and automated vehicles at intersections and merging at highway on-ramps," *IEEE Transactions on Intelligent Transportation Systems*, vol. 18, no. 5, pp. 1066–1077, 2017.

[45] L. Chen and C. Englund, "Cooperative intersection management: A survey," *IEEE Transactions on Intelligent Transportation Systems*, vol. 17, no. 2, pp. 570–586, 2016.

[46] E. Namazi, J. Li, and C. Lu, "Intelligent intersection management systems considering autonomous vehicles: A systematic literature review," *IEEE Access*, vol. 7, pp. 91 946–91 965, 2019.

[47] D. Čakija, L. Assirati, E. Ivanjko, and A. L. Cunha, "Autonomous intersection management: A short review," in *Proceedings of the 2019 International Symposium ELMAR*. IEEE, 2019, pp. 21–26.

[48] H. A. Borhan, A. Vahidi, A. M. Phillips, M. L. Kuang, and I. V. Kolmanovsky, "Predictive energy management of a power-split hybrid electric vehicle," in *Proceedings of the 2009 American Control Conference (ACC)*. IEEE, 2009, pp. 3970–3976.

[49] B. Zhang, Y. Deng, and D. Yu, "An investigation on energy management system of CJY6470 parallel hybrid electric off-road vehicle with fuzzy logic," in *Proceedings of the 2008 IEEE Vehicle Power and Propulsion Conference (VPPC)*. IEEE, 2008, pp. 1–9.

[50] J.-Y. Park, Y.-K. Park, and J.-H. Park, “Optimal power distribution strategy for series—parallel hybrid electric vehicles,” *Proceedings of the Institution of Mechanical Engineers, Part D: Journal of Automobile Engineering*, vol. 222, no. 6, pp. 989–1000, 2008.

[51] K. Ahn and P. Papalambros, “Engine optimal operation lines for power-split hybrid electric vehicles,” *Proceedings of the Institution of Mechanical Engineers, Part D: Journal of Automobile Engineering*, vol. 223, no. 9, pp. 1149–1162, 2009.

[52] B. Zhang, C. C. Mi, and M. Zhang, “Charge-depleting control strategies and fuel optimization of blended-mode plug-in hybrid electric vehicles,” *IEEE Transactions on Vehicular Technology*, vol. 60, no. 4, pp. 1516–1525, 2011.

[53] D. Sun, X. Lin, D. Qin, and T. Deng, “Power-balancing instantaneous optimization energy management for a novel series-parallel hybrid electric bus,” *Chinese Journal of Mechanical Engineering*, vol. 25, no. 6, pp. 1161–1170, 2012.

[54] X. Li and S. A. Evangelou, “Torque-leveling threshold-changing rule-based control for parallel hybrid electric vehicles,” *IEEE Transactions on Vehicular Technology*, vol. 68, no. 7, pp. 6509–6523, 2019.

[55] M. Kim, D. Jung, and K. Min, “Hybrid thermostat strategy for enhancing fuel economy of series hybrid intracity bus,” *IEEE Transactions on Vehicular Technology*, vol. 63, no. 8, pp. 3569–3579, 2014.

[56] F. U. Syed, D. Filev, and H. Ying, “Fuzzy rule-based driver advisory system for fuel economy improvement in a hybrid electric vehicle,” in *Proceedings of the NAFIPS 2007-2007 Annual Meeting of the North American Fuzzy Information Processing Society*. IEEE, 2007, pp. 178–183.

[57] S. Wahsh, H. Hamed, M. Nashed, and T. Dakrory, “Fuzzy logic based control strategy for parallel hybrid electric vehicle,” in *Proceedings of the 2008 IEEE International Conference on Mechatronics and Automation*. IEEE, 2008, pp. 27–31.

[58] A. Poursamad and M. Montazeri, “Design of genetic-fuzzy control strategy for parallel hybrid electric vehicles,” *Control Engineering Practice*, vol. 16, no. 7, pp. 861–873, 2008.

[59] H. Khayyam and A. Bab-Hadiashar, “Adaptive intelligent energy management system of plug-in hybrid electric vehicle,” *Energy*, vol. 69, pp. 319–335, 2014.

[60] A. Sciarretta, L. Serrao, P. Dewangan, P. Tona, E. Bergshoeff, C. Bordons, L. Charmpa, P. Elbert, L. Eriksson, T. Hofman *et al.*, “A control benchmark on the energy management of a plug-in hybrid electric vehicle,” *Control Engineering Practice*, vol. 29, pp. 287–298, 2014.

[61] A. Rousseau, S. Pagerit, and D. W. Gao, “Plug-in hybrid electric vehicle control strategy parameter optimization,” *Journal of Asian Electric Vehicles*, vol. 6, no. 2, pp. 1125–1133, 2008.

[62] M. Koot, J. T. Kessels, B. De Jager, W. Heemels, P. Van den Bosch, and M. Steinbuch, “Energy management strategies for vehicular electric power systems,” *IEEE Transactions on Vehicular Technology*, vol. 54, no. 3, pp. 771–782, 2005.

[63] J. Liu and H. Peng, “Modeling and control of a power-split hybrid vehicle,” *IEEE Transactions on Control Systems Technology*, vol. 16, no. 6, pp. 1242–1251, 2008.

[64] S. Nazari, J. Siegel, and A. Stefanopoulou, “Optimal energy management for a mild hybrid vehicle with electric and hybrid engine boosting systems,” *IEEE Transactions on Vehicular Technology*, vol. 68, no. 4, pp. 3386–3399, 2019.

[65] N. Kim, S. W. Cha, and H. Peng, “Optimal equivalent fuel consumption for hybrid electric vehicles,” *IEEE Transactions on Control Systems Technology*, vol. 20, no. 3, pp. 817–825, 2012.

[66] T. J. Boehme, M. Schori, B. Frank, M. Schultalbers, and W. Drewelow, “A predictive energy management for hybrid vehicles based on optimal control theory,” in *Proceedings of the 2013 American Control Conference (ACC)*. IEEE, 2013, pp. 5984–5989.

[67] B. Chen, S. A. Evangelou, and R. Lot, “Series hybrid electric vehicle simultaneous energy management and driving speed optimization,” *IEEE/ASME Transactions on Mechatronics*, vol. 24, no. 6, pp. 2756–2767, 2019.

[68] C. Hou, M. Ouyang, L. Xu, and H. Wang, “Approximate pontryagin’s minimum principle applied to the energy management of plug-in hybrid electric vehicles,” *Applied Energy*, vol. 115, pp. 174–189, 2014.

[69] Z. Wang, B. Huang, Y. Xu, and W. Li, “Optimization of series hybrid electric vehicle operational parameters by simulated annealing algorithm,” in *Proceedings of the 2007 IEEE International Conference on Control and Automation*. IEEE, 2007, pp. 1536–1541.

[70] Z. Chen, C. C. Mi, R. Xiong, J. Xu, and C. You, “Energy management of a power-split plug-in hybrid electric vehicle based on genetic algorithm and quadratic programming,” *Journal of Power Sources*, vol. 248, pp. 416–426, 2014.

[71] Z. Wang, B. Huang, W. Li, and Y. Xu, “Particle swarm optimization for operational parameters of series hybrid electric vehicle,” in *Proceedings of the 2006 IEEE International Conference on Robotics and Biomimetics*. IEEE, 2006, pp. 682–688.

[72] X. Lin, H. Banvait, S. Anwar, and Y. Chen, “Optimal energy management for a plug-in hybrid electric vehicle: Real-time controller,” in *Proceedings of the 2010 American Control Conference (ACC)*. IEEE, 2010, pp. 5037–5042.

[73] S.-i. Jeon, S.-t. Jo, Y.-i. Park, and J.-m. Lee, “Multi-mode driving control of a parallel hybrid electric vehicle using driving pattern recognition,” *Journal of Dynamic Systems Measurement and Control*, vol. 124, no. 1, pp. 141–149, 2002.

[74] C. Musardo, G. Rizzoni, Y. Guezennec, and B. Staccia, “A-ECMS: An adaptive algorithm for hybrid electric vehicle energy management,” *European Journal of Control*, vol. 11, no. 4-5, pp. 509–524, 2005.

[75] C. Zhang, A. Vahidi, P. Pisu, X. Li, and K. Tennant, "Role of terrain preview in energy management of hybrid electric vehicles," *IEEE Transactions on Vehicular Technology*, vol. 59, no. 3, pp. 1139–1147, 2010.

[76] G. Li and D. Goerges, "Hybrid modeling and predictive control of the power split and gear shift in hybrid electric vehicles," in *Proceedings of the 2017 IEEE Vehicle Power and Propulsion Conference (VPPC)*. IEEE, 2017, pp. 1–6.

[77] J. Zhang and T. Shen, "Real-time fuel economy optimization with nonlinear MPC for PHEVs," *IEEE Transactions on Control Systems Technology*, vol. 24, no. 6, pp. 2167–2175, 2016.

[78] R. Bartholomaeus, M. Klingner, and M. Lehnert, "Prediction of power demand for hybrid vehicles operating in fixed-route service," *IFAC Proceedings Volumes*, vol. 41, no. 2, pp. 5640–5645, 2008.

[79] W. Liu, G. Chen, and A. Knoll, "Matrix inequalities based robust model predictive control for vehicle considering model uncertainties, external disturbances, and time-varying delay," *Frontiers in Neurorobotics*, vol. 14, p. 110, 2021.

[80] M. Joševski and D. Abel, "Tube-based MPC for the energy management of hybrid electric vehicles with non-parametric driving profile prediction," in *Proceedings of the 2016 American Control Conference (ACC)*. IEEE, 2016, pp. 623–630.

[81] P. Pisu, E. Silani, G. Rizzoni, and S. M. Savaresi, "A lmi-based supervisory robust control for hybrid vehicles," in *Proceedings of the 2003 American Control Conference, 2003.*, vol. 6. IEEE, 2003, pp. 4681–4686.

[82] R. Bellman, "Dynamic programming," *Science*, vol. 153, no. 3731, pp. 34–37, 1966.

[83] D. Bertsekas, *Dynamic programming and optimal control: Volume I*. Athena Scientific, 2012, vol. 1.

[84] R. S. Gesser, D. M. Lima, and J. E. Normey-Rico, "Robust model predictive control: Implementation issues with comparative analysis," *IFAC-PapersOnLine*, vol. 51, no. 25, pp. 478–483, 2018.

[85] M. M. Morato, J. E. Normey-Rico, and O. Sename, "Model predictive control design for linear parameter varying systems: A survey," *Annual Reviews in Control*, vol. 49, pp. 64–80, 2020.

[86] Y. L. Murphey, J. Park, Z. Chen, M. L. Kuang, M. A. Masrur, and A. M. Phillips, "Intelligent hybrid vehicle power control—part I: Machine learning of optimal vehicle power," *IEEE Transactions on Vehicular Technology*, vol. 61, no. 8, pp. 3519–3530, 2012.

[87] R. Liu, D. Shi, and C. Ma, "Real-time control strategy of Elman neural network for the parallel hybrid electric vehicle," *Journal of Applied Mathematics*, vol. 2014, no. 1, pp. 1–11, 2014.

[88] H. Tian, X. Wang, Z. Lu, Y. Huang, and G. Tian, “Adaptive fuzzy logic energy management strategy based on reasonable soc reference curve for online control of plug-in hybrid electric city bus,” *IEEE Transactions on Intelligent Transportation Systems*, vol. 19, no. 5, pp. 1607–1617, 2017.

[89] X. Lin, P. Bogdan, N. Chang, and M. Pedram, “Machine learning-based energy management in a hybrid electric vehicle to minimize total operating cost,” in *Proceedings of the 2015 IEEE/ACM International Conference on Computer-Aided Design (ICCAD)*. IEEE, 2015, pp. 627–634.

[90] Y. Hu, W. Li, K. Xu, T. Zahid, F. Qin, and C. Li, “Energy management strategy for a hybrid electric vehicle based on deep reinforcement learning,” *Applied Sciences*, vol. 8, no. 2, p. 187, 2018.

[91] C. Sun, S. J. Moura, X. Hu, J. K. Hedrick, and F. Sun, “Dynamic traffic feedback data enabled energy management in plug-in hybrid electric vehicles,” *IEEE Transactions on Control Systems Technology*, vol. 23, no. 3, pp. 1075–1086, 2014.

[92] E. Kural and B. A. Güvenç, “Integrated adaptive cruise control for parallel hybrid vehicle energy management,” *IFAC-PapersOnLine*, vol. 48, no. 15, pp. 313–319, 2015.

[93] S. E. Li, H. Peng, K. Li, and J. Wang, “Minimum fuel control strategy in automated car-following scenarios,” *IEEE Transactions on Vehicular Technology*, vol. 61, no. 3, pp. 998–1007, 2012.

[94] L. Li, X. Wang, and J. Song, “Fuel consumption optimization for smart hybrid electric vehicle during a car-following process,” *Mechanical Systems and Signal Processing*, vol. 87, pp. 17–29, 2017.

[95] K. Huang, X. Yang, Y. Lu, C. C. Mi, and P. Kondlapudi, “Ecological driving system for connected/automated vehicles using a two-stage control hierarchy,” *IEEE Transactions on Intelligent Transportation Systems*, vol. 19, no. 7, pp. 2373–2384, 2018.

[96] S. Tajeddin, M. Vajedi, and N. L. Azad, “A Newton/GMRES approach to predictive ecological adaptive cruise control of a plug-in hybrid electric vehicle in car-following scenarios,” *IFAC-PapersOnLine*, vol. 49, no. 21, pp. 59–65, 2016.

[97] S. Akhegaonkar, L. Nouvelière, S. Glaser, and F. Holzmann, “Smart and green ACC: energy and safety optimization strategies for EVs,” *IEEE Transactions on Systems, Man, and Cybernetics: Systems*, vol. 48, no. 1, pp. 142–153, 2016.

[98] S. Bae, Y. Kim, J. Guanetti, F. Borrelli, and S. Moura, “Design and implementation of ecological adaptive cruise control for autonomous driving with communication to traffic lights,” in *Proceedings of the 2019 American Control Conference (ACC)*. IEEE, 2019, pp. 4628–4634.

[99] Y. Dahmane, R. Abdrakhmanov, and L. Adouane, “Stochastic MPC for optimal energy management strategy of hybrid vehicle performing ACC with stop&go maneuvers,” *IFAC-PapersOnLine*, vol. 51, no. 9, pp. 223–229, 2018.

[100] A. Weißmann, D. Görges, and X. Lin, "Energy-optimal adaptive cruise control combining model predictive control and dynamic programming," *Control Engineering Practice*, vol. 72, pp. 125–137, 2018.

[101] Z. Nie and H. Farzaneh, "Adaptive cruise control for eco-driving based on model predictive control algorithm," *Applied Sciences*, vol. 10, no. 15, p. 5271, 2020.

[102] Y. Luo, T. Chen, S. Zhang, and K. Li, "Intelligent hybrid electric vehicle ACC with coordinated control of tracking ability, fuel economy, and ride comfort," *IEEE Transactions on Intelligent Transportation Systems*, vol. 16, no. 4, pp. 2303–2308, 2015.

[103] S. E. Li, Z. Jia, K. Li, and B. Cheng, "Fast online computation of a model predictive controller and its application to fuel economy–oriented adaptive cruise control," *IEEE Transactions on Intelligent Transportation Systems*, vol. 16, no. 3, pp. 1199–1209, 2015.

[104] H. Chu, L. Guo, B. Gao, H. Chen, N. Bian, and J. Zhou, "Predictive cruise control using high-definition map and real vehicle implementation," *IEEE Transactions on Vehicular Technology*, vol. 67, no. 12, pp. 11 377–11 389, 2018.

[105] H. Chen, L. Guo, H. Ding, Y. Li, and B. Gao, "Real-time predictive cruise control for eco-driving taking into account traffic constraints," *IEEE Transactions on Intelligent Transportation Systems*, vol. 20, no. 8, pp. 2858–2868, 2019.

[106] D. He and B. Peng, "Gaussian learning-based fuzzy predictive cruise control for improving safety and economy of connected vehicles," *IET Intelligent Transport Systems*, vol. 14, no. 5, pp. 346–355, 2020.

[107] F. Morlock and O. Sawodny, "An economic model predictive cruise controller for electric vehicles using gaussian process prediction," *IFAC-PapersOnLine*, vol. 51, no. 31, pp. 876–881, 2018.

[108] C. Zhang and A. Vahidi, "Predictive cruise control with probabilistic constraints for eco driving," in *Proceedings of the ASME 2011 Dynamic Systems and Control Conference and Bath/ASME Symposium on Fluid Power and Motion Control*, vol. 2. ASME, 2011, pp. 233–238.

[109] D. Moser, R. Schmied, H. Waschl, and L. del Re, "Flexible spacing adaptive cruise control using stochastic model predictive control," *IEEE Transactions on Control Systems Technology*, vol. 26, no. 1, pp. 114–127, 2018.

[110] S. Yoon, H. Jeon, and D. Kum, "Predictive cruise control using radial basis function network-based vehicle motion prediction and chance constrained model predictive control," *IEEE Transactions on Intelligent Transportation Systems*, vol. 20, no. 10, pp. 3832–3843, 2019.

[111] D. Jia, H. Chen, Z. Zheng, D. Watling, R. Connors, J. Gao, and Y. Li, "An enhanced predictive cruise control system design with data-driven traffic prediction," *IEEE Transactions on Intelligent Transportation Systems*, vol. 23, no. 7, pp. 8170–8183, 2022.

[112] S. Zhang, Y. Luo, J. Wang, X. Wang, and K. Li, “Predictive energy management strategy for fully electric vehicles based on preceding vehicle movement,” *IEEE Transactions on Intelligent Transportation Systems*, vol. 18, no. 11, pp. 3049–3060, 2017.

[113] S. Xie, X. Hu, T. Liu, S. Qi, K. Lang, and H. Li, “Predictive vehicle-following power management for plug-in hybrid electric vehicles,” *Energy*, vol. 166, pp. 701–714, 2019.

[114] T. Liu, X. Hu, S. E. Li, and D. Cao, “Reinforcement learning optimized look-ahead energy management of a parallel hybrid electric vehicle,” *IEEE/ASME Transactions on Mechatronics*, vol. 22, no. 4, pp. 1497–1507, 2017.

[115] C. Sun, X. Hu, S. J. Moura, and F. Sun, “Velocity predictors for predictive energy management in hybrid electric vehicles,” *IEEE Transactions on Control Systems Technology*, vol. 23, no. 3, pp. 1197–1204, 2015.

[116] Y. Li, H. He, and J. Peng, “An adaptive online prediction method with variable prediction horizon for future driving cycle of the vehicle,” *IEEE Access*, vol. 6, pp. 33 062–33 075, 2018.

[117] N. Chen, B. van Arem, T. Alkim, and M. Wang, “A hierarchical model-based optimization control approach for cooperative merging by connected automated vehicles,” *IEEE Transactions on Intelligent Transportation Systems*, vol. 22, no. 12, pp. 7712–7725, 2021.

[118] J. Hu, Z. Zhang, L. Xiong, H. Wang, and G. Wu, “Cut through traffic to catch green light: Eco approach with overtaking capability,” *Transportation Research Part C: Emerging Technologies*, vol. 123, p. 102927, 2021.

[119] G.-P. Antonio and C. Maria-Dolores, “Multi-agent deep reinforcement learning to manage connected autonomous vehicles at tomorrow’s intersections,” *IEEE Transactions on Vehicular Technology*, vol. 71, no. 7, pp. 7033–7043, 2022.

[120] H. Yang, H. Rakha, and M. V. Ala, “Eco-cooperative adaptive cruise control at signalized intersections considering queue effects,” *IEEE Transactions on Intelligent Transportation Systems*, vol. 18, no. 6, pp. 1575–1585, 2017.

[121] Z. Wang, G. Wu, P. Hao, and M. J. Barth, “Cluster-wise cooperative eco-approach and departure application along signalized arterials,” in *Proceedings of the 2017 IEEE 20th International Conference on Intelligent Transportation Systems (ITSC)*. IEEE, 2017, pp. 145–150.

[122] M. A. S. Kamal, J.-i. Imura, T. Hayakawa, A. Ohata, and K. Aihara, “A vehicle-intersection coordination scheme for smooth flows of traffic without using traffic lights,” *IEEE Transactions on Intelligent Transportation Systems*, vol. 16, no. 3, pp. 1136–1147, 2015.

[123] X. Wei, G. Tan, and N. Ding, “Batch-Light: An adaptive intelligent intersection control policy for autonomous vehicles,” in *Proceedings of the 2014 IEEE International Conference on Progress in Informatics and Computing*. IEEE, 2014, pp. 98–103.

[124] S. Gutesa, J. Lee, and D. Besenski, “Development and evaluation of cooperative intersection management algorithm under connected and automated vehicles environment,” *Transportation research record*, vol. 2675, no. 7, pp. 94–104, 2021.

[125] L. M. Castiglione, P. Falcone, A. Petrillo, S. P. Romano, and S. Santini, “Cooperative intersection crossing over 5G,” *IEEE/ACM Transactions on Networking*, vol. 29, no. 1, pp. 303–317, 2021.

[126] D. Fajardo, T.-C. Au, S. T. Waller, P. Stone, and D. Yang, “Automated intersection control: Performance of future innovation versus current traffic signal control,” *Transportation Research Record*, vol. 2259, no. 1, pp. 223–232, 2011.

[127] Y. Jiang, M. Zanon, R. Hult, and B. Houska, “Distributed algorithm for optimal vehicle coordination at traffic intersections,” *IFAC-PapersOnLine*, vol. 50, no. 1, pp. 11 577–11 582, 2017.

[128] X. Zhao, J. Wang, Y. Chen, and G. Yin, “Multi-objective cooperative scheduling of CAVs at non-signalized intersection,” in *Proceedings of the 2018 21st International Conference on Intelligent Transportation Systems (ITSC).* IEEE, 2018, pp. 3314–3319.

[129] J. Zhang, X. Jiang, Z. Liu, L. Zheng, and B. Ran, “A study on autonomous intersection management: planning-based strategy improved by convolutional neural network,” *KSCE Journal of Civil Engineering*, vol. 25, no. 10, pp. 3995–4004, 2021.

[130] Z. Du, B. HomChaudhuri, and P. Pisu, “Hierarchical distributed coordination strategy of connected and automated vehicles at multiple intersections,” *Journal of Intelligent Transportation Systems*, vol. 22, no. 2, pp. 144–158, 2018.

[131] A. P. Chouhan and G. Banda, “Autonomous intersection management: A heuristic approach,” *IEEE Access*, vol. 6, pp. 53 287–53 295, 2018.

[132] R. Hult, M. Zanon, S. Gras, and P. Falcone, “An MIQP-based heuristic for optimal coordination of vehicles at intersections,” in *Proceedings of the 2018 IEEE Conference on Decision and Control (CDC).* IEEE, 2018, pp. 2783–2790.

[133] M. Bashiri, H. Jafarzadeh, and C. H. Fleming, “PAIM: Platoon-based autonomous intersection management,” in *Proceedings of the 2018 21st International Conference on Intelligent Transportation Systems (ITSC).* IEEE, 2018, pp. 374–380.

[134] Y. J. Zhang, A. A. Malikopoulos, and C. G. Cassandras, “Optimal control and coordination of connected and automated vehicles at urban traffic intersections,” in *Proceedings of the 2016 American Control Conference (ACC).* IEEE, 2016, pp. 6227–6232.

[135] A. Hadjigeorgiou and S. Timotheou, “Optimizing the trade-off between fuel consumption and travel time in an unsignalized autonomous intersection crossing,” in *Proceedings of the 2019 IEEE Intelligent Transportation Systems Conference (ITSC).* IEEE, 2019, pp. 2443–2448.

[136] B. Liu, Q. Shi, Z. Song, and A. El Kamel, “Trajectory planning for autonomous intersection management of connected vehicles,” *Simulation Modelling Practice and Theory*, vol. 90, pp. 16–30, 2019.

[137] C. Yu, W. Sun, H. X. Liu, and X. Yang, “Managing connected and automated vehicles at isolated intersections: From reservation-to optimization-based methods,” *Transportation Research Part B: Methodological*, vol. 122, pp. 416–435, 2019.

[138] A. Mirheli, L. Hajibabai, and A. Hajbabaie, “Development of a signal-head-free intersection control logic in a fully connected and autonomous vehicle environment,” *Transportation Research Part C: Emerging Technologies*, vol. 92, pp. 412–425, 2018.

[139] H. Xu, C. G. Cassandras, L. Li, and Y. Zhang, “Comparison of cooperative driving strategies for CAVs at signal-free intersections,” *IEEE Transactions on Intelligent Transportation Systems*, vol. 23, no. 7, pp. 7614–7627, 2022.

[140] B. Li, Y. Zhang, Y. Zhang, N. Jia, and Y. Ge, “Near-optimal online motion planning of connected and automated vehicles at a signal-free and lane-free intersection,” in *Proceedings of the 2018 IEEE Intelligent Vehicles Symposium (IV)*. IEEE, 2018, pp. 1432–1437.

[141] B. Li, Y. Zhang, T. Acarman, Y. Ouyang, C. Yaman, and Y. Wang, “Lane-free autonomous intersection management: A batch-processing framework integrating reservation-based and planning-based methods,” in *Proceedings of the 2021 IEEE International Conference on Robotics and Automation (ICRA)*. IEEE, 2021, pp. 7915–7921.

[142] B. Li, Y. Zhang, N. Jia, and X. Peng, “Autonomous intersection management over continuous space: A microscopic and precise solution via computational optimal control,” *IFAC-PapersOnLine*, vol. 53, no. 2, pp. 17 071–17 076, 2020.

[143] A. Mihály, Z. Farkas, and P. Gáspár, “Model predictive control for the coordination of autonomous vehicles at intersections,” *IFAC-PapersOnLine*, vol. 53, no. 2, pp. 15 174–15 179, 2020.

[144] N. Murgovski, G. R. de Campos, and J. Sjöberg, “Convex modeling of conflict resolution at traffic intersections,” in *Proceedings of the 2015 54th IEEE conference on decision and control (CDC)*. IEEE, 2015, pp. 4708–4713.

[145] R. Hult, M. Zanon, S. Gros, and P. Falcone, “Optimal coordination of automated vehicles at intersections with turns,” in *Proceedings of the 2019 18th European Control Conference (ECC)*. IEEE, 2019, pp. 225–230.

[146] C. Liu, Y. Zhang, T. Zhang, X. Wu, L. Gao, and Q. Zhang, “High throughput vehicle coordination strategies at road intersections,” *IEEE Transactions on Vehicular Technology*, vol. 69, no. 12, pp. 14 341–14 354, 2020.

[147] X. Qian, J. Gregoire, A. De La Fortelle, and F. Moutarde, “Decentralized model predictive control for smooth coordination of automated vehicles at intersection,” in *Proceedings of the 2015 European Control Conference (ECC)*. IEEE, 2015, pp. 3452–3458.

[148] A. I. M. Medina, N. Van De Wouw, and H. Nijmeijer, "Cooperative intersection control based on virtual platooning," *IEEE Transactions on Intelligent Transportation Systems*, vol. 19, no. 6, pp. 1727–1740, 2018.

[149] R. Krajewski, P. Themann, and L. Eckstein, "Decoupled cooperative trajectory optimization for connected highly automated vehicles at urban intersections," in *Proceedings of the 2016 IEEE Intelligent Vehicles Symposium (IV)*. IEEE, 2016, pp. 741–746.

[150] A. Hadjigeorgiou and S. Timotheou, "Real-time optimization of fuel-consumption and travel-time of CAVs for cooperative intersection crossing," *IEEE Transactions on Intelligent Vehicles*, vol. 8, no. 1, pp. 313–329, 2023.

[151] A. A. Malikopoulos, C. G. Cassandras, and Y. J. Zhang, "A decentralized energy-optimal control framework for connected automated vehicles at signal-free intersections," *Automatica*, vol. 93, pp. 244–256, 2018.

[152] G. R. de Campos, P. Falcone, R. Hult, H. Wymeersch, and J. Sjöberg, "Traffic coordination at road intersections: Autonomous decision-making algorithms using model-based heuristics," *IEEE Intelligent Transportation Systems Magazine*, vol. 9, no. 1, pp. 8–21, 2017.

[153] Y. Wu, H. Chen, and F. Zhu, "DCL-AIM: Decentralized coordination learning of autonomous intersection management for connected and automated vehicles," *Transportation Research Part C: Emerging Technologies*, vol. 103, pp. 246–260, 2019.

[154] Y. Zhang, A. A. Malikopoulos, and C. G. Cassandras, "Decentralized optimal control for connected automated vehicles at intersections including left and right turns," in *Proceedings of the 2017 IEEE 56th Conference on Decision and Control (CDC)*. IEEE, 2017, pp. 4428–4433.

[155] J. Khoury, J. Khoury, G. Zouein, and J.-P. Arnaout, "A practical decentralized access protocol for autonomous vehicles at isolated under-saturated intersections," *Journal of Intelligent Transportation Systems*, vol. 23, no. 5, pp. 427–440, 2019.

[156] K. Zhang, D. Zhang, A. de La Fortelle, X. Wu, and J. Gregoire, "State-driven priority scheduling mechanisms for driverless vehicles approaching intersections," *IEEE Transactions on Intelligent Transportation Systems*, vol. 16, no. 5, pp. 2487–2500, 2015.

[157] A. Mirheli, M. Tajalli, L. Hajibabai, and A. Hajbabaie, "A consensus-based distributed trajectory control in a signal-free intersection," *Transportation Research Part C: Emerging Technologies*, vol. 100, pp. 161–176, 2019.

[158] A. Katriniok, S. Kojchev, E. Lefeber, and H. Nijmeijer, "Distributed scenario model predictive control for driver aided intersection crossing," in *Proceedings of the 2018 European Control Conference (ECC)*. IEEE, 2018, pp. 1746–1752.

[159] B. Xu, S. E. Li, Y. Bian, S. Li, X. J. Ban, J. Wang, and K. Li, "Distributed conflict-free cooperation for multiple connected vehicles at unsignalized intersections," *Transportation Research Part C: Emerging Technologies*, vol. 93, pp. 322–334, 2018.

[160] V. Savic, E. M. Schiller, and M. Papatriantafilou, “Distributed algorithm for collision avoidance at road intersections in the presence of communication failures,” in *Proceedings of the 2017 IEEE Intelligent Vehicles Symposium (IV)*. IEEE, 2017, pp. 1005–1012.

[161] M. Kloock, P. Scheffe, S. Marquardt, J. Maczijewski, B. Alrifaee, and S. Kowalewski, “Distributed model predictive intersection control of multiple vehicles,” in *Proceedings of the 2019 IEEE Intelligent Transportation Systems Conference (ITSC)*. IEEE, 2019, pp. 1735–1740.

[162] C. Liu, C.-W. Lin, S. Shiraishi, and M. Tomizuka, “Distributed conflict resolution for connected autonomous vehicles,” *IEEE Transactions on Intelligent Vehicles*, vol. 3, no. 1, pp. 18–29, 2018.

[163] A. Katriniok, P. Sopasakis, M. Schuurmans, and P. Patrinos, “Nonlinear model predictive control for distributed motion planning in road intersections using panoc,” in *Proceedings of the 2019 IEEE 58th Conference on Decision and Control (CDC)*. IEEE, 2019, pp. 5272–5278.

[164] Nissan, “Product information,” https://en.nissan.com.hk/vehicles/new/NOTE.html, access date: 30 Apr. 2023.

[165] BAE SYSTEMS, “Product information,” https://gettozero.com/transit_overview.php, access date: 30 Apr. 2023.

[166] A. Ghosh, “Possibilities and challenges for the inclusion of the electric vehicle (ev) to reduce the carbon footprint in the transport sector: A review,” *Energies*, vol. 13, no. 10, p. 2602, 2020.

[167] Y. Wang, A. Biswas, R. Rodriguez, Z. Keshavarz-Motamed, and A. Emadi, “Hybrid electric vehicle specific engines: State-of-the-art review,” *Energy Reports*, vol. 8, pp. 832–851, 2022.

[168] W. Zhou, C. Zhang, J. Li, and H. K. Fathy, “A pseudospectral strategy for optimal power management in series hybrid electric powertrains,” *IEEE Transactions on Vehicular Technology*, vol. 65, no. 6, pp. 4813–4825, 2016.

[169] J. M. Luján, C. Guardiola, B. Pla, and A. Reig, “Analytical optimal solution to the energy management problem in series hybrid electric vehicles,” *IEEE Transactions on Vehicular Technology*, vol. 67, no. 8, pp. 6803–6813, 2018.

[170] L. Serrao and G. Rizzoni, “Optimal control of power split for a hybrid electric refuse vehicle,” in *Proceedings of the 2008 American Control Conference (ACC)*. IEEE, 2008, pp. 4498–4503.

[171] S. A. Evangelou and A. Shukla, “Advances in the modelling and control of series hybrid electric vehicles,” in *Proceedings of the 2012 American Control Conference (ACC)*. IEEE, 2012, pp. 527–534.

[172] B. Chen, S. A. Evangelou, and R. Lot, “Hybrid electric vehicle two-step fuel efficiency optimization with decoupled energy management and speed control,” *IEEE Transactions on Vehicular Technology*, vol. 68, no. 12, pp. 11 492–11 504, 2019.

[173] X. Pan, B. Chen, S. A. Evangelou, and S. Timotheou, "Optimal motion control for connected and automated electric vehicles at signal-free intersections," in *Proceedings of the 2020 59th IEEE Conference on Decision and Control (CDC).* IEEE, 2020, pp. 2831–2836.

[174] D. R. Lopes and S. A. Evangelou, "Energy savings from an eco-cooperative adaptive cruise control: A BEV platoon investigation," in *Proceedings of the 2019 18th European Control Conference (ECC).* IEEE, 2019, pp. 4160–4167.

[175] A. Sciarretta, G. De Nunzio, and L. L. Ojeda, "Optimal ecodriving control: Energy-efficient driving of road vehicles as an optimal control problem," *IEEE Control Systems Magazine*, vol. 35, no. 5, pp. 71–90, 2015.

[176] B. Chen and S. A. Evangelou, "Truncated battery power following strategy for energy management control of series hybrid electric vehicles," in *Proceedings of the 2019 18th European Control Conference (ECC).* IEEE, 2019, pp. 738–743.

[177] B. Chen, X. Pan, and S. A. Evangelou, "Optimal energy management of series hybrid electric vehicles with engine start–stop system," *IEEE Transactions on Control Systems Technology*, 2023.

[178] T. Van Keulen, J. Gillot, B. De Jager, and M. Steinbuch, "Solution for state constrained optimal control problems applied to power split control for hybrid vehicles," *Automatica*, vol. 50, no. 1, pp. 187–192, 2014.

[179] I. Shafikhani and J. Åslund, "Analytical solution to equivalent consumption minimization strategy for series hybrid electric vehicles," *IEEE Transactions on Vehicular Technology*, vol. 70, no. 3, pp. 2124–2137, 2021.

[180] X. Yan, J. Fleming, C. Allison, and R. Lot, "Portable automobile data acquisition module (ADAM) for naturalistic driving study," in *Proceedings of the 15th European Automotive Congress*, 2017.

[181] P. Elbert, S. Ebbesen, and L. Guzzella, "Implementation of dynamic programming for *n*-dimensional optimal control problems with final state constraints," *IEEE Transactions on Control Systems Technology*, vol. 21, no. 3, pp. 924–931, 2013.

[182] X. Pan, B. Chen, and S. A. Evangelou, "Optimal vehicle following strategy for joint velocity and energy management control of series hybrid electric vehicles," *IFAC-PapersOnLine*, vol. 53, no. 2, pp. 14 161–14 166, 2020.

[183] M. Wang, W. Daamen, S. P. Hoogendoorn, and B. van Arem, "Rolling horizon control framework for driver assistance systems. Part I: Mathematical formulation and non-cooperative systems," *Transportation Research Part C: Emerging Technologies*, vol. 40, pp. 271–289, 2014.

[184] C. B. Math, A. Ozgur, S. H. de Groot, and H. Li, "Data rate based congestion control in V2V communication for traffic safety applications," in *Proceedings of the 2015 IEEE Symposium on Communications and Vehicular Technology in the Benelux (SCVT).* IEEE, 2015, pp. 1–6.

[185] A. Loulizi, Y. Bichiou, and H. Rakha, “Steady-state car-following time gaps: An empirical study using naturalistic driving data,” *Journal of Advanced Transportation*, vol. 2019, no. 3, pp. 1–9, 2019.

[186] V. Turri, B. Besselink, and K. H. Johansson, “Cooperative look-ahead control for fuel-efficient and safe heavy-duty vehicle platooning,” *IEEE Transactions on Control Systems Technology*, vol. 25, no. 1, pp. 12–28, 2017.

[187] S. Uebel, N. Murgovski, B. Bäker, and J. Sjöberg, “A two-level MPC for energy management including velocity control of hybrid electric vehicles,” *IEEE Transactions on Vehicular Technology*, vol. 68, no. 6, pp. 5494–5505, 2019.

[188] P. Shakouri and A. Ordys, “Nonlinear model predictive control approach in design of adaptive cruise control with automated switching to cruise control,” *Control Engineering Practice*, vol. 26, pp. 160–177, 2014.

[189] D. Ariens, B. Houska, H. Ferreau, and F. Logist, “ACADO for MATLAB user’s manual,” *Optimization in Engineering Center (OPTEC)*, vol. 1, 2010.

[190] M. Vajedi and N. L. Azad, “Ecological adaptive cruise controller for plug-in hybrid electric vehicles using nonlinear model predictive control,” *IEEE Transactions on Intelligent Transportation Systems*, vol. 17, no. 1, pp. 113–122, 2016.

[191] K. Yu and J. Yang, “Performance of a nonlinear real-time optimal control system for HEVs/PHEVs during car following,” *Journal of Applied Mathematics*, vol. 2014, 2014.

[192] S. Yu, X. Pan, B. Chen, A. Georgiou, J. I. M, and S. A. Evangelou, “Robust model predictive control framework for energy-optimal adaptive cruise control of battery electric vehicles,” in *Proceedings of the 2022 European Control Conference (ECC)*. IEEE, 2022, pp. 1728–1733.

[193] B. Chen, X. Pan, S. A. Evangelou, and S. Timotheou, “Optimal control for connected and autonomous vehicles at signal-free intersections,” *IFAC-PapersOnLine*, vol. 53, no. 2, pp. 15 306–15 311, 2020.

[194] F. Tahir and I. M. Jaimoukha, “Causal state-feedback parameterizations in robust model predictive control,” *Automatica*, vol. 49, no. 9, pp. 2675–2682, 2013.

[195] A. Georgiou, F. Tahir, S. A. Evangelou, and I. M. Jaimoukha, “Robust moving horizon state estimation for uncertain linear systems using linear matrix inequalities,” in *Proceedings of the 2020 59th IEEE Conference on Decision and Control (CDC)*. IEEE, 2020, pp. 2900–2905.

[196] A. Georgiou, S. A. Evangelou, I. M. Jaimoukha, and G. Downton, “Tracking control for directional drilling systems using robust feedback model predictive control,” *IFAC-PapersOnLine*, vol. 53, no. 2, pp. 11 974–11 981, 2020.

[197] X. Pan, B. Chen, S. Timotheou, and S. A. Evangelou, “A convex optimal control framework for autonomous vehicle intersection crossing,” *IEEE Transactions on Intelligent Transportation Systems*, vol. 24, no. 1, pp. 163–177, 2023.

[198] T. Liu and Selpi, "Comparison of car-following behavior in terms of safety indicators between China and Sweden," *IEEE Transactions on Intelligent Transportation Systems*, vol. 21, no. 9, pp. 3696–3705, 2019.

[199] F. Alizadeh and D. Goldfarb, "Second-order cone programming," *Mathematical Programming*, vol. 95, no. 1, pp. 3–51, 2003.

[200] Y. Mao, D. Dueri, M. Szmuk, and B. Açıkmeşe, "Successive convexification of non-convex optimal control problems with state constraints," *IFAC-PapersOnLine*, vol. 50, no. 1, pp. 4063–4069, 2017.

[201] M. Grant and S. Boyd, "CVX: MATLAB software for disciplined convex programming, version 2.1," 2014.

[202] X. Pan, B. Chen, L. Dai, S. Timotheou, and S. A. Evangelou, "A hierarchical robust control strategy for decentralized signal-free intersection management," *IEEE Transactions on Control Systems Technology*, 2023.

[203] J. Han, A. Vahidi, and A. Sciarretta, "Fundamentals of energy efficient driving for combustion engine and electric vehicles: An optimal control perspective," *Automatica*, vol. 103, p. 558–572, 2019.

[204] S. Rakovic, E. Kerrigan, K. Kouramas, and D. Mayne, "Invariant approximations of the minimal robust positively invariant set," *IEEE Transactions on Automatic Control*, vol. 50, no. 3, pp. 406–410, 2005.

[205] J. Löfberg, "YALMIP : A toolbox for modeling and optimization in MATLAB," in *Proceedings of the 2004 IEEE International Conference on Robotics and Automation (ICRA)*. Taipei, Taiwan: IEEE, 2004.

Appendixes

I Proofs in Chapter 6

I-A Proof of Preposition 6.1

Suppose that a feasible solution (denoted by the superscript $*$) of OCP (6.12) with control signals $\zeta^*(s)$, $F_w^*(s)$, and the states $\Delta E^*(s) = E^*(s) - E_{ref}(s)$, $\Delta t^*(s) = t^*(s) - t_{ref}(s)$, is found for which it holds that $\zeta_i^*(s) > 1/\sqrt{2(E_i^*(s))/m}$, and therefore we have

$$\zeta^*(s) = \frac{1}{\sqrt{2(E^*(s))/m}} + \tilde{\zeta}(s), \text{ with } \tilde{\zeta}(s) > 0, \tag{9.1a}$$

$$t^*(s) = t(0) + \sum_{\xi=0}^{s} \frac{1}{\sqrt{2(E^*(\xi))/m}} \Delta s + \sum_{\xi=0}^{s} \tilde{\zeta}(\xi) \Delta s, \tag{9.1b}$$

where the slack variable $\tilde{\zeta}$ inflates the travel time of the ego vehicle, and therefore it relaxes the inter-vehicular distance constraint (6.2). It is also possible to construct an alternative feasible solution $\left(\Delta\breve{E}(s), \Delta\breve{t}(s), \breve{\zeta}(s), \breve{F}_w(s)\right)$ with the same initial conditions $E^*(0) = \breve{E}(0)$ and $t^*(0) = \breve{t}(0)$, and

$$\breve{\zeta}(s) = \frac{1}{\sqrt{2(\breve{E}(s))/m}} = \zeta^*(s), \tag{9.2}$$

where $\Delta\breve{E}(s) = \breve{E}(s) - E_{ref}(s)$, $\Delta\breve{t}(s) = \breve{t}(s) - t_{ref}(s)$. It can be inferred from (9.1a) and (9.2) that $\breve{E}(s) < E^*(s)$, and therefore by integrating (9.2) $\breve{t}_i(s) = t_i^*(s), \forall s$. The alternative solution corresponds to the case when the ego vehicle slows down for the reference vehicle without inflating the time variable (tightness of (6.9b) is guaranteed). In this context, the kinetic energy difference between the two solutions can be obtained by

$$E^*(s) - \breve{E}(s) = E^*(s) - \frac{1}{2}m\left(\frac{1}{\breve{\zeta}(s)}\right)^2 = E^*(s) - \frac{1}{2}m\frac{2E^*(s)}{(\sqrt{m} + \sqrt{2E^*(s)}\tilde{\zeta}(s))^2} > 0, \tag{9.3}$$

where $\frac{1}{\breve{\zeta}(s)} = \frac{1}{\zeta^*(s)}$ owing to (9.2), and therefore can be determined by (9.1a). Such a kinetic energy difference results by the deviation between $\breve{F}_w$ and F_w^*. For both solutions cases, by integrating both sides of the longitudinal dynamic equation (6.3a), it holds that

$$\Delta E^*(s) = E^*(s) - E_{ref}(s) = E(0) + \sum_{\xi=0}^{s} \{F_w^*(\xi) - F_r + \varepsilon E^*(\xi) - F_{ref}(s)\}\Delta s, \tag{9.4a}$$

$$\Delta \breve{E}(s) = \breve{E}(s) - E_{ref}(s) = E(0) + \sum_{\xi=0}^{s} \{\breve{F}_{w,i}(\xi) - F_r + \varepsilon \breve{E}_i(\xi) - F_{ref}(s)\}\Delta s, \tag{9.4b}$$

where $\varepsilon = -\frac{2f_d}{m}$ is a constant. By subtracting (9.4b) from (9.4a), we obtain

$$E^*(s) - \breve{E}(s) = \sum_{\xi=0}^{s} \{F^*(\xi) - \breve{F}(\xi)\}\Delta s + \varepsilon \sum_{\xi=0}^{s} \{E^*(\xi) - \breve{E}(\xi)\}\Delta s > 0, \forall s. \tag{9.5}$$

Let $V^*(F_w^*, \zeta^*)$ and $\breve{V}(\breve{F}_w, \breve{\zeta})$ denote the cost for the ego vehicle in both solution cases. Then, their difference can be calculated by

$$\begin{aligned}
&V^*(F_w^*, \zeta^*) - \breve{V}(\breve{F}_w, \breve{\zeta}) \\
&\quad = \sum_{s=0}^{s_f} \{W_1(E^*(s) - \frac{m\bar{v}^2}{2})^2 + W_2 F_w^*(s) + \zeta^*(s)\}\Delta s \\
&\quad - \sum_{s=0}^{s_f} \{W_1(\breve{E}(s) - \frac{m\bar{v}^2}{2})^2 + W_2 \breve{F}_w(s) + \breve{\zeta}(s)\}\Delta s \\
&\quad = W_1 \sum_{s=0}^{s_f} \{[(E^*(s))^2 - (\breve{E}(s))^2] - m\bar{v}^2(E^*(s) - \breve{E}(s))\}\Delta s + W_2 \sum_{s=0}^{s_f} \{F^*(s) - \breve{F}(s)\}\Delta s.
\end{aligned} \tag{9.6}$$

From (9.3), it can be found that $(E^*(s))^2 > (\breve{E}(s))^2$, and by utilising (9.5), the (9.6) can be written as below:

$$\begin{aligned}
&V^*(F_w^*, \zeta^*) - \breve{V}(\breve{F}_w, \breve{\zeta}) \\
&\quad > -W_1 m\bar{v}^2 \sum_{s=0}^{s_f} \{E^*(s) - \breve{E}(s)\}\Delta s + W_2(E^*(s_f) - \breve{E}(s_f)) - W_2 \varepsilon \sum_{s=0}^{s_f} \{E^*(s_f) - \breve{E}(s_f)\}\Delta s \\
&\quad > -W_1 m\bar{v}^2 \sum_{s=0}^{s_f} \{E^*(s) - \breve{E}(s)\}\Delta s - W_2 \varepsilon \sum_{s=0}^{s_f} \{E^*(s_f) - \breve{E}(s_f)\}\Delta s \\
&\quad = (-W_1 m\bar{v}^2 - W_2 \varepsilon) \sum_{s=0}^{s_f} \{E^*(s) - \breve{E}(s)\}\Delta s.
\end{aligned} \tag{9.7}$$

Since $E^*(s) - \breve{E}(s) > 0$, equation (9.7) implies that if $(-W_1 m\bar{v}^2 - W_2 \varepsilon) > 0$, which is guaranteed by the necessary condition in Proposition 6.1, such that

$$V^*(F_w^*, \zeta^*) - \breve{V}(\breve{F}_w, \breve{\zeta}) > 0. \tag{9.8}$$

Hence, given a solution set $(\zeta^*(s), F_w^*(s), E^*(s), t^*(s))$ without holding the equality condition of (6.9b) (subject to a slack variable $\tilde{\zeta}(s)$), there always exists an alternative solution $\left(\breve{\zeta}(s), \breve{F}_w(s), \breve{E}(s), \breve{t}(s)\right)$ with guaranteed tightness that is more optimal of the cost J.

Thus, the proof ends.

I-B Proof of Lemma 6.1

Consider a candidate solution of the ego vehicle $(E^*(k), t^*(k), F_w^*(k), \zeta^*(k))$ by solving (6.12), which satisfies the Preposition 6.1 $\left(\zeta^*(k) = 1/\sqrt{2E^*(k)/m_i}\right)$ without satisfying the lower-bound of the rear-end collision constraint (6.11), the following inequality holds that,

$$\begin{aligned} t^*(k) - t_{ref}(k) &< T_\sigma + \frac{a_1 E^*(k) + a_0 - v_{ref}(k)}{|a_{\min}|} \\ \Rightarrow t(0) + \sum_{\xi=0}^{k} \zeta^*(\xi)\Delta s - t_{ref}(k) &< T_\sigma + \frac{a_1 E^*(k) + a_0 - v_{ref}(k)}{|a_{\min}|} \\ \Rightarrow \sum_{\xi=0}^{k} \frac{\Delta s}{2E^*(k)/m} - \frac{a_1 E^*(k)}{|a_{\min}|} &< T_\sigma + \frac{a_0 - v_{ref}(k)}{|a_{\min}|} - t(0), \end{aligned}$$

where T_σ, a_0, $v_{ref}(k)$, $a_{\min}$ and $t_i(0)$ are prior-known constant information. Since $E(s)$ is bounded by

$$\frac{1}{2} m v_{\min}^2 \leq E_i(s) \leq \frac{1}{2} m v_{\max}^2$$

and therefore, we can conclude from the Lemma 6.1 that by continuing reducing $v_{\min}$ to a sufficient small constant $\sigma > 0$, we have

$$\frac{1}{\sqrt{2E^*(k)/m}} = \frac{1}{\sigma} \to \infty$$

and

$$\frac{a_1 E^*(k)}{|a_{\min}|} = \frac{a_1 m \sigma^2}{2|a_{\min}|} \to 0.$$

As such, the lower-bound of the rear-end collision constraint can be satisfied,

$$\sum_{\xi=0}^{k} \frac{\Delta s}{2E^*(k)/m} - \frac{a_1 E^*(k)}{|a_{\min}|} = \sum_{\xi=0}^{k} \frac{\Delta s}{\sigma} - \frac{a_1 m \sigma^2}{2|a_{\min}|} \geq T_\sigma + \frac{a_0 - v_{ref}(k)}{|a_{\min}|} - t(0).$$

Thus, the proof ends.

II Proofs in Chapter 7

II-A Proof of Preposition 7.1

In view of (7.46a), the multi-objective function of a single vehicle i can be denoted by $\tilde{J}_i = W_1\tilde{J}_{t,i} + W_2\bar{J}_{w,i}$, where $\tilde{J}_{t,i}(\zeta_i(s)) = \int_0^{2L+\delta(d_i)} \zeta_i(s)ds (= t_i(2L+\delta(d_i)) - t_i(0))$. Thus, $\tilde{J}_{t,i}$ only depends on $\zeta_i(s)$ whereas $\bar{J}_{w,i}$ solely depends on $F_{w,i}(s)$,

$$\bar{J}_{w,i} = \int_0^{2L+\delta(d_i)} \left(\bar{b}_2 F_{w,i}^2(s) + \bar{b}_1 F_{w,i}(s) + \bar{b}_0\right) ds. \tag{9.9}$$

Suppose that a feasible solution (denoted by the superscript $*$) of OCP 7.4, with control signals $\zeta_i^*(s)$, $F_{w,i}^*(s)$, and the states $E_i^*(s)$, $t_i^*(s)$, is found for which it holds that $\zeta_i^*(s) > 1/\sqrt{2(E_i^*(s))/m_i}$, and therefore we have

$$\zeta_i^*(s) = \frac{1}{\sqrt{2(E_i^*(s))/m_i}} + \Delta\zeta_i(s), \text{ with } \Delta\zeta_i(s) > 0, \tag{9.10a}$$

$$t_i^*(s) = t_i(0) + \int_0^s \frac{1}{\sqrt{2(E_i^*(\xi))/m_i}} d\xi + \int_0^s \Delta\zeta_i(\xi) d\xi, \tag{9.10b}$$

where the slack variable $\Delta\zeta_i$ inflates the travel time of the ith vehicle, and therefore it relaxes the rear-end and lateral collision avoidance constraints (e.g., if the velocity of CAV i arriving at the CZ is much faster than that of CAV $i-1$ with $i, i-1 \in \mathcal{N}$, it does not need to decelerate for CAV $i-1$, avoiding energy loss). It is also possible to construct an alternative feasible solution $\left(\breve{\zeta}_i(s), \breve{E}(s), \breve{t}_i(s), \breve{F}_{w,i}(s)\right)$ with the same initial conditions $E_i^*(0) = \breve{E}_i(0)$ and $t_i^*(0) = \breve{t}_i(0)$, and

$$\breve{\zeta}_i(s) = \frac{1}{\sqrt{2(\breve{E}_i(s))/m_i}} = \zeta_i^*(s), \tag{9.11}$$

with $\breve{E}_i(s) < E_i^*(s)$, and therefore by integrating (9.11) $\breve{t}_i(s) = t_i^*(s), \forall s$. The alternative solution corresponds to the case when the ith vehicle slows down for the preceding vehicle without inflating the time variable (tightness of (7.33b) is guaranteed). In this context, the kinetic energy difference between the two solutions can be obtained by

$$\begin{aligned} \Delta E_i(s) &= E_i^*(s) - \breve{E}_i(s) = E_i^*(s) - \frac{1}{2}m_i\left(\frac{1}{\breve{\zeta}_i(s)}\right)^2 \\ &= E_i^*(s) - \frac{1}{2}m_i\frac{2E_i^*(s)}{(\sqrt{m_i} + \sqrt{2E_i^*(s)}\Delta\zeta_i(s))^2} > 0, \end{aligned} \tag{9.12}$$

where $\frac{1}{\breve{\zeta}_i(s)} = \frac{1}{\zeta_i^*(s)}$ owing to (9.11), and therefore can be determined by (9.10a). Such a kinetic energy difference results by the deviation between $\breve{F}_{w,i}$ and $F_{w,i}^*$, $\Delta F_{w,i}(s) = F_{w,i}^*(s) - \breve{F}_{w,i}(s)$. The relationship between $\Delta E_i(s)$ and $\Delta F_{w,i}(s)$ can be found by (7.32a). For both solutions cases, by integrating both sides of the longitudinal dynamic equation, it holds that

$$E_i^*(s) = E_i(0) + \int_0^s F_{w,i}^*(\xi)d\xi - \int_0^s F_{r,i}d\xi + \varepsilon_i \int_0^s E_i^*(\xi)d\xi, \tag{9.13a}$$

$$\breve{E}_i(s) = E_i(0) + \int_0^s \breve{F}_{w,i}(\xi)d\xi - \int_0^s F_{r,i}d\xi + \varepsilon_i \int_0^s \breve{E}_i(\xi)d\xi, \tag{9.13b}$$

where $\varepsilon_i = -\frac{2f_{d,i}}{m_i}$ is a constant. By subtracting (9.13b) from (9.13a), we obtain

$$\Delta E_i(s) = \int_0^s \Delta F_{w,i}(\xi)d\xi + \varepsilon_i \int_0^s \Delta E_i(\xi)d\xi > 0, \forall s. \tag{9.14}$$

Since $\varepsilon_i < 0$ and $\Delta E_i(s) > 0$, then $\varepsilon_i \int_0^s \Delta E_i(\xi)d\xi < 0$, which implies from (9.14)

$$\int_0^s \Delta F_{w,i}(\xi)d\xi > 0. \tag{9.15}$$

Let $\tilde{J}_i(F_{w,i}^*, \zeta_i^*)$ and $\tilde{J}_i(\breve{F}_{w,i}, \breve{\zeta}_i)$ denote the cost for a single vehicle i in both solution cases. Then, their difference can be calculated by

$$\begin{aligned} \tilde{J}_i(F_{w,i}^*, \zeta_i^*) - \tilde{J}_i(\breve{F}_{w,i}, \breve{\zeta}_i) &= W_1 J_{t,i}(\zeta_i^*(s)) + W_2 J_{w,i}(F_{w,i}^*(s)) - W_1 J_{t,i}(\breve{\zeta}_i(s)) - W_2 J_{w,i}(\breve{F}_{w,i}(s)) \\ &= W_2 (J_{w,i}(F_{w,i}^*(s)) - J_{w,i}(\breve{F}_{w,i}(s))). \end{aligned} \tag{9.16}$$

In virtue of the quadratic form of $\overline{J}_{w,i}(\cdot)$, (9.16) can be rearranged as

$$\begin{aligned} \tilde{J}_i(F_{w,i}^*, \zeta_i^*) - \tilde{J}_i(\breve{F}_{w,i}, \breve{\zeta}_i) &= W_2 \int_0^{2L+\delta(d_i)} \overline{b}_2 F_{w,i}^*(s)^2 + \overline{b}_1 F_{w,i}^*(s) + \overline{b}_0 \, ds \\ &\quad - W_2 \int_0^{2L+\delta(d_i)} \overline{b}_2 \breve{F}_{w,i}(s)^2 + \overline{b}_1 \breve{F}_{w,i}(s) + \overline{b}_0 \, ds \\ &= W_2 \int_0^{2L+\delta(d_i)} \left[\overline{b}_2 (F_{w,i}^*(s) + \breve{F}_{w,i}(s)) + \overline{b}_1\right] \Delta F_{w,i}(s) ds. \end{aligned} \tag{9.17}$$

Then let us define $g_i(s) = \frac{F_{w,i}^*(s) + \breve{F}_{w,i}(s)}{2} \in [F_{w,\min}, F_{w,\max}]$ with $F_{w,\max} = \max\{\frac{g_{r,i}}{r_{w,i}} T_{\max,i}\}$, $F_{w,\min} = \min\{m_i a_{\min,i}\}$ $\forall i \in \mathcal{N}$ and $F_{w,\min} < 0$ and $F_{w,\max} > 0$, (27) can be rewritten as:

$$\begin{aligned} &\tilde{J}_i(F_{w,i}^*, \zeta_i^*) - \tilde{J}_i(\breve{F}_{w,i}, \breve{\zeta}_i) \\ &= W_2 \int_0^{2L+\delta(d_i)} \left[\overline{b}_2 (F_{w,i}^*(s) + \breve{F}_{w,i}(s)) + \overline{b}_1\right] \Delta F_{w,i}(s) ds \\ &= W_2 \overline{b}_1 \int_0^{2L+\delta(d_i)} \Delta F_{w,i}(s) ds + W_2 \overline{b}_2 \int_0^{2L+\delta(d_i)} 2 g_i(s) \Delta F_{w,i}(s) ds \\ &= W_2 \overline{b}_1 \int_0^{2L+\delta(d_i)} \Delta F_{w,i}(s) ds + W_2 \overline{b}_2 \int_0^{2L+\delta(d_i)} 2 g_i(s) \left(\Delta F_{w,i}(s) - \Delta F_{w,\min}\right) + 2 g_i(s) \Delta F_{w,\min} ds. \end{aligned} \tag{9.18}$$

where $\Delta F_{w,\min} < 0$ is the lower bound of $\Delta F_{w,i}(s)$. Since the coefficient $\overline{b}_2$ is positive, $g_i(s)$ is continuous, and the integrable function of $\big(\Delta F_{w,i}(s) - \Delta F_{w,\min}\big) \geq 0, \forall s \in [0, 2L + \delta(d_i)]$ does not change sign, it can be inferred from the Mean Value Theorem that there exists $\overline{F}_{w,i} \in [F_{w,\min}, F_{w,\max}]$ such that

$$
\begin{aligned}
&\tilde{J}_i(F^*_{w,i}, \zeta^*_i) - \tilde{J}_i(\breve{F}_{w,i}, \breve{\zeta}_i) \\
&= W_2\overline{b}_1 \int_0^{2L+\delta(d_i)} \Delta F_{w,i}(s)ds + W_2 2\overline{b}_2\overline{F}_{w,i} \int_0^{2L+\delta(d_i)} \big(\Delta F_{w,i}(s) - \Delta F_{w,\min}\big)\, ds \\
&\qquad + W_2 \int_0^{2L+\delta(d_i)} 2g_i(s)\Delta F_{w,\min} ds \\
&= W_2(2\overline{b}_2\overline{F}_{w,i} + \overline{b}_1) \int_0^{2L+\delta(d_i)} \Delta F_{w,i}(s)ds - 2W_2\overline{b}_2\overline{F}_{w,i}\Delta F_{w,\min}(2L + \delta(d_i)) \\
&\qquad + 2W_2\overline{b}_2\Delta F_{w,\min} \int_0^{2L+\delta(d_i)} g_i(s)ds.
\end{aligned}
\tag{9.19}
$$

As $g_i(s) \in [F_{w,\min}, F_{w,\max}]$, (9.19) satisfies

$$
\begin{aligned}
&\tilde{J}_i(F^*_{w,i}, \zeta^*_i) - \tilde{J}_i(\breve{F}_{w,i}, \breve{\zeta}_i) \\
&\geq W_2(2\overline{b}_2\overline{F}_{w,i} + \overline{b}_1) \int_0^{2L+\delta(d_i)} \Delta F_{w,i}(s)ds - 2W_2\overline{b}_2 F_{w,\min}\Delta F_{w,\min}(2L + \delta(d_i)) \\
&\qquad + 2W_2\overline{b}_2\Delta F_{w,\min} \int_0^{2L+\delta(d_i)} F_{w,\min} ds \\
&= W_2(2\overline{b}_2\overline{F}_{w,i} + \overline{b}_1) \int_0^{2L+\delta(d_i)} \Delta F_{w,i}(s)ds - 2W_2\overline{b}_2 F_{w,\min}\Delta F_{w,\min}(2L + \delta(d_i)) \\
&\qquad + 2W_2\overline{b}_2 F_{w,\min}\Delta F_{w,\min}(2L + \delta(d_i)) \\
&= W_2(2\overline{b}_2\overline{F}_{w,i} + \overline{b}_1) \int_0^{2L+\delta(d_i)} \Delta F_{w,i}(s)ds.
\end{aligned}
\tag{9.20}
$$

From (9.15), equation (9.20) implies that $\tilde{J}_i(F^*_{w,i}, \zeta^*_i) > \tilde{J}_i(\breve{F}_{w,i}, \breve{\zeta}_i)$ if $2\overline{b}_2\overline{F}_{w,i} + \overline{b}_1 > 0$:

$$
\big(2\overline{b}_2\overline{F}_{w,i} + \overline{b}_1\big) > 2\overline{b}_2 F_{w,\min} + \overline{b}_1 > 0\,. \tag{9.21}
$$

Hence, given a solution set $\Big(\zeta^*_i(s), F^*_{w,i}(s), E^*_i(s), t^*_i(s)\Big)$ without holding the equality condition of (7.33b) (subject to a slack variable $\Delta\zeta_i(s)$), there always exists an alternative solution $\Big(\breve{\zeta}_i(s), \breve{F}_{w,i}(s), \breve{E}_i(s), \breve{t}_i(s)\Big)$ with guaranteed tightness that is more optimal in terms of the individual cost $\tilde{J}_i$, which in turn applies to all CAVs (i.e., $\forall i \in \mathcal{N}$).

Thus, the proof ends.

II-B Proof of Lemma 7.1

Consider a candidate solution $\left(E_i^*(s), t_i^*(s), F_{w,i}^*(s), \zeta_i^*(s)\right)$ is found, which violates the lateral collision avoidance constraint (7.14), then we have,

$$\begin{aligned} t_i(L) &< t_k(L+\delta(d_i)+l_k) \\ \Rightarrow t_i(0)+\int_0^L \zeta_i^*(s)ds &< t_k(L+\delta(d_i)+l_k) \\ \Rightarrow \int_0^L \frac{1}{\sqrt{2E_i^*(s)/m_i}}ds &< t_k(L+\delta(d_i)+l_k)-t_i(0), \end{aligned}$$

where $i \in \mathcal{L}_k$, L is the position of the entry of the MZ, $L+\delta(d_i)+l_k$ is the position of vehicle k at the exit of the MZ, and $t_i(0)$ are pre-known constants. Since $E_i(s)$ is bounded by

$$\frac{1}{2}m_i v_{\min}^2 \leq E_i(s) \leq \frac{1}{2}m_i v_{\max}^2,$$

and therefore, we can conclude from Lemma 7.1 that vehicle i can maintain the speed at $\sigma < v_k$, such that as $\sigma \to 0$ we have $1/\sqrt{2E_i^*(s)/m_i} = 1/\sigma \to \infty$. As such, the lateral collision avoidance constraint can be satisfied as follows:

$$\int_0^L \frac{1}{\sqrt{2E_i^*(s)/m_i}}ds = \int_0^L \frac{1}{\sigma}ds \geq t_k(L+\delta(d_i)+l_k)-t_i(0).$$

Similarly, the satisfaction of the rear-end collision avoidance constraint (7.13) and the constraint to fulfil the crossing order (7.20) can be justified.

Thus, the proof ends.

III Proofs in Chapter 8

III-A Proof of Preposition 8.1

In view of (8.16a), the multi-objective function of a single vehicle i can be denoted by $J_i = W_1 J_{t,i} + W_2 J_{w,i}$, where $J_{t,i}(\zeta_i(s)) = t_i(L+S+l_i) - t_i(0) = \int_0^{L+S+l_i} \zeta_i(s)$. Thus, $J_{t,i}$ only depends on $\zeta_i(s)$ whereas $J_{w,i}$ solely depends on $F_{w,i}(s)$, as it can be seen in (8.15). Suppose that a feasible solution (denoted by the superscript $*$) of problem OCP 8.2, with control signals $\zeta_i^*(s)$, $F_{w,i}^*(s)$, and the states $E_i^*(s)$, $t_i^*(s)$, is found for which it holds that $\zeta_i^*(s) > 1/\sqrt{2(E_i^*(s))/m}$, and therefore we have

$$\zeta_i^*(s) = \frac{1}{\sqrt{2(E_i^*(s))/m}} + \Delta\zeta_i(s), \text{ with } \Delta\zeta_i(s) > 0, \tag{9.22a}$$

$$t_i^*(s) = t_i(0) + \int_0^s \frac{1}{\sqrt{2(E_i^*(\xi))/m}}d\xi + \int_0^s \Delta\zeta_i(\xi)d\xi, \tag{9.22b}$$

where the slack variable $\Delta\zeta_i$ inflates the travel time of the ith vehicle, and therefore it relaxes the rear-end and lateral collision avoidance constraints (e.g., if the velocity of CAV i

arriving at the CZ is much faster than that of CAV $i-1$ with $i, i-1 \in \mathcal{N}$, it does not need to decelerate for CAV $i-1$, avoiding energy loss). It is also possible to construct an alternative feasible solution $\left(\breve{\zeta}_i(s), \breve{E}(s), \breve{t}_i(s), \breve{F}_{w,i}(s)\right)$ with the same initial conditions $E_i^*(0) = \breve{E}_i(0)$ and $t_i^*(0) = \breve{t}_i(0)$, and

$$\breve{\zeta}_i(s) = \frac{1}{\sqrt{2(\breve{E}_i(s))/m_i}} = \zeta_i^*(s)\,, \tag{9.23}$$

with $\breve{E}_i(s) < E_i^*(s)$, and therefore by integrating (9.23) $\breve{t}_i(s) = t_i^*(s), \forall s$. The alternative solution corresponds to the case when the ith vehicle slows down for the preceding vehicle without inflating the time variable (tightness of (8.12) is guaranteed). In this context, the kinetic energy difference between the two solutions can be obtained by

$$\begin{aligned} \Delta E_i(s) &= E_i^*(s) - \breve{E}_i(s) = E_i^*(s) - \frac{1}{2} m_i \left(\frac{1}{\breve{\zeta}_i(s)}\right)^2 \\ &= E_i^*(s) - \frac{1}{2} m_i \frac{2E_i^*(s)}{(\sqrt{m_i} + \sqrt{2E_i^*(s)}\Delta\zeta_i(s))^2} > 0\,, \end{aligned} \tag{9.24}$$

where $\frac{1}{\breve{\zeta}_i(s)} = \frac{1}{\zeta_i^*(s)}$ owing to (9.23), and therefore can be determined by (9.22a). Such a kinetic energy difference results by the deviation between $\breve{F}_{w,i}$ and $F_{w,i}^*$, $\Delta F_{w,i}(s) = F_{w,i}^*(s) - \breve{F}_{w,i}(s)$. The relationship between $\Delta E_i(s)$ and $\Delta F_{w,i}(s)$ can be found by (8.3). For both solutions cases, by integrating both sides of the longitudinal dynamic equation, it holds that

$$E_i^*(s) = E_i(0) + \int_0^s F_{w,i}^*(\xi)d\xi - \int_0^s F_{r,i} d\xi + \varepsilon_i \int_0^s E_i^*(\xi)d\xi\,, \tag{9.25a}$$

$$\breve{E}_i(s) = E_i(0) + \int_0^s \breve{F}_{w,i}(\xi)d\xi - \int_0^s F_{r,i} d\xi + \varepsilon_i \int_0^s \breve{E}_i(\xi)d\xi\,, \tag{9.25b}$$

where $\varepsilon_i = -\frac{2f_{d,i}}{m_i}$ is a constant. By subtracting (9.25b) from (9.25a), we obtain

$$\Delta E_i(s) = \int_0^s \Delta F_{w,i}(\xi)d\xi + \varepsilon_i \int_0^s \Delta E_i(\xi)d\xi > 0, \forall s\,. \tag{9.26}$$

Since $\varepsilon_i < 0$ and $\Delta E_i(s) > 0$, then $\varepsilon_i \int_0^s \Delta E_i(\xi)d\xi < 0$, which implies from (9.26)

$$\int_0^s \Delta F_{w,i}(\xi)d\xi > 0\,. \tag{9.27}$$

Let $J_i^*(F_{w,i}^*, \zeta_i^*)$ and $\breve{J}_i(\breve{F}_{w,i}, \breve{\zeta}_i)$ denote the cost for a single vehicle i in both solution cases. Then, their difference can be calculated by

$$\begin{aligned} J_i^*(F_{w,i}^*, \zeta_i^*) - \breve{J}_i(\breve{F}_{w,i}, \breve{\zeta}_i) &= W_1 J_{t,i}(\zeta_i^*(s)) + W_2 J_{w,i}(F_{w,i}^*(s)) - W_1 J_{t,i}(\breve{\zeta}_i(s)) - W_2 J_{w,i}(\breve{F}_{w,i}(s)) \\ &= W_2(J_{w,i}(F_{w,i}^*(s)) - J_{w,i}(\breve{F}_{w,i}(s)))\,. \end{aligned} \tag{9.28}$$

In virtue of the quadratic form of $J_{w,i}(\cdot)$, (9.28) can be rearranged as

$$\begin{aligned} J_i^*(F_{w,i}^*,\zeta_i^*) - \breve{J}_i(\breve{F}_{w,i},\breve{\zeta}_i) &= W_2\int_0^{L+S+l_i} b_2F_{w,i}^*(s)^2+b_1F_{w,i}^*(s)+b_0\,ds \\ &\quad - W_2 \int_0^{L+S+l_i} b_2\breve{F}_{w,i}(s)^2+b_1\breve{F}_{w,i}(s)+b_0\,ds \\ &= W_2\int_0^{L+S+l_i}\left[b_2(F_{w,i}^*(s)+\breve{F}_{w,i}(s))+b_1\right]\Delta F_{w,i}(s)ds\,. \end{aligned} \tag{9.29}$$

Considering $F_{w,i} \in [F_{w,\min}, F_{w,\max}]$ with $F_{w,\max} = \max\{\frac{g_{r,i}}{r_{w,i}}T_{\max,i}\}$, $\forall i \in \mathcal{N}$, and the positiveness of the coefficients b_2, b_1, it can be inferred from the mean value theorem by following similar steps from (9.18) to (9.20) that

$$J_i^*(F_{w,i}^*,\zeta_i^*) - \breve{J}_i(\breve{F}_{w,i},\breve{\zeta}_i) \geq W_2\left(2b_2\overline{F}_{w,i}+b_1\right)\int_0^{L+S+l_i}\Delta F_{w,i}(s)ds\,, \tag{9.30}$$

where $\overline{F}_{w,i} \in [F_{w,\min}, F_{w,\max}]$. From (9.27), equation (9.30) implies that $J_i^*(F_{w,i}^*,\zeta_i^*) > \breve{J}_i(\breve{F}_{w,i},\breve{\zeta}_i)$ if $2b_2\overline{F}_{w,i}+b_1 > 0$, which is guaranteed by (8.13) in Assumption 8.3:

$$\left(2b_2\overline{F}_{w,i}+b_1\right) > 2b_2F_{w,\min}+b_1 > 0\,. \tag{9.31}$$

Hence, given a solution set $\left(\zeta_i^*(s), F_{w,i}^*(s), E_i^*(s), t_i^*(s)\right)$ without holding the equality condition of (8.12) (subject to a slack variable $\Delta\zeta_i(s)$), there always exists an alternative solution $\left(\breve{\zeta}_i(s), \breve{F}_{w,i}(s), \breve{E}_i(s), \breve{t}_i(s)\right)$ with guaranteed tightness that is more optimal in terms of the individual cost J_i, which in turn applies to all CAVs (i.e., $\forall i \in \mathcal{N}$).

Thus, the proof ends.

III-B Proof of Lemma 8.1

Consider a candidate solution $\left(\zeta_i^*(s), F_{w,i}^*(s), E_i^*(s), t_i^*(s)\right)$ is found, which violates the lateral collision avoidance constraint (8.7), then we have,

$$\begin{aligned} & t_i^*(L) < t_h(L+S+l_h) \\ \Rightarrow\ & t_i(0)+\int_0^L \zeta_i^*(s)ds < t_h(L+S+l_h) \\ \Rightarrow\ & \int_0^L \frac{1}{\sqrt{2E_i^*(s)/m_i}}ds < t_h(L+S+l_h) - t_i(0), \end{aligned}$$

where $t_h(L+S+l_h)$ and $t_i(0)$ are preknown constants information. Since E_i is bounded by (8.8) and we can conclude from Lemma 8.1 that vehicle i can maintain the speed at σ, such that as $\sigma \to 0$ we have $1/\sqrt{2E_i^*(s)/m_i} = 1/\sigma \to \infty$. As such, the lateral collision avoidance constraint can be satisfied as follows:

$$\int_0^L \frac{1}{\sqrt{2E_i^*(s)/m_i}} ds = \int_0^L \frac{1}{\sigma} ds \geq t_h(L+S+l_h) - t_i(0).$$

Similarly, the satisfaction of the rear-end collision avoidance constraint (8.6) and the constraint to fulfil the crossing order (8.9) can be justified.

III-C Proof of Corollary 8.1

Assume a feasible solution sequence is found within an MPC horizon with $k+j+1=\alpha_1$ such that:

$$E_i^*(k+j+1|k) = E_i^*(k|k) + \sum_{j_k=0}^{j} \{F_{w,i}^*(k+j_k|k) - F_{r,i} + \varepsilon_i E_i^*(k+j_k|k) + \omega_{E,i}(k+j_k|k)\}\Delta s \tag{9.32a}$$

$$t_i^*(k+j+1|k) = t_i^*(k|k) + \sum_{j_k=0}^{j} \{\zeta_i^*(k+j_k|k) + \omega_{t,i}(k+j_k|k)\}\Delta s \tag{9.32b}$$

$$\zeta_i^*(k+j_k|k) \geq \frac{1}{\sqrt{2E_i^*(k+j_k|k)/m}} \tag{9.32c}$$

$$t_i^*(k+j+1|k) - \hat{t}_h^{\mathcal{L}} \geq 0, \tag{9.32d}$$

$$t_i^*(k+j+1|k) - \hat{t}_h^{\mathcal{O}} \geq 0, \tag{9.32e}$$

$$\textbf{given: } E_i^*(k|k) = E_i^*(k), t_i^*(k|k) = t_i^*(k). \tag{9.32f}$$

Considering $\zeta_i^* = \breve{\zeta}_i + \Delta\zeta_i$, where $\breve{\zeta}_i$ is the solution in (9.23) that satisfies Proposition 8.1 with $\Delta\zeta_i > 0$, the constraint (9.32d) can be expanded as:

$$\begin{aligned}
0 &\leq t_i^*(k+j+1|k) - \hat{t}_h^{\mathcal{L}} \\
&\leq t_i^*(k) + \sum_{j_k=0}^{j} \{\zeta_i^*(k+j_k|k) + \omega_{t,i}(k+j_k|k)\}\Delta s - \hat{t}_h^{\mathcal{L}} \\
&\leq t_i^*(k) + \sum_{j_k=0}^{j} \{\breve{\zeta}_i(k+j_k|k) + \Delta\zeta_i(k+j_k|k) + \omega_{t,i}(k+j_k|k)\}\Delta s - \hat{t}_h^{\mathcal{L}} \\
&\leq \left[t_i^*(k) + \sum_{j_k=0}^{j} \{\Delta\zeta_i(k+j_k|k) + \omega_{t,i}(k+j_k|k)\}\Delta s \right] + \sum_{j_k=0}^{j} \breve{\zeta}_i(k+j_k|k)\Delta s - \hat{t}_h^{\mathcal{L}}.
\end{aligned} \tag{9.33}$$

In virtue of the augmented objective function (8.36), it can be claimed that if there exists a feasible solution, by finely tuning $\Delta t_i^{\mathcal{L}}$ to enforce the CAV i to accelerate at a slow rate or start to decelerate before step k, the feasible solution with initial condition $\breve{t}_i(k)$ at step k can be found such that:

$$\breve{t}_i(k) \geq t_i^*(k) + \sum_{j_k=0}^{j} \{\Delta\zeta_i(k+j_k|k) + \omega_{t,i}(k+j_k|k)\}\Delta s\,, \tag{9.34}$$

and constraint (9.33) can be reformulated as

$$\breve{t}_i(k) + \sum_{j_k=0}^{j} \breve{\zeta}_i(k+j_k|k)\Delta s - \hat{t}_h^{\mathcal{L}} \geq 0\,. \tag{9.35}$$

Thus, the feasible solution with its initial condition satisfying (9.34) and (9.35) consequently satisfies the tightness of (8.12). By analogy to the forgoing analysis of (9.32d), the same design approach can be applied to $\Delta t_i^{\mathcal{O}}$. As a result, by suitably selecting the value of parameter $\Delta t_i^{\mathcal{L}}$ and $\Delta t_i^{\mathcal{O}}$, the solution of the decentralised MPC framework for autonomous intersection can be guaranteed to be valid under Proposition 8.1.